A TWO-FLUID MODEL FOR PARTICLE ACCELERATION AND DYNAMICS IN BLACK-HOLE ACCRETION FLOWS

by

Jason P. Lee
A Dissertation
Submitted to the
Graduate Faculty
of
George Mason University
In Partial fulfillment of
The Requirements for the Degree
of
Doctor of Philosophy
Physics

Committee:

____________________ Dr. Peter A. Becker, Dissertation Director

____________________ Dr. Mario Gliozzi, Committee Member

____________________ Dr. Jeng-Eng Lin, Committee Member

____________________ Dr. Maria Dworzecka, Acting Department Chair

____________________ Dr. Donna M. Fox, Associate Dean, Office of Student Affairs & Special Programs, College of Science

____________________ Dr. Peggy Agouris, Dean, College of Science

Date: ____________________ Fall Semester 2015
George Mason University
Fairfax, VA

A Two-Fluid Model for Particle Acceleration and Dynamics in Black-Hole Accretion Flows

A dissertation submitted in partial fulfillment of the requirements for the degree of Doctor of Philosophy at George Mason University

By

Jason P. Lee
Master of Science
George Mason University, 2008
Bachelor of Science
James Madison University, 2005

Director: Dr. Peter A. Becker, Professor
Department of Physics and Astronomy

Fall Semester 2015
George Mason University
Fairfax, VA

Dedication

I dedicate this dissertation to my family for their love and support through my entire graduate school experience, and to my lovely wife EJ, with whom I wouldn't have met had I not been crazy enough to pursue this adventure for myself.

Acknowledgments

I would like to thank the following people who made this possible: my family for providing me food and shelter whenever I needed it, and for being patient through this whole ordeal. To EJ for her patience, love and support while we both tackled our respective degree requirements. To Alex and her family for their love and support as well. To John and Tiffany, with whom our conversations into our respective work with our shared advisor helped to balance out the overall conceptual picture into what we all were doing. To Maria for giving me the chance to pursue this degree without having the typical background. To Becky, Mary and Joe for their teachings and guidance through my entire graduate academic career. And finally to my advisor PAB, whose mentoring and knowledge is inspirational that I hope to continue to follow in my career and one day, guide students the way he taught me.

Table of Contents

List of Tables

List of Figures

Abstract

A TWO-FLUID MODEL FOR PARTICLE ACCELERATION AND DYNAMICS IN BLACK-HOLE ACCRETION FLOWS

Jason P. Lee, PhD

George Mason University, 2015

Dissertation Director: Dr. Peter A. Becker

Hot, tenuous Advection-Dominated Accretion Flows (ADAFs) are ideal sites for the Fermi acceleration of relativistic particles at standing shock waves in the accretion disk. Previous work has demonstrated that the shock-acceleration process can be efficient enough to power the observed, strong outflows in radio-loud active galaxies such as M87. However, the dynamical effect (back-reaction) on the flow, due to the pressure of the relativistic particles, has not been previously considered, as this effect can have a significant influence on the disk structure. We reexamine the problem by creating a new two-fluid model that includes the dynamical effect of the relativistic particle pressure, as well as the background (thermal) gas pressure. The new model is analogous to the incorporation of the cosmic-ray pressure in the two-fluid model of cosmic-ray-modified supernova shock waves. We derive a new set of shock jump conditions and obtain dynamical solutions that describe the structure of the disk, the discontinuous shock, and the outflow. From this, we show that smooth (shock-free) global flows are impossible when relativistic particle diffusion is included in the dynamical model.

Chapter 1: Introduction

When it comes to science, we often seek to explore the unknown, whether it be on Earth or among the stars. In Astronomy, we seek to understand the Universe by observing all the celestial bodies and phenomena that we can. No matter the field, often the goal/pursuit is the same: the hope that by obtaining a better grasp of the cosmos, perhaps we gain a better perspective of our own existence.

In the case of black holes, it is generally accepted that anything (e.g. matter) in proximity to its gravitational field is immediately sucked in; a one-stop destination. But we know that's not the complete picture. For one thing, matter is not immediately sucked in. Extensive observations show that matter experiences an effect similar to being trapped in a whirlpool, or a marble going down a drain. The circular area surrounding the center of a black hole is known as the accretion disk, in which matter within this disk spirals towards the event horizon. That should be the end of it, but another curiosity emerges as well. For certain black-hole systems, a detectable outflow-burst of relativistic particles (which looks similar to an outflow from a jet engine) appears to emit from the disk itself, in a bipolar formation from a region just outside the event horizon. An example of this can be seen in an artistic expression for Messier 87 (M87, also known as Virgo A or NGC 4486) given in Figure 1.1. These observations have boggled astronomers and physicists alike, because it brings into question whether our perceptions of black holes are correct. If nothing can escape from being sucked into a black hole, then why are we seeing these outflows? Even recently, Professor Stephen Hawking postulated a work-around to the information-loss-paradox by suggesting that 'information' can indeed escape the event horizon itself, but it's more of a mirrored-jumbled version of the original information and practically useless (Feltman 2015).

Determining how anything can escape from a black hole's gravity has been an ongoing study for many years, and has evolved into a broad subject. While the question has been

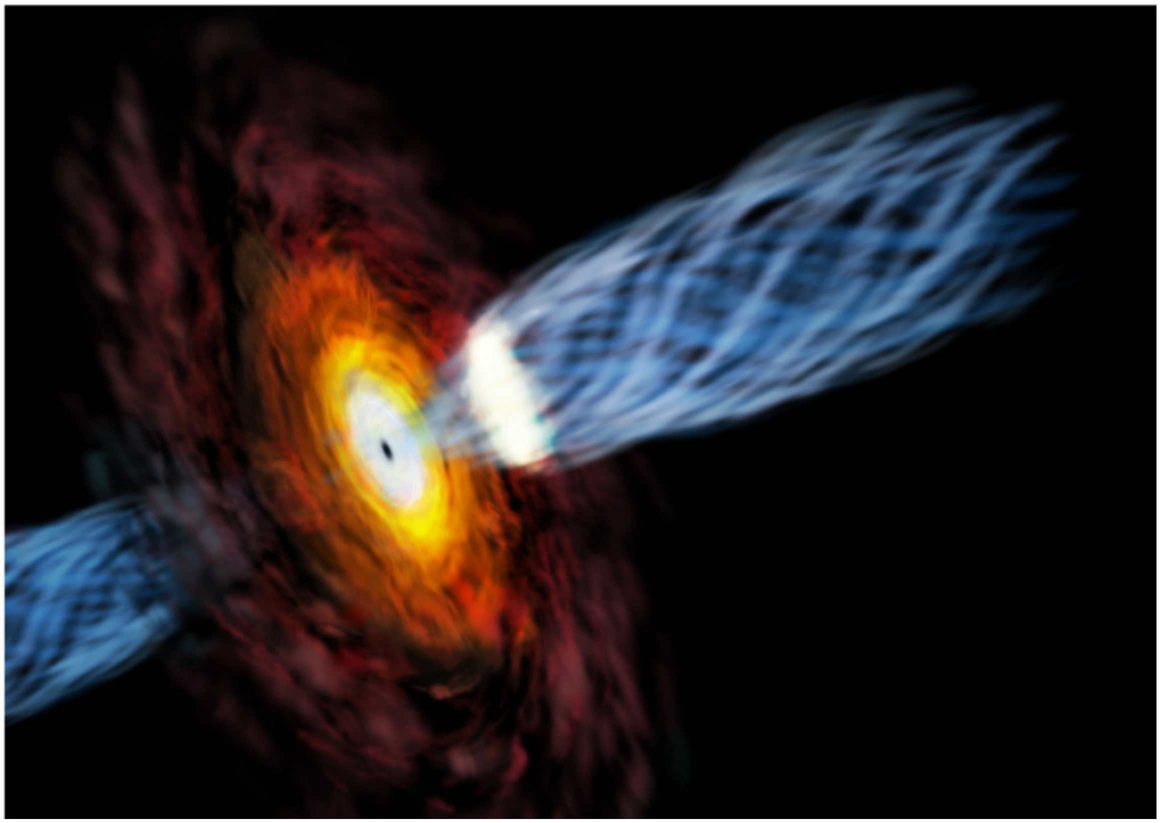

Figure 1.1: Radio-loud galaxy M87 (also known as NGC 4486). This is an artist rendition of the accretion disk showing the bipolar jetted outflows, found at: http://i.space.com/images/i/000/011/929/original/black-hole-jet.jpg?1315414855.

addressed in one form or another, this work continues the trend focusing on one topic, specifically the formation of the jets themselves, while at the same time reassessing the roots of its theoretical framework. It should be noted to the reader that this chapter serves to provide a *generalized* overview of the field, without delving too much into the intricate details.

1.1 Active Galactic Nuclei

1.1.1 Overview

Active galactic nuclei (AGNs) have been studied for several decades using a wide range of multi-wavelength observational data. AGNs are galaxies containing supermassive (millions to billions of $M_{\odot}$) black holes at their centers (or nuclei). They are typically known as quasars, blazars, and Seyfert galaxies. A point of interest are the bipolar, bulk relativistic outflows (or jets) commonly seen from some AGNs (see Figure 1.1 for example). These jets are matter outflows propagating away at relativistic speeds; these jets are believed to contain high-energy relativistic particles. Depending on whether or not an AGN exhibits a strong jet will classify it in one of two categories, the 'radio loud' or the 'radio quiet.' And in each category, AGNs are distinguished by their emission properties. This radiation includes X-rays, γ-rays, ultraviolet and radio waves, where specific AGNs are typically strong in one, and weak in others.

1.1.2 Mass and Luminosity

The total radiation luminosity, L, generated near a black hole is proportional with its mass, M, and the accretion rate, $\dot{M}$. Astrophysical black-hole sources are measured in units of solar mass ($M_{\odot}$), and are categorized i.e. as stellar-mass ($\sim 3 - 10\ M_{\odot}$), which have been detected in our own galaxy, as well as intermediate-mass ($\sim 10^2 - 10^4\ M_{\odot}$), which have been observed in nearby galaxies. Larger black holes are found at the center of their host galaxy. These can range from massive ($\sim 10^5 - 10^7\ M_{\odot}$) black holes in the center of our galaxy, to supermassive ($\sim 10^8 - 10^9\ M_\odot$) black holes in more distant galaxies. Because of its mass, a supermassive black hole (SMBH) at the center of an active galaxy can be brighter than the combined luminosities of all the stars in that galaxy. The total luminosity from a SMBH typically exceeds $\sim 10^{44}$ ergs s^{-1} and can reach $\sim 10^{49}$ ergs s^{-1}. To put that into perspective, our own Sun has a luminosity of $L_\odot = 3.8 \times 10^{33}$ erg/s, and a large spiral galaxy (like the Milky Way) has a stellar luminosity $\sim 10^{45}$ ergs s^{-1}. The critical quantity to be obtained from this is the ratio of the accretion rate and the black hole mass ($\dot{M}/M$), which is the determining factor in the observed radiation and outflow power that's discussed later on.

1.2 Observations of AGNs

1.2.1 General History

Observations of AGNs started in the early twentieth century and up to the mid-1950's, where Seyfert galaxies were identified as the first class due to their similar emission spectra on the basis of high central surface brightness, indicative of stellar-appearing cores. They also display strong high-ionization emission lines. With the application of radio observatories in the late 1950's, astronomers were able to observe galaxies that had strong radio emission, the first an associated strong optical stellar source being 3C-48, with a magnitude 16 times greater than the Sun (Matthews and Sandage 1963). The observed emission spectra were confusing at the time until the sixties when Maarten Schmidt (1963) realized that these quasi-stellar radio sources (or quasars) were point-like radio emitters, whose optical counterparts displayed unusual spectra with prominent emission lines were redshifted systems. The large redshifts indicated great distances, according to Hubble's Law, and therefore the redshifts implied that quasars are extremely luminous, commonly producing 10^{46} erg s^{-1}. Further sensitive imaging of the nebulosities, which often were seen to surround quasars, indicated that they are the nuclei of galaxies. As such, quasars were identified to be the higher-luminosity counterparts of the compact nuclei of Seyfert galaxies.

1.2.2 Radio-loud vs. Radio-quiet

Quasi-Stellar Objects (QSOs) are denoted as either 'radio-quiet' or 'radio-loud'. Quasars are radio-loud QSOs, and comprise roughly $\sim 5-10\%$ of the QSO population. The two classes of QSOs are distinguished by the value of the radio-optical flux ratio $R_{\text{r-o}}$ (Kellermann et al. 1989). Radio-loud QSOs have $R_{\text{r-o}} \geq 10$, while radio-quiet QSOs have $0.1 < R_{\text{r-o}} < 1$.

Radio galaxies are described broadly in terms of being 'extended' (or spatially resolved) and 'compact' (or spatially unresolved), and each type has different spectral characteristics. Generally speaking, radio galaxies have been observed to contain two 'lobes' of radio emission symmetrically located on either side of the central core, along with additional synchrotron radiation (usually in the X-ray range) from relativistic electrons that form jets connecting the core with the lobes. Compact sources are typically found to be optically thick (more opaque) than extended sources, which are optically thin (less opaque). This means that compact sources (which are core-dominated) have stronger X-ray emissions than extended sources, which are lobe-dominated and have higher radio emissions. For the extended radio structures, they are further divided into classes FR I and FR II, where FR I sources are considered 'limb-darkened', meaning their surface luminosity is brightest in the center while decreasing towards the edges, thus weaker radio emissions. Whereas FR II sources are considered 'limb-brightened', meaning their surface luminosity remains bright throughout the extended lobes. M87, as well as Cygnus A (see Figure 1.2), are examples of FR II, radio-loud quasars (with Cygnus A having extended emission). In this dissertation we shall look at two specific AGNs (M87 and Sgr A*), whose radio, X-ray, and optical observations are given in Figures 1.3, 1.4 and 1.5, respectively. Additionally, the astrophysical properties for both sources are given in Table 1.1. What's also interesting about the distinction between the two classes is how they relate to the observations pertaining to the jets (see § 1.2.5).

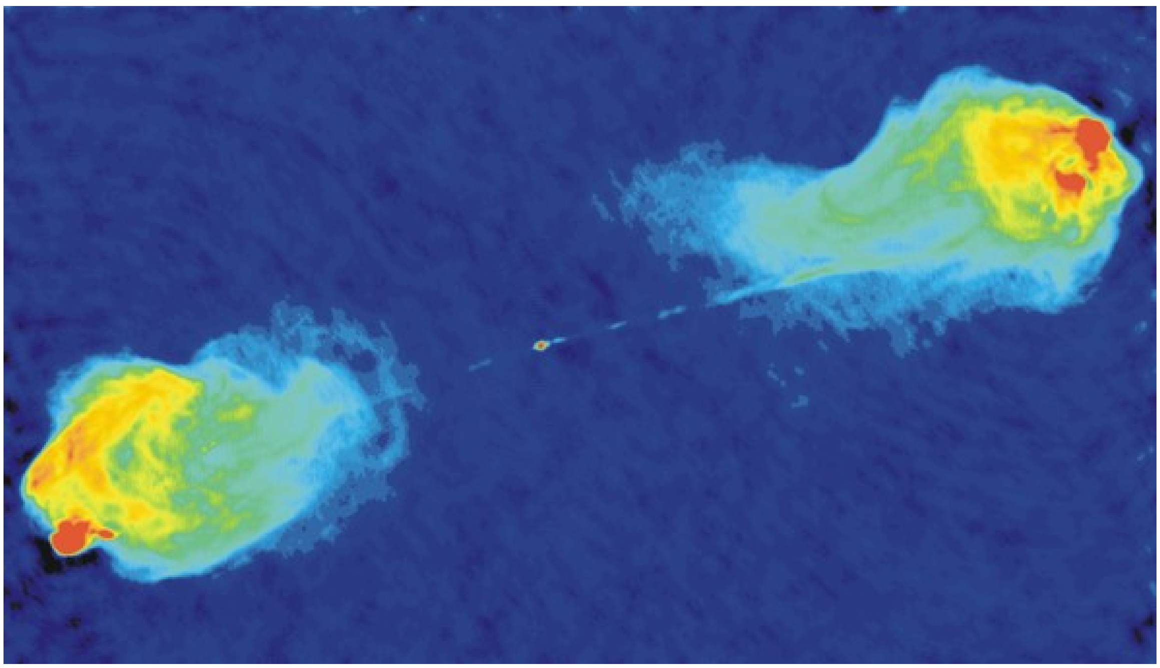

Figure 1.2: Radio galaxy Cygnus A, where we see the radio jet moving outward from the central engine to and the lobes. The red areas are indicative of regions with bright radio emission, while the blue regions show fainter emission. This image was taken from: http://images.nrao.edu/260.

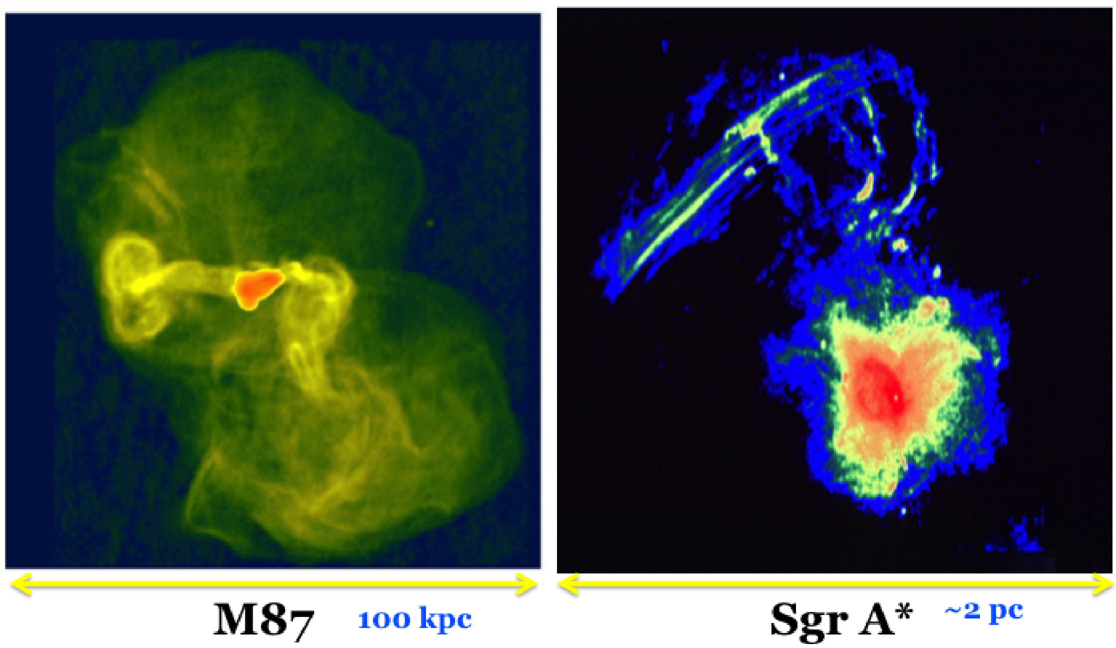

Figure 1.3: Radio emission output of (left-panel) M87 showing the central core and the two radio lobes, taken by the VLA radio telescope: http://images.nrao.edu/AGN/Radio_Galaxies/57, and (right-panel) of Sgr A* showing the central core, taken from: http://www.eventhorizontelescope.org/science/images/GalCntr_lg.jpg. Both images indicate the scaling factors observed for each source.

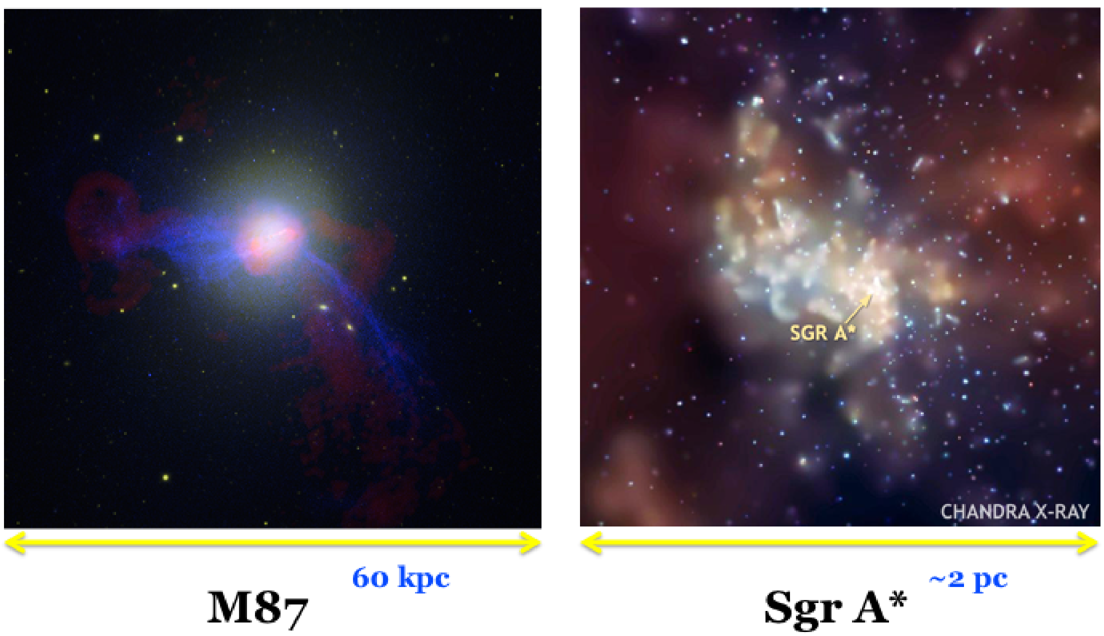

Figure 1.4: X-ray images of (left-panel) M87 taken from: https://www.spacetelescope.org/images/heic0815j/, and (right-panel) of Sgr A* taken from: https://universe-review.ca/F05-galaxy10.htm. Both images indicate the scaling factors observed for each source.

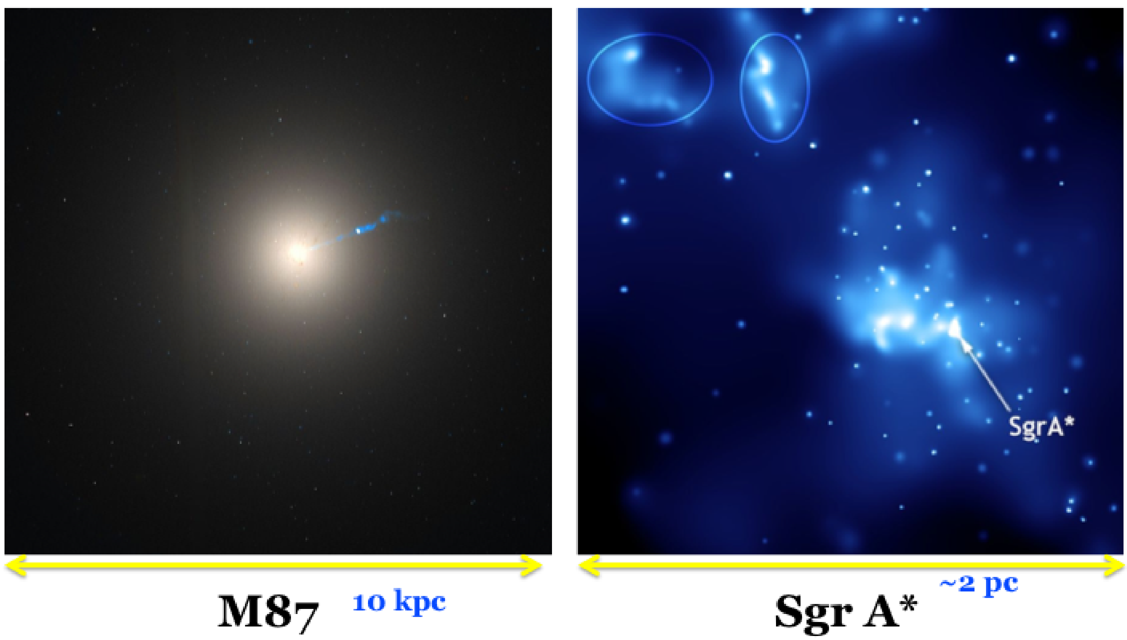

Figure 1.5: Optical images of (left-panel) M87, taken from: http://phys.org/news/2014-04-entire-star-cluster-thrown-galaxy.html, and of (right-panel) Sgr A* taken from: https://en.wikipedia.org/wiki/Sagittarius_A∗. Both images indicate the scaling factors observed for each source.

Table 1.1: M87 and Sgr A* (Galactic Center) Properties.

	M87	**Sgr A***
X-ray L (ergs s^{-1}):	7×10^{40}	2×10^{35}
Radio L (ergs s^{-1}):	5×10^{41}	1×10^{36}
Distance:	16.4 Mpc	8.0 kpc
Mass ($M_\odot$):	3.0×10^{9}	2.6×10^{6}
Outflow Rate ($M_\odot$ yr^{-1}):	0.13	8.8×10^{-7}
$L_{\rm jet}$ (ergs s^{-1}):	5.5×10^{43}	5.0×10^{38}

1.2.3 Observational Methods for Determining the Mass of AGNs

The consensus is that it's likely that many normal local galaxies (not just active ones) harbor supermassive black holes. Although when in doubt, there are two general lines of argument used to validate the existence of black holes in AGNs, which are discussed overtly by several sources (e.g. Peterson 1997; Dermer & Menon 2009; Abramowicz et al. 1999). We need to measure the total mass within a given volume, and argue that nothing besides a black hole can be that dense. This is done by using Kepler's laws to measure the stellar or gaseous velocities in the vicinity of the black hole.

The first method is to estimate the central mass by tracking the detailed orbital motion of stars in the center of the AGN. However this cannot be done in distant galaxies, but it has been applied to determine the mass of the central black hole in the Milky Way. The second method focuses on the distortion that appears in the emission line profiles due to the influence of strong gravity, resulting from the presence of a black hole. While the first method is considered the most reliable, both of these arguments led to the classifications of M87 and Sgr A* as they are known today. Though it should be noted that another technique known as reverberation mapping is used to estimate the volume and density structure of the accreting gas from variability data (via the light travel time arguments as a result of the changes in the central UV flux) and mass from the luminosity. It's a way to study the structure of the central engine and the hot corona overlaying it, however it is not considered a means for demonstrating that the central object is a black hole.

1.2.4 Observing M87 and Sgr A*

The radio galaxy known as M87 is an AGN whose black hole presence was revealed by measuring the velocity and thermal properties of the matter emitting close to its central mass. This dates back to the ground-based observations made in the late 70's, when Sargent et al. (1978) showed that M87's stellar velocity dispersion increases to 350 km s^{-1} in the innermost 1.11" from the nucleus (Kormendy & Richstone 1995). Ford et al. (1994) was able to observe this galaxy using the Planetary Camera, and likewise Harms et al (1994) with the Faint Object Spectrograph onboard the Hubble Space Telescope (hereafter HST). The images showed evidence of the presence of a disk-like structure of ionized gas in the innermost region (a few arc seconds). What was provided from the spectroscopy was a measure of the velocity of the gas at an angular distance of 0.25" from the nucleus, which corresponds to $\sim$ 20 parsecs, or $\sim 6 \times 10^{19}$ cm. This determines a velocity difference of $\sim$ 920 km s^{-1} as the galaxy recedes from Earth on one side, and approaches it on the other, in the galaxy's reference frame. This implies that the central object has a mass of $\sim 3 \times 10^9\ M_\odot$.

In the case of M87, the Event Horizon Telescope has been used to detect emission from the vicinity of the event horizon itself (Broderick et al. 2015). The fact that the result spectra lie in the infrared-optical range, rather than in the X-ray range, implies the presence of relatively low temperature matter, which is expected near the event horizon. In the case of MCG-6-30-15, evidence for the presence of a supermassive black hole is provided via the Doppler interpretation of the observed double-peaked X-ray spectra, which indicate simultaneous, extreme blueshifts and redshifts, as shown in Figure 1.6. No other object, other than a black hole, possesses a mass concentration that can explain these observations.

It should be noted that M87 is considered a possible blazar, and as such has served to be the closest evidence that blazars likewise contain black holes at their centers. This AGN is also considered a variable black-hole on a timescale of weeks (Broderick et al. 2011), which can be seen in the form of bright knots propagating away from the radio core (see

Figure 1.11b of the jet observed from the Very Long Baseline Interferometry, or VLBI). Figure 1.7 illustrates its multi-wavelength energy spectrum, which shows a double-hump in the lower part of the spectrum. The low-frequency hump is believed indicative of synchrotron radiation, while the high-frequency hump results from inverse-Compton scattering (see § 1.5.3).

There have been similar spectroscopy observations done with the HST that revealed high stellar velocities in the central regions of other normal galaxies, which show no evidence of an active nucleus (e.g. Ford et al. 1998; Madejski 1999). The presence of massive ($10^8 - 10^9$ $M_\odot$) black holes in the center of these galaxies is the only thing that can explain how such high velocities can exist in their innermost regions. For instance, the infrared data and velocity measurements gathered for our Milky Way galaxy (or Sgr A*) has revealed its center to contain a 'modest' nuclear black hole with a mass of $\sim 3 \times 10^6$ $M_\odot$. For Sgr A* the velocity detection technique is direct imaging of the relativistic star velocity orbital motion, which can be seen in Figure 1.8. This data was obtained from the ground (cf. Eckart & Genzel 1997) at a much higher resolution than the data gathered from the HST for external galaxies. Hence, Sgr A* is considered a supermassive black hole containing a 'nearly quiescent' active galactic center, so it's considered a low-level AGN compared to M87. In both cases, the technique reveals relativistic orbital motion, implying a very compact mass; thus a central black hole in both cases. These and other observations led to the implication that supermassive black holes are rather common and may inhabit as much as half of all galaxies, some may well be the quasars that were observed in the past (e.g. Ford et al. 1998, Ho et al. 1998). Figure 1.9 shows the multi-wavelength energy spectrum for Sgr A* . It should be noted that the energy spectra for both M87 and Sgr A* shows the general pattern that the luminosity for supermassive AGNs carries observations across the whole energy spectrum.

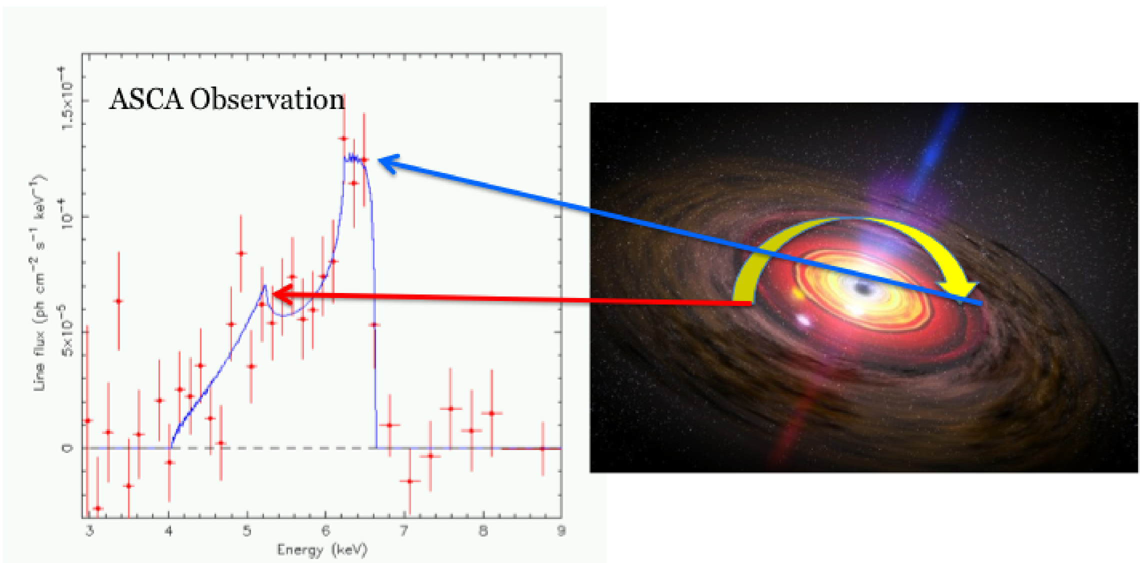

Figure 1.6: AGN iron line profile of MCG-6-30-15 observed by the ASCA satellite (left-panel), taken from: http://science.nasa.gov/science−news/science-at-nasa/2001/ast23oct_1/, in reference to an artistic representation of an AGN (right-panel) taken from: https://www.uni-goettingen.de/en/216897.html. The yellow arrow around the AGN indicates direction of rotation, in which the right-side is observed from Earth, and the left-side is moving away from Earth. Hence the first peak signifies extreme redshift (denoted with a red arrow accordingly), while the second peak represents extreme blueshift and is given by a blue arrow. Extreme redshift implies an orbital velocity of $c/3$, evidence for a black hole in the center of the galaxy.

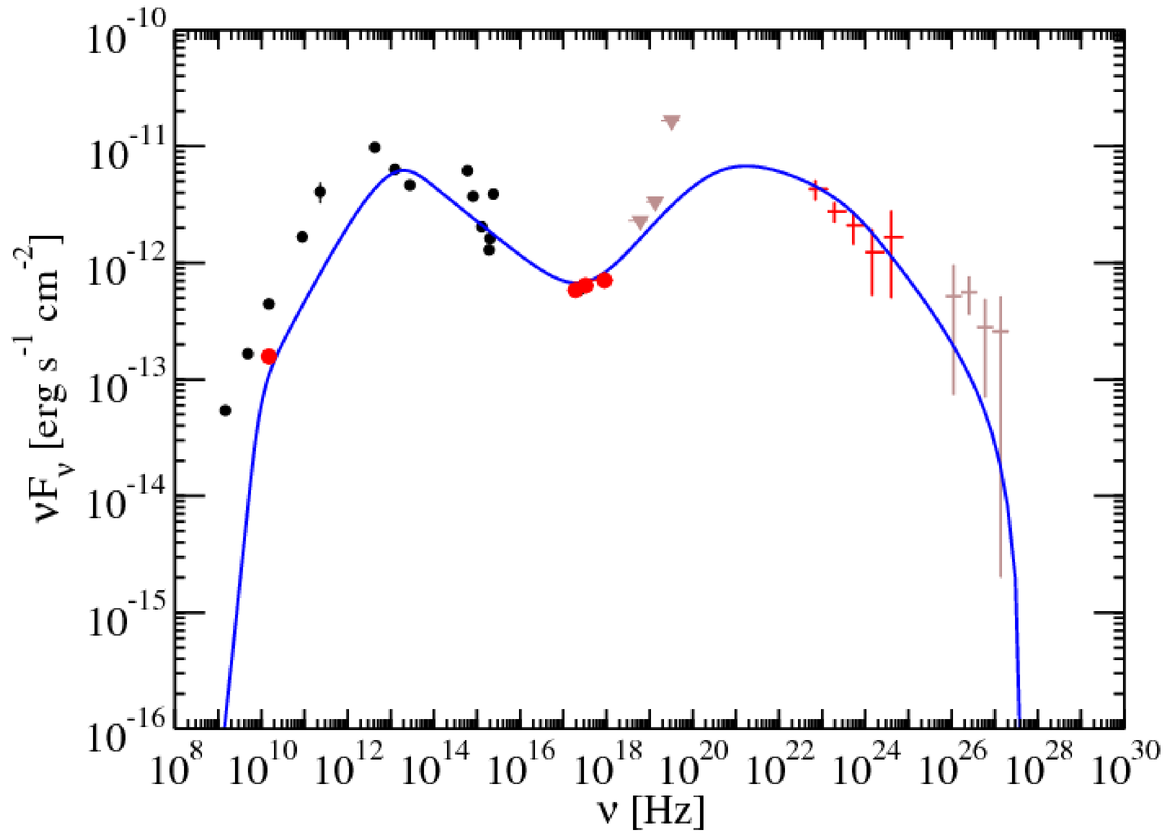

Figure 1.7: Taken from Abdo et al. (2009). SED of M87. The red are (in order) the LAT spectrum, the 2009 VLBA, and Chandra X-ray measurements of the core. The light brown represent (in order) the 2004 TeV spectrum and the X-ray limits worked out in the paper. The black circles are measurements of the compact core taken from VLA (Biretta et al. 1991), IRAM (Despringre et al. 1996), SMA (Tan et al. 2008), Spitzer (Shi et al. 2007), Gemini (Perlman et al. 2001), HST optical/UV (Sparks et al. 1996), and Chandra (Marshall et al. 2002). The blue line is a model fit outlined in the paper.

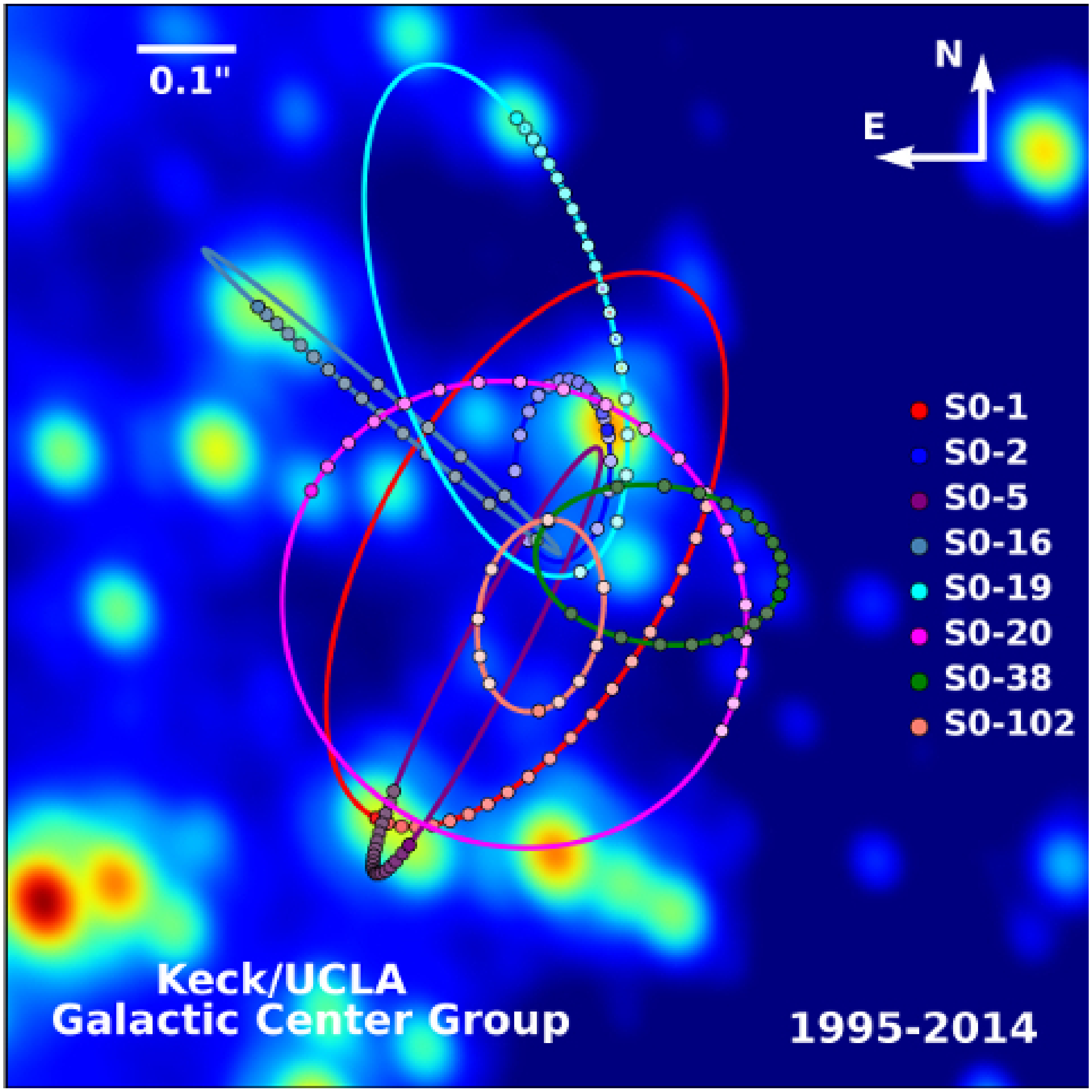

Figure 1.8: Evidence for a black hole at the Galactic center, taken from: http://www.galacticcenter.astro.ucla.edu/blackhole.html. Stellar orbits are within the central arc second of our Galaxy. The orbits imply the presence of a compact mass, in which the central mass is non-stellar, thus implying the presence of a black hole.

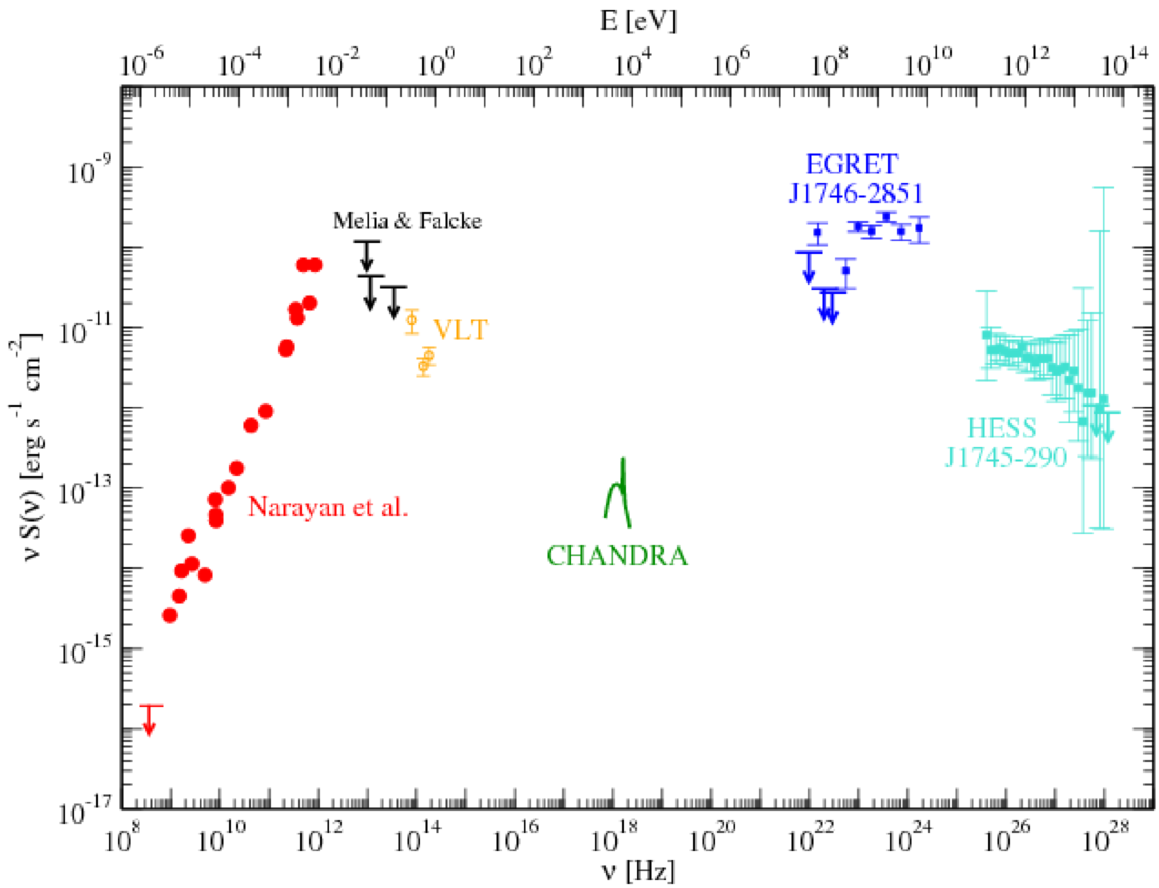

Figure 1.9: Taken from Regis & Ullio (2008). Multiwavelength spectrum of Sgr A* , see paper for full details.

1.2.5 Relativistic Jets

Which brings us to the point of interest in this thesis: the relativistic jets, which have been observed in many radio galaxies (in addition to the compact and extended components) and have been reviewed extensively (see Frank et al. 2002; Peterson 1997; Carroll & Ostlie 1995; Abramowicz et al. 1999; Novikov & Thorne 1973; Rees 1984; Ford et al. 1994). Typically seen in FR II AGNs like M87 (Figure 1.10a) and Sgr A* (Figure 1.10b), the jets themselves are considered proton-electron beams; streams of hot, highly collimated, magnetized gas that appear narrow, fast and straight, and seen ejected from the compact core (see Figure 1.11), extending out to the outer lobe at a few kpc. Figure 1.12 shows the short-timescale variability of the VLBI images of blob variability in M87, indicating that the jet is not a continuous plasma beam, but consists of blobs of various sizes. It should be noted that the jets can also be considered electron-positron or neutron beams, as long as they are charge neutral. The physical observation of the jet was actually first mentioned by Curtis (1918) while observing M87, who described it as "a curious straight ray [that] lies in a gap in the nebulosity....apparently connected with the nucleus by a thin line of matter....[which] is brightest at its inner end." Though he didn't describe it as a 'jet', the term itself did not describe it until it was coined by Baade & Minkowski (1954).

Though jets sometimes appear stronger on one side of the radio source and fainter on the other (also known as the counter-jet, if any), this is usually attributed to Doppler beaming, which refers to the perspective of the observer and the instrument in question. Hence, it's generally believed that the jets are bipolar, moving away in opposite directions from compact source. However, the direction in which the jet is moving can be affected by either the spin axis of the black hole or the angular momentum of the accretion disk. Since the jets have radiation from the radio (which the VLBI can study) to the γ-ray spectrum, they are considered a secondary source for the observed emission spectrum (with the compact torus being the primary source).

Over the course of the last century, several theoretical models have emerged to explain

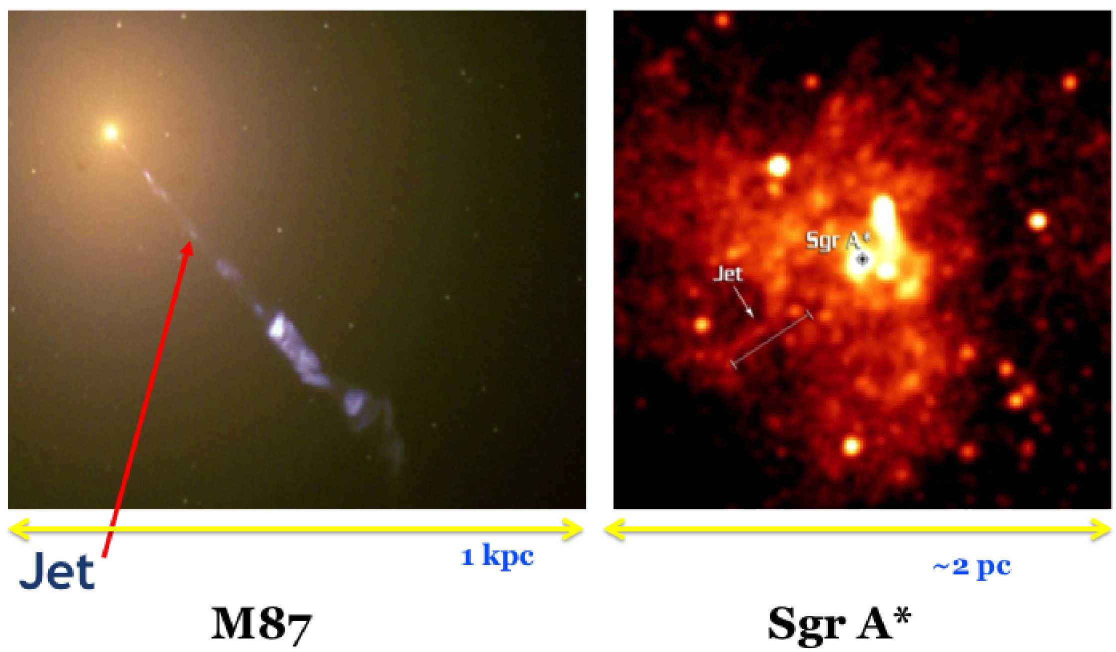

Figure 1.10: (left-panel) Radio-loud galaxy M87 (also known as NGC 4486), taken from the Hubble Space Telescope. Pictured is the observed jetted outflow, found at: http://hubblesite.org/newscenter/archive/releases/2000/20/image/a/. (right-panel) A closer examination of the core of Sgr A* with the jet emanating from the base of the disk, taken from the Chandra X-ray observatory: http://chandra.harvard.edu/photo/2003/0203long/0203long_xray_jet_label.jpg. Both images indicate the scaling factors observed for each source.

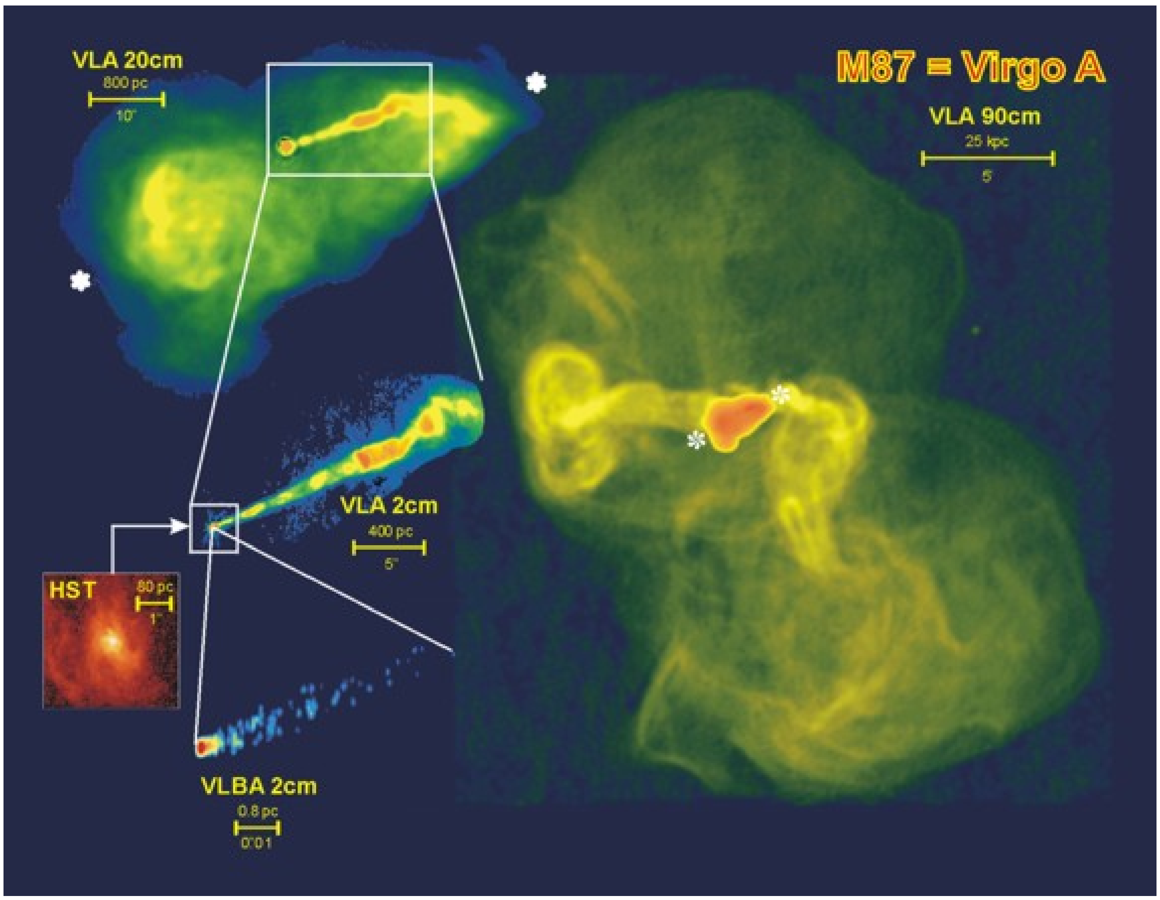

Figure 1.11: Radio emission output of M87 showing a closer examination of the core with the jet emanating from the base of the disk, taken from http://images.nrao.edu/AGN/Radio_Galaxies/270.

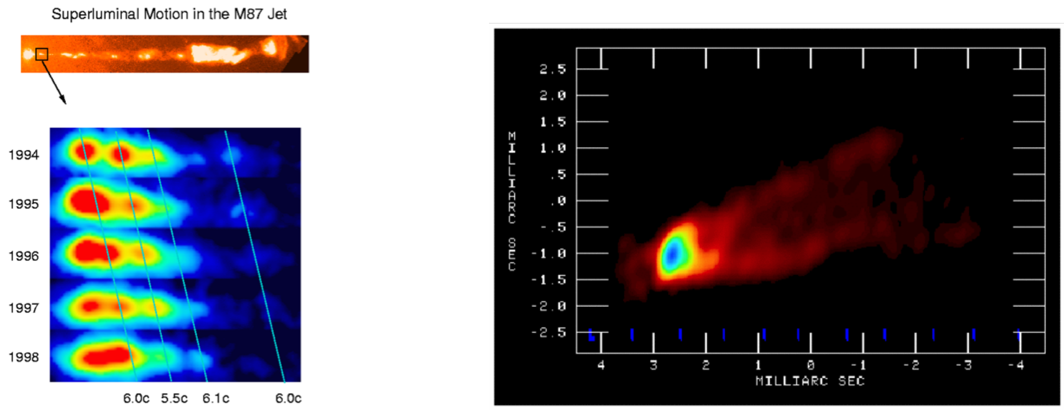

(a) (b)

Figure 1.12: (a) Sequence of Hubble images showing the short-timescale variability of the VLBI images of blob variability in M87, taken between 1994 and 1998 with the Faint Object Camera on the Hubble Space Telescope (http://www.stsci.edu/ftp/science/m87/m87.html). The slanting lines track the moving features and correspond to a broader image, with the speeds given in units of c. (b) Still image from a movie of the M87 jet at 43 GHz with the VLBA, taken from: http://www.aoc.nrao.edu/ cwalker/M87/.

how the jets are produced. However, it should be clear to the reader that these remain broad and ambiguous because at the present, the mechanism responsible for this is yet to be understood. This is primarily due to the fact that observations are still limited to the low resolution of astronomical instruments, thus it makes it extremely difficult to justify (or verify) the logistics behind one model over another. Though, extensive research in this field has at least produced a general consensus. In the next section, we now transcend from the observations to theoretical backbone of black hole accretion.

1.3 Earlier Model Approaches

1.3.1 Rotating vs. Stationary Black Holes

The primary distinction in all of the theoretical models starts at the core, specifically the black hole, and whether it's spinning (rotating) or not (stationary). Rotating black holes are subject to the laws that govern General Relativity (GR), specifically Einstein's equations, and are commonly referred to as Kerr black holes, named after the physicist who solved the associated Einstein equations (see Kerr 1963). What distinguishes a Kerr black hole from a stationary black hole is that it contains an ergosphere (not just an event horizon) where space is distorted due to the black hole rotation, yet matter and energy can escape from this region via Penrose processes (function of the black hole's rotation), and the angular momentum is axially-symmetric (dependent on the radius and polar coordinate). It is said that the region outside the ergosphere is the stationary (or static) limit, just before normal space. Also, it's been known that black holes have to be electrically charge neutral, since any net charge that's acquired would rapidly cancel out due to attracting charge of the opposite sign. Thus, Kerr black holes are considered realistic in nature as they describe sources with no electric charge.

Stationary black holes (commonly known as Schwarzschild black holes) are the simplest forms to study, as they contain just the event horizon, and are spherically symmetric. The distance between the singularity and the event horizon is defined by the Schwarzschild radius,

$$r_{\mathrm{S}} = \frac{2GM}{c^2} \ , \tag{1.1}$$

where G is the gravitational constant, M is the black hole's mass, and c is the speed of light. It should be noted that when all of the energy and matter is extracted from the ergosphere, Kerr black holes become Schwarzschild black holes. As such, they became the more popular forms of study due to the possibility that the large amounts of energy extracted could be used to explain energetic phenomena. This overview is reviewed extensively in a variety of GR textbooks (e.g. Zee 2013; Weinberg 1972).

1.3.2 Black Hole Accretion

While a variety of scenarios were explored in order to explain the nature of quasars, it wasn't until the mid-60's when the idea that quasars are powered by an accretion of surrounding matter onto a black hole was proposed and advanced by Salpeter (1964) and Zeldovich &

Novikov (1965). This became the established paradigm used today. The concept that a quasar is a black hole surrounded by an accretion *disk* was first hypothesized by Lynden-Bell (1969), where the accretion disk is threaded by a magnetic field. He was the first to conclude that the emissions observed from quasars came from the heated gas in the disk, and also that the torque due to the magnetic field is what accelerates some of the electrons in the gas to higher energies. The electrons spiral around the magnetic force lines which creates the observed synchrotron radio emission in quasars. However, his conclusions didn't account for the jets. What came out of this was the introduction of transonic flow in accretion disks and the prospect of a fluid shock responsible for the heat generated and radiated away (thus the continuum spectrum), especially in regards to radio-loud quasars. We discuss spherical and disk accretion in more detail below.

1.3.3 Spherical Accretion Model

Hoyle & Lyttleton (1939, 1940, 1940) and Bondi & Hoyle (1944) studied spherical accretion of interstellar gas as stars interacted with it. Also, these papers focused on the dynamical effects but ignored the pressure effects, with the argument being that whatever heat was generated was rapidly radiated away, making the thermal gas temperature rather low (Bondi 1952). Later, Bondi explored this further by adding thermal gas pressure to the spherical accretion model. This became known as Bondi accretion, which not only simplified the physics considerably, but it also agreed with most cases of astrophysical interest outlined in Hoyle & Lyttleton (1940). The Bondi model is transonic but there are no shocks, at least for the black-hole application. This is because there is no solid surface or centrifugal wall in this case. Most accretion models derived for celestial bodies came from this concept, and while the physics was far simpler and applicable to pulsars, it didn't take long for it to be applied to black holes. However, it quickly became apparent that the physics of black hole accretion was much more complex (Shakura & Sunyaev 1973).

1.3.4 Accretion Rate and Disk Morphology

When we talk about an accretion disk, we are referring to a flattened astronomical object with a differentially-rotating gas flow, governed by gravitational potential energy while orbiting a black-hole source. The basic mechanism that leads to the formation of a disk rather a spherical shell is the conservation of angular momentum as the gas collapses down towards the black hole. As the cloud collapses, the angular velocity increases in order to conserve angular momentum. The associated centripetal force balances gravity in the plane perpendicular to the spin axis of the gas cloud. On the other hand, along the spin axis, there is no force that can resist gravitational contraction, and therefore in the end one obtains a disk of rotating matter orbiting the black hole.

Accretion disks are believed responsible for powering stellar binaries, AGNs, protoplanetary systems and some γ-ray bursts. Generally speaking, the high angular momentum of rotating matter in accretion disks is gradually transported outwards by viscous stresses, which are frictional forces due to the interactions between the particles, such as turbulence, shear and magnetic fields. With the gradual loss of angular momentum, matter progressively moves inwards towards the center of gravity. This process describes the gravitational energy of the gaseous, infalling matter being converted into kinetic and thermal energy. Part of this thermal energy is converted into radiation, which partially escapes and cools down the accretion disc. Thus the physics that governs accretion disks is a non-linear combination of gravity, hydrodynamics, radiation and stresses.

Two important quantities in describing the structure of an accretion disk are the half-thickness, H, and the optical thickness to absorption, τ. Depending on the temperature and accretion rate, the accretion disk can 'puff' up due to gas or radiation pressure. The height of this puffiness determines whether the disk is 'thick' with $H \gtrsim r$, or 'thin' $H \lesssim r$, where r is the radial distance along the disk. Also, disks can either be described as opaque ($\tau \gg 1$), or transparent ($\tau \ll 1$). Opaque disks have a temperature much less than the virial value and exhibit black-body radiation, whereas transparent disks have relatively high temperatures and emit optically thin spectra. The transparent disk scenario has proven to be an attractive model for ADAF emission spectra. These models have been reviewed in detail by Narayan & Yi (1995a, 1995b).

The luminosity L radiated by the accretion disk is related to the accretion rate $\dot{M}$ via the expression

$$L = \beta \dot{M} c^2 \ , \tag{1.2}$$

where $\beta \leq 10\%$ is the radiative efficiency. There is a maximum possible luminosity at which gravity is able to balance out the outward pressure due to radiation. This maximum limit for the steady, spherically symmetric accretion of pure, fully ionized hydrogen is known as the Eddington luminosity,

$$L_{\rm Edd} \equiv \frac{4\pi G M m_p c}{\sigma_{\rm T}} = 1.15 \times 10^{38} \left(\frac{M}{M_\odot} \right) \ {\rm erg\ s^{-1}} \ , \tag{1.3}$$

where $\sigma_{\rm T}$, M, m_p, and c denote the Thomson cross section, the mass of the gravitational source, the proton mass and the speed of light, respectively. This luminosity limit is also related to the Eddington mass accretion rate $\dot{M}_{\rm Edd}$ and the radiative efficiency parameter β via $L_{\rm Edd} = \beta \dot{M}_{\rm Edd} c^2$, leading to

$$\dot{M}_{\rm Edd} \equiv c^{-2} \beta^{-1} L_{\rm Edd} \ . \tag{1.4}$$

The Eddington limit is used as a unit to quantify the luminosity of a celestial object. It should be noted that accretion discs are not spherical in nature, and often have additional stresses that can counteract the radiation pressure along with gravity. As such, they may exceed this limit and radiate at a super-Eddington luminosity.

Comparing a black hole's accretion rate $\dot{M}$ to the Eddington limit is often used to describe the physical structure of the accretion disk, with characteristics such as opacity and thermal or radiative dominance. What follows is an overview of the possible disk morphologies described in terms of $\dot{M}/\dot{M}_{\rm Edd}$, as reviewed by a variety of sources (e.g.

Frank et al. 2002).

- $\dot{M}/\dot{M}_{\rm Edd} > 0.1$: This usually describes slim disks ($H \lesssim r$), where the accretion rate is high, and the luminosity is approaching the Eddington limit, in which case the radiation pressure is supported and nearly balanced with the black hole's gravity. This happens when the radiation flowing upward becomes trapped by the accreting material, causing the disk to expand vertically into the radiation torus. In these kinds of disks, the energy that's advected into the black hole is moving faster than that which radiated away (or inefficient radiative cooling). These kinds of disks tend to resemble more star-like structures, and as such their emitted spectra are close to a single-temperature blackbody spectrum.

- $0.01 < \dot{M}/\dot{M}_{\rm Edd} < 0.1$: This is the basis for the geometrically thin disk ($H \ll r$). Here, the accretion rate is low and the disk is highly opaque, meaning that it radiates at high efficiency. This signifies that the rate of energy that's advected inward is considered negligible when compared to that which is radiated away. Here, the X-ray emission tends to arise from the innermost part of the disk (where the temperature is the hottest), while the optical-UV emissions tend to further out along the disk. This is also where the Shakura-Sunyaev model comes from (see below).

- $\dot{M}/\dot{M}_{\rm Edd} < 0.01$: A geometrically thick disk ($H \sim r$), where the accretion rate is extremely low, optically thin, and the plasma flow becomes radiatively inefficient, resulting in the gas temperature approaching the virial value. This is from the disk becoming a stable, two-temperature structure (ion torus) due to the ions and electrons being thermally decoupled, thus making it harder for the disk to cool efficiently in the inner regions. When this happens, the disk becomes advection-dominated, resulting in most of the binding energy being swallowed by the black hole. It should be noted that advection-dominated disks are inefficient with X-ray production, but are luminous in the radio and γ-ray emission spectrum (e.g. Sambruna et al. 2004; Di Matteo et al. 2000; Allen et al. 2000; Urry & Padovani 1995, and Owen et al. 2000).

In the next section, we review the various models used to describe the accretion regimes listed above.

1.3.5 The Thin-Disk Accretion Model

The standard model (or thin-disk model) for accretion disks stems from the study on the geometrically thin disk ($H \ll r,\ \dot{M}/\dot{M}_{\rm Edd} < 0.1$) by Shakura & Sunyaev (1973, hereafter SS73). This was applied to a stationary, axially-symmetric black hole. The disk was considered optically thick (high opacity), emitted locally black body radiation, had a Keplerian orbit (see § 1.6.1), high luminosity and highly efficient radiative cooling. This model also established the possibility that the radiative processes were specifically Compton scattering and bremsstrahlung, not just synchrotron radiation. Some of the findings that came out of this work were: 1) that a thin disk containing vertical equilibrium and a Keplerian orbit will have efficient radiative cooling, assuming that there's a thermal balance between the viscous heating and radiative cooling; 2) that viscosity (see § 1.3.7) is magnetic in origin and can be applied in an *ad hoc* manner to the dynamical equations.

This work has attributed to the development of the accretion disk models that came after it, all purely theoretical, and as has been heavily cited/reviewed (e.g. Novikov & Thorne 1973; Rees 1984; Ford et al. 1994). The SS73 model described the disk being balanced by gas (thermal) and radiation pressure, which thermal pressure dominated further out along the disk and was thermally stable, while radiation pressure dominated near the central black hole and was considered rather unstable. The Shapiro, Lightman, & Eardley (1976, hereafter SLE) model is the optically-thin, geometrically thick version of the SS73 model, and was developed from the work done by Thorne and Price (1975) who postulated that this instability may change the inner part of the disk into an optically thin, hot, thermally-dominated state. The SLE model effectively made the gas-pressure dominant over the radiative pressure ($T_e \ll T_p$), though was very thermally unstable. As such, according to Abramowicz (1999), it was widely used as a viable fit to the observed high-energy spectra from accreting black holes.

This changed with the development of the advection-dominated accretion flow (ADAF) model (Narayan & Yi 1994, see next section for more). Cooling via bremsstrahlung (free-free) emission is a two-body process. This is therefore a non-linear process, and that is why the radiative efficiency changes as the ratio $\dot{M}/M$ is varied. Lower values of the ratio lead to lower radiative efficiency, as in the ADAF flows. Specifically, optically-thin ADAF disks had low accretion rates and were considered very hot yet radiatively inefficient, as such, that made them under-luminous with very hard spectra (see Figure 1.13 for a geometric representation of this), which seemed to fit better with the observational data than the earlier models (see Figure 1.14). This is the reason that the ADAF scenario has become the preferred model for the inflow of gas onto black holes with a sub-Eddington accretion rate (e.g. Pringle 1981). For a full review of the differences between the three models, see Chen et al. (1995) who summarized their structure and properties.

1.3.6 Advection-Dominated Accretion Model

This model has been covered and reviewed extensively (e.g. Narayan & Yi 1995; Pringle 1981; Abramowicz et al. 1995). Originally, the ADAF concept was proposed by Ichimaru, (1977), however this work was largely ignored. Rees et al. (1982) then developed its definitive characteristic: an accretion flow with very sub-Eddington accretion rates will be radiatively inefficient due to being very hot and optically thin. Rees (1978), Begelman (1978, 1979), and Katz (1977) suggested that this kind of low efficiency is characteristic of spherical accretion with a near Eddington accretion rate ($\dot{M} \sim \dot{M}_{\rm Edd}$). Eventually, Narayan & Yi (1995) revisited the concept in the context of disk accretion. This led to the modern formation of the ADAF scenario, in which the accretion is occurring at a sub-Eddington rate, and the disk is hot and puffy, and radiatively inefficient. The ADAF disk is therefore primarily cooled by advection of energy into the black hole, rather than via the emission of radiation. A precursor of the ADAF model was the 'slim disk' model of Abramowicz et al. (1988). Slim disks are less radiatively efficient than the SS73 model, but ADAFs are much

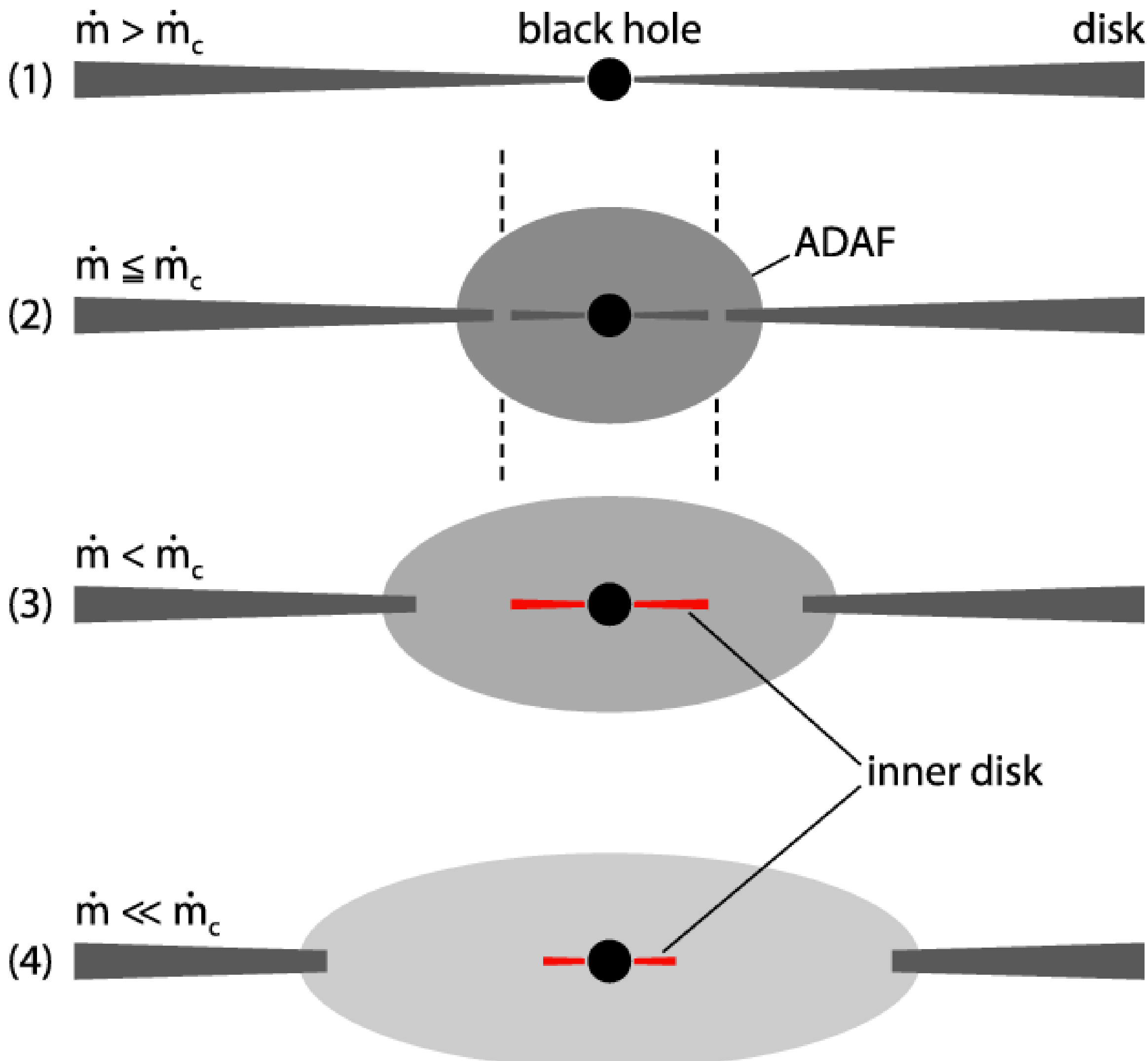

Figure 1.13: Taken from Meyer-Hofmeister et al. (2009). Geometry of the accretion flow as a function of the mass accretion rate $\dot{m}$ scaled to the Eddington rate $\dot{m}_c$. The images show the change from a soft state with high mass flow rate (1), to the beginning of the hard state (2-4), with the mass flow rate in the ADAF indicated by contrast in gray.

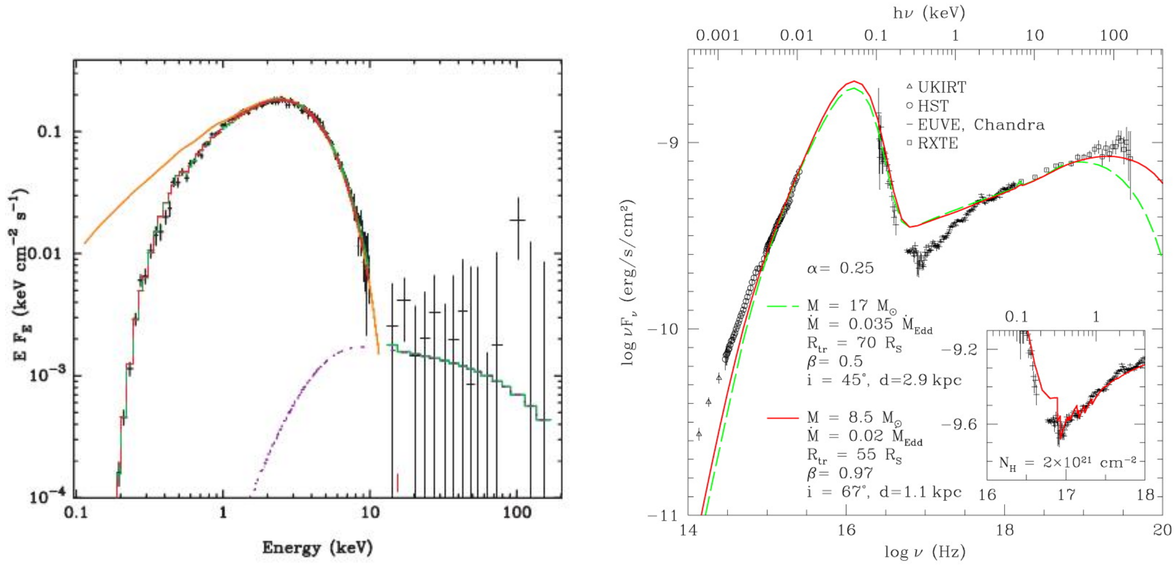

(a) SS73 fit, taken from Davis et al. (2006). (b) ADAF fit, taken from Esin et al. (2001).

Figure 1.14: Comparative plots between the two disk models: (a) A variation of the SS73 fit to the BeppoSAX observation of LMC X-3 (in black), represented by the orange solid curve; see Davis et al. (2006) for further details. (b) An ADAF model fit (red and green lines) to the observed spectrum of the X-Ray Nova XTE J1118+480 (crosses, triangles and squares); see Esin et al. (2001) for further details. It can be seen between the two that the ADAF model fits the observed spectrum better than the SS73 model.

less radiatively efficient in comparison. These two advection-dominated accretion models are both considered dynamically, viscously and thermally stable. See Narayan & Yi (1995) for a complete review on the ADAF disk, and Abramowicz et al. (1988) for the slim disk.

1.3.7 Viscosity

As stated in § 1.3.4, stresses are involved in transporting out the angular momentum in the disk in order to allow for matter to accrete onto the black hole. Typically for thin accretion disks ($H \ll r$), the most common stressor is the kinetic viscosity ν, which is generally defined as (via the Shakura-Sunyaev paradigm).

$$\nu(r) = \alpha H(r) a_g(r) \ , \tag{1.5}$$

where α is a constant, and a_g is the thermal sound speed for the gas in the plasma. Viscosity is believed to be the result of the MHD waves from the black hole, which is excited by the magnetic shearing (magnetorotational) instability (or MRI), which was proposed by Velikhov (1959), Chandrasekhar (1960, 1981), and revisited by Balbus & Hawley (1991, 1992), and is currently considered the only viable mechanism for the turbulence in disks (Brandenburg 1999). This kind of frictional force between the particles is responsible for producing a torque in the accretion disk that transports angular momentum outward. The viscous stress also converts the gravitational potential energy of the infalling matter into kinetic and thermal energy, thus heating the gas as it slowly spirals in toward the central mass. This leads to the super-adiabatic variation of the energy density U, as expressed by the co-moving time derivative,

$$v \frac{d}{dr} \ln\left(\frac{U}{\rho^\gamma}\right) = \frac{\rho \nu r^2}{U}\left(\frac{d\Omega}{dr}\right)^2 \ , \tag{1.6}$$

where γ is the adiabatic index of heat, ρ is the volumetric mass density, and Ω is the viscous torque. In the case of solid-body rotation, $\Omega = \text{const}$, and therefore we find that $U \propto \rho^\gamma$, as expected for adiabatic flow. It should be noted that Shakura & Sunyaev (1973) included this viscosity in an *ad hoc* manner (via dimensional analysis) because before, no one was able to derive the viscosity from the microphysical processes themselves.

However, it has been determined that inviscid disks can just as well produce accretion models, as long as it's provided with an appropriate angular momentum (e.g. Chakrabarti 1989; Chakrabarti & Molten 1993; Kafatos & Yang 1994; Lu & Yuan 1997; Das et al. 2001a). Accretion disks were believed to be driven by viscosity, but recent models show that inviscid disks can produce the same results, provided that $\alpha \lesssim 0.01$ (e.g. Narayan et al. 1997). It should be noted that in the inviscid case, the right-hand side of Equation (1.6) vanishes, and therefore U/ρ^γ is constant, which is consistent with adiabatic flow.

1.4 Energy Extracted to Produce the Outflows

There are generally two different types of models for the observed outflows: the electrodynamic models, and the shock-acceleration models. We will first summarize the electromagnetic model and then move into the motivation for our use of the shock-acceleration model.

1.4.1 The Electrodynamic Model for Outflows

Black hole accretion is believed to be the result of a cascade effect between the black hole's magnetic field and centrifugal motion, which became the basis for the electrodynamic model. In this model, the magnetic field is the catalyst for the conversion of gravitational potential energy into heat and radiation. This process results in the formation of outflows that produce synchrotron radiation, which contributes to the AGN continuous spectrum. The synchrotron radiation is produced by electrons that spiral around the magnetic field lines that surround the jets.

This is the basis for the Blandford-Znajek model (Blandford & Znajek 1977), as well as the electromagnetic cocoon (or dynamo) model (Lovelace 1976; Blandford & Payne 1982). In both magnetohydrodynamic models, the magnetic field from the black hole transfers the angular momentum outward, removing the need for the *ad hoc* viscosity of the SS73 model. In the Blandford-Znajek model (Figure 1.15), there are two regions of interest: the force-free region and the acceleration region. A rotating magnetic field will induce current, however due to the proximity to the black hole's gravity, the current flow near the event horizon is neutralized. This allows the neutrally charged particles to become mobile (hence force-free) and 'carried' through the force-free region from the disk to the acceleration region via the Poynting vector (Equation 9.25 of Frank, King, & Raine 2002),

$$\vec{S} = \left[\frac{4\pi}{\mu_0 c}\right] \frac{c}{4\pi} \vec{E} \times \vec{B} \ , \tag{1.7}$$

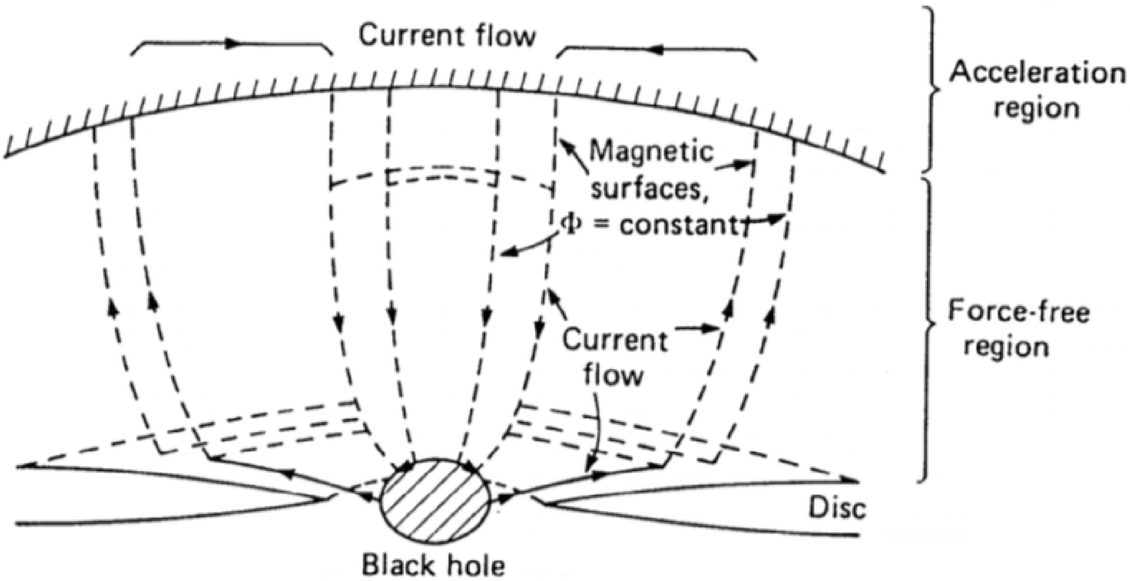

Figure 1.15: Schematic representation of the Blandford-Znajek model, showing the magnetic surface and current flows in the vicinity of the black hole and disc. This image is from Frank, King, & Raine (2002), though it was adapted from D. Macdonald & K.S. Thorne (1982).

where μ_0 is the vacuum permeability, and $\vec{E}$ and $\vec{B}$ are the electric and magnetic fields of the disk. Once exposed to the second current flow, they become accelerated to relativistic energies. The dynamo model (Figure 1.16) follows the same setup as the Blandford-Znajek model, except the centrifugal motion of the accreting plasma is what first drives the gas from the disk, which when exposed to the magnetic pressure in the force-free region, becomes accelerated to an ultra-relativistic proton beam with cold electrons. Further out along the disk, these cold electrons could get "trapped and untrapped in the unstable plasma waves [in the intergalactic medium] and accelerated to relativistic energies" (Lovelace 1976).

As discussed by Le & Becker (2005), this kind of model (while attractive) is rather complex in that the physics loses sight of the fundamental microphysical processes that may play a role in generating the observed outflows. Specifically, as they point out, the relativistic particles that escape to form the jet in the electrodynamic models are invoked in an *ad hoc* manner without any reference to the dynamical processes involved in the

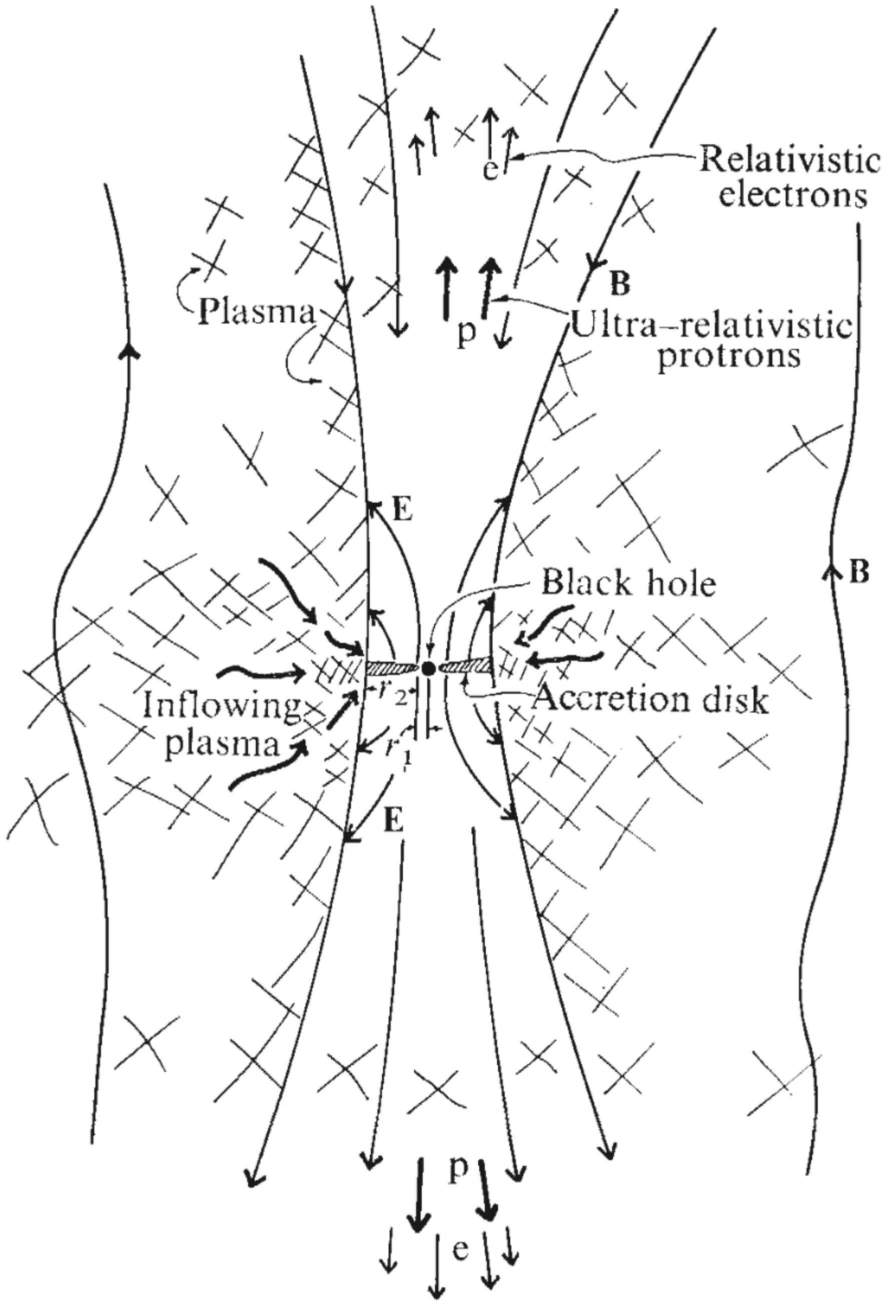

Figure 1.16: The electromagnetic dynamo model, taken from Lovelace 1976.

accretion disk; this is similar to the way in which the viscosity was included in the SS73 model. Because of this kind of complexity, it is interesting to examine the alternative presented by the shock-acceleration model.

1.4.2 The Shock-Acceleration Model

The generation of outflows from thin accretion disks can also be explored using the theory of shock acceleration. As matter accretes towards the black hole, it encounters a ‘wall’ or ‘centrifugal barrier’ (Hawley et al. 1984a, 1984b), at which point the fluid passes through a shock, and the velocity decreases abruptly (either continuous or discontinuous). The centrifugal barrier occurs where the centripetal force, $F_{\rm C}$, balances gravity, $F_{\rm G}$, given by

$$F_{\rm C} = \frac{mv^2}{r}; \qquad F_{\rm G} = \frac{GMm}{r^2} \ , \tag{1.8}$$

where m is the mass and v is the orbital speed of a particle in the disk, G is the gravitational constant, and M is the mass of the black hole. This leads to determining the centrifugal barrier radius $r_{\rm C}$,

$$r_{\rm C} = \frac{l^2}{GM} \ , \tag{1.9}$$

where $l = vr$ is the specific angular momentum per unit mass, which is constant in an inviscid disk. The kinetic energy that is lost is partially converted into thermal energy and partially lost to power the jetted outflow. The cooled post-shock plasma continues onward towards the black hole. This whole process is represented in Figure 1.17 of the classic ADAF model containing the tangled magnetic field in the disk, and how it ‘opens up’ above the shock radius in order to allow the outflow to proceed. This also helps to collimate the outflow, and is analogous with the magnetic topology during solar flares.

Typically, X-ray luminous AGNs have higher relative accretion rates ($\dot{M}/\dot{M}_{\rm Edd}$), and consequently higher gas densities, compared with the radio-loud sources. The two-body nature of free-free emission creates a nonlinear dependence of the cooling timescale on the

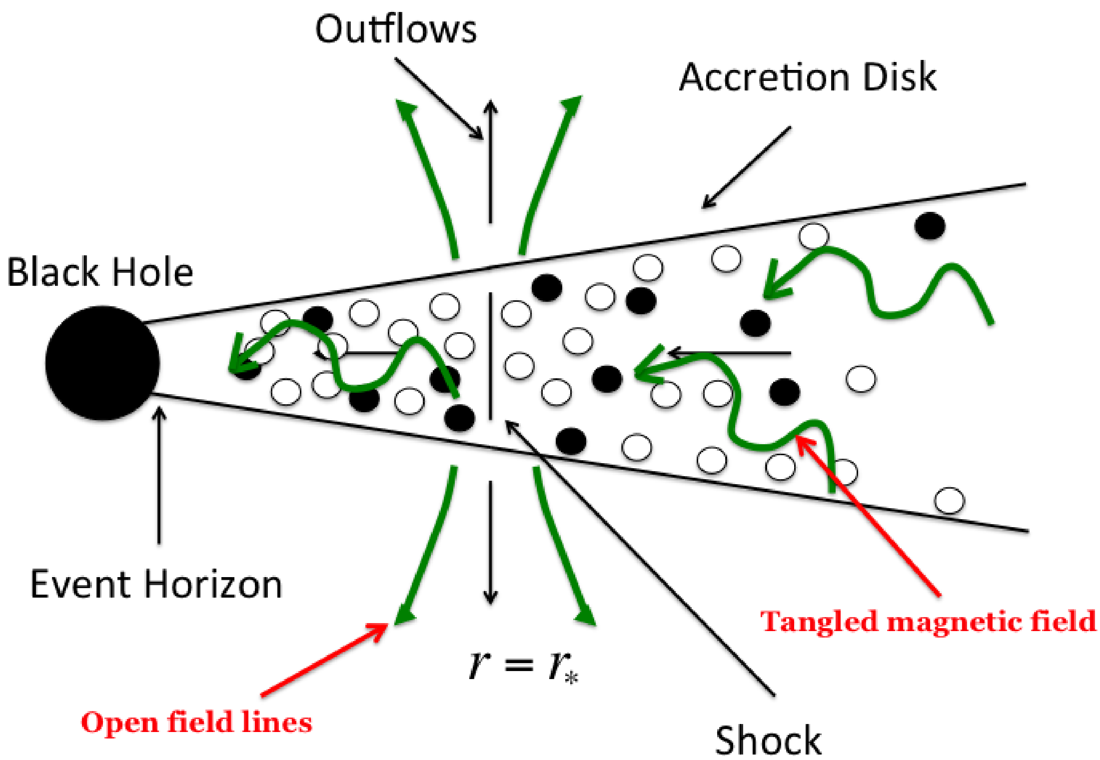

Figure 1.17: Schematic representation of the Le & Becker (2005) accretion disk with the tangled magnetic field in the disk, and how it 'opens up' above the shock radius in order to allow the outflow to proceed. This also helps to collimate the outflow.

accretion rate, which decreases the efficiency of free-free cooling in the low-luminosity AGNs. Therefore sources with accretion rates far below the Eddington value achieve temperatures close to the virial value (as stated in § 1.3.5). The high temperatures lead to a further reduction in the gas density, and as a result, the plasma becomes fully collisionless. The combination of high temperature and low density makes the low-luminosity sources radio-loud. As a result, the mean free path (which is a good tool for analyzing the efficiency of the particle-particle collision, see § 1.6.2) in these sources can exceed the disk half-thickness, which can then lead to efficient Fermi acceleration of a relativistic particle population, if a shock is present in the disk (Le & Becker 2004, 2005, 2007; Becker et al. 2011). These accelerated particles are what's believed to power the observed outflows in the radio-loud sources. Conversely, in the X-ray luminous sources, the accretion rate is higher, the cooling is more efficient, and a shock (if present) will simply lead to heating of the gas rather than particle acceleration, resulting in weaker outflow. An example representation of this can be seen in Figure 1.18 for Cygnus X-1, showing that a stronger radio flux leads to a harder X-ray spectrum. This overall picture naturally explains the observed correlation between radio luminosity and the presence of relativistic outflows in AGNs.

1.5 The Standard Model for AGNs

Which leads to the basis of this work: the underlying question as to how these luminous, energetic emissions and matter outflows are formed. What mechanism or power source is responsible for it? The standard (or unified) model for AGNs establishes that they are powered by a black-hole engine, and the only energy sources allowed are the black-hole rotation, as well as the total black-hole mass accretion rate, $\dot{M}$. Intrinsically, AGNs function by the release of gravitational potential energy due to matter accreting onto the black hole, resulting in matter outflow and energetic emissions. One of the critical parameters is the ratio of the accretion rate $\dot{M}$ divided by the black hole mass M, or $\dot{M}/M$, which is often compared to the Eddington accretion rate $\dot{M}_{\rm Edd}$ (see § 1.3.5). These parameters determine

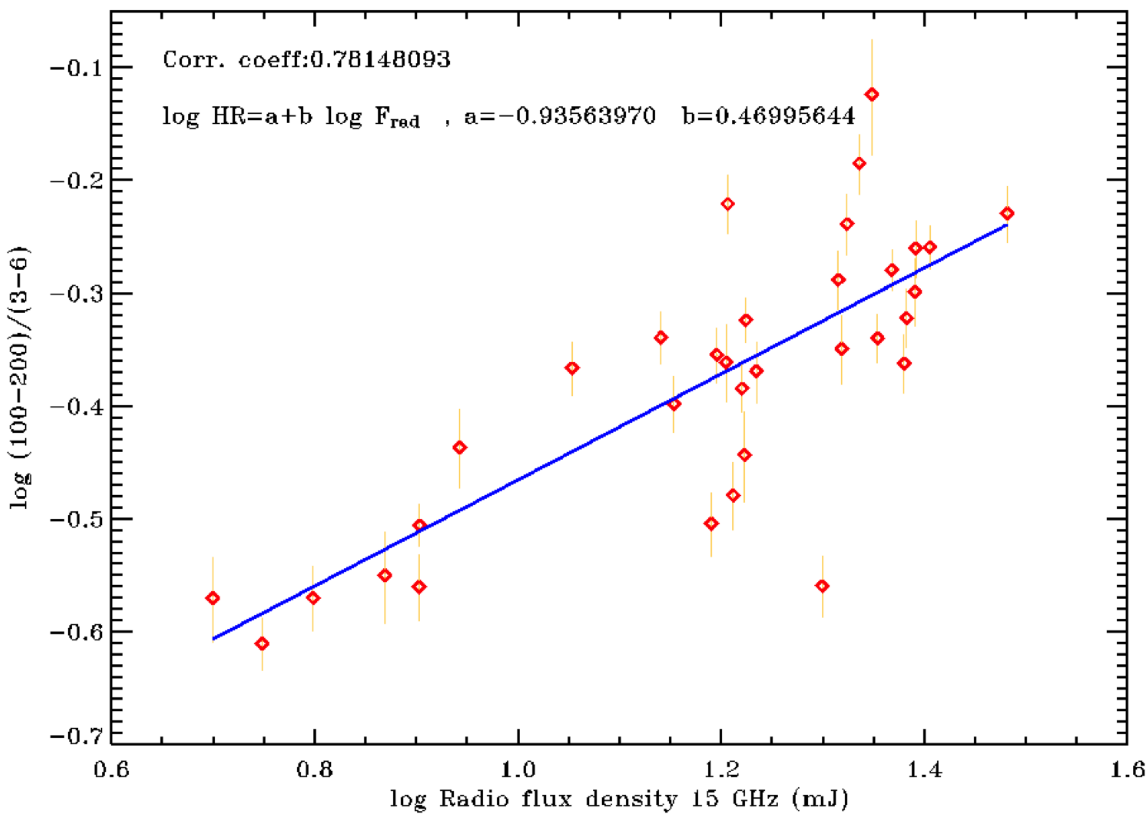

Figure 1.18: Plot of the INTEGRAL hardness ratio versus the radio flux from the observations of Cygnus X-1, taken from: http://www.isdc.unige.ch/newsletter/n16?isdclayout=a. The plot shows the correlation between the radio fluxes and X-ray spectrums, in which a stronger radio flux will have a harder spectrum, and likewise a softer radio flux will have a softer spectrum.

whether the black hole is underfed, or 'starved' ($\dot{M} \ll \dot{M}_{\rm Edd}$) or luminous ($\dot{M} \gtrsim \dot{M}_{\rm Edd}$).

1.5.1 Viewing Angle and Accretion Geometry

The other important parameter is the angle between the black-hole spin (jet) axis and the line of sight to Earth, which is what separates them into the subclasses like quasars, blazars, and Seyfert galaxies. Examples of this can be seen in Figure 1.19 and Figure 1.20 (adaptations from the scheme determined in Urry & Padovani 1995), which illustrates how depending on the viewing angle, the AGN could be classified as a type 1 or 2 Seyfert galaxy, a radio-loud quasar or a radio-quiet QSO, or even a blazar (OVV BL Lac). This largely also affects the observations of the narrow-line region (NLRG) and broad-line region (BLRG) spectrum energy distributions (SED), as they determine how strong the emissions are in the X-ray and γ-ray spectra for various classes of AGNs.

Black hole accretion is believed to be responsible for producing the radiative power in AGNs (no matter the spectrum), which has been known to typically outshines its host galaxy via observations. The accretion disk is surrounded by a hot corona plasma (or torus), containing clouds of gas. Gravitational potential energy must be released in order for matter to accrete onto the black hole. About $\lesssim 5 - 30\%$ of the gravitational potential energy is released in the form of radiation and outflows during the accretion process (Dermer & Menon 2009). The details depend on the specific angular momentum of the gas supplied to the disk at a large radius, as well as on the spin of the black hole. The processes that occur within the disk are responsible for powering the observed emissions in the broad-line and narrow-line energy spectra (see § 1.3.5). From accretion disks, the luminosity is the observable physical quantity of radiation that's produced. Generally speaking, this luminosity is what determines whether an AGN is more dominant in the X-ray, γ-ray, or radio spectrum.

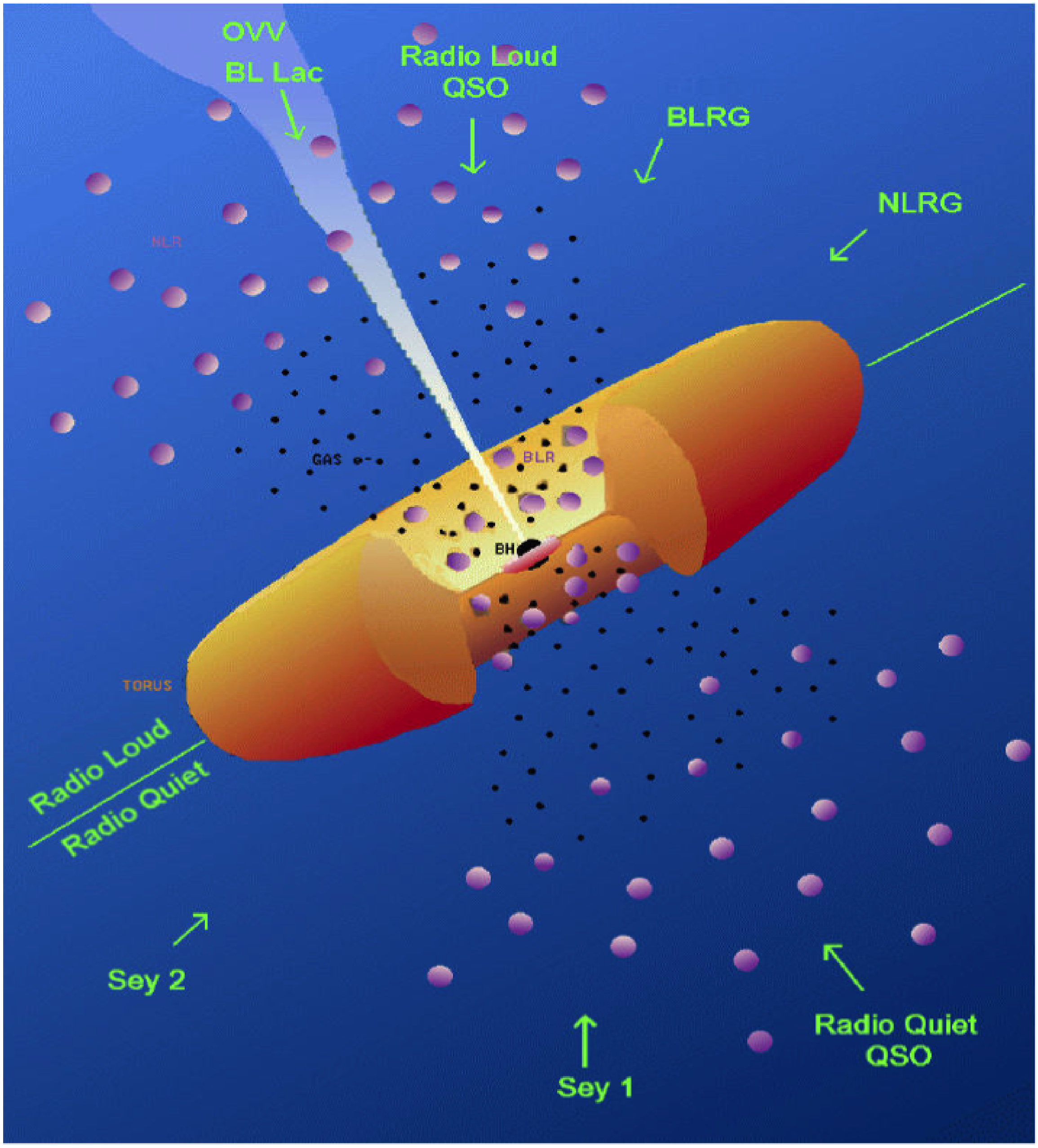

Figure 1.19: An illustration of the geometric dependency of the unified AGN model, taken from: http://astrobites.org/2011/03/07/intrinsic-differences-in-agn-accretion-rates/.

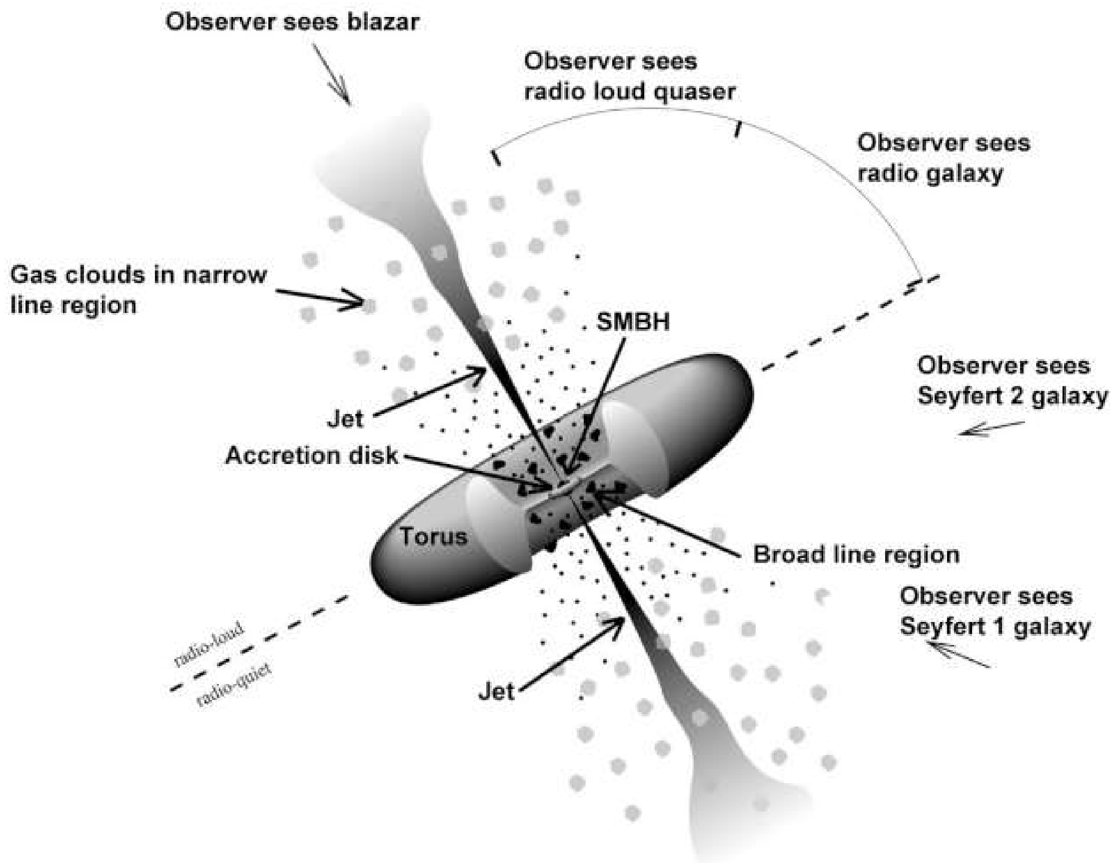

Figure 1.20: A more detailed illustration of the AGN unified model, taken from: http://www.astro-photography.net/Supermassive-Black-Holes-Active-Galactic-Nuclei.html.

1.5.2 High-Energy Radiation from AGNs

The standard model of AGNs suggests that the relatively cold material at a large distance from the black hole forms into a geometrically thin accretion disk, as described by SS73. If the accretion rate is sub-Eddington, the flow transitions into a hot ADAF in the inner region. The ADAF is composed of two-temperature plasma with ion temperature $T_i \sim 10^{12}$ K and electron temperature $T_e \sim 10^9$ K. The associated relativistic jets are made up of equal numbers of protons and electrons (or possibly electrons and positrons), as required to maintain charge neutrality.

Aside from accretion being driven by the centrifugal motion of the disk due to the black hole's gravity, the force responsible for the particle-particle (or ion-electron) interaction within the disk (which produces the continuum spectrum) is believed to be the result of magnetohydrodynamic turbulence (or MHD waves). The resulting continuum spectrum observed in AGNs is widely believed to be produced by synchrotron radiation, due to its agreement of a power-law form to the observed data. This kind of radiation is the emitted result of relativistically charged particles (e.g. electrons) spirally around magnetic field lines (believed for the electrodynamic model). However, this kind of contributed radiation in the X-ray spectrum is considered low, therefore other processes have been considered to explain the excess in X-ray brightness.

Another possible kind of process responsible for the observed emissions is Compton scattering (photons loose energy) or inverse-Compton scattering (photons gain energy). Essentially these kinds of scattering processes result in radiation being shifted to lower or higher energies, depending on the kinetic energy of the electron involved. These kinds of processes can account for possible lower energy photons being scattered to higher energies via collisions with relativistic electrons, or vice versa, as a possible explanation for the excess in X-ray production.

However, the emission spectrum can also to be the result of bremsstrahlung (or free-free) emission, due to a similar (or characteristic) power-law spectrum that's been observed with the X-ray spectrum in galaxy clusters. This process describes that a free electron can increase its speed after coming in contact with an ion and absorbing a photon, or it very well could lose its speed if a photon is emitted from the electron rather than absorbed (free-free cooling). This process has been of interest lately in regards to AGNs, especially radio-loud sources, and is the preferred method in regards to the shock-acceleration model (see Le & Becker 2004, 2005, 2007; Becker et al. 2011).

1.5.3 Primary and Secondary Emissions

The SED includes primary and secondary emission components. The primary emission produced in the disk can interact with the torus to create the broad-line (BLRG) spectrum, or with external clouds to create the narrow-line (NLRG) spectrum. These resulting interactions are known as the secondary emissions. In addition to the primary emission from the disk, the jets are believed to create another primary emission component in the form of inverse-Compton and/or synchrotron radiation, which can extend from the radio to the gamma-ray region of the spectrum. This is believed to be the explanation for the classic double-humped multi wavelength spectrum we see from M87 (see Figure 1.7).

When the jet outflows from the disk it can interact with a surrounding cloud in the galactic medium, resulting in the production of neutral and/or charged pions and then secondary radiation. An example of this for M87 can be seen in Figure 1.21, which is a sketch of the jet penetrating a slow-moving (a) red giant or (b) a generic massive cloud of matter. The X-rays and UV photons can be produced in either the disk or the jet, however the γ-rays are almost exclusively produced in the jet via inverse-Compton and/or synchrotron processes, as well as via collisions with external clouds. In order to fit the observational data for the γ-ray spectrum, previous studies have modeled a theoretical secondary-interaction between a relativistic jet and a cloud. They were just assuming that a jet existed without really postulating how it was formed. Hence, the phenomenon has never been directly connected with the process of accretion occurring in the disk surrounding the SMBH in the heart of the AGN. Filling this gap is one of the major focuses in this thesis.

This is further explored in Ch. 5 in regards to my specific work. For now, we move forward in describing the overall plan for the research.

1.6 Plan of Research

This work focuses on the two-temperature ADAF model originally introduced by Ichimaru (1977), and later standardized by Narayan & Yi (1994, 1995a, 1995b), Abramowicz et al. (1995), Chen (1995), and Chen et al. (1995). In the ADAF model, the density is relatively low, the disk is optically thin to absorption, and the accretion rate $\dot{M} \ll \dot{M}_{\rm Edd}$. The ADAF scenario is qualitatively similar to the thermally unstable (Piran 1978) accretion model developed by Shapiro, Lightman and Eardley (1976, hereafter SLE), which likewise contains a two-temperature plasma with the ion temperature greatly exceeding the electron temperature. It should be noted that these initial models operated without considering the effects of general relativity.

1.6.1 Keplerian Orbits and Pseudo-Newtonian Potential

In the earlier models, the gravitational potential energy per unit mass Φ used for either a Kerr or Schwarzschild black hole was given by the Newtonian expression,

$$\Phi = -\frac{GM}{r} \ . \tag{1.10}$$

In the case of Schwarzschild black holes, the 'particle in a circular whirlpool' as we described on the first page takes effect, for which then the Newtonian gravitational energy (Equation 1.10) can be applied to find the Keplerian angular velocity $\Omega_{\rm K}$,

$$\Omega_{\rm K}^2 = \frac{1}{r}\frac{d\Phi}{dr} = \frac{GM}{r^3} \ , \tag{1.11}$$

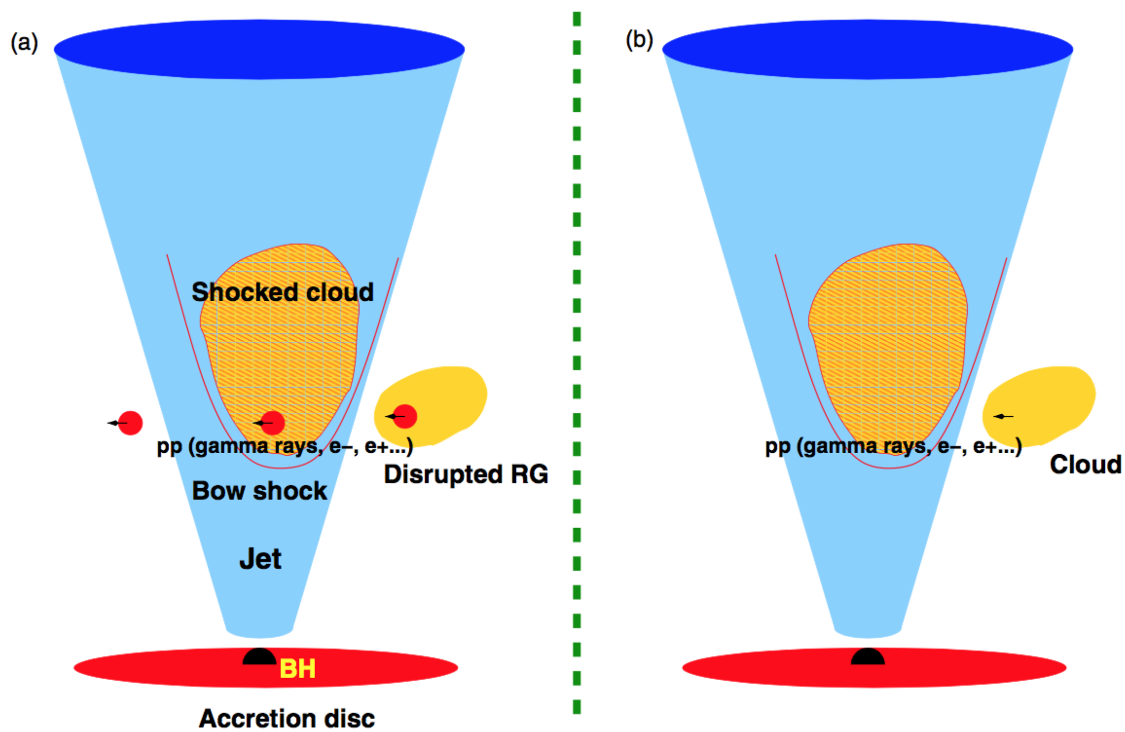

Figure 1.21: From Barkov et al. (2012). An outgoing jet from M87 interacting with a slow moving (a) red giant (RG) or (b) a generic massive clump of matter (cloud), resulting in gamma-ray production.

and specific angular momentum per unit mass $l_{\mathrm{K}} = \Omega_{\mathrm{K}} r^2$,

$$l_{\mathrm{K}}^2 = r^3 \frac{d\Phi}{dr} = GMr \ . \tag{1.12}$$

Based on General Relativity (GR), we find that for Schwarzschild black holes, there is a critical angular momentum in which a particle can maintain a stable orbit l_c, which coincides with a radius for the innermost stable circular orbit of $r_{\mathrm{isco}} = 3r_{\mathrm{S}}$ (Zee 2013). If $l < l_c$, and likewise if $r < r_{\mathrm{isco}}$, the particle falls into the black hole. However, for the general relativistic treatment of perfect fluid disks around a black hole, this limit was adjusted to include the marginally bound circular orbit $r_{\mathrm{mb}} = 2r_{\mathrm{S}}$, in which case r_{isco} was redefined as the last stable circular orbit, r_{ms} (Abramowicz et al. 1978, Kozlowski et al. 1978, Fishbone and Moncrief 1976). Though it still remains that $r > r_{\mathrm{ms}}$ is defined for stable orbits, and $r < r_{\mathrm{ms}}$ for unstable orbits. Also, that orbits that have $r < r_{\mathrm{mb}}$ are considered unbound, containing positive binding energy, while those at $r = r_{\mathrm{mb}}$ have zero binding energy (Abramowicz 1999). The range between $r = r_{\mathrm{mb}}$ and $r = r_{\mathrm{ms}}$ is called the inner disk edge $r = r_{\mathrm{in}}$ for black hole accretion, in which the particles in the disk experience circular orbits when $r > r_{\mathrm{in}}$, and free fall when $r < r_{\mathrm{in}}$ (see Abramowicz et al. 2010 more details). It's further classified between the two standard accretion models that the inner disk edge is $r_{\mathrm{in}} \approx r_{\mathrm{isco}}$ for the SS73 model and $r_{\mathrm{in}} \approx r_{\mathrm{mb}}$ for radiatively inefficient flow models (like ADAFs).

The thin-disk and SLE models utilized the standard Newtonian form for the gravitational potential energy, which introduces significant errors close to the event horizon. The technical difficulty associated with fully implementing general relativity led to the development of the pseudo-Newtonian approximation for the gravitational potential, given by (Paczyński and Wiita 1980)

$$\Phi = -\frac{GM}{r - r_{\mathrm{S}}} \ , \tag{1.13}$$

for the purpose of exploring the disk inner edge. This lead to a new sub-Keplerian angular velocity,

$$\Omega_{\rm K}^2 = \frac{1}{r}\frac{d\Phi}{dr} = \frac{GM}{r\left(r - r_{\rm S}\right)^2} \ , \tag{1.14}$$

and angular momentum,

$$l_{\rm K}^2 = r^3 \frac{d\Phi}{dr} = \frac{GMr^3}{\left(r - r_{\rm S}\right)^2} \ . \tag{1.15}$$

This is a surprisingly accurate approximation that provides a convenient method for exploring the structure of the inner region of a sub-Keplerian disk. Not only were they able to successfully explore the inner edge region, but their results further out along the disk agreed well with previous models who operated on Newtonian gravitational energy, even with viscosity included (see § 1.3.7).

By adopting the pseudo-Newtonian approximation, we are able to the treat the physical processes occurring within the accretion disk using a semiclassical methodology. Narayan et al. (1999) and Becker & Subramanian (2005), amongst other authors, used this approach in developing their models for ADAF disks. The dynamical solutions obtained successfully describe the global structure of the accretion flow. It should be noted that the maximum angular momentum $l_{\rm max}$ for steady-state inviscid accretion corresponds to a circular orbit with radius $r = r_{\rm mb} = 2r_{\rm S}$ (Le & Becker 2005). Setting $r = r_{\rm mb}$ in Equation (1.15) yields

$$l_{\rm max} = l_{\rm K}\left(r_{\rm mb}\right) = \frac{\sqrt{GMr_{\rm mb}^3}}{r_{\rm mb} - r_{\rm S}} = \frac{4GM}{c} \ . \tag{1.16}$$

The radius of marginal stability only exists in the case of GR, and therefore inviscid accretion only occurs in relativistic disks.

1.6.2 Magnetic Mean Free Path

When a shock is present, magnetohydrodynamical (MHD) waves can lead to the first-order Fermi acceleration of charged particles. However, this depends critically on the value of the mean free path for ion-ion collisions, which is given by (Subramanian et al. 1996)

$$\lambda_{ii} = 1.20 \times 10^5 \frac{T_i^2}{n_i \ln \Lambda} , \tag{1.17}$$

where n_i is the thermal ion number density, and $\ln \Lambda$ is the Coulomb logarithm. In ADAF disks, λ_{ii} can exceed the disk half-thickness, which allows the formation of a distribution of relativistic particles via multiple shock crossings. A series of previous investigations have established that particle acceleration in the shock can channel a significant fraction of the kinetic energy of the accreting gas into the acceleration of relativistic particles that can escape to form the observed outflows (Le & Becker 2004, 2005, 2007; Becker et al. 2011).

1.6.3 Summary of the Le & Becker Shock-Acceleration Model

Of the many accretion models that exist, my work branches off from the model created by Le & Becker (2004, 2005, 2007), hereafter known as LB04, LB05, and LB07. Below is a summary of the motivation and the results obtained from their work.

This model in particular began with Blandford & Ostriker (1978), who were the first to suggest that shock acceleration existed in the environment of AGNs. This was later explored in spherically symmetric accretion flows (Protheroe & Kazanas 1983; Kazanas & Ellison 1986) as a possible explanation for the energetic radio and γ-radiation emitted by many AGNs. However, these papers did not account for a detailed transport equation. This was changed when Webb & Bogdan (1987) and Spruit (1987) employed a transport equation in order to solve for the distribution of energetic particles in a spherical accretion flow, one defined as a velocity profile terminating at a standing shock. This did enhance the state of the theory, though it was considered to be more quantitative in nature compared to the earlier models. But accretion disks around black holes are not spherical (well perhaps in the innermost region), they are cylindrical in geometry. Therefore the solutions obtained in the earlier models were not appropriately applicable to disks. Plus the velocity distribution also was derived for a spherical flow and therefore was likewise inappropriate to a disk structure.

Therefore, to quote LB07, "none of these previous models can be used to develop a single, global, self-consistent picture for the acceleration of relativistic particles in an accretion disk containing a shock".

LB07 was the first to develop a transport equation written in the appropriate cylindrical geometry in order to describe the acceleration of energetic particles in the accreting plasma of a hot, ADAF disk containing an isothermal shock. They created a self-consistent cylindrical symmetric model that describes specifically the acceleration of protons and/or electrons via first-order Fermi acceleration processes operating in the disk. This was to be applied to the model developed in LB04; a new inflow/outflow model that was successfully applied in order to explain the observed kinetic power of the outflows in M87 and Sgr A*. This was further explored in LB05 where a discussion was made on the detailed dynamics of ADAF disks containing isothermal shocks. Specifically, they explored the relationship between the dynamical structure of the disk/shock system and accelerated relativistic particles that escape form the disk and can become the jets.

In both papers, they were able to compute a self-consistent dynamical model for the structure of a shocked disk while maintaining that the rate of which the particles and energy escape from the shock location is consistent. LB07: they provided more information regarding how the accelerated particles are distributed in space and in energy. Furthermore, they also look into the distribution of the escaping relativistic particles from the disk at the shock location. They did this by computing the Green's function for monoenergetic particle injection. They finished up with a discussion of the spectrum of the observed (observable) secondary radiation produced by the escaping particles. This includes radio (synchrotron), inverse Compton X-ray and γ-ray emissions. This discussion served as a quantitative basis for the observational tests developed for the single-fluid model.

1.7 Motivation: Two-Fluid Model for Cosmic-Ray Shocks

While it has been demonstrated that the shock-acceleration process can be efficient enough to power the observed strong outflows in radio-loud active galaxies, such as M87, these early models neglected the back-reaction of the particle pressure onto the dynamical structure of the disk. Essentially, these models described a single-fluid accretion disk. This structure is largely assumed to contain a thermally-dominant fluid, with no microphysical connection to the relativistic particles, in which the thermal pressure firmly exceeds the particle pressure. Usually the dynamical structure is compared to the relativistic particle energy distribution in order to determine self-consistency. However, it has been shown that the pressure of the accelerated particles can actually exceed the pressure of the thermal background gas in the vicinity of the shock (see Figure 1.22a). This same phenomenon is also observed in the early models for the acceleration of cosmic-rays in supernova-driven shock waves (Figure 1.22b). In the cosmic-ray case, this problem was remedied through the inclusion of the cosmic-ray pressure in the two-fluid model of cosmic-ray-modified supernova shock waves (Drury & Volk 1981; Becker & Kazanas 2001).

The majority of the cosmic rays observed in our galaxy are thought to be accelerated by shock waves driven by supernova explosions (Axford et al. 1977). The exception is the population of ultra-high energy cosmic rays, whose origin is still not well understood, and which are probably created outside our galaxy. In the shock-acceleration model, energetic charged particles scatter elastically with magnetic irregularities (MHD waves) convected with the background gas (Drury & Völk 1981; Becker & Kazanas 2001). This is synonymous with the production of relativistic particles due to MHD in a shocked ADAF disk. Cosmic rays can travel freely when crossing a shock, but experience an increase in momentum. The convergence of the MHD waves at the shock, combined with the effect of spatial diffusion, allows the cosmic rays to cross the shock multiple times, gaining energy continuously. These particles avoid thermalization because the ion-ion mean free path, λ_{ii}, is much larger than the magnetic mean free path (coherence length), $\lambda_{\rm mag}$. Repeated shock crossings result in the characteristic power-law energy spectrum associated with first-order Fermi acceleration. The real difference between the two models (as depicted in Figure 1.23) is that cosmic-ray particles are accelerated at a supernova-expanding shock, while relativistic particles in the disk are accelerated at a standing shock.

Although the cosmic rays and the thermal background gas do not interact directly via collisions, the two populations are coupled together through interactions with the MHD waves. However, despite this, the earliest models for the acceleration of cosmic rays in supernova-driven shocks neglected to include the dynamical effect of the cosmic ray pressure. It was soon realized that the resulting cosmic ray pressure could exceed the pressure of the background thermal gas. In the next generation of models, this problem was remedied by treating the nonlinear coupling of the gas dynamics and the energization of the cosmic rays in a self-consistent manner. The resulting 'two-fluid' model for diffusive shock acceleration has become an accepted paradigm for studying the self-consistent cosmic-ray-modified shock problem.

The cosmic-ray-modified shock model can include both globally smooth solutions as well as solutions that contain discontinuous, gas-mediated 'sub-shocks.' In the case of a discontinuous shock, one observes a deceleration precursor in the fluid just upstream from the shock. This precursor phenomenon is not observed in the classical case, and is a unique characteristic of the two-fluid shock model. I anticipate that this type of behavior will also be observed in the disk context when the pressure of the accelerated particles is included in the dynamical equations self-consistently.

1.8 Thesis Objectives

Just to clarify, observing the effect of the cosmic-ray pressure to the background pressure has been done by comparing the dynamical structure to the particle distribution function. The struggle in previous studies has been verifying the self-consistency between them, rather than mixing them together. The importance of particle pressure in both the cosmic-ray-modified shock model and the two-temperature ADAF disk model is a strong motivation to reexamine the whole dynamical structure of the ADAF disk to include the relativistic particle pressure.

In this thesis, we intend to perform the same modification in the disk context in order to create a fully self-consistent model for the structure of the accretion disk, and the energy distribution of the accelerated relativistic particles that form the outflow. The work in this thesis branches off from the work of LB04, LB05, and LB07. From this, we will create a new two-fluid disk accretion model demonstrating the dynamical effect of both the relativistic particle pressure and the background (thermal) gas pressure. Here, we focus on the hydrodynamic structure of the disk, the modifications to the standard shock jump conditions that come into play due to the inclusion of the relativistic particle pressure, and how it feeds back into the relativistic particle energy transport function. The relativistic particle number and energy densities will also be determined self-consistently along with the structure of the disk. In essence, this model is a generalization of the one outlined and developed in LB04, LB05, and LB07. This thesis will cap off with examining the secondary radiation that can form from the outflows.

For the layout of this thesis: Ch. 2 will address the general theoretical framework between the dynamical single-fluid and two-fluid disk/shock models, and Ch. 3 will address the theoretical particle distributions computed using the two models. Ch. 4 provides a detailed application analysis of the number and energy density distributions of the relativistic particles to the disks/outflows in M87 and Sgr A* . Ch. 5 goes into observational predictions regarding the high-energy spectra (or secondary radiation) produced by the outflows. Finishing up this document is a discussion and conclusion (Ch. 6) regarding the astrophysical implications of these results.

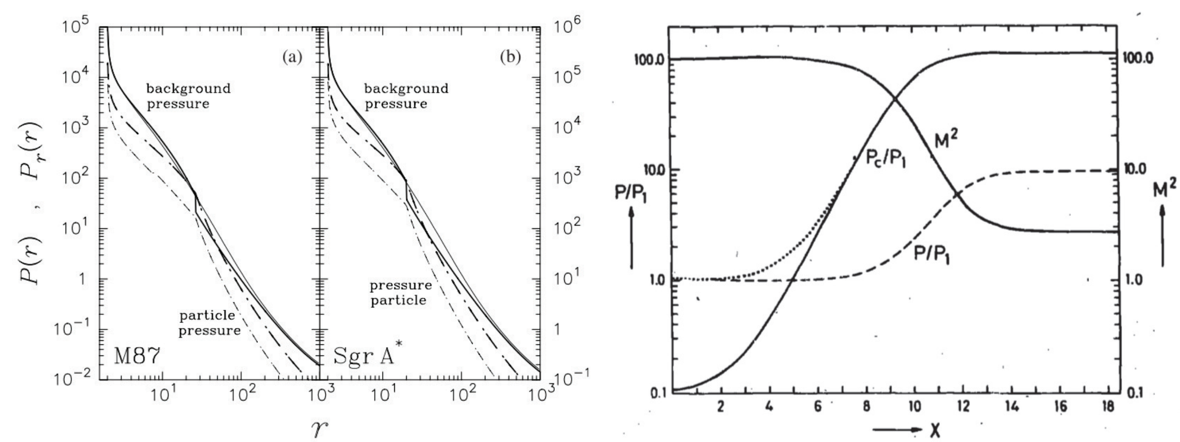

(a) (b)

Figure 1.22: Comparative plots of the two pressures. (a) From Becker et al. (2011): the background pressure P (solid lines) and relativistic particle pressure P_r (dot-dashed lines) plotted in cgs units as functions of radius r for two celestial bodies, where the thick lines represent the shocked-disk solution. (b) From Axford et al. (1977): ratios of the cosmic-ray P_c and background P pressures, and Mach number M, as functions of radius x. In both cases it can be seen that the relativistic particle pressure can exceed the background pressure if a shock is present.

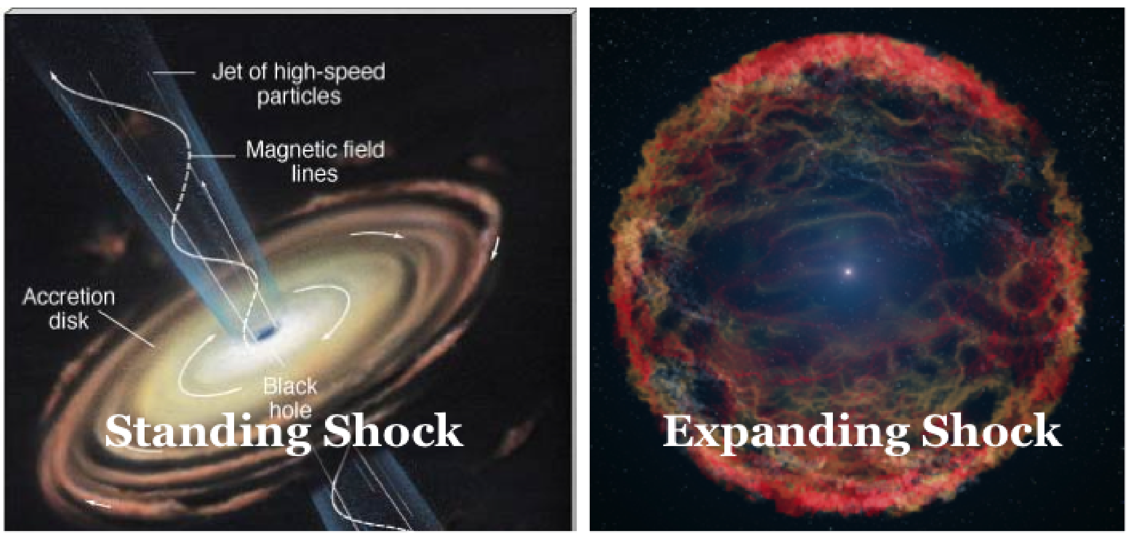

Figure 1.23: (a) An accretion disk with a standing shock (white arrows in the inner region), taken from: http://168.176.8.14/sagan/QAGN.html, and (b) a supernova with an expanding shock, taken from: http://www.spacetelescope.org/images/opo1438a/.

Chapter 2: Theory - Dynamical Disk Structure

In this chapter we will provide the theoretical background for the dynamical disk structure developed in this thesis. In moving forward, we will define the components for three different models, labeled Model 1, 2, and 3, respectfully. Model 1 is a representation of the single-fluid model and largely follows the work of LB04, LB05, and LB07, describing an inviscid disk with no relativistic particles in the dynamical equations. In Model 2, we introduce the relativistic particle pressure into the dynamical equations. Model 3 is the only self-consistent model, which also includes the dynamical effect of relativistic particle diffusion. Due to the similar structure and physics behind all three models, it was best to include them all into one chapter. Before we move into that, let's first go over some preliminary identities used in this work.

2.1 Preliminaries

This work uses the full Lagrangian derivative,

$$\frac{D}{Dt} = \frac{\partial}{\partial t} + \vec{v} \cdot \vec{\nabla} \ . \tag{2.1}$$

as well as Newton's second law in fluid mechanics,

$$\rho \frac{D\vec{v}}{Dt} = -\nabla P + \nabla \cdot \vec{T} + \vec{f} \ , \tag{2.2}$$

where $\rho D\vec{v}/Dt$ represents the inertia (per volume), $D\vec{v}/Dt$ is the material derivative that incorporates the full Lagrangian derivative (Equation 2.1) and represents the flow of the fluid in the disk, ∇P is the total pressure gradient, $\vec{T}$ is the stress tensor that corresponds to viscosity, and $\vec{f}$ represents the body forces (per unit volume) acting on the fluid. When expanding out the material derivative, Equation (2.2) becomes

$$\rho\left(\frac{\partial\vec{v}}{\partial t}+\vec{v}\cdot\nabla\vec{v}\right)=-\nabla P+\nabla\cdot\vec{T}+\vec{f}\ , \tag{2.3}$$

where $\partial\vec{v}/\partial t$ is the unsteady acceleration, and $\vec{v}\cdot\nabla\vec{v}$ is the convective acceleration. Equation (2.3) is also known as the general form of the Navier-Stokes equation. In this work we focus on a system without viscosity, in which applying $\nabla\cdot\vec{T}\rightarrow 0$ to Equation (2.3),

$$\rho\left(\frac{\partial\vec{v}}{\partial t}+\vec{v}\cdot\vec{\nabla}\vec{v}\right)=-\vec{\nabla}P+\vec{f}\ , \tag{2.4}$$

becomes Euler's equation in fluid dynamics. Next, we move forward into describing the transonic flow structure of the disk.

2.2 Transonic Flow Structure

2.2.1 The Relationship Between Shocks and Outflows

A shock is formed from the centrifugal motion of the plasma in the disk, which has been pointed out via simulations by Hawley et al. (1984a, 1984b) and Chakrabarti (1990) to be a 'wall' as a result of the gas falling in with some rotation. In the vicinity of the shock, the acceleration of the relativistic particles is concentrated, which is what "channels a significant fraction of the binding energy of the accreting gas into a population of relativistic particles" (LB07). These particles become high-energy relativistic particles, and via diffusion are allowed to escape through the disk vertically, containing the energy and entropy created from the accelerated particles. What's remaining in the gas/plasma is accreted into the black hole.

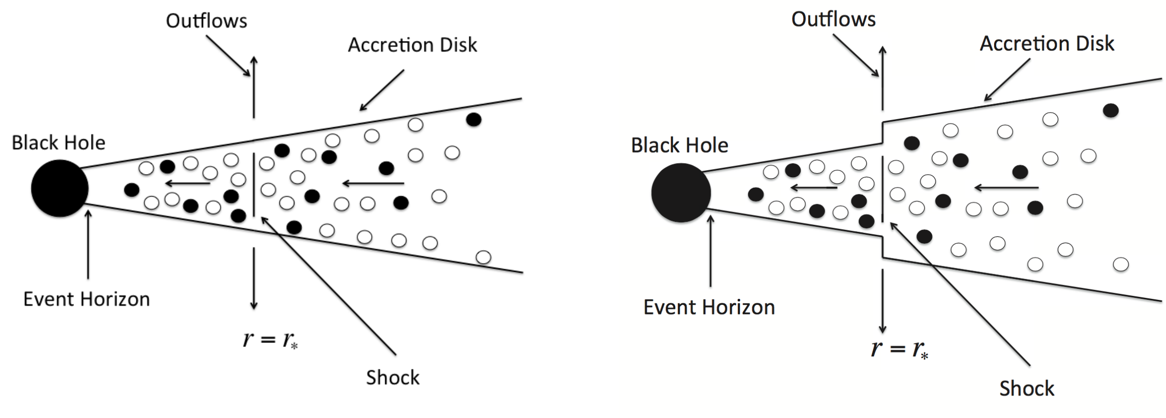

(a) (b)

Figure 2.1: A schematic diagram of our disk/shock/outflow model for (a) the single-fluid model, and (b) our two-fluid model. Both contain the test particles (filled circles) injected at the shock location, and the MHD scattering centers (open circles) moving with the background gas throughout the disk. The compression of the scattering centers at the shock leads to efficient particle acceleration, which is analogous to the acceleration of cosmic rays in supernova-driven shocks.

In the model considered here (depicted in Figure 2.1), the gas is accelerated gravitationally toward the central mass, and experiences a shock transition due to an obstruction near the event horizon, which is a consequence of the centrifugal 'barrier' located between the inner and outer sonic points. Relativistic particles accelerated at the shock are transported throughout the disk until they either (1) escape via diffusion through the disk surface (forming the outflow from the upper/lower edges of the cylindrical shock), (2) advect through to the event horizon, or (3) diffuse radially outward through the disk (see §3 of LB05 for further detail). We employ the standard set of physical conservation equations discussed by Chakrabarti (1989a) and Abramowicz & Chakrabarti (1990) describing a vertically-averaged, one-dimensional, steady-state accretion disk that incorporates the effects of general relativity using the pseudo-Newtonian approximation for the gravitational potential. However, the conservation equations used here will be generalized to include relativistic particle pressure.

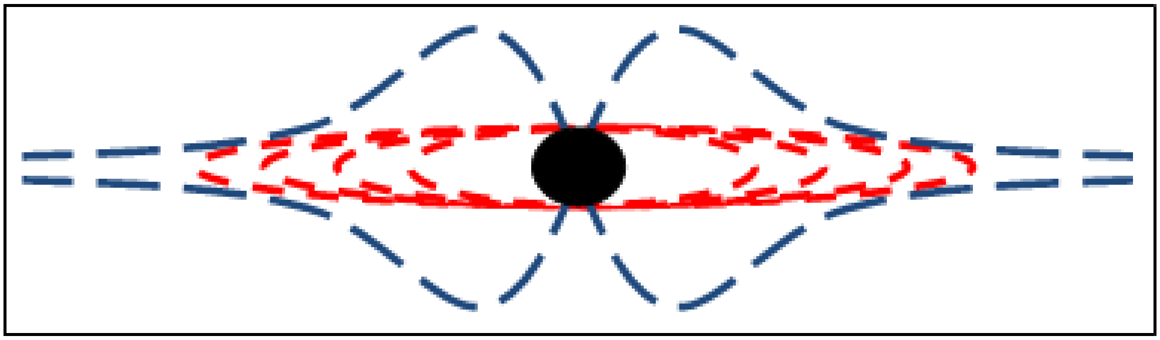

Figure 2.2: Black hole accretion system.

2.2.2 The System: An Accretion Disk with Gas and Relativistic Particles

To paraphrase Chakrabarti's book (1990), the black hole has a mass M and is at rest in the center of an infinite cloud of gas (the accretion disk), which at infinity is also at rest and has uniform density ρ_∞ and pressure P_∞. The motion of the gas in the accretion disk is symmetric (depending on the disk's geometry) and steady, and the increase in mass of the black hole is ignored so that the field of force is unchanging. The accretion disk is depicted in Figure 2.2. Here, the flat part represents a cool, thin accretion disk (with high accretion rate), and the curved part represents a hot, thick disk (with low accretion rate). This work incorporates both types but will largely focus on the mechanics of the hot disk. The convective acceleration $\vec{v} \cdot \nabla \vec{v}$ defined in Equation (2.4) is an acceleration caused by a change in velocity over position, while individual fluid particles are being accelerated and thus are under unsteady motion.

The accretion disk is considered a compressible fluid; by assuming that the fluid is comprised of an ideal gas the system becomes simpler. Here the disk becomes a closed, isolated system limited to the mechanizations and interactions of the individual particles; here it is considered adiabatic. The pressure (either thermal pressure, particle pressure, or both) acted on by an adiabatic fluid is generally defined as

$$P = (\gamma - 1)U \ , \tag{2.5}$$

where U is the internal energy density of the fluid and γ is the isentropic heat index. If the disk fluid contains gas particles, there is thermal particle pressure,

$$P_g = (\gamma_g - 1)U_g \ . \tag{2.6}$$

If the fluid also contains non-thermal particles, there is relativistic particle pressure,

$$P_r = (\gamma_r - 1)U_r \ , \tag{2.7}$$

where γ_g and γ_r now represent the isentropic, adiabatic index of the thermal and relativistic particles, respectively. In the single-fluid model (Model 1), typically γ was set to represent either a thermally-dominated $\gamma = 5/3$, or radiatively-dominated $\gamma = 4/3$ accretion disk. Here, in this work, we will set $\gamma_r = 4/3$ since it represents the relativistic pressure, while $\gamma_g = 3/2$ in order for the thermal pressure to contain equal amounts of gas and magnetic pressure (Narayan & Yi 1995), which is considered appropriate for an optically thin advection-dominated flow (Narayan et al. 1997). It should be noted that from this point forward, we use the subscripts 'g' and 'r' to refer to quantities associated with the gas and relativistic particles, respectively.

As these particles interact with each other in the fluid, a sound speed is generated. Considering that the adiabatic sound speed is generally defined as

$$a^2(r) = \frac{\gamma P}{\rho} \ ,$$

we can use this correlation to define the adiabatic sound speed due to the gas (thermal particles),

$$a_g^2(r) = \frac{\gamma_g P_g}{\rho} \ , \tag{2.8}$$

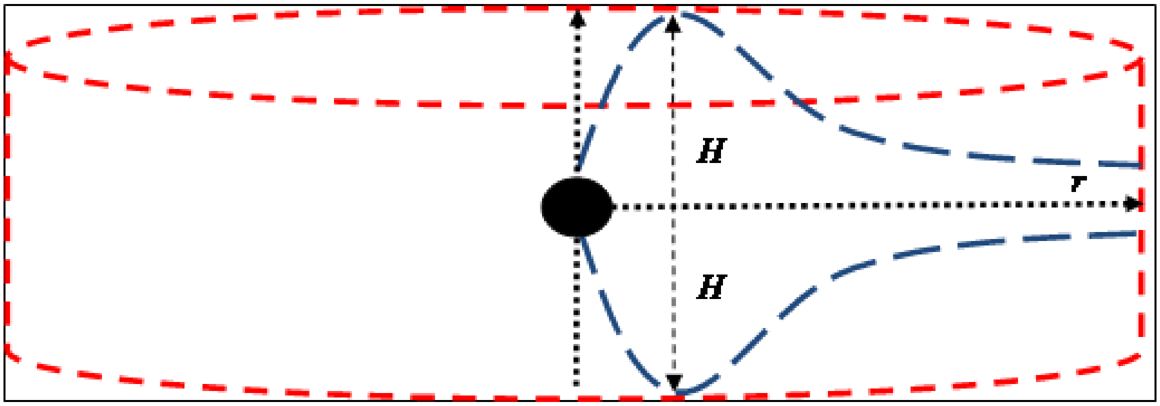

Figure 2.3: Hot-accretion disk-system with imaginary cylindrical shell.

as well as the adiabatic sound speed due to the relativistic (non-thermal) particles,

$$a_r^2(r) = \frac{\gamma_r P_r}{\rho} \ . \tag{2.9}$$

2.2.3 The Geometry of the Disk

The ADAF disk is represented with an imaginary cylindrical shell, with H being the disk half-thickness of the accretion flow (with respect to the center-axis of the shell) and r is the radius of the cylinder, as seen in Figure 2.3. The radius of the cylindrical shell can be adjusted depending on location in the accretion disk; in Figure 2.3 the radius is the maximum of the hot accretion disk where the black hole is the center reference. This work assumes a steady state/cylindrical symmetry with mass conservation. From Figure 2.3, the shell area A_* (or area of a cylinder) is defined as,

$$A_* = 2\pi r h = 2\pi r \,(2H) = 4\pi r H \ . \tag{2.10}$$

2.2.4 Deriving the Hydrostatic Relation for an Inviscid Disk

Imagine that the flow to be in vertical hydrostatic equilibrium, where the force balance (or conservation of momentum) is in the vertical ($\hat{z}$) direction: Here, the main forces operating

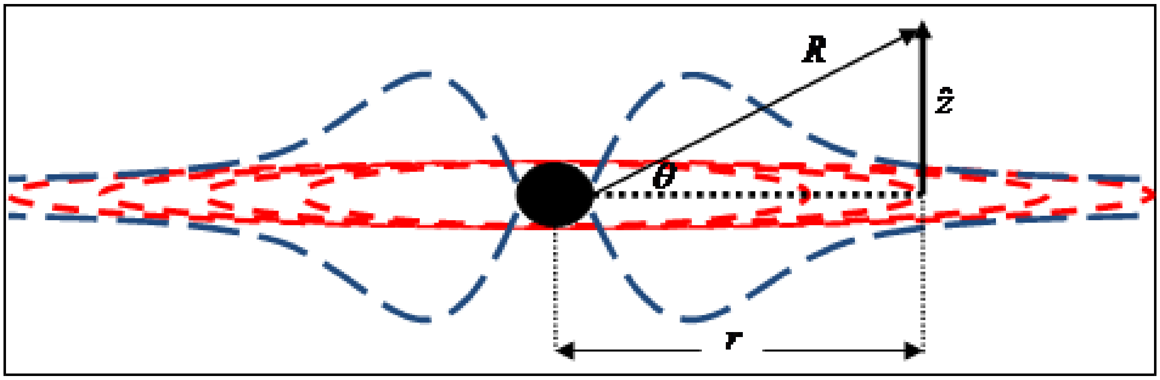

Figure 2.4: Force balance in the vertical (z) direction in cylindrical coordinates.

are gravity (the normal force due to the black hole) and internal pressure (or pressure gradient) in the disk. Consider a force balance across a thin disk shell of mass dm, in which the two forces are incorporated where the internal pressure and volumetric density become functions of the radius, with height dz and whose face is given by the area A. The shell given in Figure 2.5 has a mass dm defined as,

$$dm = \rho dV = \rho A dz \ . \tag{2.11}$$

Hydrostatic equilibrium occurs when these two forces are in balance. Even under the guise of the disk shell above, the minute changes in the forces due to pressure dF_P and gravity df_{G} have to be equal to one another $dF_P + df_{\mathrm{G}} = 0$ for this condition to be satisfied. The force due to the internal pressure is a product of the disk shell area and the pressure itself $dF_P = AdP$. For now we will make a small substitution where we will define the change in pressure as

$$dP = \frac{dP}{dz} dz \ , \tag{2.12}$$

in which case we can substitute in Equation (2.12) and define the change in the force due the pressure as

$$dF_P = AdP = A\frac{dP}{dz} dz \ . \tag{2.13}$$

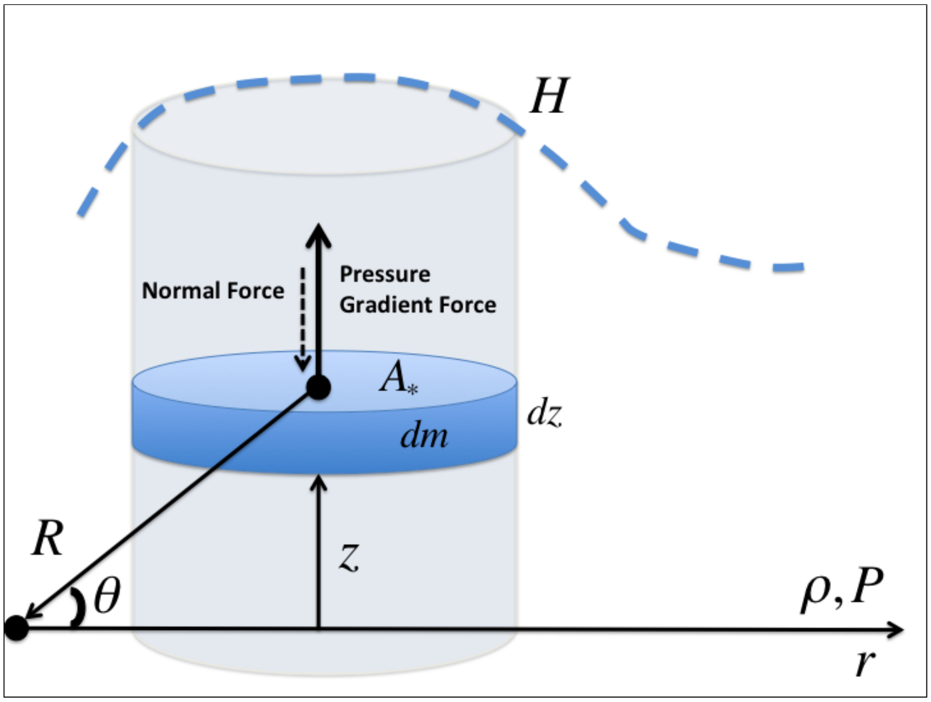

Figure 2.5: Closer examination of the force balance in the vertical direction.

Now the force due to gravity here references to Newton's law of universal gravitation,

$$F = \frac{Gm_1m_2}{R^2} \ ,$$

where G is the gravitational constant and R refers to the distance between the center of two masses. In this system m_1 refers to the mass M of the black hole and m_2 corresponds to the mass of the shell dm, while R is now the distance from the shell to the black hole, which is denoted by the Schwarzschild radius r_{S}. Considering that the change in the gravitational force will depend on the mass of the shell, there is an additional angle θ reference in the geometry, and thus from Figure 2.5 this force is defined as

$$df_{\mathrm{G}} = -\frac{GM}{(R - r_{\mathrm{S}})^2} \sin\theta dm = -\frac{GM}{(R - r_{\mathrm{S}})^2} \frac{z}{R} dm \ . \tag{2.14}$$

In order to satisfy the hydrostatic equilibrium we equate Equations (2.13) and (2.14) to get

$$A\frac{dP}{dz}dz = \frac{GM}{(R - r_{\mathrm{S}})^2}\frac{z}{R}dm \ .$$

By subtituting in Equation (2.12),

$$\frac{dP}{dz} = \frac{GM\rho}{(R - r_{\mathrm{S}})^2}\frac{z}{R} \ . \tag{2.15}$$

Under the limit that $z \to H$, then the change in the internal pressure becomes just the total pressure $dP \to P$, in which case Equation (2.15) becomes

$$\frac{P}{H} = \frac{GM\rho}{(R - r_{\mathrm{S}})^2}\frac{H}{R} \ .$$

Assuming that $z \ll R$, then $R \sim r$, where now the generic form of the hydrostatic equilibrium defines that the disk half-thickness H as

$$H^2 = \frac{Pr\,(r - r_{\mathrm{S}})^2}{GM\rho} \ . \tag{2.16}$$

For the purposes of this work though we do make a minor correction to Equation (2.16), where we define the true disk half-thickness for this system as

$$H^2 \approx \frac{Pr\,(r - r_{\mathrm{S}})^2\,\gamma_g}{GM\rho} \ , \tag{2.17}$$

where P is now the total pressure, considering though that pressure will be different depending on the model. For Model 1, the total pressure of system is due to the gas itself

$P \to P_g$,

$$H^2 \approx \frac{r\left(r - r_{\rm S}\right)^2 \gamma_g}{GM\rho} P_g \; . \tag{2.18}$$

For Models 2 and 3, the total pressure is actually a linear combination of the thermal and relativistic pressures $P = P_g + P_r$,

$$H^2 \approx \frac{r\left(r - r_{\rm S}\right)^2 \gamma_g}{GM\rho} \left(P_r + P_g\right) \; . \tag{2.19}$$

It is generally accepted that with AGNs, the accretion disk follows Keplerian rotation (see § 1.6.1), subjecting the particles to simple celestial mechanics. The Keplerian angular velocity used in this model is defined under a pseudo-Newtonian context (Equation 1.14)

$$\Omega_{\rm K}^2 = \frac{GM}{r\left(r - r_{\rm S}\right)^2} \; . \tag{2.20}$$

This serves to further simplify the derived hydrostatic relations. Thus by combining Equation (2.18) with Equations (2.8) and (2.20), the disk half-thickness for Model 1 becomes

$$H = \frac{a_g}{\Omega_{\rm K}} \; . \tag{2.21}$$

And likewise, combining Equation (2.19) with Equations (2.8), (2.9) and (2.20), the disk half-thickness for Models 2 and 3 becomes

$$H = \frac{1}{\Omega_{\rm K}} \sqrt{\left(\frac{\gamma_g}{\gamma_r}\right) a_r^2 + a_g^2} \; . \tag{2.22}$$

2.3 The Transport Rates

There are three conserved transport rates in viscous ADAF disks: the mass transport rate $\dot{M}$, the angular momentum transport rate $\dot{J}$, and the energy transport rate $\dot{E}$, which are all defined to be positive for inflow. The transport rates are determined as follows.

2.3.1 Deriving the Mass Transport Rate $\dot{M}$

Upon mass conservation, we use the mass continuity equation

$$\frac{\partial \rho}{\partial t} = -\vec{\nabla} \cdot (\rho \vec{v}) \tag{2.23}$$

where ρ is the volumetric fluid mass density, and $\vec{v}$ is the bulk velocity. There are two ways to derive the mass transport rate. First is directly defining the mass accretion rate,

$$\dot{M} = A_* F_m \ , \tag{2.24}$$

as a product of the mass flux F_m and the shell area A_* (Equation 2.10). The mass flux is a result from integrating the radial component of Equation (2.23) with respect to r in cylindrical coordinates. First we expand the right-hand-side of Equation (2.23),

$$\vec{\nabla} \cdot (\rho \vec{v}) = \frac{1}{r} \frac{\partial}{\partial r} (r \rho v_r) + \frac{\rho}{r} \frac{\partial v_\phi}{\partial \phi} + \rho \frac{\partial v_z}{\partial z} \ . \tag{2.25}$$

Since all particles in the fluid are advected into the black hole, it should be noted that for the radial component for $\vec{v}$: $v_r = -v$, since the radial velocity v is considered positive for inflowing particles. Focusing on the radial component of Equation (2.25), the mass continuity equation becomes

$$\frac{\partial \rho}{\partial t} = -\frac{1}{r} \frac{\partial}{\partial r} (r \rho v) \ . \tag{2.26}$$

Considering that my work focuses on the steady-state solution, $\partial \rho / \partial t \to 0$ and $\partial / \partial r$ can be replaced by the ordinary derivative d/dr. Integrating Equation (2.26) with respect to r will bring up the mass flux $F_m = \rho v$,

$$F_m = \int \frac{1}{r} \frac{\partial}{\partial r} (r \rho v) \, dr = \frac{1}{r} (r \rho v) = \rho v \tag{2.27}$$

which is a constant. Combining this with Equation (2.10), the mass accretion rate (Equation 2.24) becomes,

$$\dot{M} = 4\pi r H \rho v \ , \tag{2.28}$$

which is a universal relation for all three Models, in which H is the only thing that differentiates between them.

From the positive sign of the radial flow velocity, it can be seen that the mass transport rate is also positive for inflowing particles. Note that the mass transport rate is in units of mass per unit time and is considered a constant. On a final note, the second method for determining the mass accretion rate is through direct calculation for Equation (2.23) and a full volumetric integration dV over the radial component, with $v = -v_r$:

$$\dot{M} = -\int \nabla \cdot (\rho \vec{v}) \, dV = \int \frac{1}{r} \frac{\partial}{\partial r} (r \rho v) \, r dr d\phi dz = \int_0^r \rho v dr \int_0^{2\pi} d\phi \int_0^{2H} dz = 4\pi r H \rho v \ . \tag{2.29}$$

This agrees with Equation (2.28).

2.3.2 The Angular Momentum Transport Rate $\dot{J}$

The angular momentum transport rate is defined by (LB05),

$$\dot{J} = \dot{M} r^2 \Omega - \mathcal{G} \ , \tag{2.30}$$

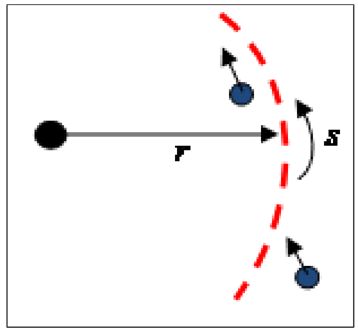

Figure 2.6: Angular momentum of the disk.

where Ω is the angular velocity and $\mathcal{G}$ is the torque. The gradient of the angular velocity Ω is related to the torque $\mathcal{G}$ by (e.g., Frank et al. 2002)

$$\mathcal{G} = -4\pi r^3 H \rho \nu \frac{d\Omega}{dr} \; , \tag{2.31}$$

where ν is the kinematic viscosity. Particles rotating around the disk (see Figure 2.6) will not follow along the arc path S, but rather through it while rotating since they are inflow. In this work, we will consider the energy due to the torque to be negligible ($\mathcal{G} = 0$; see § 2.4 for further details), as the torque in the system corresponds to the azimuthal direction only, and we will be working under the radial component. Therefore the velocity in the azimuthal direction v_ϕ corresponds to the specific angular momentum l as

$$l = r v_\phi \; . \tag{2.32}$$

Likewise the specific angular momentum is also related to the angular velocity Ω,

$$l = r^2 \Omega \; . \tag{2.33}$$

Since angular momentum is conserved in this system, the specific angular momentum will effectively be the same even if the angular velocity is Keplerian,

$$l = r^2 \Omega_{\mathrm{K}} \ . \tag{2.34}$$

Following this we can see that the Keplerian angular velocity (Equation 2.20) actually comes from the velocity in the azimuthal direction,

$$\Omega_{\mathrm{K}} = \frac{v_\phi}{r} \ . \tag{2.35}$$

2.3.3 The Total Radial Energy Flux

It's been shown in Appendix A that the total energy density U_{tot} is related to the total energy flux $\vec{F}_{\mathrm{tot}}$ via the following relationship,

$$\frac{\partial U_{\mathrm{tot}}}{\partial t} = -\vec{\nabla} \cdot \vec{F}_{\mathrm{tot}} \ , \tag{2.36}$$

where,

$$\vec{F}_{\mathrm{tot}} = (U_g + P_g)\,\vec{v} + (U_r + P_r)\,\vec{v} - \frac{GM\rho\vec{v}}{R - R_s} + \frac{1}{2}\rho\,(\vec{v}\cdot\vec{v})\,\vec{v} - \kappa\vec{\nabla}U_r \ . \tag{2.37}$$

In Appendix A, we show that this relation stems from the full Lagrangian derivatives for the thermal U_g and relativistic U_r energy densities (Equation A.5),

$$\frac{DU_r}{Dt} = \frac{\gamma_r U_r}{\rho}\frac{D\rho}{Dt} - \vec{\nabla}\cdot\left(-\kappa\vec{\nabla}U_r\right) \ , \qquad \frac{DU_g}{Dt} = \frac{\gamma_g U_g}{\rho}\frac{D\rho}{Dt} \ . \tag{2.38}$$

In moving forward, now we must split the components apart accordingly. If we go with the vector notation for velocity in cylindrical coordinates,

$$\vec{v} = v_r \hat{r} + v_\phi \hat{\phi} + v_z \hat{z} \ , \tag{2.39}$$

then the term $\vec{v} \cdot \vec{v}$ becomes a scalar:

$$\vec{v} \cdot \vec{v} = v_r^2 + v_\phi^2 + v_z^2 \ .$$

However, it should be noted that in this work, there's no velocity in the $\hat{z}$ direction as everything's been vertically averaged. So the product $(\vec{v} \cdot \vec{v})\, \vec{v}$ becomes,

$$(\vec{v} \cdot \vec{v})\, \vec{v} = v_r^3 \hat{r} + v_\phi^2 v_r \hat{r} + v_r^2 v_\phi \hat{\phi} + v_\phi^3 \hat{\phi} \ .$$

The divergence of the relativistic energy density U_r in cylindrical coordinates is written as,

$$\vec{\nabla} U_r = \frac{dU_r}{dr} \hat{r} + \frac{1}{r} \frac{dU_r}{d\phi} \hat{\phi} + \frac{dU_r}{dz} \hat{z} \ .$$

Note that $R - R_s \to r - r_\mathrm{s}$ in the gravitational potential term, and when you combine Equation (2.5) with everything above and focus on the $\hat{r}$ components, we get the total radial energy flux,

$$F_{\mathrm{tot,r}} = \gamma_g U_g v_r + \gamma_r U_r v_r - \frac{GM\rho v_r}{r - r_\mathrm{s}} + \frac{1}{2}\rho v_r^3 + \frac{1}{2}\rho v_\phi^2 v_r - \kappa \frac{dU_r}{dr} \ . \tag{2.40}$$

Note that v_r refers to the cylindrical radial component of the bulk velocity, which extends outward from zero to infinity, and is positive for inflow, $v_r = -v$.

2.3.4 The Energy Transport Rate $\dot{E}$

In this work, the total energy transport rate $\dot{E}$ can be written as a linear combination

$$\dot{E} = \dot{E}_g + \dot{E}_r \ , \tag{2.41}$$

where $\dot{E}_g$ and $\dot{E}_r$ denote the rates for the gas and relativistic particles, respectively. Generally, the energy transport rate is defined as,

$$\dot{E} = A_* F \ , \tag{2.42}$$

where F is the energy flux and A_* is the shell area (Equation 2.10). In § 2.3.3 the total radial energy flux $F_{\rm tot,r}$ ignored the energy due to torque $\mathcal{G}$, so we should be more clear that the total energy transport rate is actually,

$$\dot{E} = \dot{E}_{\rm tot,r} - \mathcal{G}\Omega \ , \tag{2.43}$$

where,

$$\dot{E}_{\rm tot,r} = -4\pi r H F_{\rm tot,r} \ . \tag{2.44}$$

Since $v_r = -v$ for positive inflow, Equation (2.44) ensures that the energy transport rate likewise remains positive for inflowing particles. Combining this with Equations (1.14), (2.28), (2.40) and (2.44), we redefine Equation (2.43) as

$$\dot{E} = -\mathcal{G}\Omega + \dot{M}\left(\frac{1}{2}v_\phi^2 + \frac{1}{2}v^2 + \frac{\gamma_g U_g}{\rho} + \frac{\gamma_r U_r}{\rho} + \Phi + \frac{\kappa}{\rho v}\frac{dU_r}{dr}\right) \ , \tag{2.45}$$

in which now, the components of Equation (2.41) are given by

$$\dot{E}_g = -\mathcal{G}\Omega + \dot{M}\left(\frac{1}{2}v_\phi^2 + \frac{1}{2}v^2 + \frac{\gamma_g U_g}{\rho} + \Phi\right) \ , \tag{2.46}$$

and

$$\dot{E}_r = \dot{M}\left(\frac{\gamma_r U_r}{\rho} + \frac{\kappa}{\rho v}\frac{dU_r}{dr}\right) , \tag{2.47}$$

where ρ is the mass density, v is the radial velocity (defined to be positive for inflow), Ω is the angular velocity, $\mathcal{G}$ is the torque, H is the disk half-thickness, $v_\phi = r\Omega$ is the azimuthal velocity, and κ is the spatial diffusion coefficient in the radial direction. Each quantity is interpreted as a vertical average over the disk structure, and it is assumed that the adiabatic indices γ_g and γ_r remain constant throughout the flow. Following LB05 and LB07, we describe the variation of the spatial diffusion coefficient using

$$\kappa(r) = \kappa_0 v\,(r)\,r_{\rm S}\left(\frac{r}{r_{\rm S}} - 1\right)^2 , \tag{2.48}$$

where κ_0 is a dimensionless constant. In this work, the torque $\mathcal{G}$ is eliminated between Equations (2.30) and (2.45), which can then be combined with Equations (2.6), (2.7), (2.8), and (2.9) to express the energy transport per unit mass as

$$\epsilon \equiv \frac{\dot{E}}{\dot{M}} = \frac{1}{2}v^2 - \frac{1}{2}\frac{l^2}{r^2} + \frac{l_0 l}{r^2} + \frac{a_g^2}{\gamma_g - 1} + \frac{a_r^2}{\gamma_r - 1} + \Phi + \frac{\kappa}{\rho v}\frac{dU_r}{dr} , \tag{2.49}$$

where

$$l(r) \equiv r^2\Omega(r) , \quad l_0 \equiv \dot{J}/\dot{M} , \tag{2.50}$$

respectively, represent the specific angular momentum at radius r and the (constant) angular momentum transport per unit mass. Equation (2.49) is considered valid for both viscid and inviscid flows.

2.4 Inviscid Flow Equations

With viscosity neglected, the torque $\mathcal{G}$= 0 and the specific angular momentum becomes

$$l(r) = l_0 = \text{constant} \ . \tag{2.51}$$

In the inviscid case, Equation (2.49) reduces to

$$\epsilon = \frac{1}{2}v^2 + \frac{1}{2}\frac{l^2}{r^2} + \frac{a_g^2}{\gamma_g - 1} + \frac{a_r^2}{\gamma_r - 1} + \Phi + \frac{\kappa}{\rho v}\frac{dU_r}{dr} \ , \tag{2.52}$$

Since radiative losses are negligible in ADAF disks, in the absence of viscosity, the thermal flow is purely adiabatic, and the gas pressure and density are related by

$$P_g = D_0 \rho^{\gamma_g} \ , \tag{2.53}$$

where the parameter D_0 remains constant, except at the location of the isothermal shock if one exists in the flow. Combining Equation (2.53) with Equations (2.6), (2.7), (2.8) and (2.9) defines the derivative of the particle energy density,

$$\frac{dU_r}{dr} = \frac{\rho}{\gamma_r\left(\gamma_r - 1\right)}\left[\frac{da_r^2}{dr} + \frac{a_r^2}{a_g^2\left(\gamma_g - 1\right)}\frac{da_g^2}{dr}\right] \ . \tag{2.54}$$

This combined with Equation (2.52) redefines the energy transport rate in terms of the sound speeds

$$\epsilon = \frac{1}{2}v^2 + \frac{1}{2}\frac{l^2}{r^2} + \frac{a_g^2}{\gamma_g - 1} + \frac{a_r^2}{\gamma_r - 1} + \Phi + \frac{\kappa}{v\gamma_r\left(\gamma_r - 1\right)}\left[\frac{da_r^2}{dr} + \frac{a_r^2}{a_g^2\left(\gamma_g - 1\right)}\frac{da_g^2}{dr}\right] \ . \tag{2.55}$$

It should be noted that Equation (2.55) purely defines the energy transport for Model 3, however it does link back to Models 1 and 2. In the case of a non-diffusive, purely adiabatic disk, $\kappa = 0$ in Equation (2.55), we get the energy transport rate for Model 2,

$$\epsilon = \frac{1}{2}v^2 + \frac{1}{2}\frac{l^2}{r^2} + \frac{a_g^2}{\gamma_g - 1} + \frac{a_r^2}{\gamma_r - 1} + \Phi \ , \tag{2.56}$$

and likewise for when $a_r \to 0$, we get back the energy transport rate defined for Model 1,

$$\epsilon = \frac{1}{2}v^2 + \frac{1}{2}\frac{l^2}{r^2} + \frac{a_g^2}{\gamma_g - 1} + \Phi \ . \tag{2.57}$$

Determining the Entropy Parameter

In an adiabatic disk, the entropy of the thermal background gas is conserved. It is therefore convenient to define the gas entropy parameter, K_g, which is related to the entropy per particle, S_g, via (Becker & Le 2003)

$$S_g = k \ln K_g + c_0 \ , \tag{2.58}$$

where k is the Boltzmann constant and c_0 is a constant that is independent of the state of the gas. The entropy parameter is a constant specific to each Model, and acts as a variable consistent throughout the accretion disk; one which can be used to simplify down the dynamic equations. Normally this is derived from the mass transport rate (Equation 2.28), which when combined with Equation (2.21) becomes for Model 1,

$$\dot{M} = \frac{4\pi r \rho v a_g}{\Omega_{\rm K}} \ . \tag{2.59}$$

Likewise, by combining Equations (2.28) and (2.22), the mass transport rate for Models 2 and 3 becomes,

$$\dot{M} = \frac{4\pi r \rho v}{\Omega_{\rm K}} \sqrt{\left(\frac{\gamma_g}{\gamma_r}\right) a_r^2 + a_g^2} \ . \tag{2.60}$$

Considering that we are looking at a system where pressure and mass density are both functions of the radius, it is actually easier to not keep track of the mass density ρ. With the disk being adiabatic we can use the polytropic relation (Equation 2.53) and can make a substitution for the adiabatic sound speed (Equation 2.8),

$$a_g^2 = \gamma_g D_0 \rho^{\gamma_g - 1} \ . \tag{2.61}$$

Note that in the case where there's no diffusion but the fluid comprises both the thermal and relativistic particles (Model 2), then it stands to reason that the non-thermal particles would follow the same adiabatic properties as the thermal particles. Therefore, we can argue that in this case the relativistic flow is purely adiabatic, and the nonthermal pressure and density are related by

$$P_r = D_1 \rho^{\gamma_r} \ , \tag{2.62}$$

where D_1 is also a constant, except in the presence of a shock. Thus in that case we can likewise define the adiabatic sound speed for the relativistic particles using Equations (2.8) and (2.62) as

$$a_r^2 = \gamma_r D_0 \rho^{\gamma_r - 1} \ . \tag{2.63}$$

Thus, by combining Equations (1.14), (2.22), (2.28) and (2.61), we obtain

$$K_g \equiv r^{3/2} \left(r - r_{\rm S}\right) v a_g^{2/(\gamma_g - 1)} \left(\frac{\gamma_g}{\gamma_r} a_r^2 + a_g^2\right)^{1/2} \ , \tag{2.64}$$

which is constant throughout an adiabatic disk, except at the location of an isothermal shock. It should be noted that Equation (2.64) is a generalization of the corresponding result obtained by Becker & Le (2003) with the inclusion of the relativistic particle sound speed a_r. If $a_r \to 0$, we end up back with the familiar relation defined in Model 1,

$$K_g \equiv r^{3/2} \left(r - r_{\rm S}\right) v a_g^{(\gamma_g+1)/(\gamma_g-1)} \ . \tag{2.65}$$

By analogy with K_g, we also can define the entropy parameter for the relativistic particles using Equations (1.14), (2.22), (2.28) and (2.63) to get

$$K_r \equiv r^{3/2} \left(r - r_{\rm S}\right) v a_r^{2/(\gamma_r-1)} \left(\frac{\gamma_g}{\gamma_r} a_r^2 + a_g^2\right)^{1/2} \ . \tag{2.66}$$

This quantity approaches a constant value near the horizon where the fluid becomes non-diffusive and purely adiabatic. However at larger radii, K_r is not conserved, and will increase due to spatial diffusion. Combining Equations (2.64) and (2.66) produces an entropy ratio defined as

$$\frac{K_g}{K_r} \equiv \frac{a_g^{2/(\gamma_g-1)}}{a_r^{2/(\gamma_r-1)}} \ . \tag{2.67}$$

2.4.1 Wind Equation with Diffusion (Model 3)

The wind equation is derived as a method for analyzing the implications of the transonic (critical) nature of the accretion flow. Previously it was a first-order differential equation in terms of the flow velocity v (Model 1), which is computed using a simple root-finding procedure. In this work, the wind equation is defined as the first-order differential equation that governs the square of the thermal sound speed a_g. It should be noted that one cannot use a simple root-finding procedure to solve for the thermal sound speed a_g as a function of r, when diffusion is included, as it is an unstable computation. By first obtaining the steady-state radial momentum equation (Equation B.10)

$$v\frac{dv}{dr} = -\frac{1}{\rho}\frac{dP}{dr} - \frac{GM}{(r - r_{\mathrm{S}})^2} + \frac{l^2}{r^3} \ , \tag{2.68}$$

where here, $P = P_g + P_r$. Substituting in Equations (2.8) and (2.9), we can see that

$$\frac{dP}{dr} = \frac{dP_g}{dr} + \frac{dP_r}{dr} = \left(\frac{a_g^2}{\gamma_g} + \frac{a_r^2}{\gamma_r}\right)\frac{d\rho}{dr} + \frac{\rho}{\gamma_g}\frac{da_g^2}{dr} + \frac{\rho}{\gamma_r}\frac{da_r^2}{dr} \ . \tag{2.69}$$

We can also see from Equation (2.61) that,

$$\frac{d\rho}{dr} = \frac{\rho}{a_g^2(\gamma_g - 1)}\frac{da_g^2}{dr} \ . \tag{2.70}$$

Thus, after combining with Equation (2.70), Equation (2.69) simplifies down to,

$$\frac{dP}{dr} = \frac{\rho\left(a_r^2 + \gamma_r a_g^2\right)}{\gamma_r a_g^2(\gamma_g - 1)}\frac{da_g^2}{dr} + \frac{\rho}{\gamma_r}\frac{da_r^2}{dr} \ . \tag{2.71}$$

Therefore, by substituting in Equation (2.71), the steady-state radial momentum equation for Model 3 (Equation 2.68) becomes

$$v\frac{dv}{dr} = \frac{l^2}{r^3} - \frac{GM}{(r - r_{\mathrm{S}})^2} - \frac{1}{\gamma_r}\frac{da_r^2}{dr} - \frac{\left(a_g^2\gamma_r + a_r^2\right)}{a_g^2\gamma_r(\gamma_g - 1)}\frac{da_g^2}{dr} \ , \tag{2.72}$$

then by taking the first-order derivative of the thermal entropy parameter (Equation 2.64)

$$-\frac{1}{v}\frac{dv}{dr} = \frac{3}{2r} + \frac{1}{(r - r_{\mathrm{S}})} + \frac{\gamma_g}{2\left(a_r^2\gamma_g + a_g^2\gamma_r\right)}\frac{da_r^2}{dr} + \left[\frac{1}{a_g^2\left(\gamma_g - 1\right)} + \frac{\gamma_r}{2\left(a_r^2\gamma_g + a_g^2\gamma_r\right)}\right]\frac{da_g^2}{dr} \ , \tag{2.73}$$

Equations (2.72) and (2.73) can now be combined with Equation (2.55) to construct the wind equation for the case with $\kappa \neq 0$.

$$\frac{da_g^2}{dr} = \frac{N}{D} \ , \tag{2.74}$$

where the numerator and denominator functions (N and D) are given by

$$\begin{aligned} N = {} & \frac{v\left(\gamma_r - 1\right)}{\kappa}\left[v^2\frac{\gamma_g\gamma_r}{2\left(a_r^2\gamma_g + a_g^2\gamma_r\right)} - 1\right]\left(\epsilon - \frac{1}{2}v^2 - \frac{1}{2}\frac{l^2}{r^2} - \frac{a_g^2}{\gamma_g - 1} - \frac{a_r^2}{\gamma_r - 1} - \Phi\right) \\ & + \frac{l^2}{r^3} - \frac{GM}{\left(r - r_{\mathrm{S}}\right)^2} + v^2\frac{\left(5r - 3r_{\mathrm{S}}\right)}{2r\left(r - r_{\mathrm{S}}\right)} \ , \\ D = {} & -\left\{\frac{a_r^2\gamma_g + \gamma_r a_g^2\left(\gamma_g + 1\right)}{2a_g^2\left(\gamma_g - 1\right)\left(a_r^2\gamma_g + a_g^2\gamma_r\right)}\right\}\left(v^2 - a_{\mathrm{eff},\kappa}^2\right) \ , \end{aligned} \tag{2.75}$$

and $a_{\mathrm{eff},\kappa}$ denotes the effective sound speed for the diffusive model,

$$a_{\mathrm{eff},\kappa}^2 = \frac{2a_g^2\left(a_r^2\gamma_g + a_g^2\gamma_r\right)}{a_r^2\gamma_g + \gamma_r a_g^2\left(\gamma_g + 1\right)} \ . \tag{2.76}$$

2.4.2 Wind Equation without Diffusion (Models 1 and 2)

Model 2

In the case of an adiabatic disk ($\kappa = 0$), where both the gas and relativistic particles experience non-diffusive transonic flow (Model 2), the particle pressure P_r relates to the density via Equation (2.62). Combining this with Equation (2.53) creates a symmetrical relationship between the two sound speeds

$$\frac{da_r^2}{dr} = \frac{a_r^2 (\gamma_r - 1)}{a_g^2 (\gamma_g - 1)} \frac{da_g^2}{dr} , \tag{2.77}$$

where now, when combined with Equations (2.72), (2.73) and Equation (2.57), the numerator and denominator functions become

$$\begin{aligned} N &= \frac{l^2}{r^3} - \frac{GM}{(r - r_{\rm S})^2} + v^2 \frac{(5r - 3r_{\rm S})}{2r (r - r_{\rm S})} , \\ D &= - \left\{ \frac{a_g^2 \gamma_r (\gamma_g + 1) + a_r^2 \gamma_g (\gamma_r + 1)}{2 \left(a_r^2 \gamma_g + a_g^2 \gamma_r\right) a_g^2 (\gamma_g - 1)} \right\} \left(v^2 - a_{\rm eff}^2\right) , \end{aligned} \tag{2.78}$$

with $a_{\rm eff}$ defined as the effective sound speed for the purely adiabatic disk

$$a_{\rm eff}^2 = \frac{2 \left(a_r^2 \gamma_g + a_g^2 \gamma_r\right) \left(a_g^2 + a_r^2\right)}{a_g^2 \gamma_r (\gamma_g + 1) + a_r^2 \gamma_g (\gamma_r + 1)} . \tag{2.79}$$

This becomes useful (later shown in § 2.5.1), when combined with the adiabatic critical conditions, in solving for the thermal sound speed a_g as a function of r using a simple root-finding procedure. But it should be noted that this is only true for the non-diffusive disk (Model 2).

Model 1

The wind equation derived for Model 1 is not much different for that Models 2 and 3, except it follows in a derivative jump in the velocity v rather than the thermal sound speed a_g. We first start with the steady-state radial momentum equation (Equation 2.68), except here the total pressure $P \to P_g$,

$$v\frac{dv}{dr} = -\frac{1}{\rho}\frac{dP_g}{dr} - \frac{GM}{(r-r_{\rm S})^2} + \frac{l^2}{r^3} \ . \tag{2.80}$$

It should be noted that this has already been solved for Model 3 in Equation (2.72), except in Model 1, $a_r \to 0$, thus it reduces down to the radial momentum equation described in LB05,

$$v\frac{dv}{dr} = \frac{l^2}{r^3} - \frac{GM}{(r-r_{\rm S})^2} - \frac{2a_g}{(\gamma_g - 1)}\frac{da_g}{dr} \ . \tag{2.81}$$

It should be noted that Equation (2.81) can also be derived from the first-order derivative of Equation (2.57). Then we take the first-order derivative of the thermal entropy parameter (Equation 2.73) by setting $a_r \to 0$,

$$-\frac{1}{v}\frac{dv}{dr} = \frac{3}{2r} + \frac{1}{(r-r_{\rm S})} + \frac{(\gamma_g+1)}{(\gamma_g-1)}\frac{1}{a_g}\frac{da_g}{dr} \ , \tag{2.82}$$

which again, is exactly the relation defined in LB05 for Model 1. Combining Equations (2.81) and (2.82) will obtain the wind equation for Model 1,

$$\frac{1}{v}\frac{dv}{dr} = \frac{N}{D} \ , \tag{2.83}$$

where the numerator and denominator functions are

$$N = \frac{l^2}{r^3} - \frac{GM}{\left(r - r_{\rm S}\right)^2} + v^2 \frac{\left(5r - 3r_{\rm S}\right)}{2r\left(r - r_{\rm S}\right)} \ , \quad D = \frac{2a_g^2}{\left(\gamma_g + 1\right)} - v^2 \ , \tag{2.84}$$

which are exactly like those derived in LB05. It should be noted that there is indeed a correlation between the numerator and denominator functions derived for Models 1 and 2, in which by setting $a_r = 0$ in Equation (2.78), we get back the same function determined in Equation (2.84) with a slight adjustment in the denominator function D determined by Equation (2.82). We move forward in laying out all of the material that goes with creating a global solution flow by first discussing the critical point analyses.

2.5 Critical Point Analysis

In the previous sections we have analyzed the properties of the wind equation for the diffusive and non-diffusive cases with $\kappa \neq 0$ and $\kappa = 0$, respectively. Now we must understand the implications of the transonic (critical) nature of the accretion flow in both cases. It should be noted that when applied, we shall use natural gravitational units with $GM = c = 1$ and $r_{\rm S} = 2$.

2.5.1 Critical Conditions for $\kappa = 0$ (Models 1 and 2)

Model 2

For the purposes of this section, we feel it pertinent to derive the critical point analysis for Model 2 first, then show what was done for Model 1. As stated in LB04 and LB05, the simultaneous vanishing of N and D (Equations 2.78) yields the critical conditions

$$\frac{l^2}{r_c^3} - \frac{GM}{\left(r_c - r_{\rm S}\right)^2} + v_c^2 \frac{\left(5r_c - 3r_{\rm S}\right)}{2r_c\left(r_c - r_{\rm S}\right)} = 0 \ , \tag{2.85}$$

$$v_c^2 - \frac{2\left(a_{rc}^2\gamma_g + a_{gc}^2\gamma_r\right)\left(a_{gc}^2 + a_{rc}^2\right)}{a_{gc}^2\gamma_r\left(\gamma_g+1\right) + a_{rc}^2\gamma_g\left(\gamma_r+1\right)} = 0 \ , \tag{2.86}$$

where v_c, a_{gc} and a_{rc} denote the values of the velocity and the thermal and relativistic sound speeds, respectively, at the critical radius, $r = r_c$. From the denominator function D in Equation (2.86) it can be seen that the critical velocity is symmetrically related to the two sound speeds via

$$v_c^2 = \frac{2\left(a_{rc}^2\gamma_g + a_{gc}^2\gamma_r\right)\left(a_{gc}^2 + a_{rc}^2\right)}{a_{gc}^2\gamma_r\left(\gamma_g+1\right) + a_{rc}^2\gamma_g\left(\gamma_r+1\right)} \ . \tag{2.87}$$

It can also be seen from the numerator function N in Equation (2.85) that the critical velocity is a function of the critical radius r_c and the specific angular momentum l,

$$v_c^2 = \frac{2r_c\left(r_c - r_{\rm S}\right)}{\left(5r_c - 3r_{\rm S}\right)}\left[\frac{GM}{\left(r_c - r_{\rm S}\right)^2} - \frac{l^2}{r_c^3}\right] \ . \tag{2.88}$$

It's interesting that Equation (2.88) is the same as Equation (23) of LB05. Note that if $a_{rc} \to 0$ in Equation (2.87), and is then combined with Equation (2.88), it will yield the same relationship for the critical thermal sound speed as given by Equation (24) from LB05. This confirms how this new 'transitional' model rebounds back to the previous models for a non-diffusive disk, while also synchronizing with the newer analysis that yields to a diffusive disk (see § 4).

This new approach does not allow for an elegant analytical solution for r_c like the quartic equation derived for Model 1, a thermal-based, inviscid disk (e.g. LB05, Das et al. 2001a). But there are steps to remedy that, even in this transitional model, with a more numerical approach. Starting with the energy transport rate (Equation 2.55) in the case where $\kappa = 0$, and combining it with Equation (2.88), we can solve for the thermal sound speed at the critical radius, $r = r_c$,

$$a_{gc}^2 = (\gamma_g - 1)\left[\epsilon - \frac{1}{2}\frac{l^2}{r_c^2} - \frac{a_{rc}^2}{\gamma_r - 1} + \frac{GM}{r_c - r_\mathrm{S}} - \frac{r_c\,(r_c - r_\mathrm{S})}{(5r_c - 3r_\mathrm{S})}\left\{\frac{GM}{(r_c - r_\mathrm{S})^2} - \frac{l^2}{r_c^3}\right\}\right] \ . \tag{2.89}$$

It serves to know that the entropy ratio in Equation (2.67) remains constant in an adiabatic disk, even at the critical point,

$$\frac{K_{gc}}{K_{rc}} \equiv \frac{a_{gc}^{2/(\gamma_g - 1)}}{a_{rc}^{2/(\gamma_r - 1)}} \ . \tag{2.90}$$

Note that in this model we assume that $\gamma_g = 1.5$ as an approximate equipartition between the gas and magnetic pressures (e.g. Narayan et al. 1997), while $\gamma_r = 4/3$ for the relativistic particles.

Combining Equations (2.89) and (2.90) yields a cubic function, in the form of the standard formula (e.g., Abramowitz & Stegun 1965), for the relativistic sound speed at the critical point,

$$a_{rc}^3 + \mathcal{N} a_{rc}^2 + \mathcal{P} = 0 \ , \tag{2.91}$$

where

$$\begin{aligned} \mathcal{N} &= \frac{(\gamma_g - 1)}{(\gamma_r - 1)}\sqrt{\frac{K_{rc}}{K_{gc}}} \ , \\ \mathcal{P} &= -\,(\gamma_g - 1)\sqrt{\frac{K_{rc}}{K_{gc}}}\left\{\epsilon - \frac{1}{2}\frac{l^2}{r_c^2} + \frac{GM}{r_c - r_\mathrm{S}} - \frac{r_c\,(r_c - r_\mathrm{S})}{(5r_c - 3r_\mathrm{S})}\left[\frac{GM}{(r_c - r_\mathrm{S})^2} - \frac{l^2}{r_c^3}\right]\right\} \ . \end{aligned} \tag{2.92}$$

Of the three possible solutions to this cubic function, only one is actually a real, valid answer. Combining this solution with Equations (2.85) and (2.89) to the denominator function D (Equation 2.86), we can numerically obtain three solutions for r_c in terms of the fundamental parameters ϵ, l, γ_g, γ_r, and K_{gc}/K_{rc}. Here we refer to the roots using the notation r_{c1}, r_{c2}, and r_{c3} in order of decreasing radius.

Previous models have demonstrated that with the given parameters ϵ, l, and γ_g, only one solution was viable for a shock or shock-free inviscid ADAF disk. The additional parameters γ_r and K_{gc}/K_{rc} opens up the possibility for multiple solutions to be viable, as well as deciding the type of each critical point. For instance, depending on the values of these parameters, a fourth solution r_{c4} remains possible; however this critical radius always lies inside the event horizon and therefore is not physically relevant, whereas the other three lie outside of the horizon. Previously, these critical point types would have been determined by computing the two possible values for the derivative da_g^2/dr at the critical point via L'Hôpital's rule to see if they were real or complex. Currently, a simple root-finding method is more efficient.

This model is rather sensitive to the fundamental parameters, resulting in r_{c1} being either a real or complex value. Based on the criteria (e.g. LB05, Abramowicz & Chakrabarti 1990), a complex r_{c1} is automatically an O-type critical point, which doesn't yield a physically acceptable solution. However, if real, then it's considered a physically acceptable sonic point and remains an α-type critical point. Any accretion flow that passes through this point goes through a shock transition below r_{c1}, that is if it originated at a large distance. Then, the flow becomes subsonic and is required to pass through another α-type critical point in order to become supersonic before entering the black hole, that is according to Weinberg (1972). The critical point r_{c2} is a real value, however it was previously considered an O-type because the two possible values for the derivative were determined complex, and thus a non-physically acceptable solution. We likewise consider it as such in this new analysis.

The final root r_{c3} remains a X-type critical point as it is a physically acceptable sonic point due to its two real derivative values. It allows for a smooth, global, shock-free solution to exist where the flow is transonic at r_{c3}, and continues to be supersonic as it moves towards the event horizon. Once r_{c3} is determined, then it can be relayed back into the adjoining relations (Equations 2.87, 2.89, and 2.91) to find the corresponding conserved entropy parameter K_g at this critical point

$$K_{gc} \equiv r_c^{3/2} \left(r_c - r_{\rm S}\right) v_c a_{gc}^{2/(\gamma_g - 1)} \left(\frac{\gamma_g}{\gamma_r} a_{rc}^2 + a_{gc}^2\right)^{1/2} \ . \tag{2.93}$$

The values for r_{c3} are used in transition when determining the transonic flow profiles for the diffusive shock model, considering how similar the diffusive and non-diffusive profiles are near the event horizon due to advection dominating over diffusion.

While Equations (2.53) and (2.62) remain valid for a purely adiabatic disk, they likewise remain valid at the critical point (in terms of the sound speeds)

$$a_{gc}^2 = \gamma_g D_0 \rho_c^{(\gamma_g - 1)} \ , \qquad a_{rc}^2 = \gamma_r D_1 \rho_c^{(\gamma_r - 1)} \ . \tag{2.94}$$

This combined with Equations (2.8), (2.9) and (2.53) yields a symmetrical, adiabatic relation for the relativistic sound speed in terms of the thermal sound speed for a known critical value

$$a_r^2 = a_{rc}^2 \left(\frac{a_g^2}{a_{gc}^2}\right)^{(\gamma_r - 1)/(\gamma_g - 1)} \ . \tag{2.95}$$

This can be applied back to Equations (2.55) and (2.64) to yield the energy transport rate per unit mass in terms of the thermal sound speed a_g^2,

$$\begin{aligned} \epsilon = \frac{1}{2}\frac{l^2}{r^2} + \Phi + \frac{a_g^2}{\gamma_g - 1} + \frac{a_{rc}^2}{\gamma_r - 1} \left(\frac{a_g^2}{a_{gc}^2}\right)^{(\gamma_r - 1)/(\gamma_g - 1)} \\ + \frac{K_{gc}^2}{2r^3 \left(r - r_{\rm S}\right)^2 a_g^{4/(\gamma_g - 1)}} \left[\frac{\gamma_g}{\gamma_r} a_{rc}^2 \left(\frac{a_g^2}{a_{gc}^2}\right)^{(\gamma_r - 1)/(\gamma_g - 1)} + a_g^2\right]^{-1} \ . \end{aligned} \tag{2.96}$$

Equation (2.96) can be solved using a simple root-finding procedure for any value of the fundamental parameters, which can then be applied in either a shock or shock-free case.

Model 1

Just like in Model 2, the simultaneous vanishing of N and D in Equation (2.84) yields the critical conditions,

$$\frac{l^2}{r_c^3} - \frac{GM}{(r_c - r_{\rm S})^2} + v_c^2 \frac{(5r_c - 3r_{\rm S})}{2r_c\,(r_c - r_{\rm S})} = 0 \ , \tag{2.97}$$

$$\frac{2a_{gc}^2}{(\gamma_g + 1)} - v_c^2 = 0 \ , \tag{2.98}$$

at the critical radius, $r = r_c$. It can be seen in Equation (2.98) that there's a direct connection between the critical velocity v_c and thermal sound speed a_{gc},

$$v_c^2 = \frac{2a_{gc}^2}{(\gamma_g + 1)} \ . \tag{2.99}$$

Combining Equations (2.97) and (2.99) allows for a_{gc} to expressed explicitly as a function of the critical radius r_c,

$$a_{gc}^2 = (\gamma_g + 1) \left[\frac{GMr_c^3 - l^2\,(r_c - r_{\rm S})^2}{r_c^2\,(r_c - r_{\rm S})\,(5r_c - 3r_{\rm S})} \right] \ , \tag{2.100}$$

which can then be substituted into Equation (2.99) to likewise find an explicit function for v_c in terms of r_c,

$$v_c^2 = 2 \left[\frac{GMr_c^3 - l^2\,(r_c - r_{\rm S})^2}{r_c^2\,(r_c - r_{\rm S})\,(5r_c - 3r_{\rm S})} \right] \ . \tag{2.101}$$

Determining the critical points $\hat{r}_c$ is done by looking at the energy transport equation (Equation 2.57) at the critical point,

$$\epsilon = \frac{1}{2}v_c^2 + \frac{1}{2}\frac{l^2}{r_c^2} + \frac{a_{gc}^2}{\gamma_g - 1} + \Phi_c \ , \tag{2.102}$$

where $\Phi_c = \Phi(r_c)$. Combining Equations (1.13), (2.100) and (2.100) to Equation (2.102), the energy transport parameter ϵ can be expressed in terms of l, γ_g and r_c,

$$\epsilon = \frac{1}{2}\frac{l^2}{r_c^2} - \frac{GM}{(r_c - r_\mathrm{S})} + \frac{2\gamma_g}{(\gamma_g - 1)}\left[\frac{GMr_c^3 - l^2\left(r_c - r_\mathrm{S}\right)^2}{r_c^2\left(r_c - r_\mathrm{S}\right)\left(5r_c - 3r_\mathrm{S}\right)}\right] . \tag{2.103}$$

Unlike Model 2, Equation (2.103) for Model 1 allows for a direct way to rewrite the expression into a quartic equation for r_c, which is first expanded into terms like,

$$\begin{aligned}\epsilon r_c^2\left(r_c - r_\mathrm{S}\right)\left(5r_c - 3r_\mathrm{S}\right) = \frac{1}{2}l^2\left(r_c - r_\mathrm{S}\right)\left(5r_c - 3r_\mathrm{S}\right) - GMr_c^2\left(5r_c - 3r_\mathrm{S}\right) \\ + \frac{2\gamma_g}{(\gamma_g - 1)}\left(GMr_c^3 - l^2\left(r_c - r_\mathrm{S}\right)^2\right) ,\end{aligned} \tag{2.104}$$

which is then rewritten into the form (after applying natural gravitational units $GM = c = c1$ and $r_\mathrm{S} = 2$),

$$\mathcal{N}r_c^4 - \mathcal{O}r_c^3 + \mathcal{P}r_c^2 - \mathcal{Q}r_c + \mathcal{R} = 0 , \tag{2.105}$$

where

$$\begin{aligned}\mathcal{N} = 5\epsilon , \quad \mathcal{O} = 16\epsilon - 3 + \frac{2}{\gamma_g - 1} \\ \mathcal{P} = 12\epsilon + \frac{1}{2}\left(\frac{5 - \gamma_g}{\gamma_g - 1}\right)l^2 - 6 , \\ \mathcal{Q} = \left(\frac{8}{\gamma_g - 1}\right)l^2, \quad \mathcal{R} = \left(\frac{2\gamma_g + 6}{\gamma_g - 1}\right)l^2 .\end{aligned} \tag{2.106}$$

Just like in Model 2, the roots are referred in the notation r_{c1}, r_{c2}, r_{c3}, and r_{c4} in order of decreasing radius. Unlike Model 2, these critical point types are determined by computing the two possible values for the derivative da_g^2/dr at the critical point via L'Hôpital's rule to see if they were real or complex. As discussed in Model 2 and LB05 regarding the critical point criteria, r_{c4} lies inside the event horizon so it's physically irrelevant; r_{c2} has two complex roots which yield a physically unacceptable solution, therefore it's an O-type critical point; r_{c1} is an α-type critical point, meaning that any accretion flow that passes through this point must go through a shock transition below r_{c1}; and finally r_{c3} is a X-type critical point as it allows for a smooth, global, shock-free solution to exist where the flow is transonic at r_{c3}, and continues to be supersonic as it moves towards the event horizon.

2.5.2 Alternative Method for Smooth-Shock Flow

For a purely adiabatic disk, we can see from Equation (2.52) that the energy transport rate per unit mass becomes

$$\epsilon = \frac{a_{g\infty}^2}{\gamma_g - 1} + \frac{a_{r\infty}^2}{\gamma_r - 1} \ , \qquad r \to \infty \ . \tag{2.107}$$

If we adopt a ratio defined as T between the two sound speeds as $r \to \infty$,

$$T = \frac{a_{r\infty}}{a_{g\infty}} \ , \tag{2.108}$$

the constant entropy ratio (Equation 2.67) can be redefined in terms of this ratio,

$$\frac{K_g}{K_r} = \frac{1}{T^6 a_{g\infty}^2} \ . \tag{2.109}$$

Combining Equations (2.107), (2.108), and (2.109) yields the following relationship,

$$\epsilon = \frac{K_r}{K_g} \left[\frac{1}{T^6 \left(\gamma_g - 1\right)} + \frac{1}{T^4 \left(\gamma_r - 1\right)} \right] \ , \tag{2.110}$$

which means that the T-ratio is highly dependent on the fundamental parameters ϵ, K_g/K_r and the two adiabatic indices. Solving Equation (2.110) and combining the result with Equations (2.107) and (2.108) will yield the asymptotic values for the thermal and relativistic sound speeds, respectively, as $r \to \infty$. These in turn can be combined with Equations

(2.89) and (2.95), as $r \to \infty$, to form another cubic function for a_{rc} (similar to Equation (2.91)),

$$a_{rc}^3 + \mathcal{N} a_{rc}^2 + \mathcal{P} = 0 \ , \tag{2.111}$$

where

$$\mathcal{N} = \frac{(\gamma_g - 1)}{(\gamma_r - 1)} \frac{a_{r\infty}^3}{a_{g\infty}^2} \ , \qquad \mathcal{O} = 0 \ ,$$

$$\mathcal{P} = -(\gamma_g - 1) \frac{a_{r\infty}^3}{a_{g\infty}^2} \left[\epsilon - \frac{1}{2}\frac{l^2}{r_c^2} + \frac{GM}{r_c - r_{\rm S}} - \frac{r_c (r_c - r_{\rm S})}{(5r_c - 3r_{\rm S})} \left\{ \frac{GM}{(r_c - r_{\rm S})^2} - \frac{l^2}{r_c^3} \right\} \right] \ . \tag{2.112}$$

Likewise, of the three possible solutions to this cubic function, only one is actually a real, valid answer. The same process outlined in § 3.1 can then be implemented to solve for the thermal sound speed $a_g(r)$. This approach becomes useful when solving for the smooth-shock solutions for the diffusive and non-diffusive cases.

2.5.3 Critical Conditions for $\kappa \neq 0$ (Model 3)

In this paper we focus on using the transitional values determined near the horizon, and at the inner r_{c3} critical point, since their profiles are rather similar near the horizon. These values are used in order to compute the global profiles for the shocked disk in the diffusive two-fluid model. But before we do so we must first determine its own critical values. Here, the simultaneous vanishing of N and D yields the critical conditions

$$\begin{aligned} \frac{v_c (\gamma_r - 1)}{\kappa_c} \left[\frac{\gamma_g \gamma_r v_c^2}{2\left(a_{rc}^2 \gamma_g + a_{gc}^2 \gamma_r\right)} - 1 \right] \left(\epsilon - \frac{1}{2} v_c^2 - \frac{1}{2}\frac{l^2}{r_c^2} - \frac{a_{gc}^2}{\gamma_g - 1} - \frac{a_{rc}^2}{\gamma_r - 1} - \Phi_c \right) \\ + \frac{l^2}{r_c^3} - \frac{GM}{(r_c - r_{\rm S})^2} + \frac{(5r_c - 3r_{\rm S}) v_c^2}{2r_c (r_c - r_{\rm S})} = 0 \ , \end{aligned} \tag{2.113}$$

$$v_c^2 - \frac{2a_{gc}^2 \left(a_{rc}^2 \gamma_g + a_{gc}^2 \gamma_r\right)}{a_{rc}^2 \gamma_g + \gamma_r a_{gc}^2 (\gamma_g + 1)} = 0 \ , \tag{2.114}$$

where κ_c denotes the diffusion coefficient (Equation 2.48) at the critical radius, $r = r_c$. From the denominator function D in Equation (2.114), it can be seen that the critical velocity is related to the two sound speeds via

$$v_c^2 = \frac{2a_{gc}^2\left(\gamma_g a_{rc}^2 + \gamma_r a_{gc}^2\right)}{\gamma_g a_{rc}^2 + \gamma_r a_{gc}^2\left(\gamma_g + 1\right)} \ , \tag{2.115}$$

which is slightly different from that in the non-diffusive model (Equation 2.93).

Even though the critical point r_c was solved analytically in previous work, in this new model there is no clear way to do so with the new sets of equations. If a critical radius is known, then these new relations can be applied to numerically solve for the sound speeds a_{gc} and a_{rc} at the critical point. Combining Equations (2.93) and (2.114) will yield an analytical function for a_{rc}^2 as a function of a_{gc}^2. This can then be combined with Equation (2.113) to yield two possible numerical results for a_{gc}^2, where only one is a real physical quantity. From there, the other critical quantities a_{rc} and v_c (Equation 2.115) can be determined for the diffusive two-fluid model.

2.6 Isothermal Shock Model

Moving forward into the core of the thesis, it should be noted that like the primary goal of LB05, we too are interested in analyzing the acceleration of relativistic particles due to the presence of a standing, isothermal shock in an accretion disk. The focus in Model 1 was on flows passing smoothly through the outer critical radius r_{c1}, and then experiencing a discontinuous velocity jump at the shock location r_*. Here, in Model 3, we are interested in flows passing smoothly through the inner critical radius r_{c3} first, and then moving outward until encountering that velocity discontinuity at r_*. In this new method, we too need to understand how the structure of the disk responds to the presence of a shock, in order for any self-consistent global model to form. This means also analyzing the shock jump conditions using the standard fluid dynamical conservation equations.

In all three Models, we designate ϵ_- and ϵ_+ as the values of the energy transport parameter ϵ on the upstream and downstream sides of the isothermal shock at $r = r_*$, respectively. Here, $\epsilon_- > \epsilon_+$ as a result of energy being lost through the upper and lower surfaces of the disk at the shock location. In Model 1, the flow moved inward toward the event horizon, in which the drop in ϵ at the shock had a way of altering the flow's transonic structure in the post-shock region. In Model 3, the jump in ϵ at the shock will alter the transonic structure of the flow in the *pre-shock* region. In Model 1, the post-shock flow originally had to pass through an inner critical point to become supersonic before crossing the event horizon. This value was different from the inner critical point calculated for a smooth-shock transonic flow.

In Model 3, the pre-shock flow has to pass through a new outer critical radius (not one calculated from the downstream energy transport parameter ϵ_+) in order to become supersonic further out along the disk. This can be done using the upstream value of the energy transport parameter ϵ_-. It's required that $c^2 + \epsilon_+ > 0$ since the total energy inflow rate across the horizon, which includes the rest mass contribution, has to be positive as no energy can escape from the black hole. In determining the isothermal shock jump conditions, we apply the same assumptions as stated in LB05.

Model 2 follows the same logistics as Model 1 (with the added particle pressure), however we found it to be a rather unrealistic model since the relativistic particle pressure should not remain adiabatic further out along the disk, even before the shock (for inflowing particles). Logistically it makes sense to assume that Model 2 is applicable near the event horizon, as all of the angular momentum has been lost and the plasma is advected onto the black hole. In proceeding forward, the isothermal shock jump conditions will be determined for Models 1 and 3, though for the most part these conditions for Model 3 are equivalent also for Model 2.

2.6.1 Isothermal Shock Jump Conditions

Adopting the premise that the escape of the relativistic particles from the disk results in negligible mass loss (due to the Lorentz factor of the escaping particles being greater than unity), essentially the mass accretion rate $\dot{M}$ is conserved as the gas in the disk crosses the shock as stated via

$$\Delta\dot{M} \equiv \lim_{\epsilon\to 0} \dot{M}\left(r_* - \epsilon\right) - \dot{M}\left(r_* + \epsilon\right) = 0 \ , \tag{2.116}$$

where Δ defines the difference between any post- and pre-shock quantities. We assume that the outflow produces no torque on the disk, and therefore the specific angular momentum $l \equiv \dot{J}/\dot{M}$ is conserved across the shock. Hence we find that

$$\Delta\dot{J} = 0 \ . \tag{2.117}$$

Likewise, the radial momentum transport rate for Models 2 and 3

$$\dot{I} \equiv 4\pi r H\left(P_g + P_r + \rho v^2\right) \ , \tag{2.118}$$

and Model 1

$$\dot{I} \equiv 4\pi r H\left(P_g + \rho v^2\right) \ , \tag{2.119}$$

is also conserved across the shock,

$$\Delta\dot{I} = 0 \ . \tag{2.120}$$

Combining Equations (2.8), (2.9), (2.22), (2.28), and (2.52) with (2.116), and (2.120) yields the following jump relationships for Models 2 and 3

$$\left(\frac{\gamma_g}{\gamma_r}a_{r+}^2 + a_{g+}^2\right)^{1/2}\rho_+ v_+ = \left(\frac{\gamma_g}{\gamma_r}a_{r-}^2 + a_{g-}^2\right)^{1/2}\rho_- v_- \ , \tag{2.121}$$

$$\frac{a_{g+}^2}{v_+} + \frac{\gamma_g a_{r+}^2}{\gamma_r v_+} + \gamma_g v_+ = \frac{a_{g-}^2}{v_-} + \frac{\gamma_g a_{r-}^2}{\gamma_r v_-} + \gamma_g v_- \ , \tag{2.122}$$

with the subscripts (minus and plus) defining those measured quantities, respectively, just upstream and downstream from the shock. The same approach can likewise be done for Model 1 using Equation (2.21), though really it's the same as setting $a_r \to 0$ in Equations (2.121) and (2.122),

$$a_{g+}\rho_+ v_+ = a_{g-}\rho_- v_- \ , \tag{2.123}$$

$$\frac{a_{g+}^2}{v_+} + \gamma_g v_+ = \frac{a_{g-}^2}{v_-} + \gamma_g v_- \ . \tag{2.124}$$

In the case of an isothermal shock, which is our focus here, we have

$$a_{g+} = a_{g-} \ , \tag{2.125}$$

and therefore Equations (2.121) and (2.122) for Models 2 and 3 reduce to

$$\left(\frac{\gamma_g}{\gamma_r} a_{r+}^2 + a_{g-}^2\right)^{1/2} \rho_+ v_+ = \left(\frac{\gamma_g}{\gamma_r} a_{r-}^2 + a_{g-}^2\right)^{1/2} \rho_- v_- \ , \tag{2.126}$$

$$\frac{a_{g-}^2}{v_+} + \frac{\gamma_g a_{r+}^2}{\gamma_r v_+} + \gamma_g v_+ = \frac{a_{g-}^2}{v_-} + \frac{\gamma_g a_{r-}^2}{\gamma_r v_-} + \gamma_g v_- \ , \tag{2.127}$$

and likewise Equations (2.123) and (2.124) for Model 1,

$$\rho_+ v_+ = \rho_- v_- \ , \tag{2.128}$$

$$\frac{a_{g-}^2}{v_+} + \gamma_g v_+ = \frac{a_{g-}^2}{v_-} + \gamma_g v_- \ . \tag{2.129}$$

From Equation (2.126), we can determine the shock compression ratio R_* of Models 2 and

3,

$$R_* = \frac{\rho_+}{\rho_-} = \frac{v_-}{v_+} \frac{\left(\frac{\gamma_g}{\gamma_r} a_{r-}^2 + a_{g-}^2 \right)^{1/2}}{\left(\frac{\gamma_g}{\gamma_r} a_{r+}^2 + a_{g-}^2 \right)^{1/2}} > 1 \ , \tag{2.130}$$

and likewise Equation (2.128) for Model 1,

$$R_* = \frac{\rho_+}{\rho_-} = \frac{v_-}{v_+} > 1 \ . \tag{2.131}$$

The compression ratios defined in Equations (2.130) and (2.131) can actually be redefined in terms of the are the upstream Mach numbers associated with the thermal gas $\mathcal{M}_{g-}$ and relativistic particles $\mathcal{M}_{r-}$ that's incident of the shock,

$$\mathcal{M} \equiv \frac{v_-}{a_{g-}} \ , \quad \mathcal{M} \equiv \frac{v_-}{a_{r-}} \ , \tag{2.132}$$

like so for Model 1 by combining Equations (2.128), (2.129) and (2.132),

$$R_* = \frac{\rho_+}{\rho_-} = \gamma_g \mathcal{M}_{g-}^2 > 1 \ . \tag{2.133}$$

Though for Models 2 and 3, in this more complicated system we first need to determine the velocity jump ratio (v_+/v_-, see § 2.6.2) before we can proceed and compare the differences between the three Models.

Moving forward, we can also determine the isothermal entropy jump for the gas in Models 2 and 3 from Equation (2.64) at $r = r_*$

$$\frac{K_{g+}}{K_{g-}} = \frac{v_+}{v_-} \frac{\left(\frac{\gamma_g}{\gamma_r} a_{r+}^2 + a_{g-}^2 \right)^{1/2}}{\left(\frac{\gamma_g}{\gamma_r} a_{r-}^2 + a_{g-}^2 \right)^{1/2}} < 1 \ . \tag{2.134}$$

Notice that even with the inclusion of relativistic particles, the gas density increases across the shock, and thermal entropy is lost from the disk at the shock location due to particles escaping to form the jet (outflow), as expected. Whereas for Model 1, in which the isothermal energy jump can be found by setting $a_r \to 0$ in Equation (2.134),

$$\frac{K_{g+}}{K_{g-}} = \frac{v_+}{v_-} < 1 \ , \tag{2.135}$$

it can be seen that the jump is directly equal to the velocity jump ratio. This remains an interesting find because it suggests that in Models 2 and 3, the entropy jump is directly equal to the inverse of the compression ratio (Equation 2.130), but not the velocity jump ratio. Whereas for Model 1, the entropy jump is not only equal to the inverse of the compression ratio (Equation 2.131) but also the velocity jump ratio.

The relativistic energy density $U_r(r)$ is a continuous function of radius r throughout the disk, meaning at the shock jump this value is conserved, $\Delta U_r = 0$. This likewise means that the particle pressure is also conserved, $\Delta P_r = 0$. If the energy density U_r is not continuous at the shock location, then an infinite diffusive flux will be generated. Combining this relation with Equations (2.6), (2.7), (2.8), (2.9), (2.130) and (2.134) shows

$$\frac{K_{g+}}{K_{g-}} = \frac{a_{r+}^2}{a_{r-}^2} \ , \tag{2.136}$$

stating that the thermal entropy jump is dependent on the squared sound speed jump for the relativistic particles. This further shows that in a thermally-dominant single-fluid disk (Model 1), the isothermal entropy jump ratio is equivalent to the inverse compression ratio and the velocity jump ratio. However with the introduction of relativistic particle pressure as it is in the two-fluid model (Models 2 and 3), the entropy ratio is still equivalent to the inverse compression ratio, and also now the squared jump in the relativistic sounds speeds, but *not* the velocity jump ratio. This suggests (as we will explore in the next section) that the velocity jump ratio has a more complicated impact on the system than was done in Model 1.

2.6.2 Velocity Shock Jump

It is worth discussing the implications of these newly derived jump conditions. From Equation (2.127) for Models 2 and 3, we can derive the downstream relativistic sound speed in terms of the upstream parameters

$$a_{r+}^2 = \frac{\gamma_r}{\gamma_g}\left(\frac{v_+}{v_-} - 1\right)a_{g-}^2 + \frac{v_+}{v_-}a_{r-}^2 + \gamma_r v_+\left(v_- - v_+\right) \ . \tag{2.137}$$

This relationship is rather symmetrical between the upstream and downstream values, which can be seen for the upstream relativistic sound speed

$$a_{r-}^2 = \frac{\gamma_r}{\gamma_g}\left(\frac{v_-}{v_+} - 1\right)a_{g+}^2 + \frac{v_-}{v_+}a_{r+}^2 + \gamma_r v_-\left(v_+ - v_-\right) \ . \tag{2.138}$$

Combining Equations (2.134), (2.136), and (2.137), one obtains a quartic equation for the isothermal velocity jump ratio $Q = v_+/v_-$. One root of the quartic equation is the trivial upstream root, $Q = 1$. We can therefore divide the quartic equation by the factor $(Q - 1)$ to obtain the cubic equation,

$$Q^3\mathcal{F} + Q^2\mathcal{H} + Q\mathcal{I} + \mathcal{J} = 0 \ , \tag{2.139}$$

where, in terms of the upstream Mach numbers (Equation 2.132)

$$\begin{aligned}
\mathcal{F} &= 1 + \gamma_r^{-1}\mathcal{M}_{r-}^{-2} - \left(\gamma_r\mathcal{M}_{r-}^{2} + \gamma_g\mathcal{M}_{g-}^{2}\right)^{-1} \ , \\
\mathcal{H} &= -2\gamma_g^{-1}\mathcal{M}_{g-}^{-2} - \gamma_r^{-2}\mathcal{M}_{r-}^{-4}\left(1 + \gamma_r\mathcal{M}_{r-}^{2}\right)^{2} \ , \\
\mathcal{I} &= \gamma_g^{-2}\mathcal{M}_{g-}^{-4}\left[2\gamma_g\mathcal{M}_{g-}^{2}\left(1 + \gamma_r^{-1}\mathcal{M}_{r-}^{-2}\right) + 1\right] \ , \\
\mathcal{J} &= -\gamma_g^{-2}\mathcal{M}_{g-}^{-4} \ ,
\end{aligned} \tag{2.140}$$

with

$$\mathcal{M}_{g-} \equiv \frac{v_-}{a_{g-}} \ , \quad \mathcal{M}_{r-} \equiv \frac{v_-}{a_{r-}} \ . \tag{2.141}$$

However, only one of the three solutions is physically valid.

The three solutions to the cubic function are given as,

$$Q_1 = S + T - \frac{1}{3}\frac{\mathcal{H}}{\mathcal{F}} \ , \tag{2.142}$$

$$Q_2 = -\frac{1}{2}(S+T) - \frac{1}{3}\frac{\mathcal{H}}{\mathcal{F}} + \frac{1}{2}i\sqrt{3}\,(S-T) \ , \tag{2.143}$$

$$Q_3 = -\frac{1}{2}(S+T) - \frac{1}{3}\frac{\mathcal{H}}{\mathcal{F}} - \frac{1}{2}i\sqrt{3}\,(S-T) \ , \tag{2.144}$$

where

$$\begin{aligned}
S &= \left(X + \sqrt{W^3 + X^2}\right)^{1/3} \\
T &= \left(X - \sqrt{W^3 + X^2}\right)^{1/3}
\end{aligned} \tag{2.145}$$

and

$$W = \frac{1}{9}\left(\frac{3\mathcal{I}}{\mathcal{F}} - \frac{\mathcal{H}^2}{\mathcal{F}^2}\right) ,$$

$$X = \frac{1}{54}\left(\frac{9\mathcal{H}\mathcal{I}}{\mathcal{F}^2} - \frac{27\mathcal{J}}{\mathcal{F}} - \frac{2\mathcal{H}^3}{\mathcal{F}^3}\right) . \tag{2.146}$$

For an arbitrary set of parameters (see e.g. Figure 2.7 and Table 2.1), the solutions show that Q_1 is unphysical since $v_+ > v_-$, therefore it is invalid. The two roots Q_2 and Q_3 are acceptable physical solutions because $v_+ < v_-$. However, when these roots are substituted into Equation (2.137), it can be seen that $a_{r+}^2 < 0$ for Q_2 and $a_{r+}^2 > 0$ for Q_3. Therefore, since $a_r^2 > 0$, this analysis determines that Q_3 (Equation 2.144) is the only physically valid solution for the velocity jump ratio in Models 2 and 3. For Model 1, the velocity jump ratio has already been determined via Equations (2.131) and (2.133),

$$\frac{v_+}{v_-} = \gamma_g^{-1}\mathcal{M}_{g-}^{-2} < 1 . \tag{2.147}$$

Based on the result given in Equation (2.147), we can likewise expect that the velocity jump ratio for Model 3 (Equation 2.144) will also be less than one.

2.6.3 Analyzing the Jump Ratios

This leads back into analyzing the difference between the compression ratios, as well as the other jump ratios, for all three Models that was touched on in § 2.6.1. For an arbitrary set of values (Table 2.1), we can see that the velocity jump ratios Q are about equal between Model 1 (Equation 2.147) and Models 2 and 3 (Equation 2.144). This suggests that there's a balance going on between the other jump ratios. As determined in § 2.6.1, the isothermal entropy jump ratio for Model 1 is the same as its velocity jump. For Models 2 and 3, we can actually redefine Equation (2.64) in terms of the upstream Mach numbers (Equation

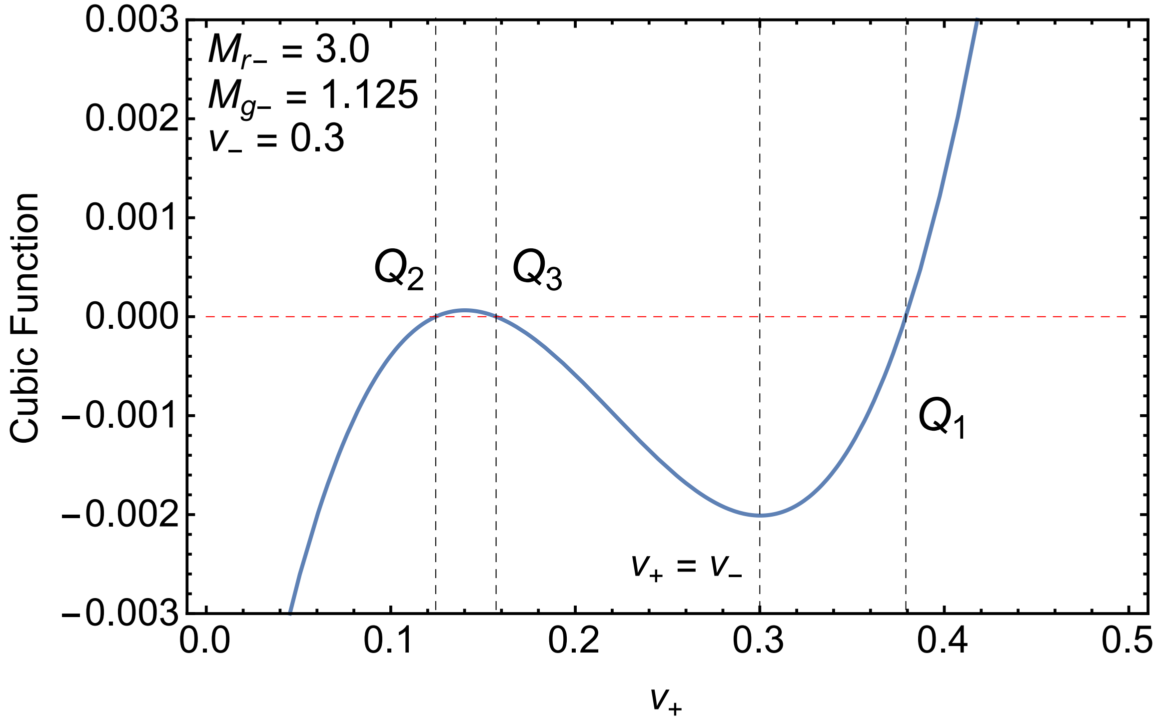

Figure 2.7: A depiction of the cubic function (Equation 2.140), solid line), the roots of which determine the shock velocity jump $Q = v_+/v_-$, for a typical set of the parameters $\mathcal{M}_{g-}$, $\mathcal{M}_{r-}$, and v_-. See the discussion in the text.

Table 2.1: Comparison between the three Models for the velocity jump ratios ($Q = v_+/v_-$), the compression ratios (ρ_+/ρ_-), and the isothermal entropy jump ratios (K_{g+}/K_{g-}) for an arbitrary set of values: $v_- = 0.3$, $\mathcal{M}_{g-} = 1.125$ and $\mathcal{M}_{r-} = 3.0$.

	Model 1	**Models 2 and 3**
$Q = v_+/v_-$	0.5267	0.5236
ρ_+/ρ_-	1.8984	2.0122
K_{g+}/K_{g-}	0.5267	0.4970

2.132),

$$\frac{K_{g+}}{K_{g-}} = Q\frac{\left(\gamma_g Q^2 \mathcal{M}_{r+}^{-2} + \gamma_r \mathcal{M}_{g-}^{-2}\right)^{1/2}}{\left(\gamma_g \mathcal{M}_{r-}^{-2} + \gamma_r \mathcal{M}_{g-}^{-2}\right)^{1/2}} < 1 \tag{2.148}$$

in order to see that the jump ratio is slightly less in Model 3 when compared to Model 1. This indicates that there's less entropy being lost from the disk at the shock location, due to particles escaping to form the jet (or outflow), than there is in Model 1.

This finally leads to comparing the compression ratios for Model 1 (Equation 2.131), and Models 2 and 3 (Equation 2.130, which is simply the inverse of Equation 2.148). It can be seen in Table 2.1 that the compression ratio is higher for Model 3 than it is more Model 1. This indicates that introducing relativistic particle pressure into the dynamical structure makes the compression ratio *larger*. The relationship between the compression ratio and the outflows has been discussed in Das et al. (2001a, 2001b), in which a low compression ratio results in a low outflow rate, and likewise a higher compression ratio results in a high outflow rate. Of course this was applied to the single-fluid model (or Model 1), but for this work it acts as a viable metric to use. Further discussion on this relationship and how it applies to Model 3 will be done more in Ch. 4, in which the model applications are done.

Before we move into analyzing the energy jump conditions, we should remind the reader that our new two-fluid model is analogous to the classic supernova-driven cosmic-ray (CR) acceleration model. Here we would like to point out that we will be able to verify that the particle Green's function, $f_{\rm G}$, given as

$$f_{\rm G} \propto E^{-\lambda_{\rm CR}} \ , \tag{2.149}$$

is proportional to a power relation between the particle energy E and the cosmic-ray spectral index, $\lambda_{\rm CR}$, which is indicative of first-order Fermi acceleration. The particle energy density, U_r, relates to the Green's function via the relation,

$$U_r = \int_{E_0}^{\infty} f_{\rm G} E^3 dE \ , \tag{2.150}$$

which when combined with Equation (2.149) becomes,

$$U_r \propto \left. \frac{E^{4-\lambda_{\rm CR}}}{4-\lambda_{\rm CR}} \right|_{E_0}^{\infty} \ . \tag{2.151}$$

In the classic CR case, the cosmic-ray spectral index, $\lambda_{\rm CR}$, relates to the compression ratio R_* via (Blandford & Ostriker 1978),

$$\lambda_{\rm CR} = \frac{3R_*}{R_* - 1} \ . \tag{2.152}$$

Thus, we can see from Equations (2.151) and (2.152) that $R_* < 4$ in order to avoid a divergent CR energy density since $\lambda_{\rm CR} > 4$. Otherwise, if $\lambda_{\rm CR} < 4$, then $U_r \to \infty$. It should be noted that the numerical value obtained from $\lambda_{\rm CR}$ is considered a rough estimate from the CR analogy and is more applicable to Model 1, but it is not properly applicable to Model 3.

2.6.4 Isothermal Shock Model: Energy

In the dynamical model considered by LB05 (Model 1), all of the terms in the energy transport rate $\dot{E}$ reflected contributions due the thermal background gas. However, in the situation considered in Model 3, both the relativistic particles and the gas contribute to $\dot{E}$. Hence we need to develop energy jump conditions for each of these two populations. It should be noted that Model 2 likewise requires both contributions, however as we proceed through this section it will be clearer why we did not move forward with building it a shock model. According to Equation (2.41), we have

$$\dot{E} = \dot{E}_g + \dot{E}_r \ , \tag{2.153}$$

where the energy transport rates for the particles and the gas can be rewritten in terms of the sound speeds as (cf. Equations (2.46) and (2.47))

$$\dot{E}_g = \dot{M} \left(\frac{1}{2} v^2 + \frac{1}{2} \frac{l^2}{r^2} + \Phi + \frac{a_g^2}{\gamma_g - 1} \right) \ , \tag{2.154}$$

and

$$\dot{E}_r = \dot{M} \left(\frac{a_r^2}{\gamma_r - 1} + \frac{\kappa}{\rho v} \frac{dU_r}{dr} \right) \ . \tag{2.155}$$

The jump in the energy transport rate can be written as

$$\Delta\dot{E} = \Delta\dot{E}_g + \Delta\dot{E}_r \ , \tag{2.156}$$

where

$$\Delta\dot{E}_g = \dot{M} \left(\frac{1}{2} \Delta v^2 + \frac{\Delta a_g^2}{\gamma_g - 1} \right) \ , \tag{2.157}$$

and

$$\Delta \dot{E}_r = \dot{M} \left(\frac{\Delta a_r^2}{\gamma_r - 1} + \Delta \left[\frac{\kappa}{\rho v} \frac{dU_r}{dr} \right] \right) \ . \tag{2.158}$$

In an isothermal shock, $\Delta a_g^2 = 0$, and therefore Equation (2.157) reduces to

$$\Delta \dot{E}_g = \frac{1}{2} \dot{M} \Delta v^2 \ . \tag{2.159}$$

We assume that the energy lost by the background thermal flow provides the kinetic luminosity $L_{\rm jet}$ that powers the outflow. This implies that

$$L_{\rm jet} = -\Delta \dot{E}_g \propto {\rm ergs\ s^{-1}} \ , \tag{2.160}$$

which also implies that the kinetic luminosity is equal to the energy of the escaped particles,

$$L_{\rm esc} = L_{\rm jet} \ , \tag{2.161}$$

since it's assumed that the relativistic particles are what populate the outflow. Energy lost from the jump in the gas becomes the energy that escapes the disk to form the jet

$$L_{\rm shock} = L_{\rm esc} = L_{\rm jet} \ , \tag{2.162}$$

which signifies that (cf. Equation 2.158)

$$\Delta \dot{E}_r = 0 \ , \quad \Delta \left[\frac{\kappa}{\rho v} \frac{dU_r}{dr} \right] = -\frac{\Delta a_r^2}{\gamma_r - 1} \ . \tag{2.163}$$

Therefore, we can write the total jump in the energy transport rate (Equation 2.156) as

$$\Delta \dot{E} = \Delta \dot{E}_g = \frac{1}{2} \dot{M} \Delta v^2 \ , \tag{2.164}$$

or more specifically,

$$\Delta\epsilon \equiv \epsilon_+ - \epsilon_- = \frac{v_+^2 - v_-^2}{2} \ . \tag{2.165}$$

It should be noted that Equation (2.165) is valid for both Models 1 and 3, but not for Model 2. This can be seen in Equation (2.158), in which since $\kappa \to 0$, we are left with the following relation,

$$\Delta\dot{E}_r = \dot{M}\frac{\Delta a_r^2}{\gamma_r - 1} \ . \tag{2.166}$$

This new relation invalidates Equation (2.163) since the relativistic particle pressure has to be diffusively radiated out in order for the energy lost from the jump in the gas to become the relativistic jets, which it is considered in Model 1. Therefore, Equation (2.165) would have to incorporate the change in a_r, which for a purely adiabatic disk could easily produce a shock profile like with what was done in Model 1. However, this shock profile would be considered 'fictitious', and thus not a valid physical model structure to pursue.

2.6.5 Shock Point Analysis

We know from LB05 that for a shock to exist in the flow, it must be located between two critical points and must satisfy the jump conditions given by Equations (2.137), (2.140), and (2.165). Below summarizes the procedure for determining the disk/shock structure for Models 1 and 3.

Model 3

The process begins by selecting the values for the fundamental parameters ϵ_+, l, κ_0, K_g/K_r, γ_g and γ_r. We remind the reader that $\gamma_g = 1.5$ and $\gamma_r = 4/3$. Determining the shock location is first done by computing the inner critical point location r_{c3} from the adiabatic model outlined in § 2.6. According to GR, the plasma flow must be adiabatic near the horizon, because the flow velocity $v \to c$, in which case diffusion becomes negligible. Hence the diffusive velocity profile (Model 3) and the non-diffusive profile (Model 2) must be identical near the horizon, and therefore Model 2 serves as an ideal starting point for the Model 3 calculations. The values associated with the critical velocity v_{c3}, the critical sound speeds a_{gc} and a_{rc}, and the critical entropy for the gas K_{gc}, are calculated next. The profile for the thermal sound speed $a_g(r)$ in the post-shock region of the adiabatic model is then calculated up to slightly above r_{c3} using a root-finding procedure based on Equation (2.96). The relativistic sound speed $a_r(r)$ can likewise be calculated using Equation (2.95). From this, we have everything to determine the starting values for v, a_g and a_r at $r = 2.1$ in the adiabatic model, which carry over into the diffusive model, along with K_{gc}.

Starting at $r = 2.1$, the sound speed profiles $a_g(r)$ and $a_r(r)$ are determined by numerically integrating Equation (2.74) up to r_{c3}. The associated values for the critical sound speeds a_{gc} and a_{rc}, and the critical velocity v_c are calculated using Equations (2.113), (2.114) and (2.115). Integrating forward requires computing the two possible values for the derivative da_g^2/dr at the inner critical point using L'Hôpital's rule. Since the flow is adiabatic in the post-shock region,

$$K_{g+} = K_{c3} \ . \tag{2.167}$$

The next step is determining a good value for the shock radius r_*, and calculating the associated pre-shock values for v and a_r. This is accomplished by implementing Equations (2.139) and (2.165) with a particular value of r_*, and calculating the associated upstream values for the thermal entropy K_{g-}, velocity v_-, and sound speeds a_{g-} and a_{r-}. The process for integrating forward is repeated until an outer critical point r_{c1} is determined, in which case then implementing L'Hôpita's rule is done to progress pass this location and outward along the disk.

This in-depth outward integration approach is reiterated for a varying ϵ_+ until a good outer critical point is determined. For any given input parameters, the outer critical point can only go out so far before the integration becomes unstable. Consequently, this point also agrees with the N and D functions (Equation 2.75), which cross zero as expected.

Subsequently, the corresponding ϵ_- determined from the jump conditions for a particular l, agrees with the parameter space outlined in LB05 for Model 1 as well as that for Model 2 (see Figure 2.8). The topology for Model 2 follows the same criteria as outlined by LB05 for Model 1, it's just interesting to note that with the inclusion of relativistic particle pressure, the parameter space shifts noticeably. The analysis of the shock location discussed above allows us to compute the structure of shocked disk solutions for a given set of parameters ϵ_+, l, κ_0, K_g/K_r, and γ_g and γ_r. The dynamical results derived in this section are then used in Ch. 4 to model the outflows observed in M87 and Sgr A* .

Model 1

The process defined for Model 1 is nearly identical to that in Model 3, but in reverse and with fewer starting parameters. Here, we start with the fundamental parameters ϵ_- and l, and then compute the outer critical point location r_{c1} from the steps mentioned in § 2.6. From there, after determining the associated critical velocity v_{c1} and thermal sound speed a_{gc}, a Wronskian method is used to determine the correct shock location in order to calculate (via a simple root finding procedure) the correct inner critical point r_{c3}. Once those associated critical values are determined, then the profile can integrate towards the event horizon at $r = 2.001$. This process for a smooth-shock solution is more simple and relies just knowing the upstream energy transport value ϵ_-, as well as the specific angular momentum l, in order to calculate the inner critical point r_{c3} and the overall profile.

This chapter closes here in which we move forward into the steady-state particle acceleration by analyzing/deriving the dynamical transport equation as well as the particle distribution function with associated eigenvalues and eigenfunctions.

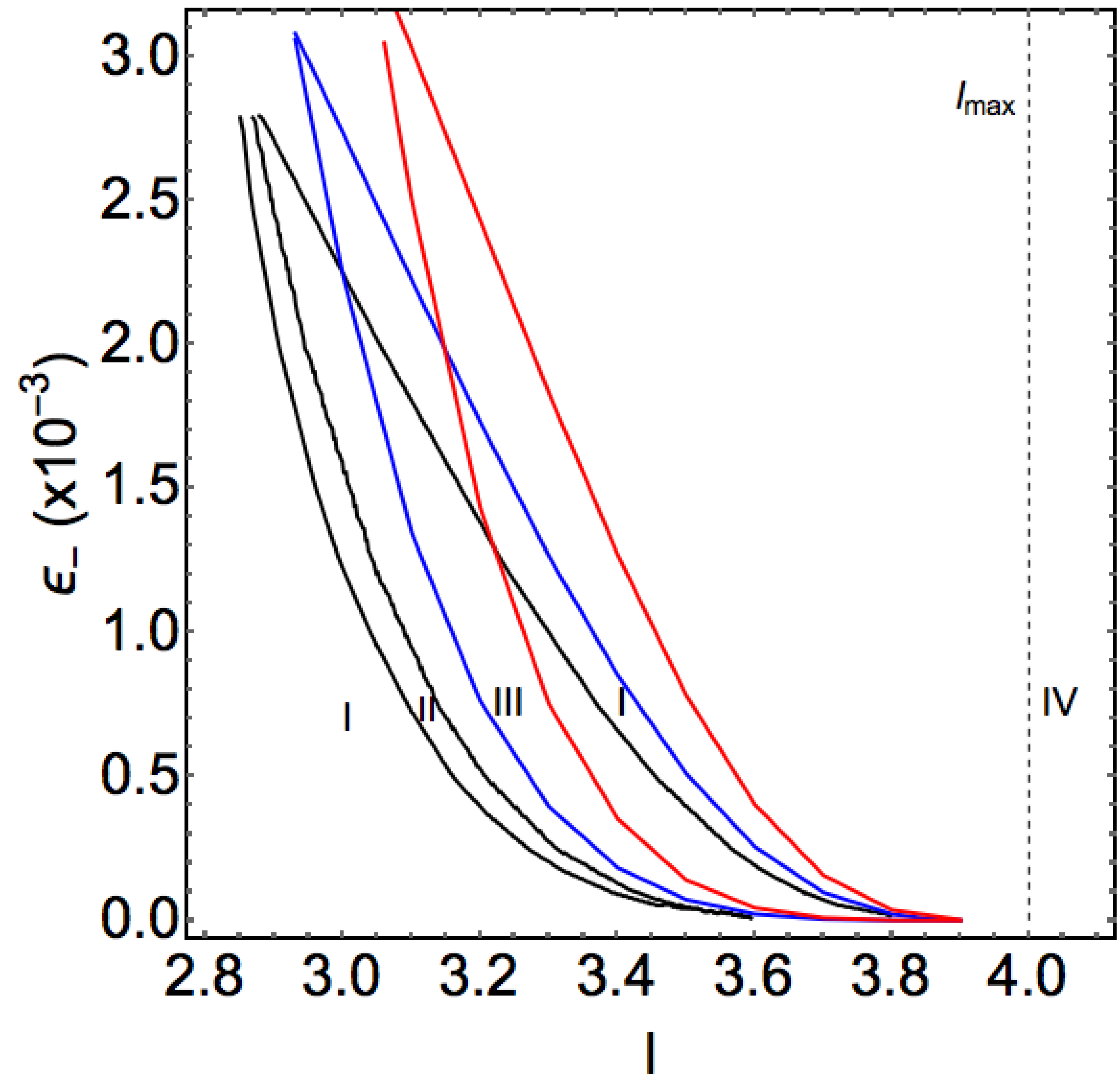

Figure 2.8: Similar to Figure 2 of LB05: plot of the (ϵ_-, l) parameter space of an ADAF disk with $\gamma_g = 1.5$ and $\gamma_r = 4/3$ for both Model 1 (LB05, black lines) and Model 2 (red and blue lines). The blue lines represent the parameter space in Model 2 with $T = 0.3$ in Equation (2.110), and $T = 0.5$ for the red lines. The layout is such that only smooth flows exist in region I, only smooth flows exist, and both shocked and smooth solutions remain possible in regions II and III. In region IV in which $l > l_{\rm max}$, no steady state dynamical solution can be obtained.

Chapter 3: Theory: Steady State Particle Acceleration

One of the goals in this thesis is to analyze the transport and acceleration of relativistic particles (electrons) in a disk governed by the two-fluid dynamical model developed (Model 3) in this work. The particle transport model considered here includes spatial diffusion, Fermi energization, advection and particle escape. From this transport equation, as well as the dynamical profiles outlined in the previous sections, we'll be able to analyze the Green's function $f_{\rm G}(E, r)$ in the disk. Overall, this is very similar to the transport formalism outlined in LB05 for the single-fluid model (Model 1). However, from the examples provided in the previous sections on how elements of the dynamical structure change in the two-fluid model, we too need to reexamine some of the fundamentals described in LB05 to compensate for the inclusion of relativistic particle pressure.

3.1 Dynamical Transport Equation

The particle transport formalism used in this work is outlined in § 5 of LB05, which includes advection, spatial diffusion, first-order Fermi acceleration, and relativistic escape particles. We've adopted the same simple, one-dimensional radial (r) model for the spatial transport, which uses the test particle approximation and assumes that the isothermal shock radius is where the injection of the seed particles and escape of the accelerated particles occur. This allows for a connection to exist between the jump in the relativistic energy flux and the energy radiated away by the escaping particles, at the shock location. Thus like in LB05 (as well as LB07), we too are essentially maintaining self-consistency between the dynamical and transport calculations.

This work focuses on the particle Green's function, $f_{\rm G}(E_0, E, r_*, r)$, which is a representation of the particle distribution resulting from the injection of $\dot{N}_0$ particles per second, containing energy E_0, from a source located at the shock radius, $r = r_*$, and it satisfies this steady-state transport equation (Becker 1992)

$$\frac{\partial f_{\rm G}}{\partial t} = 0 = -\vec{\nabla} \cdot \vec{F} - \frac{1}{3E^2} \frac{\partial}{\partial E} \left(E^3 \vec{v} \cdot \vec{\nabla} f_{\rm G} \right) + \dot{f}_{\rm source} - \dot{f}_{\rm esc} \ . \tag{3.1}$$

It should be noted that integrating Equation (3.1) with $\int_0^\infty 4\pi E^3 dE$, without the source or escape terms, achieves Equation (2.38, see Appendix E for further details). The source and escape terms are given by

$$\dot{f}_{\rm source} = \frac{\dot{N}_0 \delta\left(E - E_0\right) \delta\left(r - r_*\right)}{\left(4\pi E_0\right)^2 r_* H_*} , \quad \dot{f}_{\rm esc} = A_0 c \delta\left(r - r_*\right) f_{\rm G} \ , \tag{3.2}$$

the specific flux $\vec{F}$ is evaluated using

$$\vec{F} = -\kappa \vec{\nabla} f_{\rm G} - \frac{\vec{v} E}{3} \frac{\partial f_{\rm G}}{\partial E} \ , \tag{3.3}$$

and the quantities E signifies the particle energy, $H_* \equiv H\left(r_*\right)$ the disk half-thickness at the shock location, and A_0 as the dimensionless parameter that determines the rate at which particles escape through the surface of the disk at the shock location (c.f. Appendix D). It should be noted that the presence of the δ-functions given in Equation (3.2) indicate that the particle escape and injection are localized to the shock radius.

The alternative form of the Green's function is found by combining Equations (3.1) and (3.3),

$$\vec{v} \cdot \vec{\nabla} f_{\rm G} = \frac{\vec{\nabla} \cdot \vec{v}}{3} E \frac{\partial f_{\rm G}}{\partial E} + \vec{\nabla} \cdot \left(\kappa \vec{\nabla} f_{\rm G} \right) + \dot{f}_{\rm source} - \dot{f}_{\rm esc} \ , \tag{3.4}$$

where here, the left-hand side is defined as the comoving (advective) time derivative. On the right-hand side, respectively, are the terms for first-order Fermi acceleration, spatial diffusion, and the particle source and escape from the disk at the shock location. It should be noted that Equation (3.4) only contains the first-order Fermi acceleration of relativistic particles at a standing shock in an accretion disk. It's possible for second-order Fermi processes to occur in the flow due to MHD turbulence (e.g., Schlickeiser 1989a, 1989b; Subramanian et al. 1999), but it's ignored here. Considering cylindrical and azimuthal symmetries, Equation (3.4) can be combined with Equation (3.2) to express the steady state transport equation as,

$$
\begin{aligned}
v_r \frac{\partial f_{\mathrm{G}}}{\partial r} + v_z \frac{\partial f_{\mathrm{G}}}{\partial z} - \frac{1}{3}\left[\frac{1}{r}\frac{\partial}{\partial r}\left(r v_r\right) + \frac{d v_z}{d z}\right] E \frac{\partial f_{\mathrm{G}}}{\partial E} - \frac{1}{r}\frac{\partial}{\partial r}\left(r\kappa \frac{\partial f_{\mathrm{G}}}{\partial r}\right) - \frac{\partial}{\partial z}\left(\kappa \frac{\partial f_{\mathrm{G}}}{\partial z}\right) \\
= \frac{\dot{N}_0 \delta\left(E - E_0\right) \delta\left(r - r_*\right)}{\left(4\pi E_0\right)^2 r_* H_*} - A_0 c \delta\left(r - r_*\right) f_{\mathrm{G}} \ ,
\end{aligned}
\tag{3.5}
$$

where the vertical variation that occurs with the velocity component v_z is dealt with in Appendix C, in which the transport equation is vertically integrated. Considering the focus in this work is on the radial variations in the disk, thus we obtain the radial transport equation used in this work,

$$
\begin{aligned}
H v_r \frac{\partial f_{\mathrm{G}}}{\partial r} = \frac{1}{3r}\frac{\partial}{\partial r}\left(r H v_r\right) E \frac{\partial f_{\mathrm{G}}}{\partial E} + \frac{1}{r}\frac{\partial}{\partial r}\left(r H \kappa \frac{\partial f_{\mathrm{G}}}{\partial r}\right) + \frac{\dot{N}_0 \delta\left(E - E_0\right) \delta\left(r - r_*\right)}{\left(4\pi E_0\right)^2 r_*} \\
- A_0 c H_* \delta\left(r - r_*\right) f_{\mathrm{G}} \ ,
\end{aligned}
\tag{3.6}
$$

where $v = -v_r$ for positive inflow. The quantities f_{G}, v_r, H and κ are now considered vertically averaged.

3.2 Deriving the Energy Moments

The Green's function is also related to the total number and energy densities of the relativistic particles, denoted by n_r and U_r, respectively, via

$$
n_r\left(r\right) = \int_0^\infty 4\pi E^2 f_{\mathrm{G}} dE, \quad U_r\left(r\right) = \int_0^\infty 4\pi E^3 f_{\mathrm{G}} dE \ , \tag{3.7}
$$

which constitute to the normalization of f_{G}. However, these can be generalized in terms of the energy moments of the Green's function, $I_n(r)$, defined as

$$I_n(r) \equiv \int_0^\infty 4\pi E^n f_{\mathrm{G}} dE \ , \tag{3.8}$$

where essentially $n_r(r) = I_2(r)$ and $U_r(r) = I_3(r)$. If we were to operate Equation (3.8) with $\int_0^\infty 4\pi E^n dE$ and integrate the parts once, the differential equation for I_n becomes

$$\begin{aligned} Hv_r \frac{\partial I_n}{\partial r} &= -\left(\frac{n+1}{3}\right) \frac{I_n}{r} \frac{\partial}{\partial r}(rHv_r) + \frac{1}{r}\frac{\partial}{\partial r}\left(rH\kappa \frac{\partial I_n}{\partial r}\right) \\ &+ \frac{\dot{N}_0 E_0^{n-2} \delta(r - r_*)}{4\pi r_*} - A_0 c H_* I_n \delta(r - r_*) \ . \end{aligned} \tag{3.9}$$

We can see from Equation (3.9) that the vertically integrated transport equation for the total relativistic particle density $n_r(r) = I_2(r)$ is

$$Hv_r \frac{dn_r}{dr} = -\frac{n_r}{r}\frac{d}{dr}(rHv_r) + \frac{1}{r}\frac{d}{dr}\left(rH\kappa \frac{dn_r}{dr}\right) + \frac{\dot{N}_0 \delta(r - r_*)}{4\pi r_*} - A_0 c H_* n_{r*} \delta(r - r_*) \ , \tag{3.10}$$

and for the energy density $U_r(r) = I_3(r)$, upon substitution with $\gamma_r = 4/3$,

$$\begin{aligned} Hv_r \frac{dU_r}{dr} &= -\frac{\gamma_r U_r}{r}\frac{d}{dr}(rHv_r) + \frac{1}{r}\frac{d}{dr}\left(rH\kappa \frac{dU_r}{dr}\right) \\ &+ \frac{\dot{N}_0 E_0 \delta(r - r_*)}{4\pi r_*} - A_0 c H_* U_{r*} \delta(r - r_*) \ . \end{aligned} \tag{3.11}$$

It should be noted that Equations (3.10) and (3.11) are valid for both Models 1 and 3, as they are both applicable, and Equation (3.11) is actually equal to the first-order derivative of the energy transport rate per unit mass (Equation 2.55) for Model 3. Equation (3.9) can also be rewritten in the flux conservation form,

$$\frac{dG_n}{dr} = 4\pi r H \left[\left(\frac{2-n}{3} \right) v \frac{dI_n}{dr} + \frac{\dot{N}_0 E_0^{n-2} \delta\left(r - r_*\right)}{4\pi r_* H_*} - A_0 c \delta\left(r - r_*\right) I_n \right] \ , \tag{3.12}$$

where

$$G_n = 4\pi r H F_n \tag{3.13}$$

represents the rate of transport of the nth moment, and

$$F_n \equiv -\left(\frac{n+1}{3} \right) v I_n - \kappa \frac{dI_n}{dr} \ , \tag{3.14}$$

denotes the flux F_n of the nth moment, naturally. Integrating Equation (3.12) around the shock location $r = r_*$ yields,

$$\Delta \dot{G}_n = -\dot{N}_0 E_0^{n-2} + 4\pi r_* H_* A_0 c I_{n*} \ . \tag{3.15}$$

The global solution for the energy moments $I_n(r)$ is expressed as

$$I_n\left(r\right) = \begin{cases} A Q_{\rm I}\left(r\right) , & r > r_* \\ B Q_{\rm II}\left(r\right) , & r < r_* \end{cases} \tag{3.16}$$

where A and B are defined as normalization constants, and the functions $Q_{\rm I}(r)$ and $Q_{\rm II}(r)$ satisfy the homogeneous differential equation (via Equation 3.9),

$$H v_r \frac{dQ}{dr} = -\left(\frac{n+1}{3} \right) \frac{Q}{r} \frac{d}{dr} \left(r H v_r\right) + \frac{1}{r} \frac{d}{dr} \left(r H \kappa \frac{dQ}{dr} \right) \ , \tag{3.17}$$

with the boundary conditions (which are related to the asymptotic forms given in § 3.3),

$$Q_{\rm I}\left(r_{\rm out}\right) = C_0 + C_1 \left(\frac{r_{\rm out}}{r_{\rm S}}\right)^{-1} , \qquad Q_{\rm II}\left(r_{\rm in}\right) = \left(\frac{r_{\rm in}}{r_{\rm S}} - 1\right)^{-(n+1)/(3\gamma_g+3)} , \tag{3.18}$$

where $r_{\rm in}$ and $r_{\rm out}$ denote, respectively, the radii at which the inner and outer boundary conditions are applied, and the constants C_0 and C_1 have yet to be determined. By requiring that the energy moments are conserved through the shock $\Delta I_n = 0$, and operating $4\pi r H$ to Equation (3.14) at the shock location $r = r_*$,

$$\Delta\dot{G}_n = -4\pi r_* \Delta \left[\frac{n+1}{3} H v I_n + H\kappa \frac{dI_n}{dr}\right] , \tag{3.19}$$

these constants can be calculated generally by combining Equations (3.15) and (3.19),

$$A = B \frac{Q_{\rm II}}{Q_{\rm I}}\bigg|_{r=r_*} , \tag{3.20}$$

$$\begin{aligned} B = \frac{\dot{N}_0 E_0^{n-2}}{4\pi r_*} Q_{\rm I} \bigg[& \frac{(n+1)}{3}\left(H_+ v_+ - H_- v_-\right) Q_{\rm I} Q_{\rm II} - H_- \kappa_- Q_{\rm II} Q_{\rm I}^{'} \\ & + H_+ \kappa_+ Q_{\rm I} Q_{\rm II}^{'} + H_* A_0 c Q_{\rm II} Q_{\rm I} \bigg]^{-1} \bigg|_{r=r_*} , \end{aligned} \tag{3.21}$$

where the primes denote differentiation with respect to radius. Obtaining the solutions for the functions $Q_{\rm I}(r)$ and $Q_{\rm II}(r)$ are done by numerically integrating Equation (3.17), subject to the boundary conditions (Equation 3.18). Once these constants are computed, the global solution for $I_n(r)$ is evaluated using Equation (3.16). Applying these methods can be used to evaluate the global solutions for the number $n_r = I_2$ and energy $U_r = I_3$ densities. This completes the solution procedure for the energy moments.

3.2.1 Relativistic Particle Number Density

By setting $n = 2$, Equation (3.12) becomes the governing transport equation for the particle number density n_r given as

$$\frac{d\dot{N}_r}{dr} = \dot{N}_0 \delta\left(r - r_*\right) - 4\pi r_* H_* A_0 c n_r \left(r - r_*\right) \ , \tag{3.22}$$

where $\dot{N}_r(r)$ is defined as the relativistic particle transport rate. This quantity is written in the form (via Equations 3.13 and 3.14)

$$\dot{N}_r(r) \equiv -4\pi r H \left(v n_r + \kappa \frac{dn_r}{dr}\right) \ , \tag{3.23}$$

where $\dot{N}_r > 0$ for an outward directed transport. The particle transport has two spatial regions in the calculations, designated domain I ($r > r_*$) and domain II ($r < r_*$), since the source, where particle injection and escape occur, is located at the shock. The global solution is written in the form

$$\dot{N}_r(r) = \begin{cases} \dot{N}_{\rm I} \ , & r > r_* \ , \\ \dot{N}_{\rm II} \ , & r < r_* \ , \end{cases} \tag{3.24}$$

where $\dot{N}_{\rm I} > 0$ and $\dot{N}_{\rm II} < 0$ denote the rate at which particles are radially transported outward along the disk and inward toward the event horizon, respectively, from the source location. Integrating Equation (3.22) in a very small region around $r = r_*$ gives the magnitude of the jump in the particle transport rate,

$$\dot{N}_{\rm I} - \dot{N}_{\rm II} = \dot{N}_0 - \dot{N}_{\rm esc} \ , \quad \dot{N}_{\rm esc} \equiv 4\pi r_* H_* A_0 c n_* \ , \tag{3.25}$$

where $n_* \equiv n_r\left(r_*\right)$, and $\dot{N}_{\rm esc}$ is the positive rate at which particles escape the disk at the shock location in order to form the jet outflow. We demonstrated the vertically averaged transport equation for the total relativistic number density (via Equation 3.10), where $v_r = -v$ for positive inflow. It should be pointed out that the discontinuity at the shock location, seen in $\dot{N}_r$, will produce a jump in the derivative dn_r/dr as shown in this function.

The global solution for the particle number density $n_r = I_2$ is expressed as

$$n_r\left(r\right) = \begin{cases} AQ_{\rm I}\left(r\right), & r > r_* \\ BQ_{\rm II}\left(r\right), & r < r_* \end{cases} \tag{3.26}$$

where A and B are defined as normalization constants, and the functions $Q_{\rm I}(r)$ and $Q_{\rm II}(r)$ satisfy the homogeneous differential equation (e.g. Equation 3.10),

$$Hv_r\frac{dQ}{dr} = -\frac{Q}{r}\frac{d}{dr}\left(rHv_r\right) + \frac{1}{r}\frac{d}{dr}\left(rH\kappa\frac{dQ}{dr}\right) \ , \tag{3.27}$$

with the boundary conditions (see Equation 3.18),

$$Q_{\rm I}\left(r_{\rm out}\right) = C_0 + C_1\left(\frac{r_{\rm out}}{r_{\rm S}}\right)^{-1}, \qquad Q_{\rm II}\left(r_{\rm in}\right) = \left(\frac{r_{\rm in}}{r_{\rm S}} - 1\right)^{-1/(\gamma_g+1)} \ , \tag{3.28}$$

where $r_{\rm in}$ and $r_{\rm out}$ denote, respectively, the radii at which the inner and outer boundary conditions are applied. The normalizing constants A and B are determined (cf , Equations 3.20 and 3.21) for $n = 2$ as,

$$A = B\frac{Q_{\rm II}}{Q_{\rm I}}\bigg|_{r=r_*} \ , \tag{3.29}$$

$$B=\frac{\dot{N}_0}{4\pi r_*}Q_{\rm I}\Big[\left(H_+v_+-H_-v_-\right)Q_{\rm I}Q_{\rm II}-H_-\kappa_-Q_{\rm II}Q_{\rm I}^{'}$$

$$+H_+\kappa_+Q_{\rm I}Q_{\rm II}^{'}+H_*A_0cQ_{\rm II}Q_{\rm I}\Big]^{-1}\Bigg|_{r=r_*}\ , \tag{3.30}$$

where the primes denote differentiation with respect to radius. Obtaining the solutions for the functions $Q_{\rm I}(r)$ and $Q_{\rm II}(r)$ are done by numerically integrating Equation (3.27), subject to the boundary conditions (Equation 3.28). Once these constants are computed, the global solution for $n_r(r)$ is evaluated using Equation (3.26). This section is valid for both Models 1 and 3, except in Model 1 the disk half-thickness is conserved, $H_+ = H_- = H_*$. This completes the solution procedure for the particle number density.

3.2.2 Relativistic Particle Energy Density

The differential equation that is satisfied by the relativistic particle energy density U_r is given by Equation 3.11), where $v_r = -v$ for positive inflow. This expression can be redefined in the flux conservation form of the relativistic particle energy transport rate $\dot{E}_r(r)$ (by setting $n = 3$ in Equations 3.13 and 3.14),

$$\frac{d\dot{E}_r}{dr}=4\pi rH\left[-\frac{v}{3}\frac{dU_r}{dr}+\frac{\dot{N}_0E_0\delta\left(r-r_*\right)}{4\pi r_*H_*}-A_0cU_r\delta\left(r-r_*\right)\right]\ , \tag{3.31}$$

where here, $\dot{E}_r > 0$ for outward directed transport. It has been shown from the jump in the energy transport rate (Equation 2.163) that the derivative dU_r/dr will display a discontinuity at $r = r_*$. This can also be seen by integrating Equation (3.31) in a very small region around $r = r_*$

$$\Delta\dot{E}_r=L_{\rm esc}-\dot{N}_0E_0\ ,\qquad L_{\rm esc}\equiv 4\pi r_*H_*A_0cU_*\propto {\rm ergs\ s^{-1}}\ , \tag{3.32}$$

where $L_{\rm esc}$ is the rate of escape energy from the disk into the jet outflow at the shock location (Equation 2.161), E_0 and $\dot{N}_0$ denote the injection energy and rate of the seed particles, respectively, and $U_* \equiv U_r\,(r_*)$.

In this work, the global solution for $U_r(r)$ is expressed as

$$U_r\,(r) = \begin{cases} AQ_{\rm I}\,(r)\,, & r > r_* \\ BQ_{\rm II}\,(r)\,, & r < r_* \end{cases} \tag{3.33}$$

in which A and B are the normalization constants for the functions $Q_{\rm I}(r)$ and $Q_{\rm II}(r)$, which satisfy the homogeneous differential equation (cf. Equation 3.11, upon substitution with γ_r),

$$Hv_r \frac{dQ}{dr} = -\gamma_r \frac{Q}{r}\,(rHv_r) + \frac{1}{r}\frac{d}{dr}\left(rH\kappa \frac{dQ}{dr}\right) \ . \tag{3.34}$$

This function operates with the boundary conditions (see Equation 3.18)

$$Q_{\rm I}\,(r_{\rm out}) = C_0 + C_1 \left(\frac{r_{\rm out}}{r_{\rm S}}\right)^{-1} \ , \qquad Q_{\rm II}\,(r_{\rm in}) = \left(\frac{r_{\rm in}}{r_{\rm S}} - 1\right)^{-4/(3\gamma_g+3)} \ , \tag{3.35}$$

in which $r_{\rm in}$ and $r_{\rm out}$ represent the radii where the inner and outer boundary conditions are applied, respectively. Since we know from Equation (2.161) that $\Delta\dot{E}_r = 0$, this signifies (cf. Equation 3.32)

$$L_{\rm esc} = \dot{N}_0 E_0 \ . \tag{3.36}$$

The normalization constants A and B are determined by ensuring the derivative dU_r/dr satisfies this energy conservation, along with the jump condition given by Equation (2.163), and mandating that U_r is continuous across the shock at $r = r_*$. The generalized results obtained (Equations 3.20 and 3.21 for $n = 3$) are

$$A = B \frac{Q_{\rm II}}{Q_{\rm I}}\bigg|_{r=r_*} \ , \tag{3.37}$$

$$
\begin{aligned}
B = \frac{\dot{N}_0 E_0}{4\pi r_*} Q_{\mathrm{I}} \Bigg[\frac{4}{3} \left(H_+ v_+ - H_- v_- \right) Q_{\mathrm{II}} Q_{\mathrm{I}} + H_+ \kappa_+ Q_{\mathrm{I}} Q_{\mathrm{II}}^{\prime} \\
- H_- \kappa_- Q_{\mathrm{II}} Q_{\mathrm{I}}^{\prime} + A_0 H_* c Q_{\mathrm{I}} Q_{\mathrm{II}} \Bigg]^{-1} \Bigg|_{r=r_*} ,
\end{aligned} \tag{3.38}
$$

where the primes denote differentiation with respect to radius.

Obtaining the solutions for the functions $Q_{\mathrm{I}}(r)$ and $Q_{\mathrm{II}}(r)$ are done by numerically integrating Equation (3.34). Normally these functions are subject to the boundary conditions (Equation 3.35), but in this work they are subject to the dynamical values obtained for U_r near the horizon $r \to r_{\mathrm{S}}$, and at the shock location $r = r_*$, where we apply the upstream values for the derivative dU_r/dr (cf. Equations (2.54))

$$
\frac{dU_{r_*}}{dr_*} = U_{r_*} \left[\frac{1}{a_{r-}^2} \frac{da_{r-}^2}{dr_*} + \frac{1}{a_{g-}^2 \left(\gamma_g - 1 \right)} \frac{da_{g-}^2}{dr_*} \right] . \tag{3.39}
$$

Once these constants are computed, the global solution for $U_r(r)$ is evaluated using Equation (3.33). It should be noted that this section is valid for both Models 1 and 3, except for Model 1 the disk half-thickness is conserved, $H_+ = H_- = H_*$. This completes the solution procedure for the particle energy density. The results derived from this can be compared with the dynamical profiles computed in Ch. 4 in modeling the outflows observed in M87 and Sgr A* . Now we need to take into account the remaining requirements for energy conservation. This will ensure that the energy that escapes from the disk remains consistent with the energy lost from the jump.

3.2.3 Energy Conservation Conditions

The goal in our work is to determine the properties of the integrated disk/shock/outflow model using the observed values of the black hole mass mass M and the jet kinetic power L_{jet}, for a given source. In order to apply these observations to our model, we need to take into account the global energy conservation conditions. We have already mentioned (cf. Equation 2.162) that the energy lost from the jump in the gas at the shock location becomes the energy that escapes the disk to form the jet. Next we ensure that the rate in which the relativistic seed particles are injected into the flow is equal to the energy-loss rate for the background gas at the isothermal shock location, via

$$\dot{N}_0 E_0 = L_{\rm shock} \ . \tag{3.40}$$

This allows for Equations (2.162) and (3.36), (3.37), (3.38), (3.39), and (3.40) to be consistent and for energy to be conserved.

The other condition is where the mean energy of the escaping particles is defined as a fraction between the relativistic particle number n_* and energy U_* densities at the shock location,

$$E_{\rm esc} \equiv \frac{U_*}{n_*} \ . \tag{3.41}$$

Since $E_{\rm esc}$ is proportional to E_0 and independent of $\dot{N}_0$, this leads to the final conservation condition

$$L_{\rm esc} = \dot{N}_{\rm esc} E_{\rm esc} \ , \tag{3.42}$$

which is a combination of Equations (3.25), (3.32) and (3.41). Satisfying these conditions ensures that energy is conserved properly in our model. We finish off this section by pointing out a need to revisit the asymptotic solutions obtained for the dynamical variables, near the event horizon and also at large radii. As it it, the global solutions to the transport function depend on the sensitive nature of the boundary conditions that are imposed at these radii. Here they play a role when applying the integrated dynamical solution to the relativistic particle and energy densities.

3.3 Asymptotic Behavior

These estimated behaviors have been derived and demonstrated via Becker & Le (2003) and Le & Becker (2005) for the single-fluid model (Model 1). These same relationships come into play in the new two-fluid hydrodynamic model (Model 3). What makes them necessary is that the global solutions are dependent on the sensitivity on the boundary conditions enforced at large and small radii, particularly as we found more so near the event horizon when analyzing the diffusive and non-diffusive cases. What follows is an analysis of how these relations are derived for each Model.

3.3.1 Asymptotic Behavior Near the Horizon

The global solutions in a viscous ADAF disk become purely adiabatic close to the event horizon, which also has been shown to be quite similar to those profiles of an inviscid disk (Becker & Le 2003). These asymptotic solutions are therefore applied to this model. Near the horizon, the radial velocity v approaches the free-fall velocity $v_{\rm ff}^2(r) \equiv 2GM/(r - r_{\rm S})$, thus

$$v^2(r) \propto (r - r_{\rm S})^{-1} \ , \qquad r \to r_{\rm S} \ . \tag{3.43}$$

It should be noted that since the velocity v diverges as $r \to r_{\rm S}$ and cannot be represented near the horizon, it is interpreted as the radial component of the four-velocity (Becker & Le 2003; Becker & Subramanian 2005). Equation (3.43) is valid for both Models 1 and 3. For Model 1, it can be combined with Equation (2.65) to determine the thermal sound speed a_g near the horizon, as

$$a_g^2 \propto (r - r_{\rm S})^{(1-\gamma_g)/(\gamma_g+1)} \qquad r \to r_{\rm S} \ . \tag{3.44}$$

For Model 3, being identical to Model 2 near the horizon, Equation (3.43) can be combined with Equations (2.64) and (2.95) to show the following relationship,

$$K_g^2 \propto (r - r_{\rm S}) \left[a_g^{2(\gamma_r+1)/(\gamma_g-1)} + a_g^{2(\gamma_g+1)/(\gamma_g-1)}\right] \ , \qquad r \to r_{\rm S} \ . \tag{3.45}$$

What Equation (3.45) shows is that near the horizon, there are two possible terms for a_g

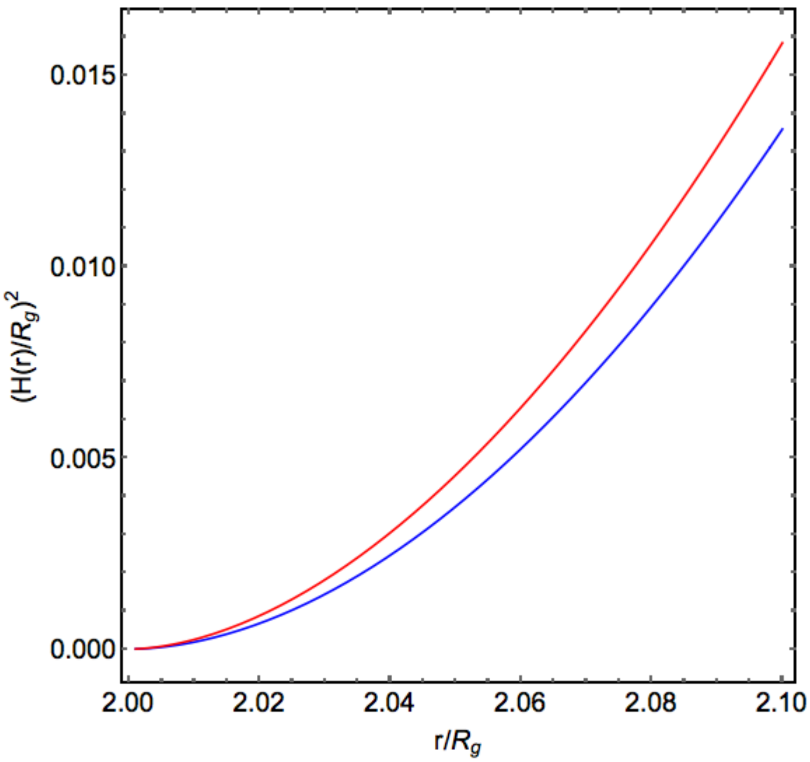

Figure 3.1: Plot of the disk half-thickness for Model 3 (Equation 3.49), in which the relativistic term (blue line, the left-most term containing the γ_r variable) is surpassed by the thermal term (red line, the right-most term). It can be seen that the thermal pressure continues to dominate the relativistic particle pressure near the horizon.

with different power values due to the contribution by both the thermal and relativistic particle pressure. However, near the horizon the particle transport is dominated by inward-bound advection, which means that not only numerically ($\gamma_g > \gamma_r$), but conceptually the thermal pressure will dominant over the relativistic pressure as the plasma is accreted onto the black hole. Hence, Equation (3.45) can be reduced to show the thermal sound speed a_g, near the horizon, for Model 3 as

$$a_g^2\,(r) \propto (r - r_{\rm S})^{(1-\gamma_g)/(1+\gamma_g)} \quad , \qquad r \to r_{\rm S} \ , \tag{3.46}$$

which is exactly the same for Model 1. Plugging this back into Equation (2.95) gives the following asymptotic for the nonthermal sound speed a_r for Model 3 near the horizon as,

$$a_r^2 \propto (r - r_{\mathrm{S}})^{(1-\gamma_r)/(\gamma_g+1)} \ , \qquad r \to r_{\mathrm{S}} \ . \tag{3.47}$$

Using Equation (3.46) results in the the asymptotic variations of the disk half-thickness H (Equation 2.21), as well as the density ρ (Equation 2.28), for Model 1 as

$$H\,(r) \propto (r - r_{\mathrm{S}})^{(\gamma_g+3)/(2\gamma_g+2)} \ , \qquad \rho\,(r) \propto (r - r_{\mathrm{S}})^{-1/(\gamma_g+1)} \ , \qquad r \to r_{\mathrm{S}} \ . \tag{3.48}$$

However, when applying Equations (3.46) and (3.47) to Equation (2.22), we end up with a double relation for the disk half-thickness H for Model 3,

$$H^2 \propto (r - r_{\mathrm{S}})^{(2\gamma_g-\gamma_r+3)/(\gamma_g+1)} + (r - r_{\mathrm{S}})^{(\gamma_g+3)/(\gamma_g+1)} \ , \qquad r \to r_{\mathrm{S}} \ . \tag{3.49}$$

This one is not as easy to determine numerically but rather analytically, which can be seen in Figure (3.1). The left-most term in Equation (3.49) represents the relativistic term (blue line, containing the γ_r variable), while the right-most term represents the thermal gas term (red line). It can be seen that the thermal gas continues to dominate over the relativistic term near the horizon, and thus we can approximate Equation (3.49) accordingly,

$$H^2 \propto (r - r_{\mathrm{S}})^{(\gamma_g+3)/(\gamma_g+1)} \ , \qquad r \to r_{\mathrm{S}} \ , \tag{3.50}$$

which is exactly the same as Model 1. Thus, the volumetric mass density ρ in Model 3 is likewise the same as it is in Model 1 (Equation 3.48).

We can use Equation (3.23) to study the behavior of n_r near the event horizon by taking the limit as $r \to r_{\mathrm{S}}$ (in which $\kappa \to 0$ due to the particle transport being dominated by advection, and $\dot{N}_r = \dot{N}_{\rm II}$),

$$n_r(r) \to -\frac{\dot{N}_{\rm II}}{4\pi r H v} \ , \qquad r \to r_{\rm S} \ , \tag{3.51}$$

which can be compared to Equation (2.28) and be rewritten as,

$$n_r(r) \propto \rho(r) \ . \tag{3.52}$$

Therefore, by combining Equations (3.48) and (3.52), we obtain this explicit asymptotic form for n_r near the horizon,

$$n_r\,(r) \propto \left(r - r_{\rm S}\right)^{-1/(\gamma_g+1)} \ , \qquad r \to r_{\rm S} \ . \tag{3.53}$$

The relativistic particle energy density U_r follows the same logic as n_r near the horizon and follows the adiabatic relation

$$U_r \propto n_r^{4/3} \ , \qquad r \to r_{\rm S} \ , \tag{3.54}$$

which can be combined with Equation (3.53) to show

$$U_r(r) \propto \left(r - r_{\rm S}\right)^{-4/(3\gamma_g-3)} \ , \qquad r \to r_{\rm S} \ . \tag{3.55}$$

Thus, the asymptotic relations near the event horizon for both energy densities are exactly identical for both Models 1 and 3. One can also see how the asymptotics defined in Equations (3.53) and (3.55) relate to the boundary conditions near the horizon ($Q_{\rm II}$) established in Equations (3.28) and (3.35), respectively.

3.3.2 Asymptotic Behavior at Infinity

In contrast with near the event horizon, far from the black hole advection is negligible and the particle transport in the disk is dominated by outward-bound diffusion (κ). In the limit $r \to \infty$, the entropy K_g for both Models 1 (Equation 2.65) and 3 (Equation 2.64) are constant in the adiabatic upstream flow, as well as the thermal $a_{g\infty}$ and relativistic $a_{r\infty}$ sound speeds (see Ch. 4). Thus, it can be seen that the asymptotic variation of the inflow velocity for both Models is

$$v \propto r^{-5/2} \ , \quad r \to \infty \ , \tag{3.56}$$

resulting in the variation of the disk half-height (Equation 2.22)

$$H \propto r^{3/2} \ , \quad r \to \infty \ , \tag{3.57}$$

as well as the density (Equation 2.28)

$$\rho \longrightarrow \text{const} \ , \quad r \to \infty \ . \tag{3.58}$$

Applying the above conditions to either Equation (2.52) or (3.11) will show that the relativistic energy density further along in the disk becomes,

$$U_r'(r) \propto \frac{1}{r^2} \ , \quad r \to \infty \ . \tag{3.59}$$

Since in this regime for the particle number density, $U_r \propto n_r$,

$$n_r'(r) \propto \frac{1}{r^2} \ , \quad r \to \infty \ . \tag{3.60}$$

It should be noted that even these asymptotic behaviors are essentially the boundary conditions (Q_{I}) set for the energy moments (Equation 3.18), as well as the particle number and energy densities (Equations 3.28 and 3.35). Thus, this completes the theoretical background for the dynamical structure of the disk for Models 1, 2, and 3. We move forward now in deriving the particle distribution function needed for these three models.

3.4 Transport Equation and Separation of Variables

The goal here, like the dynamical particle transport model, is to analyze the transport and acceleration of relativistic particles (electrons) in a disk governed by the two-fluid dynamical model developed in the previous chapter. And just like the dynamical particle transport model developed in the previous sections, this particle transport model likewise includes spatial diffusion, Fermi energization, advection and particle escape. As such we'll be able to analyze the Green's function $f_{\mathrm{G}}(E, r)$ in the disk. Overall, this is very similar to the transport formalism outlined in LB07 for the single-fluid model (Model 1). However, from the examples provided in the previous sections on how elements of the dynamical structure change in the two-fluid model (Model 3), we too need to reexamine some of the fundamentals described in LB07 to compensate for the inclusion of relativistic particle pressure.

The particle transport formalism used in this work is outlined in § 3 of LB07, which includes advection, spatial diffusion, first-order Fermi acceleration, and relativistic escape particles. We've adopted the same simple, one-dimensional radial (r) model for the spatial transport, which uses the test particle approximation and assumes that the isothermal shock radius is where the injection of the seed particles and escape of the accelerated particles occur. This allows for a connection to exist between the jump in the relativistic energy flux and the energy radiated away by the escaping particles, at the shock location. Thus like in LB07, we too are essentially maintaining self-consistency between the dynamical and transport calculations outlined in the previous sections, which will be explored more in Ch. 4.

Following LB07, in this work we focus on the vertically integrated form of the transport equation (Equation 3.6),

$$\begin{aligned} H v_r \frac{\partial f_{\mathrm{G}}}{\partial r} &= \frac{1}{3r}\frac{1}{r}\frac{\partial}{\partial r}\left(r H v_r\right) E \frac{\partial f_{\mathrm{G}}}{\partial E} + \frac{1}{r}\frac{\partial}{\partial r}\left(r H \kappa \frac{\partial f_{\mathrm{G}}}{\partial r}\right) \\ &+ \frac{\dot{N}_0 \delta\left(E - E_0\right)\delta\left(r - r_*\right)}{\left(4\pi E_0\right)^2 r_*} - A_0 c H_* \delta(r - r_*) f_{\mathrm{G}} \ , \end{aligned} \tag{3.61}$$

where $v_r = -v$ for positive inflow, and the quantities for the Green's function f_{G} and the diffusion coefficient κ are considered vertically averaged. As noted in that paper, within the vicinity of the shock the velocity v is discontinuous, and is denoted by

$$\frac{dv}{dr} \rightarrow (v_- - v_+)\,\delta\,(r - r_*)\ , \qquad r \rightarrow r_*\ , \tag{3.62}$$

where v_- and v_+ represent the positive inflow speeds just upstream and downstream from the shock, respectively. This is to indicate that the first-order Fermi acceleration of the particles is most pronounced in this region due to its presence. Applying the separation of variables function,

$$f_n\,(E, r) = \left(\frac{E}{E_0}\right)^{-\lambda_n} Y_n\,(r)\ , \tag{3.63}$$

where λ_n are the eigenvalues, and the spatial eigenfunctions $Y_n\,(r)$ to Equation (3.61) will satisfy the second-order ordinary differential equation,

$$-Hv\frac{dY_n}{dr} = \frac{\lambda_n}{3r}\frac{d}{dr}\,(rHv)\,Y_n + \frac{1}{r}\frac{d}{dr}\left(rH\kappa\frac{dY_n}{dr}\right) - A_0 c H_* \delta\,(r - r_*)\,Y_n\ . \tag{3.64}$$

This works for particle energy $E > E_0$, in which the source term in Equation (3.61) vanishes, and what's left is separable in energy and space. When combined with Equation (2.48), Equation (3.64) can be rewritten as,

$$\frac{d^2Y_n}{dr^2} + \left[\frac{r_s}{\kappa_0\,(r - r_s)^2} + \frac{d\ln\,(rHv)}{dr} + \frac{2}{(r - r_s)}\right]\frac{dY_n}{dr} + \frac{\lambda_n r_s Y_n}{3\kappa_0\,(r - r_s)^2}\frac{d\ln\,(rHv)}{dr} = 0\ . \tag{3.65}$$

This is the same as Equation (30) in LB07 for the single-fluid model (Model 1) and is valid for the two-fluid model (Model 3). However the difference for Model 3 is that it's governed by the dynamical profiles numerically determined for $H(r)$ and $v(r)$ (Equations 2.22 and 2.64, respectively), which both now experience a jump at the shock location. It should be noted that a proof of Equation (3.63)'s validity is given in Appendix F.

3.5 Revisiting the Eigenvalues and Eigenfunctions

In order to numerically solve the global function for the eigenfunction $Y_n(r)$, we must satisfy the continuity and derivative jump conditions associated with the existence of the shock/source at radius $r = r_*$. This can be determined by integrating Equation (3.64), with respect to the radius, in the vicinity of the shock,

$$\Delta(Y_n) = 0 \ , \tag{3.66}$$

$$\Delta\left(\frac{\lambda_n}{3} H v Y_n + H\kappa \frac{dY_n}{dr}\right) = -A_0 c H_* Y_n(r_*) \ , \tag{3.67}$$

where Δ represents the difference between post-shock and pre-shock quantities. Essentially, it is established in Equations (3.66) and (3.67) that $Y_n(r)$ is continuous and its derivative displays a jump at the shock location. It should be noted that in the single-fluid model, $H_+ = H_- = H_*$, and thus Equation (3.67) becomes Equation (33) in LB07, showing that we get the same jump conditions if $a_r \to 0$ for Model 1. Derivation of Equation (3.67) is seen more so in Appendix G.

There are two boundary conditions imposed in order to determine the global solutions, and associated eigenvalues λ_n, for the second-order linear differential equation (Equation 3.65). The global solutions for the spatial eigenfunctions is written as

$$Y_n(r) = \begin{cases} G_n^{\rm in}(r) \ , & r \le r_* \ , \\ a_n G_n^{\rm out}(r) \ , & r \ge r_* \ , \end{cases} \tag{3.68}$$

where $G_n^{\rm in}(r)$ and $G_n^{\rm in}(r)$ represent the fundamental solutions to Equation (3.65) in the inner and outer regions of the disk, and a_n is the matching coefficient defined as,

$$a_n = \frac{G_n^{\rm in}(r_*)}{G_n^{\rm out}(r_*)} \ . \tag{3.69}$$

In the single-fluid model (Model 1), the asymptotic behavior in the inner region $G_n^{\rm in}(r)$ can be seen in Equation (3.65) as $r \to r_{\rm S}$ (or Equation 35 of LB07),

$$G_n^{\rm in}(r) \to g_n^{\rm in}(r) \equiv \left(\frac{r}{r_{\rm S}} - 1\right)^{-\lambda_n/(3\gamma_g+3)} \ , \quad r \to r_{\rm S} \ . \tag{3.70}$$

This remains valid in the two-fluid model (Model 3) since near the horizon, the plasma becomes fully adiabatic and the thermal particles remain dominant over the relativistic particles as they are accreted onto the black hole (likewise mentioned in Ch. 2). At a large radii ($r \to \infty$), we can also see from Equation (3.65) the outer asymptotic form (Equation 35 of LB07),

$$G_n^{\rm out}(r) \to g_n^{\rm out}(r) \equiv \left(\frac{r}{r_{\rm S}}\right)^{-1} \ , \quad r \to \infty \ , \tag{3.71}$$

which is valid for the case treated by LB07 because that did not include the pressure of the relativistic particles. This is further discussed in Appendix H.

However, in the case of interest here, with relativistic particle pressure included, we showed in Ch. 2 that the dynamical profiles for the particle energy U_r and number n_r densities do not show a $1/r$ relationship, but rather they approach constants at a large radius. Therefore, for the eigenfunction solution, we too must implement the same outer boundary condition that was used for the energy transport equation (see Ch. 4),

$$G_n^{\rm out}(r) \to g_n^{\rm out}(r) \equiv U_r\,(r) \ , \quad r \to \infty \ , \tag{3.72}$$

since we likewise don't know the outer asymptotic for the spatial eigenfunctions (to be determined in future work). The validity of the asymptotic forms in Equations (3.70) and (3.72) are shown in Ch. 4 by comparing the numerical solutions obtained from the spatial eigenfunctions, similar to Figures (3) and (4) of LB07.

Model 1 (LB07) implemented a bidirectional integration technique to solve for the eigenvalues λ_n from the boundary conditions (Equations 3.70 and 3.71). This process uses a Wronskian bisection method of the inner and outer solutions until they vanish at the matching radius situated in the post-shock region. After determining a particular value for λ_n, the matching coefficient a_n is then found using Equation (3.69). Consecutive repetitions of this process is done until a desired number of eigenvalues and eigenfunctions is obtained. Figure 3.2 shows the sequences of eigenvalues associated with the parameters for models 2 and 5 (see Ch. 4 for further details), in which $\lambda_1 \sim 4$ in all cases, meaning that the acceleration is efficient and analogous with cosmic ray acceleration (see Blandford & Ostriker 1978, LB07). In Model 3 we too implement the same methodology as Model 1, from which in Ch. 4 we will explore the impact of what including relativistic particle pressure does for eigenvalues and eigenfunctions.

3.6 Revisiting Eigenfunction Orthogonality

The following section is a revision of § 3.4 of LB07, which is being generalized to include the relativistic particle pressure of Model 3. In LB07, the Sturm-Liouville form,

$$\frac{d}{dr}\left[S\left(r\right)\frac{dY_n}{dr}\right]+\lambda_n\omega\left(r\right)Y_n\left(r\right)=0\ , \tag{3.73}$$

where

$$S\left(r\right)\equiv\frac{rH\kappa}{r_*H_*\kappa_*}\exp\left\{\frac{1}{\kappa_0}\left[\left(\frac{r_*}{r_{\rm S}}-1\right)^{-1}-\left(\frac{r}{r_{\rm S}}-1\right)^{-1}\right]\right\}\ , \tag{3.74}$$

and $\omega(r)$ is the weight function given as

$$\omega(r) \equiv \frac{vS}{3\kappa} \frac{d \ln(rHv)}{dr} \ , \tag{3.75}$$

was used to rewrite Equation (3.65) in a way to verify that the eigenfunctions satisfied the orthogonality relation,

$$\int_{r_{\rm S}}^{\infty} Y_n(r) \, Y_m(r) \, \omega(r) \, dr = 0, \quad m \neq n \ . \tag{3.76}$$

This was done with the criteria that the boundary conditions (Equations 3.70 and 3.72) were able to satisfy the spatial eigenfunctions $Y_n(r)$; we likewise have demonstrated that the eigenfunctions satisfy this orthogonality relation in Appendix I. It should be noted that $\omega(r)$ continues to display a δ-function discontinuity at due to the derivative of $v(r)$ in the vicinity of the shock. In this region, we can show from combining Equations (3.62), (3.74), and (3.75) that

$$\omega(r) \to \frac{1}{3\kappa_* H_*} (H_- v_- - H_+ v_+) \, \delta(r - r_*) \ , \quad r \to r_* \ . \tag{3.77}$$

It should be noted that Equation (3.77) is a generalization of the weight function and is applicable in Model 3. For Model 1, by setting the disk half-thickness at the shock location via $H_+ = H_- = H_*$, Equation (3.77) becomes Equation (40) from LB07.

3.7 Revisiting the Eigenfunction Expansion

The following section is also a revision of § 3.5 of LB07, which is being generalized to include the relativistic particle pressure of Model 3. Aside from completing the set of eigenfunctions, LB07 also determined that the Green's function $f_{\rm G}(E, r)$ can be represented using the eigenfunction separation function (see Equation 3.63)

$$f_{\mathrm{G}}\left(E, r\right) = \sum_{n=1}^{N_{\max}} b_n f_n(E, r) = \sum_{n=1}^{N_{\max}} b_n Y_n\left(r\right) \left(\frac{E}{E_0}\right)^{-\lambda_n} \quad , \quad E \geq E_0 \ , \tag{3.78}$$

in which b_n represents the expansion coefficients (with either positive or negative signs) and $N_{\max}$ is a value determined by analyzing the term-by-term convergence of the series. These expansion coefficients $(b_1, b_2, b_3, \ldots)$ were calculated via the orthogonality of the spatial eigenfunctions. Model 1 used a value $N_{\max} = 10$ in the numerical calculations, within an accuracy of three decimal digits. We likewise found that we can also use a value of $N_{\max} = 10$ in the Model 3 numerical calculations (see Ch. 4). We also establish in both Models 1 and 3 that $f_{\mathrm{G}}\left(E, r\right) = 0$ for all $E < E_0$ as there's no deceleration processes included in the particle transport model.

In order to calculate the expansion coefficients (b_1, b_2, b_3, etc.), LB07 utilized the orthogonality of the spatial eigenfunctions and determined a quadratic normalization integral, $\mathcal{I}_n$. This was done by setting E to the source energy $E = E_0$ in Equation (3.78),

$$f_{\mathrm{G}}\left(E, r\right) = \sum_{m=1}^{N_{\max}} b_m Y_m\left(r\right) \ . \tag{3.79}$$

Both sides of Equation (3.79) were then multiplied by the product $Y_n\left(r\right) \omega\left(r\right)$ and integrated from $r = r_{\mathrm{S}}$ to $r = \infty$ to yield

$$\int_{r_{\mathrm{S}}}^{\infty} f_{\mathrm{G}}\left(E_0, r\right) Y_n\left(r\right) \omega\left(r\right) dr = \sum_{m=1}^{N_{\max}} b_m \int_{r_{\mathrm{S}}}^{\infty} Y_m\left(r\right) Y_n\left(r\right) \omega\left(r\right) dr \ . \tag{3.80}$$

In order to abide to the orthogonality of the eigenfunctions, only the $m = n$ term on the

RHS of Equation (3.80) will work,

$$\int_{r_\mathrm{S}}^{\infty} f_\mathrm{G}\left(E_0, r\right) Y_n\left(r\right) \omega\left(r\right) dr = b_n \int_{r_\mathrm{S}}^{\infty} Y_n^2\left(r\right) \omega\left(r\right) dr \ . \tag{3.81}$$

Thus the expansion coefficient b_n equates back to Equation (46) in LB07,

$$b_n = \frac{\int_{r_\mathrm{S}}^{\infty} f_\mathrm{G}\left(E_0, r\right) Y_n\left(r\right) \omega\left(r\right) dr}{\mathcal{I}_n} \ , \tag{3.82}$$

in which $\mathcal{I}_n$ is defined as

$$\mathcal{I}_n \equiv \int_{r_\mathrm{S}}^{\infty} Y_n^2\left(r\right) \omega\left(r\right) dr \ . \tag{3.83}$$

It should be noted that up to this point, Equations (3.78)-(3.83) remain valid for both Models 1 and 3.

In moving forward in completing the calculation of the expansion coefficients for Model 3, we need to do what was done for Model 1 (LB07) by reevaluate the distribution function at the source energy, $f_\mathrm{G}\left(E_0, r\right)$. This is done with the velocity derivative (Equation 3.62) being substituted back into Equation (3.61) and then integrating with respect to E in a small range around the injection energy E_0, yielding

$$f_\mathrm{G}\left(E_0, r\right) = \begin{cases} \frac{3\dot{N}_0}{(4\pi)^2 E_0^3 r_* H_* (H_- v_- - H_+ v_+)}, & r = r_* \ , \\ 0, & r \neq r_* \ . \end{cases} \tag{3.84}$$

Substituting $f_\mathrm{G}\left(E_0, r\right)$ in Equation (3.82) with Equation (3.84) and carrying out the integration, we get

$$b_n = \frac{\dot{N}_0 Y_n\left(r_*\right)}{\left(4\pi\right)^2 E_0^3 r_* H_* \kappa_* \mathcal{I}_n} \ , \tag{3.85}$$

in which we utilized the δ-function behavior close to the shock for the weight function $\omega(r)$ (see Equation 3.77). Equation (3.85) is exactly the same as Equation (49) of LB07. However when we also consider the singular nature of the weight function when computing the normalization integrals $\mathcal{I}_n$ defined in Equation (3.83),

$$\mathcal{I}_n = \lim_{\epsilon \to 0} \int_{r_{\mathrm{S}}}^{r_* - \epsilon} \omega\left(r\right) Y_n^2\left(r\right) dr + \int_{r_* + \epsilon}^{\infty} \omega\left(r\right) Y_n^2\left(r\right) dr + \frac{1}{3\kappa_* H_*} \left(H_- v_- - H_+ v_+\right) Y_n^2\left(r_*\right) \ , \tag{3.86}$$

we find that $\mathcal{I}_n$ is different in Model 3 than in Model 1, notably with the term at the shock radius r_*. We use this expression to evaluate the normalization integrals (see Ch 4). When setting for Model 1 $H_+ = H_- = H_*$, Equation (3.86) becomes Equation (50) in LB07.

We shall close off this chapter, before moving onto the model applications of Ch. 2 and 3, by summarizing the physical significance of the Green's function (f_{G}) evaluated at the injection energy E_0, as discussed in LB07. As noted in Equation (3.84), the Green's function at the injection energy is only valid at the shock ($r = r_*$) and has a finite value, whereas it's zero for radii away from the shock. This is due to the fact that the model specifically states that particle injection occurs at the shock. So while the δ-function may exist for the flow velocity (Equation 3.62), it will not for the Green's function since it's eliminated from the particles at the shock experiencing strong acceleration. Both Models 1 and 3 assume that the plasma in the disk is converging at all radii (including the shock) in the accretion flow, in which the particle acceleration causes the Green's function to vanish everywhere except at the shock $r = r_*$.

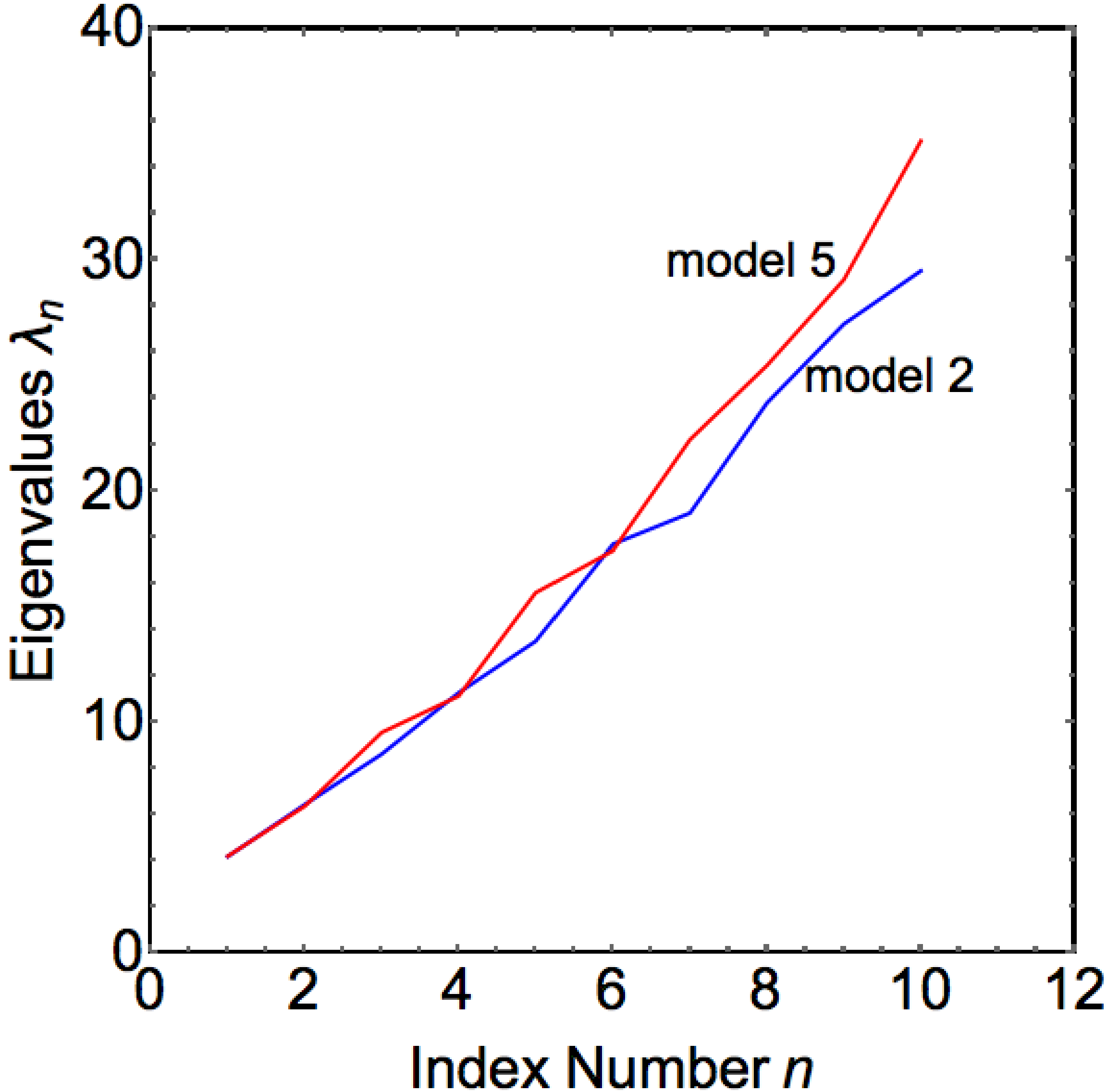

Figure 3.2: This is Figure 2 of LB07: eigenvalues of model 2 and model 5, which were associated with M87 and Sgr A* , respectively.

Chapter 4: Astrophysical Applications

4.1 Dynamical Solution

As was done for Model 1 (LB04 LB05 and LB07), the goal is to determine the properties of the integrated disk/shock/outflow model using the observed values of the black hole mass M and the jet kinetic power $L_{\rm jet}$, for a given source. For Model 3, the fundamental free parameters for the theoretical model are ϵ_+, l, κ_0, K_g/K_r, and γ_g and γ_r, where only ϵ_+, l, κ_0, K_g/K_r remain to be determined since $\gamma_g = 1.5$ and $\gamma_r = 4/3$. For Model 1, the fundamental free parameters were just ϵ_+ and l. The sound speed profiles $a_g(r)$ and $a_r(r)$ are computed by numerically integrating Equations (2.55) and (2.74), and subsequently the associated solution for the velocity $v(r)$ is obtained from Equation (2.64), as well as the effective sound speed (Equation 2.76).

After these profiles are computed, the corresponding pressure and energy density profiles for the gas and relativistic particles can be computed from Equations (2.6), (2.7), (2.8) and (2.9). Likewise, we can compute the number and energy density distributions for the relativistic particles in the disk using Equations (3.26) and (3.33), respectively. We specify that the injection energy of the seed particle $E_0 = 0.002$ ergs, which can then be used to calculate the particle injection rate $\dot{N}_0$ via Equation (3.40) for a known $L_{\rm shock}$. Taking this in addition to energy being conserved in our model, we can solve for various theoretical parameters based on observational values for M and $L_{\rm jet}$, which is explained below.

4.1.1 Model Parameters

For Model 3, six different accretion/shock scenarios are explored in detail here. All of the model profiles are dimensionless and can be scaled to any mass black hole. The simulations

Table 4.1: Disk Structure Parameters. Note: All quantities are expressed in gravitational units ($GM = c = 1$) except T_*, which is in units of 10^{11} K.

Model 3	l	κ_0	K_g/K_r	ϵ_+	ϵ_-	r_{c1}	r_{c3}	r_*	H_*	R_*	T_*
A............................	3.1340	0.02044	7,400	-0.006100	-0.000429	110.29	5.964	12.565	6.200	1.605	1.503
B............................	3.1524	0.02819	7,700	-0.007500	-0.001502	123.52	5.937	11.478	5.460	1.607	1.586
C............................	3.1340	0.03000	65,000	-0.007500	-0.001073	131.75	5.898	14.780	7.486	1.691	1.412
D............................	3.1524	0.05500	260,000	-0.009900	-0.003784	61.11	5.886	14.156	6.910	1.614	1.446
E............................	3.1340	0.02044	20,000	-0.005100	-0.000857	171.48	5.821	19.022	10.406	1.612	1.098
F............................	3.1524	0.02819	10,000	-0.007700	-0.001343	127.47	5.926	11.696	5.589	1.642	1.583
Model 1											
2............................	3.1340	0.02044	N/A	-0.005746	0.001527	98.524	5.379	21.654	11.544	1.897	1.160
5............................	3.1524	0.02819	N/A	-0.008749	0.001229	131.874	5.329	15.583	7.672	1.970	1.490

of the disk structure in M87 and Sgr A* are based on the published observational estimates for M and $L_{\rm jet}$ used in LB05. In the case of M87, we set $M = 3 \times 10^9 \, M_\odot$ (e.g., Ford et al. 1994) and for Sgr A* , we use $M = 2.6 \times 10^6 \, M_\odot$ (e.g., Schödel et al. 2002). For the kinetic luminosity of the outflow in M87, we use the value $L_{\rm jet} = 5.5 \times 10^{43}$ ergs s^{-1} (Reynolds et al. 1996; Bicknell & Begelman 1996; Owen et al. 2000). The kinetic luminosity in Sgr A* is rather uncertain, and the published values encompass a rather wide range (e.g., Yuan 2000; Yuan et al. 2002). For example, Falcke & Biermann (1999) obtained $L_{\rm jet} = 5 \times 10^{38}$ ergs s^{-1}, and Yusef-Zadeh et al. (2012) estimated $L_{\rm jet} = 1.2 \times 10^{41}$ ergs s^{-1}. Hence, in our comparisons, we adopt both of these values for $L_{\rm jet}$ for Sgr A* . This results in $\dot{N}_0 = 2.75 \times 10^{46}$ s^{-1} for M87, and $\dot{N}_0 = 2.5 \times 10^{41}$ s^{-1} or $\dot{N}_0 = 6.0 \times 10^{43}$ s^{-1}, respectively, for Sgr A* . The values for the various model parameters, l, κ_0, K_g/K_r, ϵ_+, ϵ_-, r_{c1}, r_{c3}, r_*, H_*, R_* and T_* are reported in Table 4.1, along with the associated values for models 2 and 5 from LB05, which are designated for M87 and Sgr A* , respectively. Here, T_* is the ion temperature at the shock location related to the thermal pressure $P_g = n_g k T_*$ in cgs units, where k is the Boltzmann constant, and the ion number density is related to the mass density via $n_g = \rho / m_p$, where m_p is the mass of a proton. The parameters associated with the shock jump conditions, the transport equation, and the specific sources are reported in Tables 4.2, 4.3, and 4.4, respectively, for both Models 1 and 3.

We obtain shock-disk solutions ranging between the inner radius $r_{\rm in} = 2.1$ and the outer

Table 4.2: Shock Jump Conditions. Note: All quantities are expressed in gravitational units ($GM = c = 1$).

Model 3	v_+/v_-	ρ_+/ρ_-	$a_{g+} = a_{g-}$	a_{r+}	a_{r-}	H_+/H_-	M_{g-}	M_{r-}
A.............................	0.6593	1.605	0.1440	0.0676	0.0857	0.9447	0.9839	1.6530
B.............................	0.6588	1.607	0.1479	0.0694	0.0880	0.9447	0.9843	1.6541
C.............................	0.6163	1.691	0.1395	0.0498	0.0647	0.9593	1.0318	2.2236
D.............................	0.6381	1.614	0.1412	0.0444	0.0564	0.9706	1.0174	2.5488
E.............................	0.6547	1.612	0.1230	0.0555	0.0704	0.9475	0.9904	1.7311
F.............................	0.6444	1.642	0.1478	0.0667	0.0854	0.9451	0.9979	1.7261
Model 1								
2.............................	0.5267	1.897	0.1262	N/A	N/A	1.0000	1.125	N/A
5.............................	0.5076	1.970	0.1431	N/A	N/A	1.0000	1.146	N/A

radius $r_{\rm out} = 5,000$, where $r_{\rm in}$ and $r_{\rm out}$ denote the boundaries of the computational domain for the simulations. Our numerical examples use natural gravitational units ($GM = c = 1$ and $r_{\rm S} = 2$). While LB05 (Model 1) used the values of the accretion rate for M87 $\dot{M} = 1.3 \times 10^{-1}\, M_{\odot}{\rm yr}^{-1}$ (.g. Reynolds et al. 1996), and Sgr A* $\dot{M} = 8.8 \times 10^{-7}\, M_{\odot}{\rm yr}^{-1}$ (e.g. Yuan et al 2002; Quataert 2003), respectively, Model 3 does not. Since it's required that $L_{\rm shock} = L_{\rm jet}$ (e.g. Equation 2.162), the accretion rate $\dot{M}$ is dependent on $\Delta\epsilon$ via Equation (2.160). Thus for the fundamental parameters l, κ_0 and K_g/K_r, *multiple* possible values can exist for $\Delta\epsilon$. It can no longer be concluded (cf. LB05) that $\Delta\epsilon = -0.007$ for M87 and $\Delta\epsilon = -0.01$ for Sgr A* , as there are now multiple possible values when relativistic particles and diffusion are included. The associated values used for $\Delta\epsilon$ and $L_{\rm jet}$ in each model, as well as the corresponding values for $\dot{M}$, are shown in Table 4.4. Table 4.5 shows the ratio of the jetted outflow rate $\dot{M}_{\rm esc}$ to the accretion rate ($\dot{M}_{\rm esc}/\dot{M}$) for each model. The low ratio values validates our assumption of a constant mass accretion rate at the shock location.

In using the energy conservation condition $L_{\rm esc} = L_{\rm jet}$ (Equation 2.161), we can determine the dynamical profiles for a given l, κ_0 and K_g/K_r with the M87 and Sgr A* parameters. As a point of departure, we will focus on the l and κ_0 values determined in LB05 that coincides with M87 (their model 2) and Sgr A* (their model 5), labeled in this work as Model A and Model B, respectively. What is presented in these two models are those

Table 4.3: Transport Equation Parameters. Note: All quantities are expressed in gravitational units ($GM = c = 1$).

Model 3	κ_*	A_0	$\Delta x/\lambda_{\rm mag}$	η	$\eta_{\rm rat}$	$\dot{N}_{\rm I}/\dot{N}_{\rm II}$	$\dot{N}_{\rm esc}/\dot{N}_0$	$E_{\rm esc}/E_0$	$\Gamma_{\rm esc}$
A.............................	0.1341	0.0500	6.628	11.883	1.79	-0.0045	0.3864	2.607	3.476
B.............................	0.1529	0.0515	6.411	7.303	1.14	-0.0217	0.3881	2.601	3.468
C.............................	0.2850	0.1001	3.563	7.673	2.15	-0.1401	0.5725	1.781	2.375
D.............................	0.4781	0.1248	1.418	2.895	2.04	-0.8033	0.5469	1.842	2.456
E.............................	0.2986	0.0476	4.586	6.426	1.40	-0.0925	0.4281	2.339	3.119
F.............................	0.1606	0.0587	6.178	7.896	1.23	-0.0253	0.4228	2.370	3.160
Model 1									
2.............................	0.4279	0.0124	1.000	1.000	1.000	-0.1800	0.1700	5.950	7.920
5.............................	0.3214	0.0158	1.000	1.000	1.000	-0.1500	0.1800	5.450	7.260

profiles that give the *maximum possible value* for the mean Lorentz factor of the escaping particles $\Gamma_{\rm esc} = E_{\rm esc}/m_p c^2$ while maintaining the LB05 values for l and κ_0. It should be noted that many dynamical profiles are possible provided that $l < 4$ in inviscid models, though here l is not specific to any AGN dynamically speaking. In the next set of models, we will allow ourselves to vary the value of κ_0 while fixing the value for l using the results of LB05. Models C and D utilize the same specific angular momentum l values used in Models A and B, respectively, but we vary κ_0 in order to obtain the value $\Gamma_{\rm esc} \approx 2.3$ quoted by Abdo et al. (2009) for M87. Models E and F are used to obtain the value $\Gamma_{\rm esc} \approx 3.0$ estimated by Yusef-Zadeh et al. (2012) for Sgr A* . Energy conservation in our disk/shock model creates self-consistent solutions since we enforce $L_{\rm esc}/L_{\rm jet} = 1$ with the data gathered for M87 and Sgr A* . This is a different approach from Model 1 since κ_0 was determined when $L_{\rm esc}/L_{\rm jet} = 1$, instead of enforcing it. For illustrative purposes in this section, we focus on the details of the disk structure and particle transport obtained in Models A and B, as they are associated to models 2 and 5, respectively, due to their identical values for l and κ_0.

4.1.2 Disk Structure and Particle Transport

The importance of the shock for the acceleration of high-energy particles can be seen in the examination of the structure of the accretion disk with a discontinuous shock based

Table 4.4: Source Parameters. Note: $\Delta\epsilon$ is expressed in gravitational units ($GM = c = 1$).

		$L_{\rm jet}$ (ergs s^{-1})		$\dot{M}$ ($M_\odot$ yr^{-1})		n_* (cm^{-3})		U_* (ergs cm^{-3})	
Model 3	$\Delta\epsilon$	Sgr A*	M87	Sgr A*	M87	Sgr A*	M87	Sgr A*	M87
A............................	-0.005671	5.0×10^{38}	5.5×10^{43}	1.56×10^{-6}	1.71×10^{-1}	4.46×10^{5}	3.66×10^{4}	2.31×10^{3}	1.91×10^{2}
B............................	-0.005998	5.0×10^{38}	5.5×10^{43}	1.47×10^{-6}	1.62×10^{-1}	5.40×10^{5}	4.43×10^{4}	2.79×10^{3}	2.30×10^{2}
C............................	-0.006427	5.0×10^{38}	5.5×10^{43}	1.37×10^{-6}	1.51×10^{-1}	2.32×10^{5}	1.88×10^{4}	8.12×10^{2}	6.71×10^{1}
D............................	-0.006116	5.0×10^{38}	5.5×10^{43}	1.44×10^{-6}	1.59×10^{-1}	2.01×10^{5}	1.65×10^{4}	7.38×10^{2}	6.09×10^{1}
E............................	-0.004243	1.2×10^{41}	5.5×10^{43}	4.99×10^{-4}	2.29×10^{-1}	4.90×10^{7}	1.66×10^{4}	2.29×10^{5}	7.89×10^{1}
F............................	-0.006357	1.2×10^{41}	5.5×10^{43}	3.33×10^{-4}	1.53×10^{-1}	1.18×10^{8}	4.05×10^{4}	5.63×10^{5}	1.94×10^{2}
Model 1									
2............................	-0.007	N/A	5.5×10^{43}	N/A	1.30×10^{-1}	N/A	2.01×10^{4}	N/A	2.39×10^{2}
5............................	-0.010	5.0×10^{38}	N/A	8.80×10^{-7}	N/A	4.33×10^{5}	N/A	4.71×10^{3}	N/A

on the values of the fundamental parameters. In Figures 4.1a and 4.1b, we plot the inflow speed $v(r)$ and the effective adiabatic sound speed $a_{{\rm eff},\kappa}(r)$ (Equation 2.76) for the shocked solutions for Model A and Model B, respectively, with the corresponding results tabulated in Table 4.1. We are working within the isothermal shock model, so the thermal sound speed $a_g(r)$ is continuous at the shock location, although the particle sound speed $a_r(r)$ experiences a discontinuous jump, as expected. In Figures 4.1c and 4.1d, we compare the dynamical profiles computed using our new two-fluid model with the corresponding results obtained using the one-fluid LB05 model, which does not include relativistic particles nor diffusion. The LB05 model (Model 1) relied on knowing the value for ϵ_- for a known l value, which is then used to determine a dynamic profile. In order for us to do a valid comparison seen in these figures, ϵ_- is calculated for the LB05 model via

$$\epsilon_- \to a_{g\infty}^2 / \left(\gamma_g - 1\right) \ , \quad r \to \infty \ , \tag{4.1}$$

where here we are using $a_{g\infty}$ from Models A and B for a given specific angular momentum. Right away we can see some differences between the two model versions.

An interesting feature of the new model is the distinctive precursor deceleration in the velocity profile, which was likewise seen in the cosmic-ray shock acceleration model (Axford et al. 1977). This feature is completely absent in the LB05 dynamical profile, and it clearly indicates the role of diffusive particle acceleration as relativistic particles cross the

Table 4.5: Results: mass outflow rate $\dot{M}_{\rm esc}/\dot{M}$ for each model.

Model 3	$\dot{M}_{\bf esc}/\dot{M}$
A	0.00164144
B	0.00174225
C	0.00274897
D	0.0025007
E	0.00136147
F	0.00201269

shock multiple times. These results clearly show the precursor deceleration occurring before the shock, thereby demonstrating how the inclusion of the relativistic sound speed affect the transition into the shock, compared to the discontinuous drop that occurs in previous models. With the inclusion of the dimensionless parameter η for the shock thickness (see Appendix B), these plots show that the shock is wider when relativistic particle pressure and diffusion are included in the dynamical structure. We emphasize that these new results continue the rigorous work of Blandford & Begelman (1999), Becker et al. (2001), and LB05, for a fully self-consistent calculation of the structure of an ADAF disk coupled with a shock-driven outflow, this time including relativistic particle pressure and diffusion.

Also, as mentioned in § 2.6.3, we can see the result of a harder compression ratio in Figure 4.1 for Model 3. Das et al. (2001a, 2001b) described the relationship between the compression ratio and the outflows for Model 1 in being that a low compression ratio results in a low outflow rate, while a higher compression ratio results in a high outflow rate. This is associated with the kind of shocks that can exist, in which generally weak shocks ($R_* \sim 1$) are considered to have negligible outflow rate while strong shocks ($R_* \rightarrow 7$) have a small outflow rate. In between you can have a mid-strength shock with a stronger outflow rate. Likewise, increasing the specific angular momentum l can also result in a higher outflow rate. This ties into the Keplerian rate of the disk, where a high Keplerian rate equates to a low compression ratio and outflow rate, whereas a low Keplerian rate results in a higher compression ratio and outflow rate. This illustrates the correlation that a lower compression ratio means that the gas in the post-shock region is cooled down due to inverse

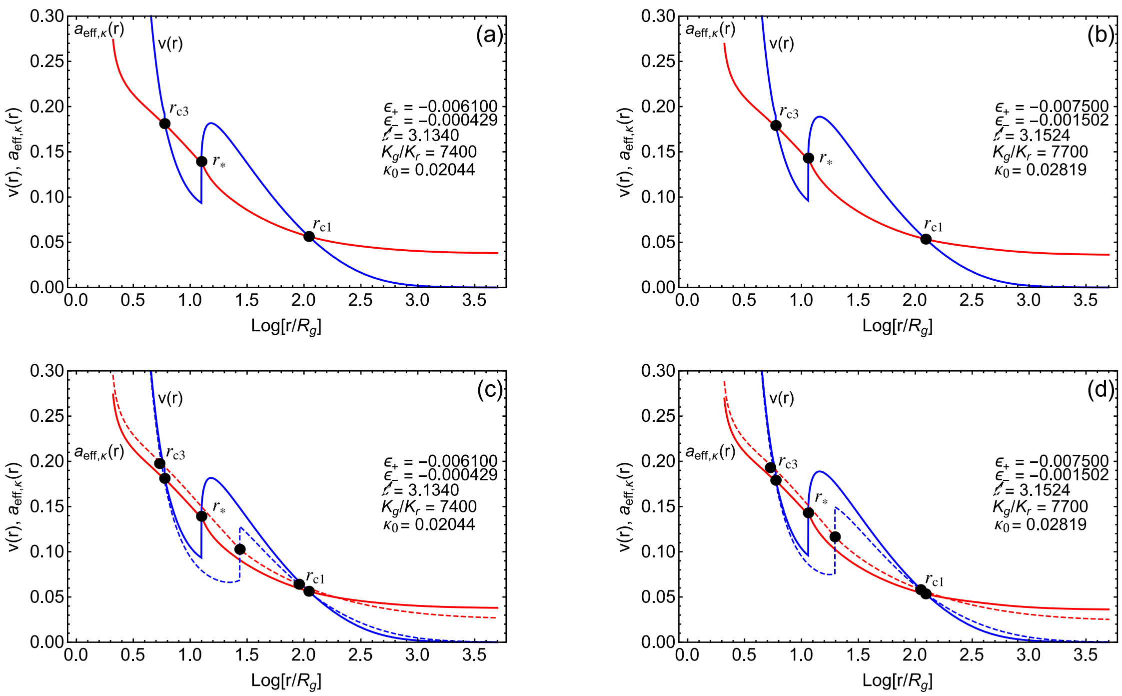

Figure 4.1: Velocity $v(r)$ (blue curves) and effective sound speed $a_{\mathrm{eff},\kappa}(r)$ (red curves), plotted in units of c, for the shocked solution of (a) Model A and (b) Model B. These curves cross at the critical points. The solid lines denote the self-consistent model results developed here, which includes relativistic particle pressure and diffusion, and the dashed lines represent the non-self-consistent results obtained by LB05.

Compton scattering in which case the shock disappears, thus reducing the thermal pressure and resulting in low outflow rate.

Of course, this conclusion for Model 1 was based on a 1:1 relation between the compression, velocity and entropy jump ratios where everything was correlated. For Model 3 we can see that's no longer the case. Yes while there still remains a link between the compression and entropy jump ratios, there's no longer a connection to the velocity jump ratio as before due to the presence of relativistic particles. Now we see that a higher compression ratio results in a lower shock outflow, in which the amount of entropy jump is likewise less than before, while the velocity jump ratios remain identical. In this case what's happening here may be very similar to the Model 1 scenario, where the inclusion of relativistic particle pressure is resulting in higher bulk pressure in the pre- and post-shock regions and lower outflows, suggesting that there's less energy to be lost than there was before. While diffusion is successfully removing the nonthermal radiation for a high Keplerian rate, the gas in the post-shock region is still efficiently cooled down due to inverse Comptonization, resulting in a lower bulk outflow. Because of this, there's a possibility that the Lorentz factor for the protons γ_p can never reach higher than anticipated in previous models.

4.1.3 Smooth-Shock Analysis

In the single-fluid model of LB05, it is always possible to obtain a smooth velocity profile that corresponds to any shocked-disk solution. However, the dynamical model of LB05 did not include either relativistic particle pressure or diffusion, and therefore we must reexamine the possible existence of globally smooth flows within the context of our new two-fluid model. Figures 4.2a and 4.2b depict the dynamical profiles for Model A and Model B, respectively, for globally smooth flow in the diffusive (thick-lines) and non-diffusive (dashed-lines) cases. It should be noted that the non-diffusive ($\kappa = 0$) model is determined via a simple root-finding procedure using Equation (2.96). We expect the two profiles to resemble one another near the horizon, as the disk becomes purely adiabatic, and this is indeed the case. However, the globally smooth diffusive model fails to pass through the inner critical point displayed by the adiabatic model, and therefore it is unphysical. After an extensive exploration of the parameter space, we find that in fact it is not possible to obtain any globally smooth solutions when diffusion is included, regardless of the values for the specific angular momentum l, entropy ratio K_g/K_r, and the energy transport rate per unit mass ϵ_-. On the other hand, it is always possible to obtain a globally smooth flow even when the pressure of the relativistic particles is included, provided there's no diffusion and $\epsilon_- > 0$. *Hence we conclude that the inclusion of diffusion ($\kappa \neq 0$) invariably leads to the formation of a standing shock in the accretion flow.*

4.1.4 Pressure Distribution Analysis

Next we study the solutions obtained for the thermal and particle pressure distributions in the disk based on the flow structures for Models A and B. We plot the global profiles obtained in a shocked disk in Figure 4.3a and 4.3b for Model A and Model B, respectively, for Sgr A* (thick lines) and M87 (dashed lines). Considering the universal nature of the dynamical profiles, what separates these specific profiles for the thermal pressure (blue lines) and the relativistic particle pressure (red lines) is based on the AGN's jet $L_{\rm jet}$ and mass M. These results show that the pressures decrease monotonically with increasing radius, much like their corresponding energy densities would. The increase near the horizon is still a consequence of advection, however the gradual leveling off as $r \to \infty$ reflects the fact that in the inviscid case, the particles injected at the shock now have a very strong chance of diffusing to large distances from the black hole. In fact it can be seen that $P_r > P_g$ as $r \to \infty$. These figures clearly show the relativistic particle pressure being comparable to the gas pressure for both Sgr A* and M87, thereby supporting Axford et al. (1977) and Becker et al. (2011) on the total pressure exceeding the background pressure.

4.1.5 Dynamical Energy Density Analysis

Moving forward, we study the solutions obtained for the relativistic number and energy density distributions in the disk based on the flow structures for both models. The related

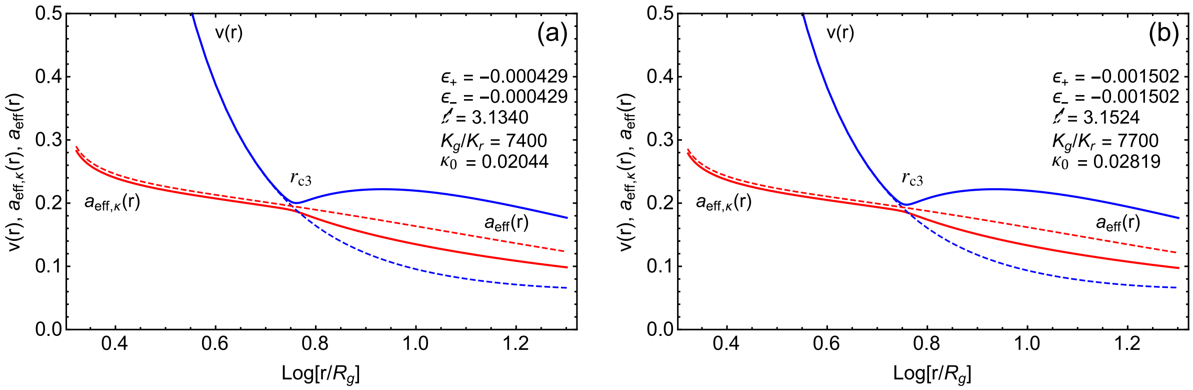

Figure 4.2: Velocity $v(r)$ (blue curves) and effective sound speed $a_{\text{eff},\kappa}(r)$ (red curves), plotted in units of c, for the globally smooth (shock-free) solutions with $\epsilon_+ = \epsilon_-$. The solid lines were computed using the diffusive model ($\kappa_0 \neq 0$), with the parameters for (a) Model A and (b) Model B. Also plotted are the corresponding adiabatic models ($\kappa_0 = 0$, dashed lines) for the velocity and effective sound speed $a_{\text{eff}}(r)$. It can be seen that a smooth solution is possible in the adiabatic case, but not in the diffusive case.

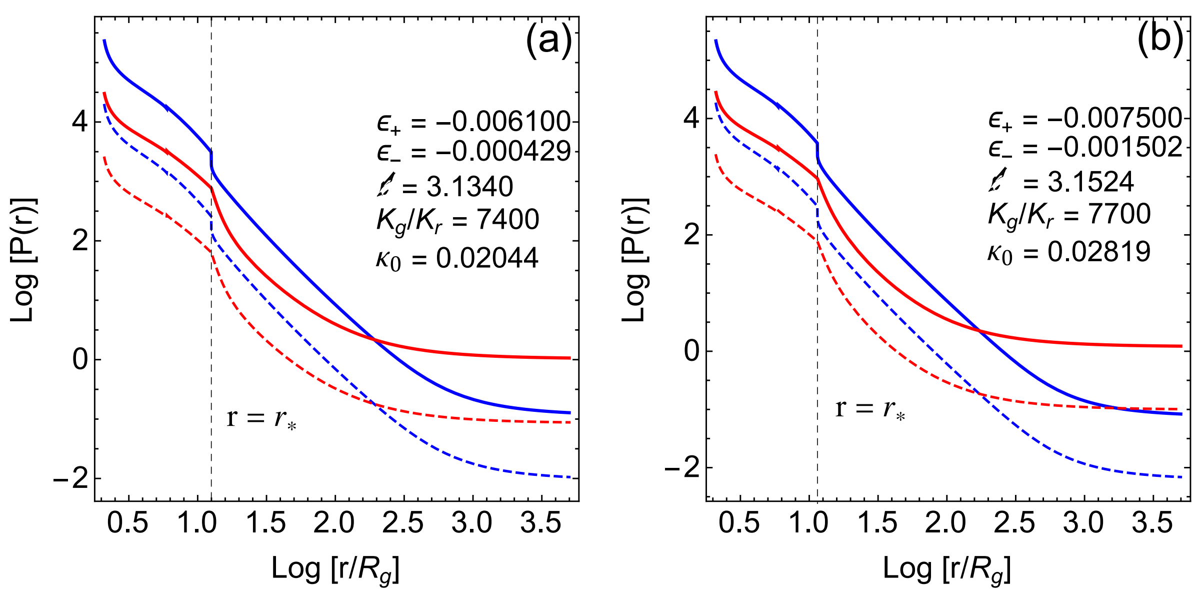

Figure 4.3: Dynamical pressure profiles for thermal pressure P_g (blue curves) and relativistic particle pressure P_r (red curves) plotted as functions of r in cgs units for (a) Model A and (b) Model B. The thick and dashed lines represent the results obtained for Sgr A* and M87, respectively. Note that the particle pressure is comparable with the thermal pressure at the shock, and it is dominant at large radii.

transport parameters are tabulated in Table 4.3, with the corresponding astrophysical values in Table 4.4. It should be noted that the astronomical values tabulated in Table 4.3 for each model are dimensionless and can be scaled to any specific AGN mass. We plot the global energy density derivations obtained in a shocked disk in Figure 4.4a and 4.4b for Model A and Model B, respectively. The kinks that appear in the energy density distributions at the shock radius $r = r_*$ reflect the derivative jump conditions given by Equations (2.163). These plots show self-consistency between the energy density derived from the vertically-integrated transport equation (thick lines) with those obtained from the dynamical profiles (dots). It should be noted that this remains true for any model, not just those shown in this paper.

The numerical solutions for the number energy density remain self-consistent with the formal solutions developed in LB05, but for the purposes of this paper it is unnecessary to show comparisons. The values for the ratios $\dot{N}_{\rm I}/\dot{N}_{\rm II}$ and $\dot{N}_{\rm esc}/\dot{N}_0$ reported in Table 4.3 indicate that most of the injected particles are advected into the black hole, with no more than $\sim 40\%$ on average escaping to form the outflow. These results, and others we've observed in this work, seem to show that for a given specific angular momentum, the highest possible escape Lorentz factor $\Gamma_{\rm esc}$ is obtainable with the lowest possible diffusion constant κ_0 and entropy ratio K_g/K_r allowed. This indicates that for an inviscid disk, with particle pressure and diffusion included, a higher volume of relativistic particles in the disk with a nudge of diffusion will result in a higher relativistic outflow. This is also indicative by the higher mass accretion rates obtained for Sgr A* and M87. However, it should be noted that there's not much variation in these specific models for the particle escape Lorentz factor, $\Gamma_{\rm esc} \sim 3.5$, as so far obtaining a profile resulting in a higher factor has yet to be found for the inviscid disk with relativistic particles and diffusion included. This may or may not be the case when viscosity is included in the dynamical structure, which will be addressed in later work.

4.1.6 Jet Formation in M87 and Sgr A*

Next we address the mean energy of the relativistic particles in the disk

$$\langle E \rangle \equiv \frac{U_r(r)}{n_r(r)} \ , \tag{4.2}$$

to where $\langle E \rangle = E_{\rm esc}$ at the shock location $r = r_*$. The mean energy as a function of radius in shocked disks is plotted in Figure 4.5 based on the parameters used for Models A and B. When a shock is present in the flow, the results again demonstrate that the relativistic particle energy experiences a boost. This time, only by a factor of 2.5 due to the presence of relativistic particles and diffusion. This work further demonstrates the essential role that a shock has in the efficiency of accelerating particles up to very high energies, far above the energy required to escape from the disk. Also, the mean energy of the relativistic particles close to the event horizon remains slightly enhanced by the strong compression of the accretion flow. This is indicated by the slight increase in $\langle E \rangle$ as $r \to r_{\rm S}$.

Now we can move in comparing our predictions for the shock/jet location and the asymptotic Lorentz factor with the observations of M87 and Sgr A* . We find that our models agree with Biretta et al. (2002), in which the M87 jet forms in a region no larger than ~ 30 gravitational radii from the black hole, as well as Yuan (2000) for the case of Sgr A* . In regards to the asymptotic (terminal) Lorentz factor, which is estimated by

$$\Gamma_\infty = \Gamma_{\rm esc} = \frac{E_{\rm esc}}{m_p c^2} \ , \tag{4.3}$$

we note that Models C and D are in agreement with Abdo et al. (2009) who estimated $\Gamma_\infty = 2.3$, based on their observations, for M87. In the case of Sgr A* , Models E and F are in agreement with Yusef-Zadeh et al. (2012) who likewise adopted $\Gamma_\infty \sim 3$ from their observations. These values for Γ_∞ are still above the injected Lorentz factor $\Gamma_0 \equiv E_0/\left(m_p c^2\right) \sim 1.3$, with m_p denoting the proton mass, naturally. Since the shock thickness

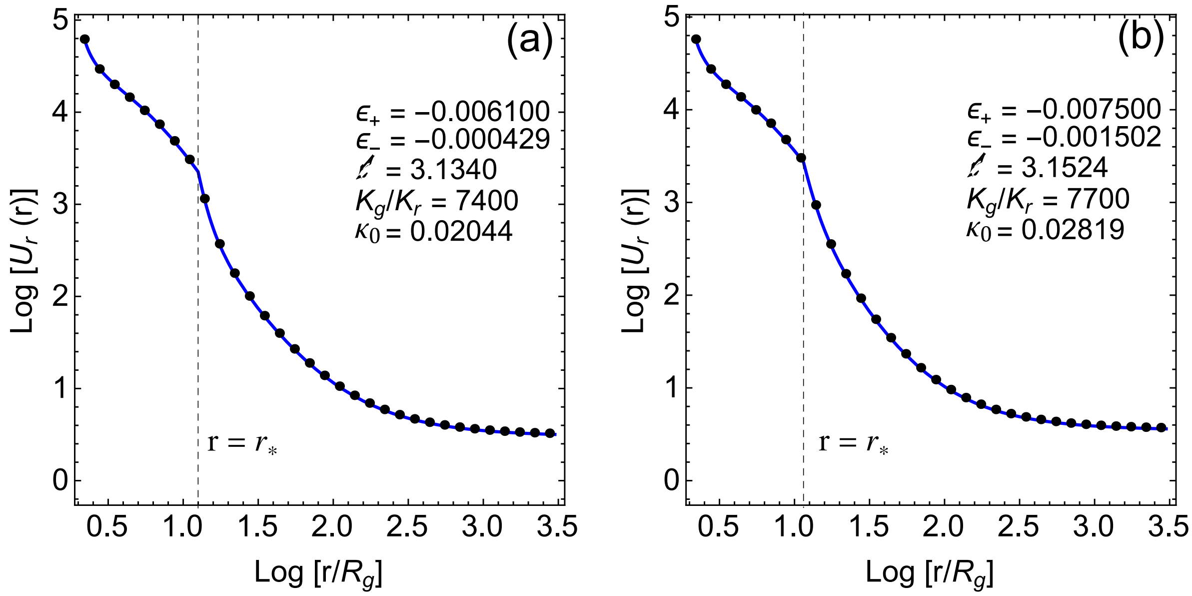

Figure 4.4: Global solutions for the relativistic particle energy density U_r, showing a comparison between the particle transport equation (thick line) and the dynamical profile (dots). These plots are self-consistent for any black hole application.

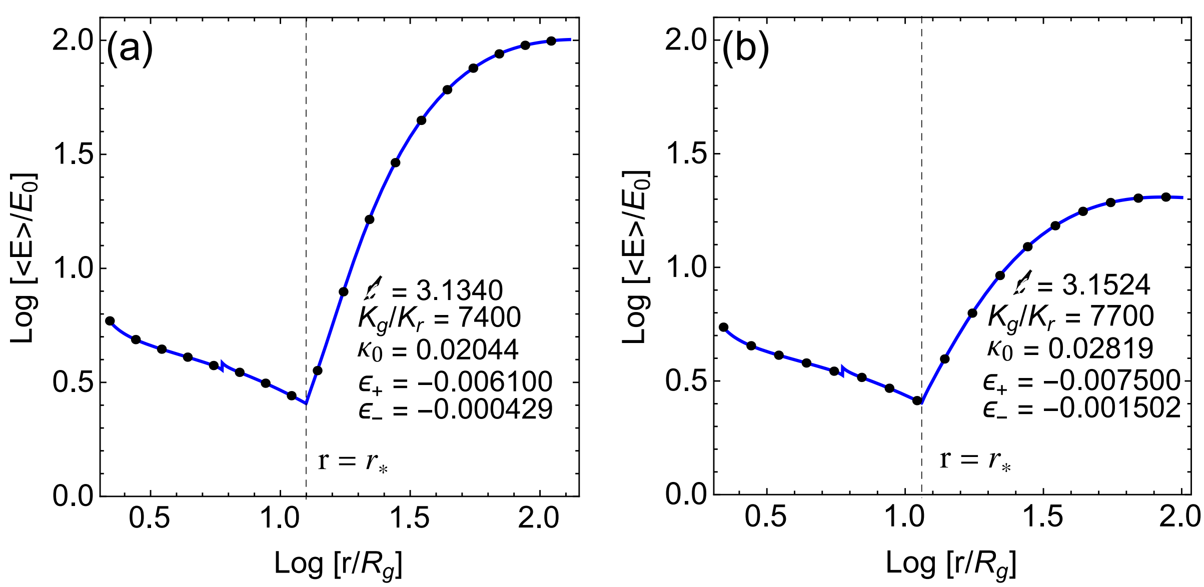

Figure 4.5: Mean energy of the relativistic particles in the disk, $\langle E \rangle \equiv U_r(r)/n_r(r)$, for Model A (a) and Model B (b), plotted in units of the injection energy E_0.

parameter η (cf. Appendix B) is also related to the mean magnetic free path $\eta = \Delta x/\lambda_{\rm mag}$, we can determine a ratio difference between the two values $\eta_{\rm rat} = \eta\lambda_{\rm mag}/\Delta x$ shown in Table 4.3. For this work we have determined a limit in which a valid solution is one where $\eta_{\rm rat} \lesssim 1.5$. Thus from this cutoff, we can see that Models B, E and F are the more self-consistent solutions. Considering the different, arbitrary nature in which the observed parameters from Abdo et al. (2009) and Yusef-Zadeh et al. (2012) were obtained from the data, we can argue that either Model B, E or F can be applied to M87 and Sgr A* . Observations in astronomy is always a matter of opinion and instrument error, therefore the Lorentz factors obtained for either galactic source can in reality be lower or higher than what was reported. Hence, more observational work is needed in the future in order to test our predictions for Γ_∞ for Sgr A* , as there is still no reliable observational estimate for that quantity.

4.1.7 Radiative Losses from the Jet and the Disk

While it remains unclear as to whether the outflows observed from many radio-loud systems containing black holes are composed of an electron-proton plasma or electron-positron pairs, or a mixture of both, the particles must maintain sufficient energy to power the observed radio emission. Though it should be noted that this can be hindered by some form of reacceleration occuring e.g., due to shocks propagating along the jet (Atoyan & Dermer 2004a). Our work assumes the proton-electron outflows, which is ideal since the ions carry most of the kinetic power, they don't radiate much, and they are not strongly coupled to the electrons under the typical conditions in a jet (e.g., Felten 1968; Felten et al. 1970; Anyakoha et al. 1987; Aharonian 2002). Operating on the speculation that the observed outflows are proton driven, LB05 explored two methods in which ions in the jet lose energy: either from 1) the production of synchrotron and inverse Compton emission, or 2) indirect radiative losses via Coulomb coupling with the electrons. These two methods were evaluated by their corresponding cooling timescales for the outflows. They concluded that synchrotron and inverse Compton losses have virtually no effect on the energy of the protons in either the M87 jet or the Sgr A* jet. The associated energy-loss timescale for this method is defined as (cf. Equation 112 of LB05)

$$t_{\rm rad} \equiv \frac{3 m_p c}{4 \sigma_{\rm T} \Gamma_{\rm esc}} \left(\frac{m_p}{m_e} \right)^2 (U_B + U_{\rm ph})^{-1} \ , \tag{4.4}$$

where m_e is the mass for electrons, $U_{\rm ph}$ is the energy density of the soft radiation, and $U_B = B^2/(8\pi)$ is defined as the energy density of the magnetic field with strength B. Even with lower values for the terminal (asymptotic) Lorentz factor in our models, and setting $B \sim 0.1$ G for M87 and $B \sim 10$ G for Sgr A* based on estimates from Biretta et al. (1991) and Atoyan & Dermer (2004b), respectively, we too come to the same conclusion.

They also concluded that Coulomb coupling between the protons and electrons cannot seriously degrade the energy of the accelerated ions escaping from the disk, as they propagate out to the radio lobes via the jet. However, this conclusion was based on extremely conservative estimates and the fact that the theoretical accretion disks were thermally dominated. They did emphasize that in reality, the density of the jet will drop rapidly as the gas expands, and thus the 'real' proton energy-loss timescales for the outflows will be much larger than what they determined. With the addition of relativistic particles, it is worth reevaluating this method of energy lose for the ions.

Coulomb coupling with thermal electrons allows the protons in the jet to lose energy, which are considered less efficient in radiating away than the electrons. The associated loss timescale for these escaping protons is defined (cf. Equation 114 of LB05) as

$$t_{\rm Coul} \equiv \frac{\Gamma_{\rm esc} m_p c^2}{(dE/dt)|_{\rm Coul}} = \frac{\Gamma_{\rm esc} m_p}{30 n_e \sigma_T c m_e} \ , \tag{4.5}$$

where m_e is the mass for electrons. In moving forward with this analysis, we adopt the same conservative assumption that since n_e decreases rapidly as the jet expands from the disk into the external medium, the strongest Coulomb coupling will occur at the base of the jet, where n_e is at maximum. This value can be estimated by first using Equation (D.4) to eliminate A_0 in Equation (3.25), in order to determine the rate at which protons escape from the disk at the shock location (in terms of $\lambda_{\rm mag}$),

$$\dot{N}_{\rm esc} \equiv \frac{4\pi r_* \eta \lambda_{\rm mag}^2 c n_*}{H_*} \ , \tag{4.6}$$

where r_*, n_*, H_*, η, and $\lambda_{\rm mag}$ represent, respectively, the radius, proton number density, vertical disk half-thickness, the shock length and magnetic mean free path inside the disk at the shock location. Using the idea that now the shock has a width comparable to $\eta\lambda_{\rm mag}$, and operating on the same relations for the sum of the upper and lower sides of the shock annulus, as well as the flux of the escaping protons into the outflow, the proton escape rate can likewise be written as

$$\dot{N}_{\rm esc} = 4\pi r_* \eta \lambda_{\rm mag} c n_p \ . \tag{4.7}$$

Combining these two relations for $\dot{N}_{\rm esc}$ yields the following,

$$\frac{n_p}{n_*} = \frac{\lambda_{\rm mag}}{H_*} < 1 \ , \tag{4.8}$$

and since the electron-proton jet is charge neutral ($n_e = n_p$),

$$n_e = \frac{\lambda_{\rm mag}}{H_*} n_* \ , \tag{4.9}$$

where n_e is the electron number density at the base of the jet and n_p is the proton number density. Combining the relation $\lambda_{\rm mag}/H_* = (A_0/\eta)^{1/2}$ (e.g. Equation D.4) with the results for A_0, η and n_* obtained in Table 4.3, we can see for Models B, E and F, we can see in Table 4.4 the corresponding values for n_e, $\Gamma_{\rm esc}$, and the electron-proton Coulomb coupling timescale (Equation 4.5) for each source, which we can see ranges between $\sim 10^1 - 10^5$ yr.

Table 4.6: Radiative losses for Models B, E, and F. Note: All quantities are expressed in gravitational units ($GM = c = 1$), unless otherwise indicated.

			n_e (cm^{-3})		t_{Coul} (yr)		$L_{\mathrm{rad}}/L_{\mathrm{jet}}$	
Model	$\lambda_{\mathrm{mag}}/H_*$	Γ_{esc}	Sgr A*	M87	Sgr A*	M87	Sgr A*	M87
B..............................	0.0840	3.468	4.53×10^{4}	3.72×10^{3}	7.38×10^{3}	9.06×10^{4}	1.32×10^{-4}	1.26×10^{-2}
E..............................	0.0861	3.119	4.22×10^{6}	1.43×10^{3}	7.18×10^{1}	2.17×10^{5}	2.28×10^{-2}	9.01×10^{-3}
F..............................	0.0862	3.160	1.02×10^{7}	3.50×10^{3}	3.00×10^{1}	8.86×10^{4}	2.36×10^{-2}	9.36×10^{-3}

For the most part, these results essentially confirm those obtained by LB05 who found that Coulomb losses were negligible in the outflowing jet. This is due to the fact that these timescale values imply, that is if the jet travels at half or more the speed of light, the length of the jet will be thousands of parsecs long before energy is drained from the protons. The exception seems to be for Sgr A* in Models E and F, but that's due to fact that we were using a $\sim 2\times$ higher kinetic luminosity power L_{jet} estimated by a source different from Model 1 There's no telling if that estimated value for the jet power is indeed more correct than the one used in Model 1. Thus for the purpose of this work, we conclude that shock acceleration of the protons in the disk is sufficient to power the observed outflows without requiring additional energization in the jets.

Radiative losses from the disk are largely ignored here, which is justified for ADAF disks. LB05 illustrated this by estimating the total bremsstrahlung X-ray luminosity via integration of Equation (5.15b) from Rybicki & Lightman (1985) over the disk volume. The result obtained for pure, fully ionized hydrogen is

$$L_{\mathrm{rad}} = \int_{r_{\mathrm{S}}}^{\infty} 1.4 \times 10^{-27} T_e^{1/2} \rho^2 m_p^{-2} dV \ , \tag{4.10}$$

where T_e represents the electron temperature, and $dV = 4\pi r H dr$ denotes the differential volume element in cylindrical coordinates. Based on the assumption that the electron temperature is equal to the ion temperature T_*, we find for all three Models that $L_{\mathrm{rad}}/L_{\mathrm{jet}}$ ranges between $\sim 10^{-2} - 10^{-4}$ for either source (see Table 4.6 for more details). Even with the electron temperature being roughly three orders of magnitude lower than the ion temperature, due to X-ray luminosity being actually much lower than these values in a real ADAF disk, our new model further supports the justification for neglecting radiative losses.

4.2 Transport Solution

In the previous section we investigated particle acceleration in an inviscid ADAF disk with an isothermal shock. For a given source with a measured jet kinetic power $L_{\rm jet}$ and black hole mass M, we found that several flow solutions can be obtained for different values of the entropy ratio K_g/K_r for a specific diffusion parameter κ_0. We adopted the value of the downstream energy flux ϵ_+ for a given K_g/K_r and κ_0 to obtain the highest possible value of the Lorentz factor for the given model parameters of models 2 and 5 of LB05, which correspond to M87 and Sgr A* , respectively. The dynamical parameters for M, $\dot{M}$, etc. associated with Models A and B are listed in Tables 4.3. What follows in this section is almost the same analysis that was performed for Model 1 in LB07.

We implement the same bidirectional integration technique outlined in LB07 (Model 1) to solve for the eigenvalues λ_n from the boundary conditions (Equations 3.70 and 3.72). This process uses a Wronskian bisection method of the inner and outer solutions until they vanish at the matching radius situated in the post-shock region. After determining a particular value for λ_n, the matching coefficient a_n is then found using Equation (3.69). Consecutive repetitions of this process is done until a desired number of eigenvalues and eigenfunctions is obtained. For illustrative purposes, Figure 4.6 shows the sequences of eigenvalues associated with the parameters for Models A and B, as the corresponding free parameters l and κ_0 tie in to models 2 and 5, respectively, shown in Figure 3.2. Though, for the duration of this analysis, we will be using the results associated with Models B, E and F, as it was determined in the previous section that are considered the most self-consistent solutions of the six models used.

Like in LB07, $\lambda_1 \sim 4$ in all cases, maintaining that even with the inclusion of particle

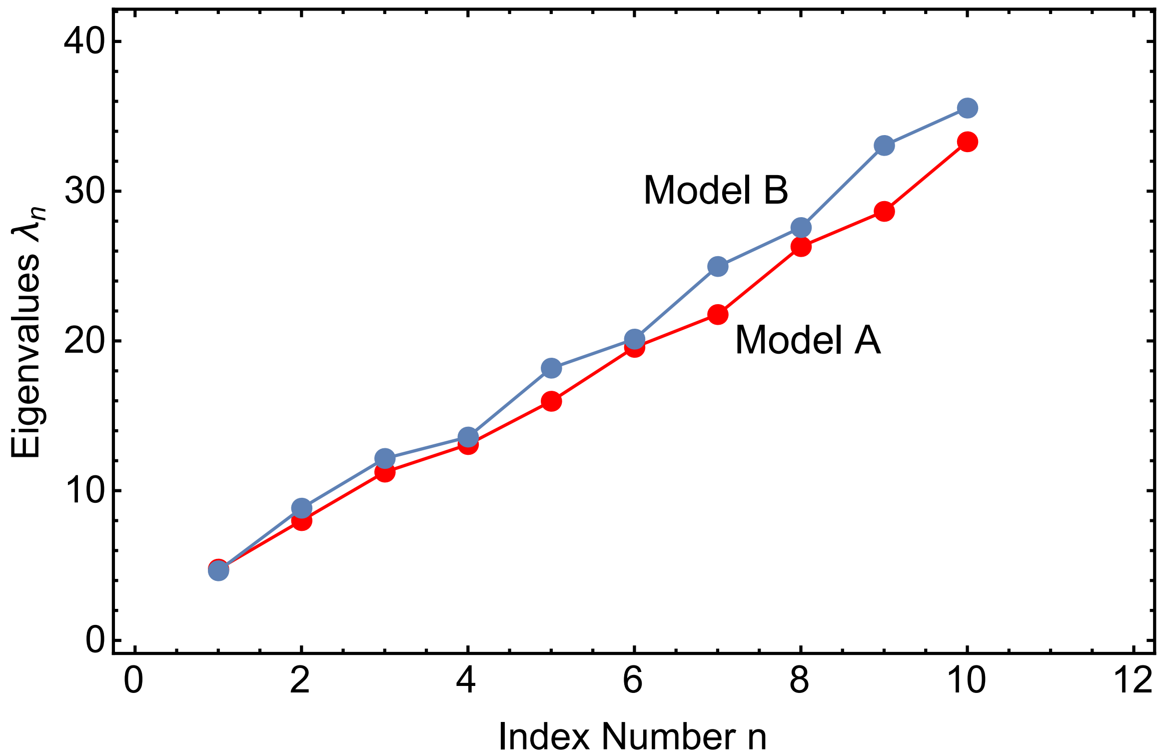

Figure 4.6: Eigenvalue plot for Models A and B.

pressure in the dynamical structure, the acceleration is indeed efficient and analogous with cosmic ray acceleration (see Blandford & Ostriker 1978, LB07). What's interesting is that unlike models 2 and 5 in LB07, the first two eigenvalues in Models B, E and F are $\lambda_1 = 4.05$ and $\lambda_2 = 4.76$, and $\lambda_1 = 4.32$ and $\lambda_2 = 4.80$, and $\lambda_1 = 4.06$ and $\lambda_2 = 4.78$, respectively. This is in contrast to LB07 where $\lambda_1 = 4.165$ and $\lambda_2 = 6.415$ and $\lambda_1 = 4.180$ and $\lambda_2 = 6.344$ for models 2 and 5, respectively. This suggests that at high energies the energy distribution is dominated by the first two eigenvalue λ_1 and λ_2, as the consecutive eigenvalues are all much larger. However, instead of a power-law slope for the energy distribution, λ_1 suggests that the slope is much flatter, and its value comes close to the limit given by $\lambda_{\max} = 4$.

4.2.1 Numerical Solutions for the Eigenfunctions

Computing the Green's function $f_{\mathrm{G}}(E, r)$ comes first from solving the eigenvalues λ_n and the eigenfunctions $Y_n(r)$ outlined in Ch. 3 and implementing the orthogonality of the eigenfunctions. Afterwards, we compute the expansion coefficients b_n (with either positive or negative signs) in order evaluate $f_{\mathrm{G}}(E, r)$ via the eigenfunction expansion (Equation 3.78),

$$f_{\mathrm{G}}(E, r) = \sum_{n=1}^{N_{\max}} b_n Y_n(r) \left(\frac{E}{E_0}\right)^{-\lambda_n} \quad , \quad E \geq E_0 \ , \tag{4.11}$$

where $N_{\max}$ is determined by analyzing the term-by-term convergence in the series, and $E \geq E_0$, otherwise $f_{\mathrm{G}}(E, r) = 0$ since there's no deceleration process included in this particle transport model. Before in LB07, it was determined that a higher value of $N_{\max}$ used in the numerical examples would generally yield an accuracy of at least three decimal places. However in our work, the accuracy from$N_{\max}$ is dependent on radius. As an example, the fundamental asymptotic solutions G^{in} and G^{out} are compared with the asymptotic solutions g^{in} and g^{out} for Model B with $n = 1$ in Figure 4.7. The agreement between the G and g functions confirms the continued validity of the asymptotic relations employed near the event horizon and at large radii. The global solution for the first eigenfunction Y_1 is also included in Figure 4.7 for Model B. Even with the inclusion of relativistic particles, a derivative jump at the shock location is visible in the global solutions, as stated in Equation (3.64). The analysis given in Figure 4.7 remains valid for Models E and F as well.

4.2.2 Green's Function Particle Distribution

Just like what was done in LB07, we can combine our results for the eigenvalues, eigenfunctions, and expansion coefficients in order to calculate the Green's function $f_{\mathrm{G}}(E, r)$ using Equation (4.11). This can be seen in Figure 4.8 which is a plot of $f_{\mathrm{G}}(E, r)$ as a function of the particle energy E at various radii r in the disk for Models B, E and F, respectively. It remains that at the injection energy ($E = E_0$) that the Green's function is equal to zero everywhere except at the shock location ($r = r_*$), as stated in Ch. 3, due to the particles being rapidly accelerated after being injected. As such, due to the similar structure of Figure 5 in LB07, we can likewise make the conclusions obtained in § 4.2: in which the particle acceleration in the disk is highly efficient, which can be seen from the relatively flat slope of the Green's function above the turnover. Also, even with the inclusion of relativistic particle pressure, only a small fraction of the particles diffuse upstream to larger radii, in which Figure 4.8 shows via the strong attenuation of the particle spectrum with increasing r. Though what remains different, as first seen with the mean energy distribution plotted in Figure 4.5, is that the particles in the inner region ($r < r_*$) appear to no longer exhibit the greatest overall energy gain. This is the first indication that with the introduction of relativistic particles, there's a greater flow of energy coming inward in which a lot of it is lost through the multiple shock crossings, yet the particles maintain a strong compression flow near the event horizon.

One other point of interest is exploring the expansion coefficients b_n (see Equation 3.82) for each of the three models when compared to those obtained for models 2 and 5 of LB07. These results are tabulated in Table 4.7. The results for the first two expansion functions indicate that the second eigenfunction actually dominates over the first eigenfunction at low energies. This can likewise be seen in Figure 4.9 which shows (at the shock radius $r = r_*$) that the first eigenvalue does not become dominant until at higher energies.

4.2.3 Number and Energy Density Distributions

We continue by following § 4.3 of LB07 in which we generate results for the Green's function $f_{\rm G}(E, r)$ by summing the eigenfunctions based on radius using Equation (4.11). At which point, once the Green's function energy distribution is determined for that radius, it can be integrated with respect to the particle energy E to obtain the corresponding values for the number and energy densities This is exactly the same as the term-by-term relations

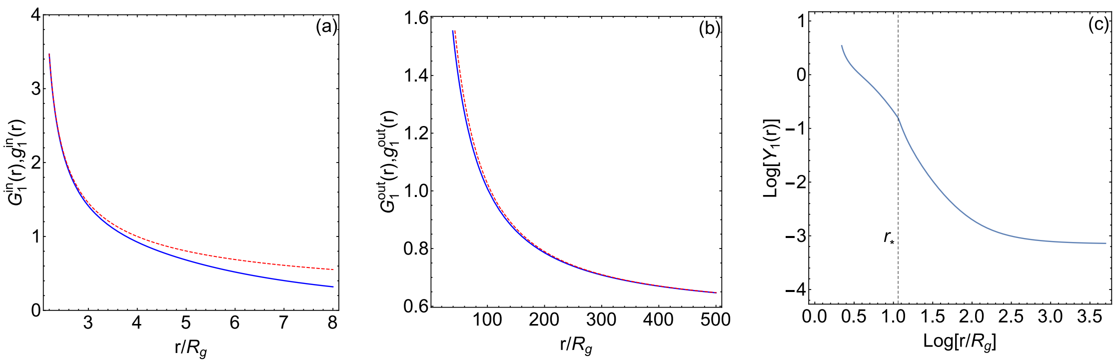

Figure 4.7: Similar to Figures 3 and 4 of LB07: fundamental solutions to Equations (3.70) and (3.72), $G_1^{\rm in}(r)$ and $G_1^{\rm out}(r)$ (blue, solid lines), for Model B, compared with the corresponding asymptotic solutions $g_1^{\rm in}(r)$ and $g_1^{\rm out}(r)$ (red, dashed lines) in panels a and b, respectively. Likewise, the associated global solution for the first eigenfunction $Y_1(r)$ (see Equation 3.68) is plotted in panel c, with the shock location at $r = r_*$ is indicated.

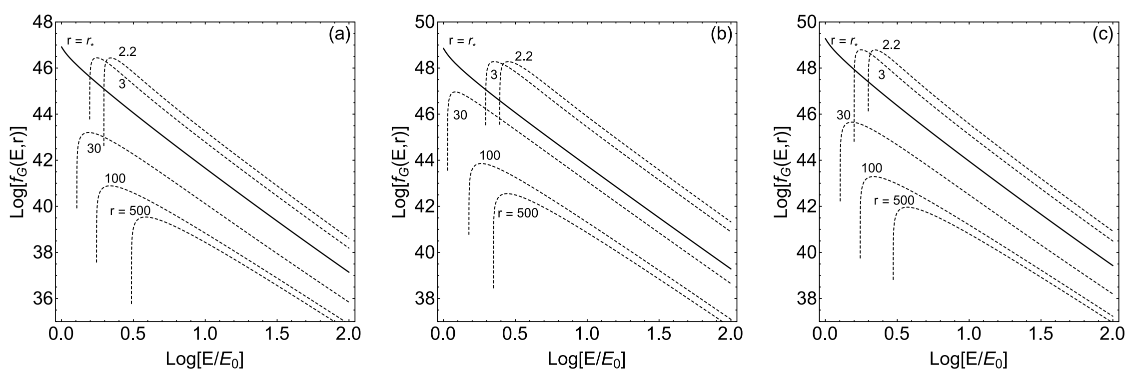

Figure 4.8: Similar to Figure 5 of LB07: results for the relativistic particle Green's function $f_{\rm G}(E, r)$ in units of ergs^{-3}cm^{-3}, computed using Equation (4.11) for (a) Model B, (b) Model E and (c) Model F. The value of the radius r in units of GM/c^2 is indicated for each curve, with $r = r_*$ denoting the shock location.

Table 4.7: Expansion coefficients (see Equation 3.82).

b_n	Model 2 (LB07)	Model 5 (LB07)	Model B	Model E	Model F
b_1	2.63×10^{47}	2.09×10^{47}	6.19×10^{45}	1.68×10^{49}	1.32×10^{48}
b_2	1.03×10^{48}	5.02×10^{47}	1.86×10^{47}	6.07×10^{49}	4.12×10^{49}
b_3	-8.85×10^{48}	-1.79×10^{48}	5.00×10^{47}	4.01×10^{50}	1.31×10^{50}
b_4	-2.93×10^{49}	-1.13×10^{49}	1.77×10^{48}	-1.81×10^{51}	4.95×10^{50}
b_5	1.89×10^{50}	2.84×10^{49}	-8.39×10^{48}	-1.06×10^{52}	-2.55×10^{51}
b_6	5.29×10^{50}	1.24×10^{50}	-3.02×10^{49}	4.96×10^{52}	-7.29×10^{51}
b_7	-2.74×10^{51}	-5.55×10^{50}	-2.26×10^{49}	2.12×10^{53}	1.02×10^{52}
b_8	8.69×10^{51}	-9.36×10^{50}	4.27×10^{50}	-9.43×10^{53}	9.19×10^{52}
b_9	2.07×10^{52}	5.25×10^{51}	1.87×10^{50}	-1.36×10^{54}	-1.29×10^{53}
b_{10}	-1.08×10^{53}	1.14×10^{52}	-3.54×10^{51}	1.02×10^{55}	-7.17×10^{53}

determined in Equation (51) of LB07,

$$n_r^{\rm G}\left(r\right) \equiv 4\pi E_0^3 \sum_{n=1}^{N_{\rm max}} \frac{b_n Y_n\left(r\right)}{\lambda_n - 3} \ ,$$

$$U_r^{\rm G}\left(r\right) \equiv 4\pi E_0^4 \sum_{n=1}^{N_{\rm max}} \frac{b_n Y_n\left(r\right)}{\lambda_n - 4} \ . \tag{4.12}$$

Equation (4.12) above is used primary for checking the self-consistency of our formalism, which is done by comparing the obtained values to those profiles of the number n_r and energy U_r densities determined in the previous section. In essence, our procedure for computing $f_{\rm G}(E,r)$ should produce results close enough to the dynamical profiles. The comparison for Model B is given in Figure 4.10, and likewise Figures 4.11 and 4.12 for Models E and F, respectively. Note that due that the close agreement between the two sets of results in all three models confirms the validity of the analysis involved in calculating the Green's function, much like it was done in LB07. More importantly, that given the new outer asymptotic relationship for Model 3, that Equation (4.11) still converges successfully with the $N_{\rm max}$ terms given for each radius in the series.

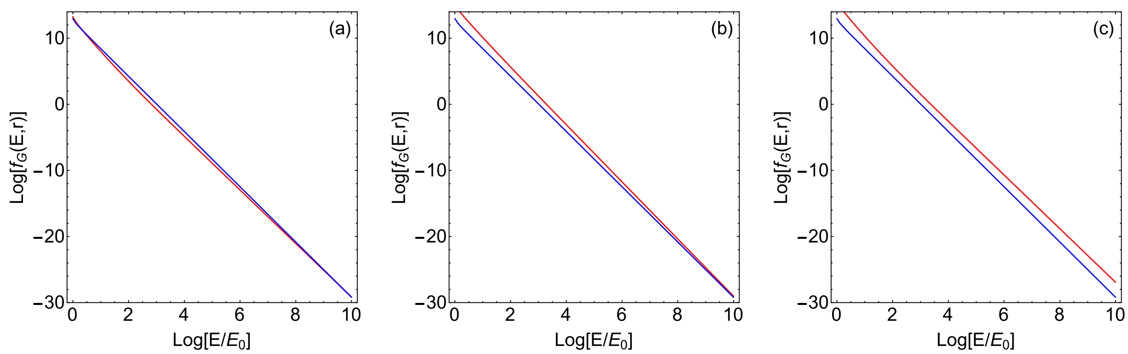

Figure 4.9: Exploration of the Green's function $f_{\rm G}(E,r)$ at the shock location $r = r_*$ across the energy range for (a) Model B, (b) Model E, (c) Model F.

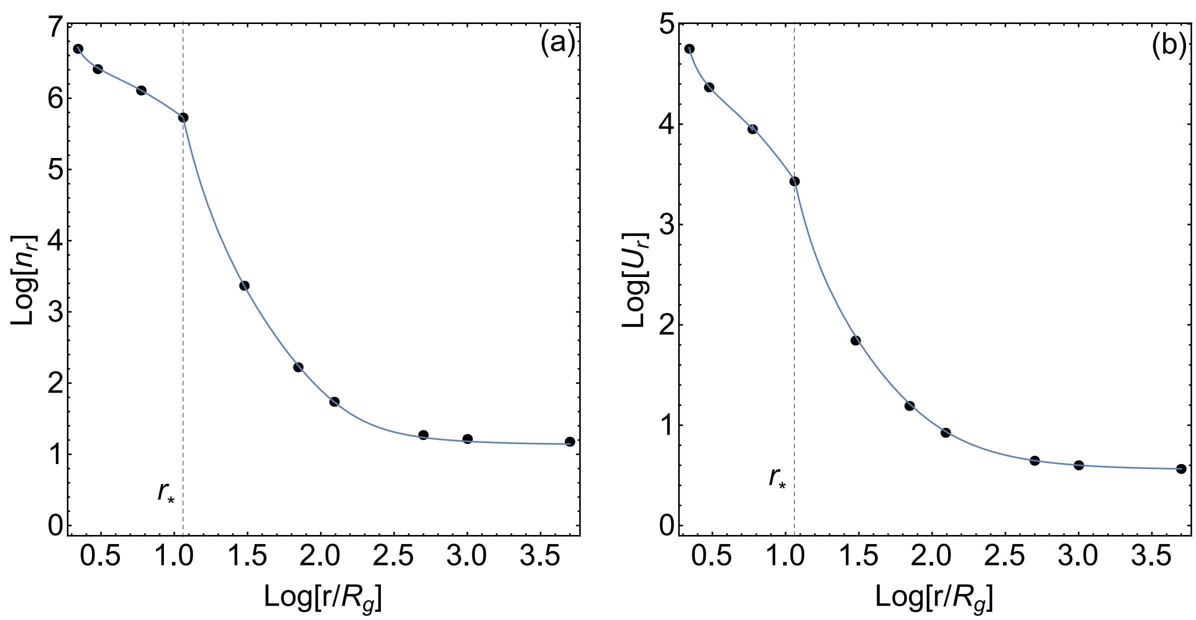

Figure 4.10: Similar to Figure 6 of LB07: plots of a) the relativistic particle number density and b) the relativistic particle energy density in cgs units for Model B. The solid lines are the dynamical profiles determined in the previous section, and the filled in circles represent the corresponding results obtained by integrating the Green's function via Equation (4.12), with the location of the shock radius $r = r_*$ indicated. It should be noted that with the introduction of relativistic particle pressure, there still remains a close agreement between the results, thus confirming the accuracy of our computational method.

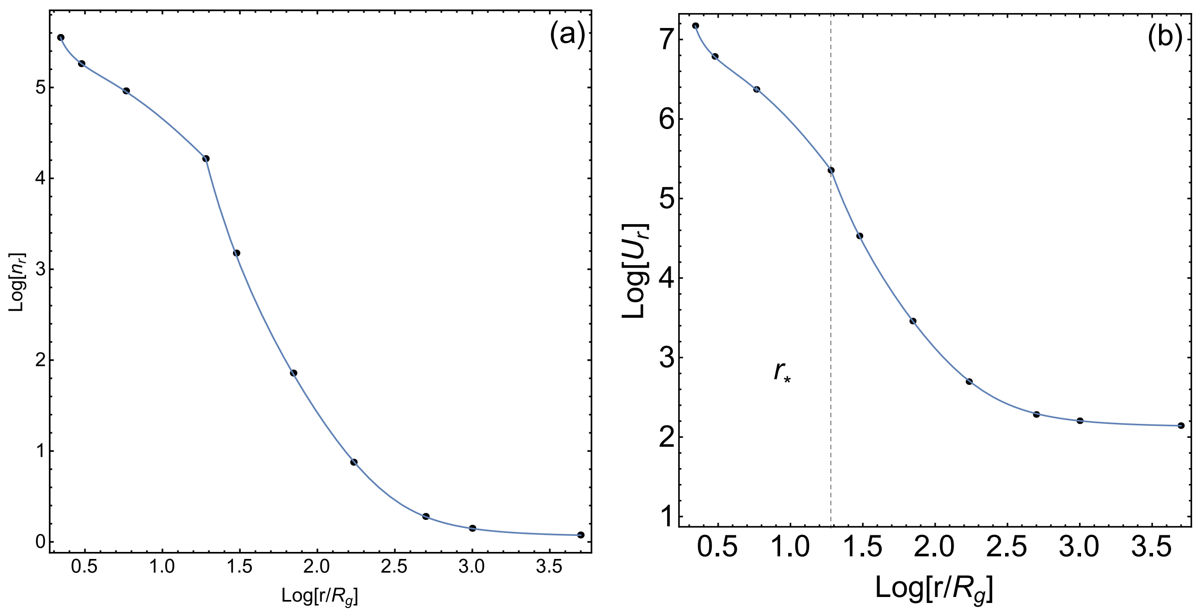

Figure 4.11: Same as Figure 4.10, but for Model E.

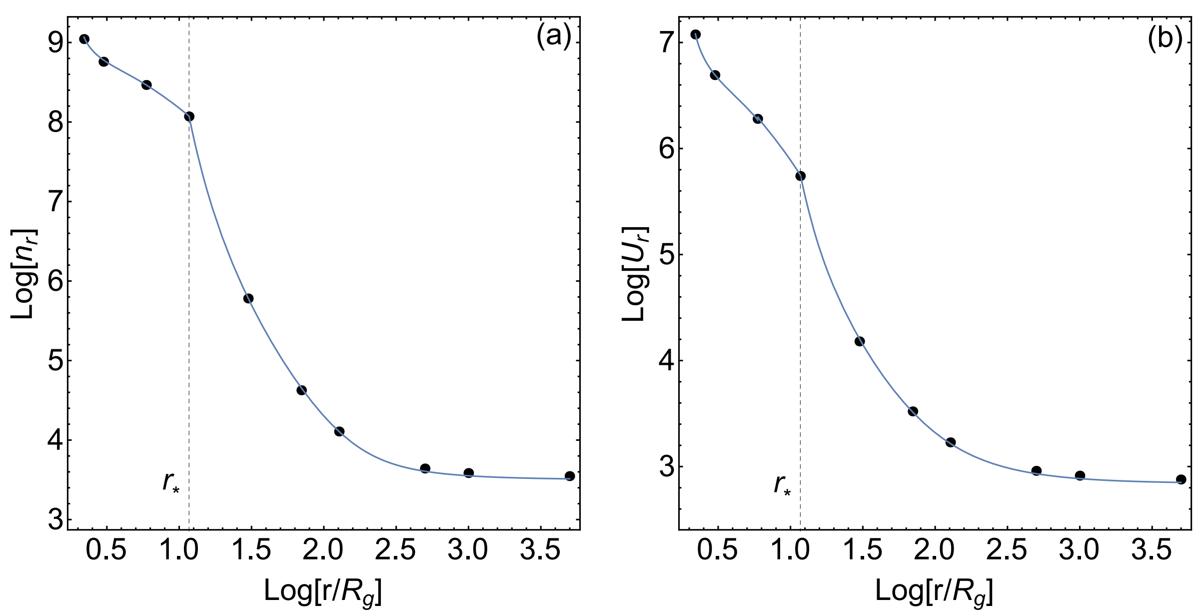

Figure 4.12: Same as Figure 4.11, but for Model F.

4.2.4 Escaping Particle Distribution

We close out this chapter by analyzing the escaping particle distribution, similar to § 4.4 of LB07. The energy spectrum of the escaping particles is computing using Equation (52) of LB07 (which is actually an integration of the escape term given in Equation 3.2),

$$\dot{N}_E^{\rm esc} = (4\pi E)^2 \, r_* H_* c A_0 f_{\rm G}(E, r_*) \ , \tag{4.13}$$

where $\dot{N}_E^{\rm esc} dE$ denotes the number of particles escaping from the disk per unit time with energies E and $E + dE$. The total number of particles escaping from the disk per second, $\dot{N}_{\rm esc}$, as well as the total energy escape rate, are related to the spectrum $\dot{N}_E^{\rm esc}$ via

$$\dot{N}_{\rm esc} = \int_0^\infty \dot{N}_E^{\rm esc} dE = 4\pi r_* H_* c A_0 n_* \ , \tag{4.14}$$

and

$$L_{\rm esc} = \int_0^\infty \dot{N}_E^{\rm esc} E dE = 4\pi r_* H_* c A_0 U_* \ , \tag{4.15}$$

where $n_* \equiv n_r(r_*)$ and $U_* \equiv U_r(r_*)$ represent the relativistic particle number and energy densities, respectively, at the shock location. The escaping particle distributions for Models B, E and F are plotted in Figure 4.13. One can see that the results vary due to the differences reported in the dynamical parameters for each model given in Tables 4.1, 4.2, 4.3 and 4.4. Just as was concluded in LB07, the values obtained for $L_{\rm esc}$ via Equation (4.15) agree well with those listed for $L_{\rm jet}$ in Table 4.4, thus confirming that our model satisfies global energy conservation. Likewise for the values obtained for Equation (4.14) when compared to those listed in Table 4.4. Thus, all of these tests confirm the validity of our new approach used to derive the Green's function given by Equation (4.11), which was very similar to that done for LB07.

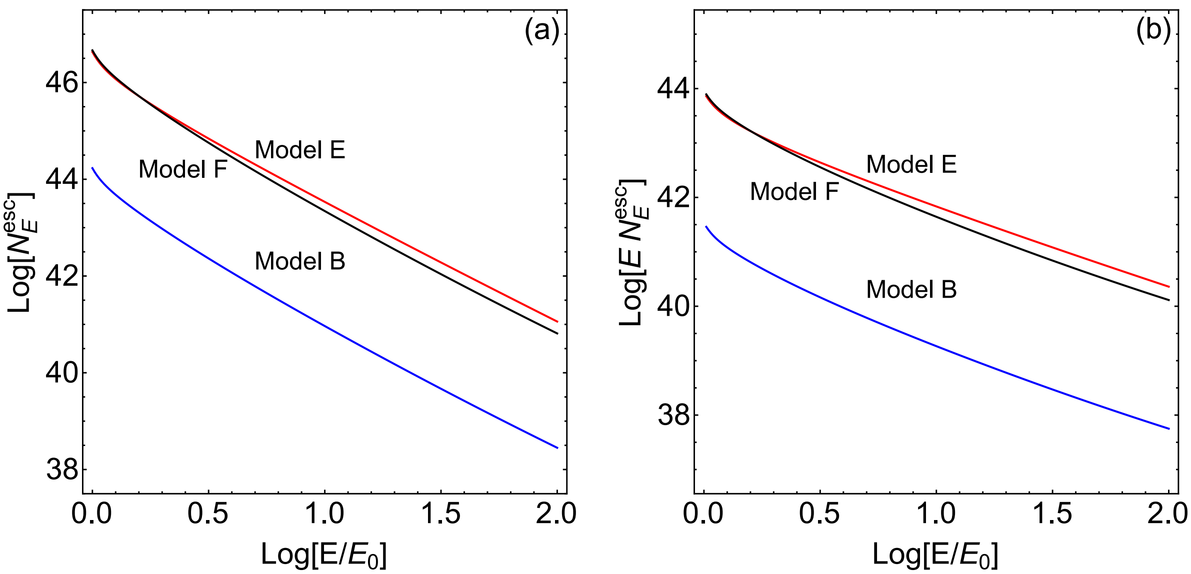

Figure 4.13: Plots of (a) the number distribution $\dot{N}_E^{\rm esc}$ and (b) the energy distribution $E\dot{N}_E^{\rm esc}$ for the relativistic particles escaping at the shock location, $r = r_*$ (see Equation 4.13). The curves are color-coded to represent each individual model.

Chapter 5: Observational Predictions

5.1 Overview

We close out this thesis by addressing the source for the spectral energy distribution (SED) observed for various black hole sources, or in this case the radio-loud sources such as M87. This is believed to be due to the jet's interaction with the surround gas in the torus as well as the outer lobes. The material behind this chapter doesn't care if the jet was from the shock-acceleration model or the electrodynamic model outlined in Ch. 1; that's all left in the disk context. What happens when the relativistic particles in the jet collide with the 'conceivably' stationary thermal particles in the intergalactic medium is a different story. This delves into areas of nuclear interactions and pair-production. For the purpose of this work, we'll assume that the only particles at work are the accelerated protons contained in the jet emanated from the disk.

As noted in § 1.5.3, energy emitted from the disk as well as the jet is known as primary radiation. When this radiation bombards with the surrounding gas and dust, the energy resulting from the nuclear reactions is known as secondary radiation. This has been covered in review (e.g. Eilek & Kafatos 1983, Barkov et al. 2012, Björnsson 1999, Dermer & Menon 2009) where the premise is simple: as the proton beam jets out from the disk in a cone-like formation with a semi-opening angle (θ, in radians), interaction with the surrounding gas creates a proton-proton (p-p) reaction and results in the creation of neutral and charged pions, represented as π^0, π^+ and π^-, respectively. Once these particles interact with other surrounding particles, the resulting pair-production of an electron and positron results in γ-ray emission. This overall process is illustrated in Figure 5.1. The γ-ray emission spectrum is one of the most observed quantities from AGNs, in which the secondary radiation makes considerable contribution. Though, it hasn't been fully understood how the dynamical processes may affect this energy spectrum. Thus, the purpose of this final chapter is to create a linear connection between our new diffusive two-fluid model to the production of the observed γ-ray spectrum; one which hasn't been done before as previous models only provided an *ad hoc* fit to observational data.

5.2 Preliminaries for Secondary Pion Production

Before we move into how we create the γ-ray spectrum, we must first figure out how we create the pions. The theoretical basis for this work will be a mix-match of various approaches from different authors, ones we feel are valid logistically, though they will be made suited to our Model 3. Turning first to basics, we note that neutral pions (π^0) generally decays into two γ-rays in its rest frame, $\pi^0 \to 2\gamma$. However, for p-p interactions, there's a more accurate formalism for this inelastic nuclear process,

$$p + p \to \pi^0 + X \to 2\gamma + X \ , \tag{5.1}$$

where X is everything else that could possibly be created in this collision (using Dermer & Menon 2009 terminology). This could even include the charged particles which decays through a muon to an electron (a positron or negaton, using Eilek & Kafatos 1983 terminology),

$$\pi^{\pm} \to \nu^{\pm} + \mu; \quad \nu^{\pm} \to e^{\pm} + 2\mu \ . \tag{5.2}$$

Next we move to Eilek & Kafatos (1983) where we define the average energy of a pion (of any charge) that arises in a p-p reaction as

$$\bar{\gamma} = 1 + (\gamma_p - 1)^{3/4} \ , \tag{5.3}$$

where γ_p is the Lorentz factor for the protons (or more specifically the jet, depending on the model). This was considered a good representation and fit to the data presented by

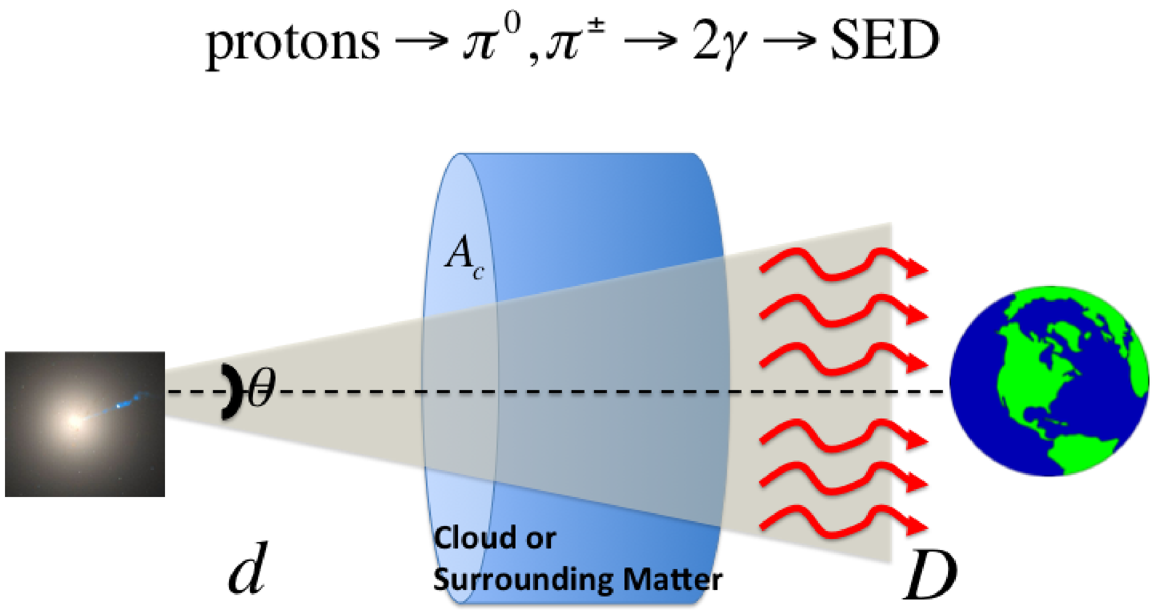

Figure 5.1: Schematic representation of secondary γ-ray production, as observed on Earth, from the jet.

Table 5.1: Neutral pion production cross sections used in calculation, from Eilek & Kafatos (1983).

$\pi^0 : \Sigma_{\pi^0}(\gamma_p) = 1.4 \times 10^{-26} (\gamma_p - 1)^{7.375}\ \mathrm{cm}^2$,	$(\gamma_p < 2)$
$\pi^0 : \Sigma_{\pi^0}(\gamma_p) = 8.4 \times 10^{-27} \gamma_p^{0.75}\ \mathrm{cm}^2$,	$(\gamma_p > 2)$

Ramaty and Lingenfelter (1966) with energies above a few GeV, even though there was a slight error in low γ_p. Keeping with Eilek & Kafatos (1983), we shall write $\bar{\gamma}_\pi = g(\gamma_p)$ generally, in which we use Equation (5.3) for its simplicity. Therefore, Equation (5.3) can be redefined as,

$$g(\gamma_p) = \bar{\gamma}_\pi = 1 + (\gamma_p - 1)^{3/4} \ . \tag{5.4}$$

Moving forward, Eilek & Kaftans (1983) defined the cross section for pion production as,

$$\sigma_\pi(\gamma_\pi, \gamma_p) = \Sigma_\pi(\gamma_p)\, \delta\left[\gamma_\pi - g(\gamma_p)\right] \ , \tag{5.5}$$

where Σ_π is considered the magnitude of the cross section for species $\pi\left(\pi^+,\ \pi^0,\ \text{or}\ \pi^-\right)$. Σ_π has been assigned specific functions of γ_p, depending on the π species in question, and are listed in Table 5.1. Of interest to us in Equation (5.5) is the δ-function, in which we can use it to define a function for the Lorentz factor of the protons γ_p in terms of that for the pions γ_π. Referring back to Equation (5.4) and setting $g(\gamma_p) = \gamma_\pi$, we can see that

$$\gamma_p = (\gamma_\pi - 1)^{4/3} + 1 \ . \tag{5.6}$$

It should be noted that the energy of the protons E from the jet, as well as the injection energy E_0 at the shock, is related to the Lorentz factor via

$$E = E_p = \gamma_p m_p c^2 \ , \quad E_0 = \gamma_{p,\tau} m_p c^2 \ , \tag{5.7}$$

where $\gamma_{p,\tau}$ is defined as the threshold Lorentz factor for the protons. From this, we can define the derivative for the energy of the protons as

$$dE = m_p c^2 d\gamma_p \ . \tag{5.8}$$

Considering that in our work we've defined $E_0 = 0.002$ ergs, this correlates to a $\gamma_{p,\tau} = 1.33959$, which is < 1.37 the value determined for the data mentioned in Eilek & Kafatos (1983).

The production of the secondary quanta (photons and electrons) outlined in Eilek & Kafatos (1983) was determined with the pion production rate per target proton $q_\pi(\gamma_\pi)$, in units of (s^{-1} per proton), which was also a function of an isotropic proton flux, $I_p\left(\gamma_p\right)$ ($\mathrm{cm}^{-2}\ \mathrm{s}^{-1}\ \mathrm{sr}^{-1}\ \mathrm{erg}^{-1}$). For our work, we set the isotropic proton flux $I_p\left(\gamma_p\right)$ in units of ($\mathrm{cm}^{-2}\ \mathrm{s}^{-1}$), where it won't be applied to the pion production rate $q_\pi(\gamma_\pi)$. Instead, it ties back into the dynamical equations established in Ch. 4, specifically the number of particles escaping from the disk per unit time per unit energy $\dot{N}_E^{\mathrm{esc}}$ (Equation 4.13),

$$\dot{N}_E^{\mathrm{esc}}(E) = (4\pi E)^2 r_* H_* c A_0 f_{\mathrm{G}}\left(E, r_*\right) \sim \mathrm{ergs}^{-1}\,\mathrm{s}^{-1} \ . \tag{5.9}$$

For us, we define the isotropic proton flux as

$$I_p\left(\gamma_p\right) = \frac{\dot{N}_E^{\mathrm{esc}}(E = E_p = \gamma_p m_p c^2)}{A_{\mathrm{c}}} \sim \mathrm{ergs}^{-1}\,\mathrm{cm}^{-2}\,\mathrm{s}^{-1} \ , \tag{5.10}$$

where A_{c} is defined as the surface area of the cloud/gas coming in contact with the jet (considered a constant). Referring to a similar model for M87 (see Barkov et al. 2012), we define this area as

$$A_{\mathrm{c}} = \pi R^2 = \pi d^2 \theta^2 \ , \tag{5.11}$$

where d is the distance of the jet from the disk to the cloud (or known as the distance from the SMBH at which the cloud crosses the jet). It should be noted that we are defining the isotropic proton flux as a function of the proton Lorentz factor $I_p(\gamma_p)$, but since the number of particles escaping from the disk per unit time per unit energy is a function of energy $\dot{N}_E^{\rm esc}(E)$, we therefore substitute Equation (5.7) into Equation (5.10) to indicate that now $\dot{N}_E^{\rm esc}(\gamma_p m_p c^2)$. In order to solve Equation (5.10), we can substitute in Equation (5.11) and redefine the relation with the respective derivative on both sides,

$$I_p(\gamma_p)\, d\gamma_p = \frac{\dot{N}_E^{\rm esc}(\gamma_p m_p c^2)}{\pi d^2 \theta^2} dE \sim \mathrm{cm}^{-2}\,\mathrm{s}^{-1} \ , \tag{5.12}$$

which when combined with Equation (5.8) becomes,

$$I_p(\gamma_p) = \frac{\dot{N}_E^{\rm esc}(\gamma_p m_p c^2) m_p c^2}{\pi d^2 \theta^2} \ . \tag{5.13}$$

5.3 Pion Production

This work considered two possible scenarios for pion production when the jet hit the cloud, one where there was pure neutral pions produced, and another where both neutral and charged pions were produced. Pure neutral pion-production is more of an ideal case, whereas the neutral-charged pion-production scenario is considered more realistic. Either way, both scenarios incorporate a concept in particle physics of the probability $\mathcal{P}$ of surviving interaction and making it out of the cloud. Figure 5.2 shows the overall system of the jet hitting the cloud of length L_0, where we denote Q_0 as the number of protons incident onto the cloud from the jet, and n_p as the proton number density (target proton per cm^3).

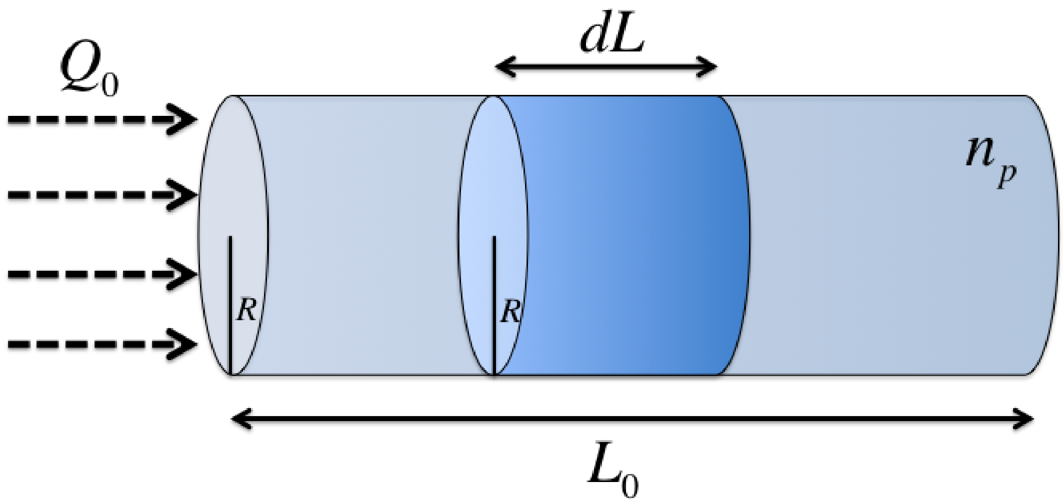

Figure 5.2: Cross-section of the Jet hitting the Cloud.

5.3.1 Probability for Pure Neutral Pion Production

Here, we can use dimensional analysis to determine the derivative of the probability of neutral pions surviving within an infinitesimal area (blue section of Figure 5.2) as

$$d\mathcal{P} = \frac{A_c dL n_p \sigma_{\pi^0}}{A_c} \ , \tag{5.14}$$

where σ_{π^0} is the cross section for only neutral pions. The probability relates to the number of protons Q as

$$dQ = -Q\left(L\right) d\mathcal{P} \ , \tag{5.15}$$

which when combined with Equation (5.14), we get the number of protons through the cloud as a function of L for the neutral pions,

$$Q\left(L\right) = Q_0 e^{-n_p \sigma_{\pi^0} L} \ . \tag{5.16}$$

The survival probability is actually defined as the ratio between the number of protons incident through a portion of the cloud Q and all of it Q_0,

$$\mathcal{P}_{\text{survive}}\left(L_0\right) = \frac{Q\left(L\right)}{Q_0} = e^{-n_p \sigma_{\pi^0} L_0} \ . \tag{5.17}$$

Therefore the probability for pure neutral pion production is given as

$$\mathcal{P}_{\pi^0}\left(L_0\right) = 1 - \mathcal{P}_{\text{survive}} = 1 - e^{-n_p \sigma_{\pi^0} L_0} \ . \tag{5.18}$$

5.3.2 Probability Regarding the Neutral and Charged Pions

In the previous section we worked out the correct approach for pure neutral pion production (that is, neglecting charged pion production). In this section, we include the effect of charged pion production, which removes protons from the incident beam without producing gamma-rays. In this instance, charged pion production really becomes a pure attenuation effect rather than a source of gamma-rays. But in order to correctly compute the gamma-ray spectrum, we do need to include this attenuation resulting from charged pion production. In essence, we are accounting for the attenuation of the charged particles in the survival probability for the neutral pions (Equation 5.17).

To do this, we need to start from the beginning. What we really end up doing is changing Equation (5.14) to include the charged pions,

$$d\mathcal{P} = \frac{AdLn_p}{A}\left(\sigma_{\pi^0} + \sigma_{\pi^+} + \sigma_{\pi^-}\right) \ , \tag{5.19}$$

where σ_{π^+} and σ_{π^-} denote the cross sections for the positively and negatively charged pions, respectively. So now, the probability is related to the number of protons Q via

$$dQ = -Q\left(L\right)d\mathcal{P} = -Q\left(L\right)n_p\left(\sigma_{\pi^0} + \sigma_{\pi^+} + \sigma_{\pi^-}\right)dL \ , \tag{5.20}$$

which when combined with Equation (5.19) now allows the number of protons through the cloud to consider all forms of pions that can be produced,

$$Q\left(L\right) = Q_0 e^{-n_p\left(\sigma_{\pi^0}+\sigma_{\pi^+}+\sigma_{\pi^-}\right)L} \ . \tag{5.21}$$

So now, the probability that an incident proton survives without suffering some kind of pion-producing event is given as,

$$\mathcal{P}_{\text{survive}}\left(L_0\right) = \frac{Q\left(L\right)}{Q_0} = e^{-n_p\left(\sigma_{\pi^0}+\sigma_{\pi^+}+\sigma_{\pi^-}\right)L_0} \ . \tag{5.22}$$

However, we are not done yet. See we cannot just follow like Equation (5.18) and assume that the probability that the incident proton doesn't survive is $1 - \mathcal{P}_{\text{survive}}$, the probability

Table 5.2: Coefficients for the high-energy asymptotic inclusive cross sections for pion productions in $p-p$ collisions. This is essentially Table 8.1 of Dermon & Menon 2009.

X	a_π	b_π	c_π
π^+	32	48.5	59.5
π^0	27	57.9	40.9
π^-	28.2	74.2	69.3

that some kind of pion is produced from a single incident proton. We have to take into consideration that in this new regime that there are now three possible pions that can be produced. Which means that the probability that an incident proton produces a neutral pion has to take into account charged pion attenuation given by,

$$\sigma_{\pi^0_{\mathrm{ATT}}} = \left(\frac{\sigma_{\pi^0}}{\sigma_{\pi^0} + \sigma_{\pi^+} + \sigma_{\pi^-}} \right) . \tag{5.23}$$

In other words, the neutral pion production is offset by the decay branching ratios for the charged particles. Thus, the new probability for neutral pion production is defined as

$$\mathcal{P}_{\pi^0}\left(L_0\right) = \left[1 - e^{-n_p\left(\sigma_{\pi^0}+\sigma_{\pi^+}+\sigma_{\pi^-}\right)L_0}\right] \left(\frac{\sigma_{\pi^0}}{\sigma_{\pi^0} + \sigma_{\pi^+} + \sigma_{\pi^-}} \right) . \tag{5.24}$$

It should be noted that the values for the cross sections of the pions can actually be defined in terms of the proton Lorentz factor (γ_p) given by (see Equation 8.55 of Dermon & Menon 2009),

$$\sigma_{\pi X}(\mathrm{cm}^2) = 10^{-27} \left(a_\pi \ln \gamma_p + \frac{b_\pi}{\sqrt{\gamma_p}} - c_\pi \right) , \tag{5.25}$$

with the corresponding values for the coefficients given in Table 5.2.

5.4 γ-ray Production

For gamma-ray production, note that the number of gamma-rays produced per second is twice the number of pions produced per second,

$$\dot{N}_\epsilon = 2\dot{N}_\pi \ . \tag{5.26}$$

From Equation (5.1), we know that the energy for the pions E_π is related to that for the gamma-rays ϵ via,

$$E_\pi = 2\epsilon \ . \tag{5.27}$$

Since the energy of the pions is related to its respective Lorentz factor via,

$$E_\pi = \gamma_\pi m_\pi c^2 \ , \tag{5.28}$$

thus we can combine this with Equation (5.27) to show

$$\gamma_\pi = \frac{2\epsilon}{m_\pi c^2} \ . \tag{5.29}$$

This comes in handy as the objective is to determine a relationship that's a function of energy rather than a Lorentz factor, which is common when plotting the gamma-ray energy flux. Let's now determine the energy flux for the gamma-ray production via dimensional analysis,

$$\frac{1}{\epsilon} F_\epsilon(\epsilon) \sim \mathrm{cm}^{-2}\,\mathrm{s}^{-1}\,\mathrm{erg}^{-1} \ . \tag{5.30}$$

It should be noted that since the particle number density is in units of $\sim \mathrm{s}^{-1}$, we can therefore use the above with Equation (5.26 to show (via dimensional analysis)

$$2\dot{N}_\pi d\gamma_\pi = \dot{N}_\epsilon d\gamma_\epsilon = \pi D^2 \theta^2 \frac{1}{\epsilon} F_\epsilon(\epsilon)\, d\epsilon \sim \mathrm{s}^{-1} \ , \tag{5.31}$$

where now we've defined D as the distance from Earth to the observed cloud. Focusing on the pion number density as a function of the gamma-ray energy,

$$2\dot{N}_{\pi} d\gamma_{\pi} = \pi D^2 \theta^2 \frac{1}{\epsilon} F_{\epsilon}\left(\epsilon\right) d\epsilon \sim \mathrm{s}^{-1} \ , \tag{5.32}$$

and noting from Equation (5.29) that,

$$d\epsilon = \frac{m_{\pi} c^2}{2} d\gamma_{\pi} \ , \tag{5.33}$$

thus the energy flux for the gamma-rays is derived as,

$$F_{\epsilon}\left(\epsilon\right) = \frac{4\epsilon \dot{N}_{\pi}\left(\gamma_{\pi} = \frac{2\epsilon}{m_{\pi} c^2}\right)}{\pi D^2 \theta^2 m_{\pi} c^2} \ , \tag{5.34}$$

where we note that $\dot{N}_{\pi}$ is a function of the gamma-ray energy ϵ via the relation given in Equation (5.29).

Next thing we need to do is determine the function of $\dot{N}_{\pi}$ itself in order to close this function completely. We derived this definition $\dot{N}_{\pi^0}\left(\gamma_{\pi^0}\right)$ ourselves using the probability relation for neutral pion production (Equation 5.24, which accounted for the charged-pion attenuation), as well as the isotropic proton flux (Equation 5.13) and dimensional analysis to show,

$$\begin{aligned} \dot{N}_{\pi^0}\left(\gamma_{\pi^0}\right) d\gamma_{\pi^0} = &\left(\frac{\sigma_{\pi^0}}{\sigma_{\pi^0} + \sigma_{\pi^+} + \sigma_{\pi^-}}\right) \left(1 - e^{-n_p\left(\sigma_{\pi^0} + \sigma_{\pi^+} + \sigma_{\pi^-}\right) L_0}\right) \\ &I_p\left(\gamma_p\right) d\gamma_p \mathrm{Min}\left[A_c, \pi\theta^2 d^2\right] \ , \end{aligned} \tag{5.35}$$

where A_c is the area of the cloud. The derivative for $d\gamma_p$ can be found from Equation (5.6) to show,

$$d\gamma_p = \frac{4}{3}(\gamma_{\pi^0} - 1)^{1/3} d\gamma_{\pi^0} \ , \tag{5.36}$$

which when combined with Equation (5.35) simplifies down to,

$$\begin{aligned} \dot{N}_{\pi^0}(\gamma_{\pi^0}) = \frac{4}{3}(\gamma_{\pi^0} - 1)^{1/3} \left(\frac{\sigma_{\pi^0}}{\sigma_{\pi^0} + \sigma_{\pi^+} + \sigma_{\pi^-}}\right) \left(1 - e^{-n_p\left(\sigma_{\pi^0} + \sigma_{\pi^+} + \sigma_{\pi^-}\right)L_0}\right) \\ I_p(\gamma_p) \, \mathrm{Min}\left[A_c, \pi\theta^2 d^2\right] \ . \end{aligned} \tag{5.37}$$

Thus, by combining Equation (5.37) with Equations (5.13) and (5.34), we simplify down the expression to

$$\begin{aligned} F_\epsilon(\epsilon) = \frac{16 m_p \epsilon}{3\pi^2 d^2 D^2 \theta^4 m_{\pi^0}} (\gamma_{\pi^0} - 1)^{1/3} \dot{N}_E^{\mathrm{esc}}(\gamma_p m_p c^2) \left(\frac{\sigma_{\pi^0}}{\sigma_{\pi^0} + \sigma_{\pi^+} + \sigma_{\pi^-}}\right) \\ \left(1 - e^{-\Sigma\left(\sigma_{\pi^0} + \sigma_{\pi^+} + \sigma_{\pi^-}\right)}\right) \mathrm{Min}\left[A_c, \pi\theta^2 d^2\right] \ , \end{aligned} \tag{5.38}$$

where $\Sigma = n_p L_0$ is known as the column density of the cloud. We can also refer back to Equation (5.9) to simplify this down even further to,

$$\begin{aligned} F_\epsilon(\epsilon) = \frac{256 m_p^3 r_* H_* c^5 A_0 \epsilon}{3 d^2 D^2 \theta^4 m_{\pi^0}} \mathrm{Min}\left[A_c, \pi\theta^2 d^2\right] (\gamma_{\pi^0} - 1)^{1/3} (\gamma_p)^2 f_{\mathrm{G}}\left(\gamma_p m_p c^2, r_*\right) \\ \left(\frac{\sigma_{\pi^0}}{\sigma_{\pi^0} + \sigma_{\pi^+} + \sigma_{\pi^-}}\right) \left(1 - e^{-\Sigma\left(\sigma_{\pi^0} + \sigma_{\pi^+} + \sigma_{\pi^-}\right)}\right) \ . \end{aligned} \tag{5.39}$$

Note that in the previous Equation, we will need to switch from $\gamma_p \to \gamma_{\pi^0} \to 2\epsilon/m_{\pi^0}c^2$ by Equations (5.6) and (5.29) in order to correctly calculate $F_\epsilon(\epsilon)$. Also, in order to avoid problems in the calculation, we set $\epsilon > m_{\pi_0}c^2/2$.

Now, in order to analyze the results obtained from Barkov et al. (2012), what we want to do first is plot $\epsilon \times F_\epsilon(\epsilon)$ $\left(\mathrm{erg\ cm^{-2}\ s^{-1}}\right)$ vs. $\epsilon\,(\mathrm{erg})$, however it should be noted that the goal is to achieve $\epsilon \times F_\epsilon(\epsilon)$ $\left(\mathrm{erg\ cm^{-2}\ s^{-1}}\right)$ vs. $\epsilon\,(\mathrm{eV})$. The problem is that this kind of figure (even on a log scale) is linear rather than what was obtained in that work. But that's alright as this serves primarily as a preliminary result for future work, in which we can apply either Models B, E or F from Ch. 4 to observe the secondary γ-ray radiation produced when the jet interacts with the surrounding cloud. Applying Model F results to Equation (5.39) for an arbitrary set of input values ($\Sigma = 10^{13}$ cm^{-2} and $A_c = 10^{9.4}$ cm^2) and those given in Barkov et al. (2012), we can fit our model to their computed SED for secondary pp gamma rays (see Figure 5.3), which matches well with the VHE data points taken from Aliu et al. (2012). This analysis can be done as well either Model B or Model E, since the secondary radiation produced doesn't care how the jet is created before it interacts with the surrounding cloud.

It should be noted that Barkov et al. (2012) were not able to derive predictions in the radio spectrum due to the particle's energy evolution timescale being either longer, or very sensitive to the dynamical evolution of the cloud. They stuck to X-ray emission. Our model fit to the data is based on the results from a radio-loud source, and thus we can show that the micro-processes occurring in the accretion disk can be used to derive predictions for secondary pp γ-ray energy production. However, we currently cannot account for the downward curve in the lower energy spectrum, which according to Barkov et al. (2012) occurs when pp collisions become optically thin to where the gamma rays reach their maximum after a sharp rise. At which point, pp collisions become strongly inefficient quenching the gamma-ray emission, explaining the drop of the gamma-ray flux, which can also be more abrupt due to $\gamma\gamma$ absorption. At the present time further study would need to be done to further explore these results.

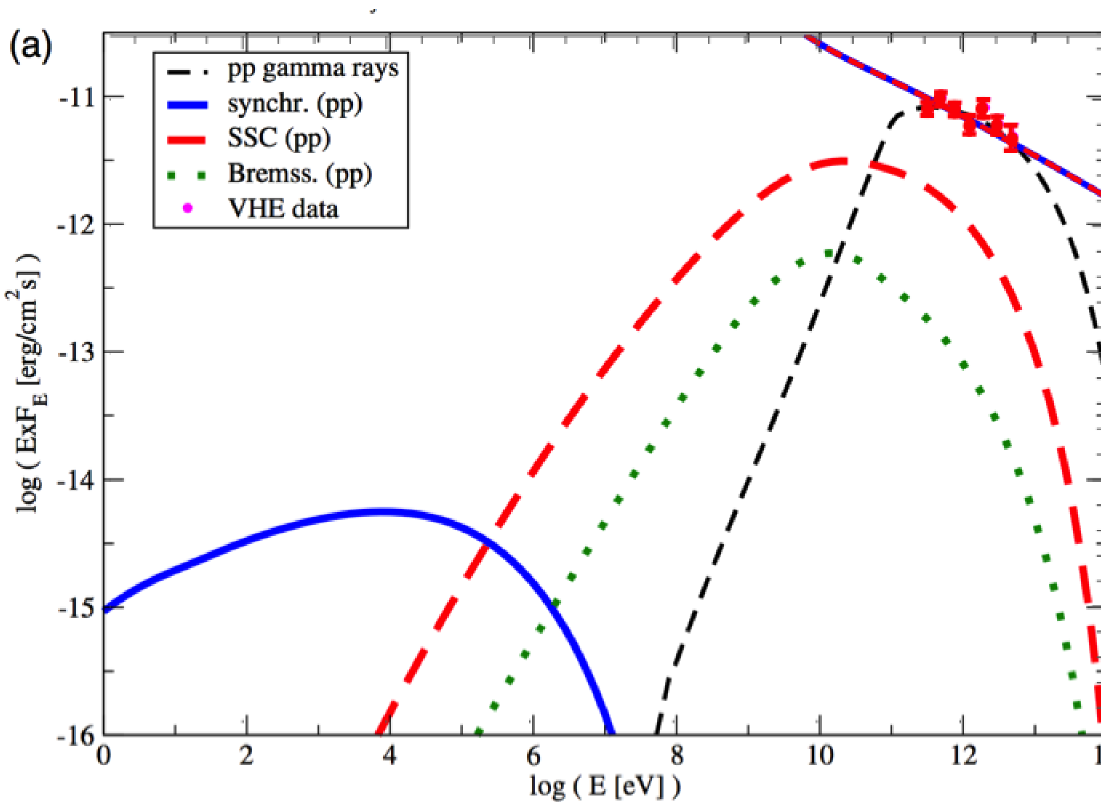

Figure 5.3: Superposition of our secondary radiation model to Figure 6a of Barkov et al. (2012) for M87. The primary focus is our model fit (blue-red line) to their computed SED for secondary *pp* gamma rays (black dashed line), which matches the VHE data points taken from Aliu et al. (2012).

Chapter 6: Conclusion

In this dissertation I have developed the first self-consistent model for the accretion hydrodynamics and the particle acceleration occurring in an inviscid black hole accretion disk. In particular, this is the first time that the 'test particle' approximation has been relaxed in studies of black hole accretion. My results show that particle acceleration at a standing, isothermal shock in an ADAF accretion disk can give relativistic protons the energy needed to power the outflows observed from radio-loud sources containing black holes. The work presented here is a modified, improved version of the model created in LB04 and LB05, which now includes relativistic particle pressure and diffusion, and is self-consistent with the dynamical results. This allows us to show the dynamical structure of the transonic flow to be self-consistent with the relativistic particle transport occurring in the disk. Since energy conservation is enforced, our model ensures that the energy lost from the background gas at the shock will result in the acceleration of some background particles to relativistic energies. Plus, it continues to support the concept of first-order Fermi acceleration in shock waves by providing a single, coherent explanation for the disk structure and the formation of the outflow.

The existence of shocks in viscous disks is a controversial issue, and it's been suggested that shock formation is possible (provided the viscosity is relatively low) by several studies. Our new inviscid model clearly indicates that a smooth-shock solution is *impossible* when particle pressure and diffusion are included in the dynamical structure. It should be noted that the dynamical profiles shown here are universal and can applied to any AGN from their known jets and masses.

Our work is in analogy with the 'cosmic-ray modified shock' scenario for cosmic-ray acceleration. It has been shown here in our new model that the pressure of the accelerated particles is comparable to that of the thermal background gas, in contrast with the earlier investigations, which adopted the 'test particle' approximation (e.g., Blandford & Ostriker 1978). In fact, we have shown that an inclusion of relativistic particles and diffusion affect the width of the shock thickness in the dynamical profiles, allowing for a precursor deceleration into the shock, compared to the discontinuous jump seen in previous models. Our result that the two pressures are comparable near the shock agrees with the results of Axford et al. (1977) and Becker et al. (2011).

Here we have shown that the total pressure is not dominated by the pressure of the background (thermal) gas throughout most of the disk, due to the fact that the particles injected at the shock have a very large chance of diffusing to large distances from the black hole. We have shown that a larger relativistic particle population and smaller diffusion effect will result in higher relativistic outflows, achieving a maximum Lorentz factor of $\Gamma_{\rm esc} \sim 3.5$, which is consistent with AGN observations. The lower value of $\Gamma_{\rm esc}$ in our new two-fluid model not only indicates that relativistic particle pressure is comparable to the gas pressure at the shock, but also that its inclusion in the dynamical profiles will create a softer particle spectrum than in Model 1 (LB04; LB05), as it was determined in the cosmic-ray models.

The results obtained in this new model continue to confirm the general properties of the jets observed in M87 and Sgr A* , particularly the terminal Lorentz factors and total powers comparable to those observed in those AGNs. Likewise, the preliminary secondary γ-ray spectrum agrees with the observed TeV spectrum for M87. However, higher efficiencies can be achieved by varying the downstream energy transport rate, the specific angular momentum, the diffusion constant and the entropy ratio, which are the fundamental free parameters in our model. The buildup of the particle pressure in such high-efficiency situations justifies our relaxation of the test particle approximation.

Much like LB05, we too shall continue this work by developing a self-consistent viscous disk model in order to explore shock formation and particle acceleration more realistically since viscosity plays a key role in determining the structure of an actual accretion disk. We expect that the inclusion of viscosity will not significantly alter the conclusions reached in this work since significant particle acceleration will occur regardless of the level of viscosity if a shock is present. In particular, we will reexamine the question of whether smooth flow is possible when particle diffusion and viscosity are both included. We conclude that our coupled, self-consistent theory for the disk structure and the particle acceleration provides for the first time a completely self-consistent explanation for the outflows observed in many radio-loud systems containing black holes.

Appendix A: Deriving the Total Energy Transport Equation

The purpose of this section is to derive the total energy transport equation. The goal is to show that from the total energy density U_{tot},

$$U_{\text{tot}} = U_g + U_r - \frac{GM\rho}{R - R_{\text{S}}} + \frac{1}{2}\rho\vec{v} \cdot \vec{v} \ , \tag{A.1}$$

the following relationship is valid,

$$\frac{\partial U_{\text{tot}}}{\partial t} = -\vec{\nabla} \cdot \vec{F}_{\text{tot}} \ , \tag{A.2}$$

where

$$\vec{F}_{\text{tot}} = (U_g + P_g)\,\vec{v} + (U_r + P_r)\,\vec{v} - \frac{GM\rho\vec{v}}{R - R_{\text{S}}} + \frac{1}{2}\rho\,(\vec{v} \cdot \vec{v})\,\vec{v} - \kappa\vec{\nabla}U_r \ , \tag{A.3}$$

is the total energy flux, U_g and U_r, as well as P_g and P_r, represent the internal energy densities and pressures for the thermal and relativistic particles, respectively, G is the gravitational constant, M is the mass of the celestial object (black hole source), R represents the distance between two objects of force, $R_{\text{S}} = 2GM/c^2$ is the Schwarzschild radius, ρ is the volumetric fluid mass density, $\vec{v}$ is the vector bulk velocity (considered positive for inflowing particles), and κ represents the diffusion coefficient (Equation (2.48)). It should be noted that the general form of the total energy flux $\vec{F}_{\text{tot}}$ is given as

$$\vec{F}_{\text{tot}} = \gamma U\vec{v} - \frac{GM\rho\vec{v}}{R - R_{\text{S}}} + \frac{1}{2}\rho\,(\vec{v} \cdot \vec{v})\,\vec{v} - \kappa\vec{\nabla}U_r \ , \tag{A.4}$$

where $\gamma U = \gamma_g U_g + \gamma_r U_r$ represents the total energy density of Model 3 as a linear combination of the thermal and relativistic particle energy densities, respectively, multiplied by their respective adiabatic index of heat γ.

First let's define the full Lagrangian derivatives for the thermal U_g and relativistic U_r energy densities,

$$\frac{DU_r}{Dt} = \frac{\gamma_r U_r}{\rho}\frac{D\rho}{Dt} - \vec{\nabla}\cdot\left(-\kappa\vec{\nabla}U_r\right) \ , \qquad \frac{DU_g}{Dt} = \frac{\gamma_g U_g}{\rho}\frac{D\rho}{Dt} \ . \tag{A.5}$$

Now let's take the partial time-derivative of the total energy density (Equation (A.1)),

$$\frac{\partial U_{\rm tot}}{\partial t} = \frac{\partial U_g}{\partial t} + \frac{\partial U_r}{\partial t} - GM\frac{\partial}{\partial t}\left(\frac{\rho}{R-R_{\rm S}}\right) + \frac{1}{2}\frac{\partial}{\partial t}\left(\rho\vec{v}\cdot\vec{v}\right) \ , \tag{A.6}$$

which from the product rule on $\partial/\partial t\left[\rho/\left(R-R_{\rm S}\right)\right]$ and $\partial/\partial t\left(\rho\vec{v}\cdot\vec{v}\right)$ expands out to become,

$$\frac{\partial U_{\rm tot}}{\partial t} = \frac{\partial U_g}{\partial t} + \frac{\partial U_r}{\partial t} - \frac{GM}{R-R_{\rm S}}\frac{\partial\rho}{\partial t} - GM\rho\frac{\partial}{\partial t}\left(R-R_{\rm S}\right)^{-1} + \frac{1}{2}\left(\frac{\partial\rho}{\partial t}\vec{v}\cdot\vec{v} + \rho\frac{\partial\vec{v}}{\partial t}\cdot\vec{v} + \rho\vec{v}\cdot\frac{\partial\vec{v}}{\partial t}\right) \ .$$

Note that the last two terms on the right-hand side are equivalent (vector multiplication rule), which simplifies the expression to,

$$\frac{\partial U_{\rm tot}}{\partial t} = \frac{\partial U_g}{\partial t} + \frac{\partial U_r}{\partial t} - \frac{GM}{R-R_{\rm S}}\frac{\partial\rho}{\partial t} - GM\rho\frac{\partial}{\partial t}\left(R-R_{\rm S}\right)^{-1} + \frac{1}{2}\frac{\partial\rho}{\partial t}\vec{v}\cdot\vec{v} + \rho\frac{\partial\vec{v}}{\partial t}\cdot\vec{v} \ . \tag{A.7}$$

The task now is finding all the terms necessary to simplify Equation (A.7) down to one clean, efficient expression.

We start by using the Lagrangian derivative (Equation (2.1)) on ρ and exploiting the mass continuity equation (Equation (2.23)),

$$\frac{D\rho}{Dt} = \frac{\partial\rho}{\partial t} + \vec{v}\cdot\vec{\nabla}\rho = -\vec{\nabla}\cdot\left(\rho\vec{v}\right) + \vec{v}\cdot\vec{\nabla}\rho \ . \tag{A.8}$$

Applying the divergence of the product of a scalar and a vector to $\vec{\nabla} \cdot (\rho\vec{v})$,

$$\vec{\nabla} \cdot (\rho\vec{v}) = \vec{v} \cdot \left(\vec{\nabla}\rho\right) + \rho \left(\vec{\nabla} \cdot \vec{v}\right) \ , \tag{A.9}$$

simplifies this relation down,

$$\frac{D\rho}{Dt} = -\rho \left(\vec{\nabla} \cdot \vec{v}\right) \ . \tag{A.10}$$

Next we can implement Euler's equation (Equation (2.4)),

$$\frac{\partial\vec{v}}{\partial t} = -\frac{1}{\rho}\vec{\nabla}P + \vec{g} - \vec{v} \cdot \vec{\nabla}\vec{v} \ , \tag{A.11}$$

where $P = P_g + P_r$ is the total pressure in Model 3. Also we can show from Equation (2.5) that γU can generally be rewritten as,

$$\gamma U = P + U \ . \tag{A.12}$$

Moving forward, we apply the full Lagrangian derivative (Equation (2.1)) to the left-hand side, as well as Equation (A.10) to the right-hand side, of the relativistic U_r energy density (Equation (A.5)),

$$\frac{\partial U_r}{\partial t} + \vec{v} \cdot \vec{\nabla}U_r = \frac{\gamma_r U_r}{\rho} \left[-\rho \left(\vec{\nabla} \cdot \vec{v}\right)\right] - \vec{\nabla} \cdot \left(-\kappa\vec{\nabla}U_r\right) \ ,$$

which simplifies down to,

$$\frac{\partial U_r}{\partial t} = -\gamma_r U_r \left(\vec{\nabla} \cdot \vec{v}\right) - \vec{\nabla} \cdot \left(-\kappa\vec{\nabla}U_r\right) - \vec{v} \cdot \vec{\nabla}U_r \ . \tag{A.13}$$

Now we apply the same technique to the thermal U_g energy density (Equation (A.5)),

$$\frac{\partial U_g}{\partial t} + \vec{v} \cdot \vec{\nabla} U_g = \frac{\gamma_g U_g}{\rho} \left[-\rho \left(\vec{\nabla} \cdot \vec{v} \right) \right] = -\gamma_g U_g \left(\vec{\nabla} \cdot \vec{v} \right) \ ,$$

which simplifies down to,

$$\frac{\partial U_g}{\partial t} = -\gamma_g U_g \left(\vec{\nabla} \cdot \vec{v} \right) - \vec{v} \cdot \vec{\nabla} U_g \ . \tag{A.14}$$

Now we combine Equation (A.7) with Equations (2.23) and (A.10–A.14) to get,

$$\begin{aligned} \frac{\partial U_{\text{tot}}}{\partial t} = & -\gamma_g U_g \left(\vec{\nabla} \cdot \vec{v} \right) - \vec{v} \cdot \vec{\nabla} U_g - \gamma_r U_r \left(\vec{\nabla} \cdot \vec{v} \right) - \vec{\nabla} \cdot \left(-\kappa \vec{\nabla} U_r \right) - \vec{v} \cdot \vec{\nabla} U_r \\ & - \frac{GM}{R - R_{\text{S}}} \left[-\vec{\nabla} \cdot (\rho \vec{v}) \right] - GM\rho \frac{\partial}{\partial t} \left(R - R_{\text{S}} \right)^{-1} + \frac{1}{2} \left[-\vec{\nabla} \cdot (\rho \vec{v}) \right] \vec{v} \cdot \vec{v} \\ & + \rho \left[-\frac{1}{\rho} \vec{\nabla} P + \vec{g} - \left(\vec{v} \cdot \vec{\nabla} \right) \vec{v} \right] \cdot \vec{v} \ . \end{aligned} \tag{A.15}$$

Note that R is not dependent on t, so the term $\partial/\partial t \left(R - R_{\text{S}} \right)^{-1} \rightarrow 0$. Also, we can implement Equation (A.9) to redefine the expression as,

$$\begin{aligned} \frac{\partial U_{\text{tot}}}{\partial t} = & -\gamma_g U_g \left(\vec{\nabla} \cdot \vec{v} \right) - \vec{v} \cdot \vec{\nabla} U_g - \gamma_r U_r \left(\vec{\nabla} \cdot \vec{v} \right) - \vec{\nabla} \cdot \left(-\kappa \vec{\nabla} U_r \right) - \vec{v} \cdot \vec{\nabla} U_r \\ & - \frac{GM}{R - R_{\text{S}}} \left[-\vec{v} \cdot \left(\vec{\nabla} \rho \right) - \rho \vec{\nabla} \cdot \vec{v} \right] + \frac{1}{2} \left[-\vec{v} \cdot \left(\vec{\nabla} \rho \right) - \rho \vec{\nabla} \cdot \vec{v} \right] \vec{v} \cdot \vec{v} \\ & + \rho \left[-\frac{1}{\rho} \vec{\nabla} P + \vec{g} - \left(\vec{v} \cdot \vec{\nabla} \right) \vec{v} \right] \cdot \vec{v} \ . \end{aligned} \tag{A.16}$$

Once the vector terms are expanded,

$$\begin{aligned}\frac{\partial U_{\mathrm{tot}}}{\partial t} = -\gamma_g U_g \left(\vec{\nabla}\cdot\vec{v}\right) - \vec{v}\cdot\vec{\nabla}U_g - \gamma_r U_r \left(\vec{\nabla}\cdot\vec{v}\right) - \vec{\nabla}\cdot\left(-\kappa\vec{\nabla}U_r\right) - \vec{v}\cdot\vec{\nabla}U_r \\ + \frac{GM}{R-R_{\mathrm{S}}}\vec{v}\cdot\left(\vec{\nabla}\rho\right) + \frac{GM}{R-R_{\mathrm{S}}}\rho\vec{\nabla}\cdot\vec{v} - \frac{1}{2}\vec{v}\cdot\left(\vec{\nabla}\rho\right)\vec{v}\cdot\vec{v} - \frac{1}{2}\rho\vec{\nabla}\cdot\vec{v}\left(\vec{v}\cdot\vec{v}\right) \\ -\vec{\nabla}P\cdot\vec{v} + \rho\vec{g}\cdot\vec{v} - \rho\left(\vec{v}\cdot\vec{\nabla}\right)\vec{v}\cdot\vec{v}\ ,\end{aligned} \tag{A.17}$$

the like-terms can be combined,

$$\begin{aligned}\frac{\partial U_{\mathrm{tot}}}{\partial t} = -\left[\gamma_g U_g + \gamma_r U_r - \frac{GM\rho}{R-R_{\mathrm{S}}} + \frac{1}{2}\rho\left(\vec{v}\cdot\vec{v}\right)\right]\left(\vec{\nabla}\cdot\vec{v}\right) - \vec{v}\cdot\vec{\nabla}U_g \\ -\vec{\nabla}\cdot\left(-\kappa\vec{\nabla}U_r\right) - \vec{v}\cdot\vec{\nabla}U_r + \frac{GM}{R-R_{\mathrm{S}}}\vec{v}\cdot\left(\vec{\nabla}\rho\right) - \frac{1}{2}\vec{v}\cdot\left(\vec{\nabla}\rho\right)\vec{v}\cdot\vec{v} \\ -\vec{\nabla}P\cdot\vec{v} + \rho\vec{g}\cdot\vec{v} - \rho\left(\vec{v}\cdot\vec{\nabla}\right)\vec{v}\cdot\vec{v}\ .\end{aligned} \tag{A.18}$$

Note that $\vec{\nabla}P$ is the gradient of the total pressure $P = P_g + P_r$, which when combined with Equation (2.5) becomes,

$$\vec{\nabla}P = \vec{\nabla}P_g + \vec{\nabla}P_r = \left(\gamma_g - 1\right)\vec{\nabla}U_g + \left(\gamma_r - 1\right)\vec{\nabla}U_r\ . \tag{A.19}$$

Combining Equations (A.18) and (A.19),

$$\begin{aligned}\frac{\partial U_{\mathrm{tot}}}{\partial t} = -\left[\gamma_g U_g + \gamma_r U_r - \frac{GM\rho}{R-R_{\mathrm{S}}} + \frac{1}{2}\rho\left(\vec{v}\cdot\vec{v}\right)\right]\left(\vec{\nabla}\cdot\vec{v}\right) - \vec{v}\cdot\vec{\nabla}U_g \\ -\vec{\nabla}\cdot\left(-\kappa\vec{\nabla}U_r\right) - \vec{v}\cdot\vec{\nabla}U_r + \frac{GM}{R-R_{\mathrm{S}}}\vec{v}\cdot\left(\vec{\nabla}\rho\right) - \frac{1}{2}\vec{v}\cdot\left(\vec{\nabla}\rho\right)\vec{v}\cdot\vec{v} \\ -\left[\left(\gamma_g - 1\right)\vec{\nabla}U_g + \left(\gamma_r - 1\right)\vec{\nabla}U_r\right]\cdot\vec{v} + \rho\vec{g}\cdot\vec{v} - \rho\left(\vec{v}\cdot\vec{\nabla}\right)\vec{v}\cdot\vec{v}\ ,\end{aligned} \tag{A.20}$$

and then simplifying the expression,

$$
\begin{aligned}
\frac{\partial U_{\text{tot}}}{\partial t} &= -\left[\gamma_g U_g + \gamma_r U_r - \frac{GM\rho}{R-R_{\text{S}}} + \frac{1}{2}\rho\left(\vec{v}\cdot\vec{v}\right)\right]\left(\vec{\nabla}\cdot\vec{v}\right) - \vec{\nabla}\cdot\left(-\kappa\vec{\nabla}U_r\right) \\
&+\vec{v}\cdot\left[\frac{GM}{R-R_{\text{S}}}\vec{\nabla}\rho - \frac{1}{2}\left(\vec{v}\cdot\vec{v}\right)\vec{\nabla}\rho - \gamma_g\vec{\nabla}U_g - \gamma_r\vec{\nabla}U_r + \rho\vec{g} - \rho\left(\vec{v}\cdot\vec{\nabla}\right)\vec{v}\right] \ ,
\end{aligned} \tag{A.21}
$$

we have everything needed to make the connection between Equation (A.2) and Equation (A.3). The final step is to simplify Equation (A.21) by applying the divergence of the product of a scalar and a vector for various terms, but in reverse.

Looking at Equation (A.4), we can start by applying the divergence to the energy density terms,

$$\vec{\nabla}\cdot\left(\gamma_g U_g \vec{v}\right) = \vec{v}\cdot\left(\gamma_g\vec{\nabla}U_g\right) + \gamma_g U_g\vec{\nabla}\cdot\vec{v} \ , \tag{A.22}$$

$$\vec{\nabla}\cdot\left(\gamma_r U_r \vec{v}\right) = \vec{v}\cdot\left(\gamma_r\vec{\nabla}U_r\right) + \gamma_r U_r\vec{\nabla}\cdot\vec{v} \ . \tag{A.23}$$

Next we can do to the same to the potential energy term,

$$\vec{\nabla}\cdot\left(\frac{GM}{R-R_{\text{S}}}\rho\vec{v}\right) = \vec{v}\cdot\left(\frac{GM}{R-R_{\text{S}}}\vec{\nabla}\rho\right) + \frac{GM\rho}{R-R_{\text{S}}}\vec{\nabla}\cdot\vec{v} + GM\rho\vec{v}\cdot\vec{\nabla}\left(R-R_{\text{S}}\right)^{-1} \ .$$

Note that the last term includes the acceleration due to gravity $\vec{g}$ since,

$$GM\rho\vec{v}\cdot\vec{\nabla}\left(R-R_{\text{S}}\right)^{-1} = -GM\rho\vec{v}\cdot\left(R-R_{\text{S}}\right)^{-2} = \rho\vec{v}\cdot\vec{g}$$

thus simplifying down the expression,

$$\vec{\nabla}\cdot\left(\frac{GM}{R-R_{\text{S}}}\rho\vec{v}\right) = \vec{v}\cdot\left(\frac{GM}{R-R_{\text{S}}}\vec{\nabla}\rho\right) + \frac{GM\rho}{R-R_{\text{S}}}\vec{\nabla}\cdot\vec{v} + \rho\vec{v}\cdot\vec{g} \ . \tag{A.24}$$

Finally, we apply the divergence to the kinetic energy term,

$$\begin{aligned}\vec{\nabla}\cdot\left[\frac{1}{2}\left(\vec{v}\cdot\vec{v}\right)\rho\vec{v}\right] &= \vec{v}\cdot\left[\frac{1}{2}\left(\vec{v}\cdot\vec{v}\right)\vec{\nabla}\rho+\rho\left(\vec{v}\cdot\vec{\nabla}\right)\vec{v}\right]+\frac{1}{2}\rho\left(\vec{v}\cdot\vec{v}\right)\vec{\nabla}\cdot\vec{v} \\ &= \frac{1}{2}\vec{v}\cdot\left(\vec{v}\cdot\vec{v}\right)\vec{\nabla}\rho+\rho\vec{v}\cdot\left(\vec{v}\cdot\vec{\nabla}\right)\vec{v}+\frac{1}{2}\rho\left(\vec{v}\cdot\vec{v}\right)\vec{\nabla}\cdot\vec{v}\ .\end{aligned} \tag{A.25}$$

Combining Equations (A.22–A.25), and applying them to Equation (A.21), we can see that the expression simplifies down to

$$\frac{\partial U_{\rm tot}}{\partial t} = -\vec{\nabla}\cdot\left(\gamma_g U_g\vec{v}+\gamma_r U_r\vec{v}-\frac{GM\rho\vec{v}}{R-R_{\rm S}}+\frac{1}{2}\rho\left(\vec{v}\cdot\vec{v}\right)\vec{v}-\kappa\vec{\nabla}U_r\right)\ . \tag{A.26}$$

Thus when we apply Equation (A.12),

$$\frac{\partial U_{\rm tot}}{\partial t} = -\vec{\nabla}\cdot\left[\left(U_g+P_g\right)\vec{v}+\left(U_r+P_r\right)\vec{v}-\frac{GM\rho\vec{v}}{R-R_{\rm S}}+\frac{1}{2}\rho\left(\vec{v}\cdot\vec{v}\right)\vec{v}-\kappa\vec{\nabla}U_r\right]\ , \tag{A.27}$$

and comparing the right-hand side to Equation (A.3), we have therefore confirmed that

$$\boxed{\frac{\partial U_{\rm tot}}{\partial t} = -\vec{\nabla}\cdot\vec{F}_{\rm tot}}$$

Appendix B: Precursor to the Wind Equation

Before we can derive the wind equation for either Model 1, 2 or 3, we must first determine the steady-state radial momentum equation. This is derived from the radial component of Euler's relation (Equation 2.4),

$$\frac{\partial \vec{v}}{\partial t} + \left(\vec{v} \cdot \vec{\nabla}\right) \vec{v} = -\frac{1}{\rho} \vec{\nabla} P + \frac{1}{\rho} \vec{f} \, , \tag{B.1}$$

when adopting cylindrical coordinates in steady-state, where the only forces acting on the fluid is a pseudo-Newtonian force, defined for this system (where it is already assumed to be vertically averaged) in the radial direction as

$$\vec{f} \equiv f_r \hat{r} = \frac{\rho d\Phi}{dr} \hat{r} = \frac{GM\rho}{\left(r - r_{\mathrm{S}}\right)^2} \hat{r} \ . \tag{B.2}$$

The first thing that needs to be addressed is the convective acceleration term, $\left(\vec{v} \cdot \vec{\nabla}\right) \vec{v}$ (also known as the material derivative), we can be spaced out as so,

$$\left(\vec{v} \cdot \vec{\nabla}\right) \vec{v} = \vec{\nabla} \left(\frac{1}{2} \vec{v}^2\right) - \vec{v} \times \left(\vec{\nabla} \times \vec{v}\right) \ . \tag{B.3}$$

The first term on the right-hand-side of Equation (B.3) can be written in cylindrical coordinates as,

$$\vec{\nabla} \left(\frac{1}{2} \vec{v}^2\right) = \frac{1}{2} \left(\hat{r} \frac{\partial v_r^2}{\partial r} + \hat{\phi} \frac{1}{r} \frac{\partial v_\phi^2}{\partial \phi} + \hat{z} \frac{\partial v_z^2}{\partial z}\right) \ . \tag{B.4}$$

Now, we focus on the innermost curl in the second term, written in cylindrical coordinates as,

$$\vec{\nabla}\times\vec{v}=\left(\frac{1}{r}\frac{\partial v_z}{\partial\phi}-\frac{\partial v_\phi}{\partial z}\right)\hat{r}+\left(\frac{\partial v_r}{\partial z}-\frac{\partial v_z}{\partial r}\right)\hat{\phi}+\frac{1}{r}\left(\frac{\partial}{\partial r}\left(rv_\phi\right)-\frac{\partial v_r}{\partial\phi}\right)\hat{z} \tag{B.5}$$

Next, we apply the cross product of $\vec{v}$ to Equation (B.5) to obtain,

$$\begin{aligned}\vec{v}\times\left(\vec{\nabla}\times\vec{v}\right)=v_r\hat{r}\times&\left[\left(\frac{1}{r}\frac{\partial v_z}{\partial\phi}-\frac{\partial v_\phi}{\partial z}\right)\hat{r}+\left(\frac{\partial v_r}{\partial z}-\frac{\partial v_z}{\partial r}\right)\hat{\phi}+\frac{1}{r}\left(\frac{\partial}{\partial r}\left(rv_\phi\right)-\frac{\partial v_r}{\partial\phi}\right)\hat{z}\right]\\
+v_\phi\hat{\phi}\times&\left[\left(\frac{1}{r}\frac{\partial v_z}{\partial\phi}-\frac{\partial v_\phi}{\partial z}\right)\hat{r}+\left(\frac{\partial v_r}{\partial z}-\frac{\partial v_z}{\partial r}\right)\hat{\phi}+\frac{1}{r}\left(\frac{\partial}{\partial r}\left(rv_\phi\right)-\frac{\partial v_r}{\partial\phi}\right)\hat{z}\right]\\
+v_z\hat{z}\times&\left[\left(\frac{1}{r}\frac{\partial v_z}{\partial\phi}-\frac{\partial v_\phi}{\partial z}\right)\hat{r}+\left(\frac{\partial v_r}{\partial z}-\frac{\partial v_z}{\partial r}\right)\hat{\phi}+\frac{1}{r}\left(\frac{\partial}{\partial r}\left(rv_\phi\right)-\frac{\partial v_r}{\partial\phi}\right)\hat{z}\right]\ ,\end{aligned}$$

which break up the components as,

$$\begin{aligned}\vec{v}\times\left(\vec{\nabla}\times\vec{v}\right)=&\,v_r\left(\frac{\partial v_r}{\partial z}-\frac{\partial v_z}{\partial r}\right)\hat{z}-\frac{1}{r}\left(\frac{\partial}{\partial r}\left(rv_\phi\right)-\frac{\partial v_r}{\partial\phi}\right)\hat{\phi}-v_\phi\left(\frac{1}{r}\frac{\partial v_z}{\partial\phi}-\frac{\partial v_\phi}{\partial z}\right)\hat{z}\\
&+\frac{v_\phi}{r}\left(\frac{\partial}{\partial r}\left(rv_\phi\right)-\frac{\partial v_r}{\partial\phi}\right)\hat{r}+v_z\left(\frac{1}{r}\frac{\partial v_z}{\partial\phi}-\frac{\partial v_\phi}{\partial z}\right)\hat{\phi}-v_z\left(\frac{\partial v_r}{\partial z}-\frac{\partial v_z}{\partial r}\right)\hat{r}\ .\end{aligned} \tag{B.6}$$

However, since $v_z=0$, as everything is vertically averaged, Equation (B.6) simplifies down to,

$$\begin{aligned}\vec{v}\times\left(\vec{\nabla}\times\vec{v}\right)&=-\frac{1}{r}\left(\frac{\partial}{\partial r}\left(rv_\phi\right)-\frac{\partial v_r}{\partial\phi}\right)\hat{\phi}+\frac{v_\phi}{r}\left(\frac{\partial}{\partial r}\left(rv_\phi\right)\right)\hat{r}\\
&=-\frac{1}{r}\left(\frac{\partial}{\partial r}\left(rv_\phi\right)-\frac{\partial v_r}{\partial\phi}\right)\hat{\phi}+\frac{v_\phi^2}{r}\hat{r}\ .\end{aligned} \tag{B.7}$$

Thus, combining Equations (B.4) and (B.7) brings the convective acceleration term (Equation B.3) to,

$$\left(\vec{v}\cdot\vec{\nabla}\right)\vec{v}=\frac{1}{2}\left\{\hat{r}\frac{\partial v_r^2}{\partial r}+\hat{\phi}\frac{1}{r}\frac{\partial v_\phi^2}{\partial \phi}+\hat{z}\frac{\partial v_z^2}{\partial z}\right\}+\frac{1}{r}\left(\frac{\partial}{\partial r}\left(rv_\phi\right)-\frac{\partial v_r}{\partial \phi}\right)\hat{\phi}-\frac{v_\phi^2}{r}\hat{r}\ . \tag{B.8}$$

Combining Equations (B.1), (B.2) and (B.8) we get,

$$\begin{aligned}\frac{\partial\vec{v}}{\partial t}+\frac{1}{2}\left\{\hat{r}\frac{\partial v_r^2}{\partial r}+\hat{\phi}\frac{1}{r}\frac{\partial v_\phi^2}{\partial \phi}+\hat{z}\frac{\partial v_z^2}{\partial z}\right\}+\frac{1}{r}\left(\frac{\partial}{\partial r}\left(rv_\phi\right)-\frac{\partial v_r}{\partial \phi}\right)\hat{\phi}-\frac{v_\phi^2}{r}\hat{r}&\\ =-\frac{1}{\rho}\vec{\nabla}P+\frac{1}{\rho}\frac{GM\rho}{\left(r-r_{\mathrm{S}}\right)^2}\hat{r}\ .&\end{aligned} \tag{B.9}$$

Focusing on just the radial components $\hat{r}$, we obtain the steady-state ($\partial\vec{v}/dt\rightarrow 0$) radial momentum equation,

$$\frac{1}{2}\frac{\partial v_r^2}{\partial r}-\frac{v_\phi^2}{r}=-\frac{1}{\rho}\frac{\partial P}{\partial r}+\frac{GM}{\left(r-r_{\mathrm{S}}\right)^2}\ ,$$

which is rewritten as,

$$v\frac{dv}{dr}=-\frac{1}{\rho}\frac{dP}{dr}-\frac{GM}{\left(r-r_{\mathrm{S}}\right)^2}+\frac{v_\phi^2}{r}\ , \tag{B.10}$$

where dP/dr is the change in the total pressure in the system with respect to the radius r, which is dependent on the model. It should be noted that Equation (B.10) is universal for all three Models, it's just dependent on the total pressure P, which separately defines it for a particular model. For Model 1, $P\rightarrow P_g$, and for Models 2 and 3, $P=P_g+P_r$. This becomes useful when deriving the wind equations (e.g. see § 2.4.1)

Appendix C: Treatment of the Vertical Structure

The following is from Appendix A of of Le & Becker (2005), but with references made to my document. In principle, the pressure P, density ρ, diffusion coefficient κ, Green's function f_{G}, and velocity components v_r and v_z in the disk all display significant variations in the vertical (z) direction. Following Abramowicz & Chakrabarti (1990), we use the first five quantities to represent vertical averages over the disk structure at radius r. However, the vertical variation of the velocity components v_z must be treated differently. Here, we assume for simplicity that the vertical expansion is *homologous*, and therefore the vertical velocity variation is given by

$$v_z\,(r,z) = B(r)z\ . \tag{C.1}$$

It follows that the vertical velocity at the surface of the disk, $z = H(r)$, can be written as

$$v_z\,(r,z) = B(r)H(r)\ . \tag{C.2}$$

In a steady state situation, we can also express the vertical velocity at the disk surface using

$$v_z\,(r,z)\big|_{z=H} = v_r \frac{dH}{dr}\ . \tag{C.3}$$

By combining the two previous expressions, we find that the function $B(r)$ is given by

$$B(r) = v_r \frac{d\ln H}{dr}\ . \tag{C.4}$$

This result will prove useful when we vertically integrate the transport equation. Note that in terms of $B(r)$, we can write the divergence of the flow velocity $\vec{v}$ in cylindrical coordinates as

$$\vec{\nabla}\cdot\vec{v} = \frac{1}{r}\frac{\partial}{\partial r}\,(rv_r) + \frac{\partial v_z}{\partial z} = \frac{1}{r}\frac{\partial}{\partial r}\,(rv_r) + B(r)\ , \tag{C.5}$$

where we have assumed azimuthal symmetry. Application of Equation (C.4) now yields

$$\vec{\nabla} \cdot \vec{v} = \frac{1}{Hr} \frac{\partial}{\partial r} \left(r H v_r \right) \ . \tag{C.6}$$

The steady state transport equation expressed in cylindrical coordinates (see Equation 3.5) is

$$\begin{aligned} v_r \frac{\partial f_{\rm G}}{\partial r} + v_z \frac{\partial f_{\rm G}}{\partial z} = \frac{1}{3} \left[\frac{1}{r} \frac{\partial}{\partial r} \left(r v_r \right) + \frac{\partial v_z}{\partial z} \right] E \frac{\partial f_{\rm G}}{\partial E} + \frac{1}{r} \frac{\partial}{\partial r} \left(r \kappa \frac{\partial f_{\rm G}}{\partial r} \right) \\ + \frac{\dot{N}_0 \delta \left(E - E_0 \right) \delta \left(r - r_* \right)}{\left(4 \pi E_0 \right)^2 r_* H_*} - A_0 c \delta \left(r - r_* \right) f_{\rm G} \ . \end{aligned} \tag{C.7}$$

Operating on equation (C.7) with $\int_0^\infty dz$ and applying equation (C.1) yields, after partially integrating the term containing v_z on the left-hand side,

$$\begin{aligned} v_r \frac{\partial}{\partial r} \left(H f_{\rm G} \right) - H B f_{\rm G} = \frac{1}{3} \left[\frac{1}{r} \frac{\partial}{\partial r} \left(r v_r \right) + B \right] H E \frac{\partial f_{\rm G}}{\partial E} + \frac{1}{r} \frac{\partial}{\partial r} \left(r H \kappa \frac{\partial f_{\rm G}}{\partial r} \right) \\ + \frac{\dot{N}_0 \delta \left(E - E_0 \right) \delta \left(r - r_* \right)}{\left(4 \pi E_0 \right)^2 r_*} - A_0 c H_* \delta \left(r - r_* \right) f_{\rm G} \ , \end{aligned} \tag{C.8}$$

where the symbols $f_{\rm G}$, v_r, and κ now refer to vertically averaged quantities. Using equations (C.4), (C.5), and (C.6), we can rewrite the vertically integrated transport equation as

$$\begin{aligned} H v_r \frac{\partial f_{\rm G}}{\partial r} = \frac{1}{3r} \frac{\partial}{\partial r} \left(r H v_r \right) E \frac{\partial f_{\rm G}}{\partial E} + \frac{1}{r} \frac{\partial}{\partial r} \left(r H \kappa \frac{\partial f_{\rm G}}{\partial r} \right) \\ + \frac{\dot{N}_0 \delta \left(E - E_0 \right) \delta \left(r - r_* \right)}{\left(4 \pi E_0 \right)^2 r_*} - A_0 c H_* \delta \left(r - r_* \right) f_{\rm G} \ . \end{aligned} \tag{C.9}$$

This expression is used in § (5.1) to analyze the transport of the relativistic particles in the disk.

Appendix D: Derivation of the Escape Parameter

The rate at which particles escape through the surface of the disk, quantified with the dimensionless parameter A_0 mentioned in Equation (3.8), occurs from random walks near the shock location. The particle acceleration is a consequence of magnetic wave collisions, in which the shock thickness is similar to the magnetic mean free path $\lambda_{\rm mag}$. Following Appendix B of Le & Becker (2005, hereafter LB05), we follow the same cylindrical pipe model with the analogy that the particles are escaping via a "leak" from a radius equal to the disk half-thickness at the shock location, H_*, in order to estimate A_0. However, the length of the open section of the pipe is now set equal to the thickness of the shock by $\eta\lambda_{\rm mag}$, where η is a dimensionless quantity that represents this thickness in units of the magnetic coherence length.

The model of LB05 dealt with a discontinuous shock, in which the shock thickness was assumed to be equal to the magnetic coherence length $\lambda_{\rm mag}$; therefore $\eta = 1$. In the case under consideration here, the relativistic particle pressure creates a precursor deceleration which increases the effective width of the shock, as seen in Figure 4.1, to which $\eta \sim 7 - 11$. This is the same behavior observed in the self-consistent models for cosmic-ray-modified shocks (Axford et al. 1977; Becker et al. 2011). In order to obtain the estimated value A_0 for this new model, we must retrace our steps from Appendix B of LB05. First we note that the particle number density in the open section of the pipe is governed by the relation

$$v_x \frac{dn_r}{dx} = -\frac{n_r}{t_{\rm esc}} \ , \tag{D.1}$$

where v_x, n_r, and $t_{\rm esc}$ denote the flow velocity, the relativistic particle number density, and the average time for the particles to "leak" through the pipe via diffusion, respectively.

Integrating Equation (D.1) leads to

$$n_r(x) = n_0 \exp\left(-\frac{x}{v_x t_{\mathrm{esc}}}\right) \ , \tag{D.2}$$

where n_0 denotes the incident number density as the flow encounters the exit in the pipe (at $x = 0$). The solution for $n_r(x)$ is approximated via Taylor expansion around $x = 0$, yielding

$$n_r(x) \approx n_0 \left(1 - \frac{x}{v_x t_{\mathrm{esc}}}\right) \ . \tag{D.3}$$

To estimate the fraction of particles that escape from the pipe, we now set $x = \eta\lambda_{\mathrm{mag}}$ to obtain

$$f_{\mathrm{esc}} = 1 - \left.\frac{n_r}{n_0}\right|_{x=\lambda_{\mathrm{mag}}} = \frac{\eta\lambda_{\mathrm{mag}}}{v_x t_{\mathrm{esc}}} \ . \tag{D.4}$$

With the assumption that advection dominates over diffusion, as the gas crosses the isothermal shock the fraction of escape particles is given as

$$f_{\mathrm{esc}} = A_0 \frac{c}{v_*} \ , \tag{D.5}$$

where the mean velocity at the shock is defined as $v_* \equiv (v_+ + v_-)/2$. By setting $v_x = v_*$ when combining Equations (D.4) and (D.5), we obtain

$$A_0 = \frac{\eta\lambda_{\mathrm{mag}}}{c t_{\mathrm{esc}}} \ . \tag{D.6}$$

Following Appendix B of LB05, we too use the definition for the mean escape time t_{esc} since our model for the particle transport in the disk is one-dimensional. This quantity is related to $\lambda_{\rm mag}$ and the disk half-thickness at the shock H_* via

$$t_{\rm esc} = \frac{H_*}{v_{\rm diff}} = \frac{H_*^2}{c\lambda_{\rm mag}} \ , \tag{D.7}$$

where $v_{\rm diff} = c\lambda_{\rm mag}/H_*$ represents the vertical diffusion velocity of the protons in the tangled magnetic field near the shock. This is only valid if $H_*/\lambda_{\rm mag} > 1$. Now in order to eliminate $t_{\rm esc}$ in Equation (D.6), the parameter A_0 can be defined in terms of $\lambda_{\rm mag}$,

$$A_0 = \eta \left(\frac{\lambda_{\rm mag}}{H_*}\right)^2 < 1 \ , \tag{D.8}$$

which when combined with the standard expression (e.g., Reif 1965) for the diffusion coefficient in an ideal dilute gas fluid at the shock

$$\kappa = \frac{c\lambda_{\rm mag}}{3} \ , \tag{D.9}$$

can be rewritten as

$$A_0 = \eta \left(\frac{3\kappa_*}{cH_*}\right)^2 \ , \tag{D.10}$$

where $\kappa_* \equiv (\kappa_+ + \kappa_-)/2$ is the average of the upstream and downstream values of the diffusion coefficient (Equation (2.48)) on either side of the shock.

Appendix E: Deriving the Lagrangian Particle Energy Density

The purpose of this section is to verify that by integrating the steady-state transport equation (Becker 1992),

$$\frac{\partial f_{\mathrm{G}}}{\partial t} = 0 = -\vec{\nabla} \cdot \vec{F} - \frac{1}{3E^2} \frac{\partial}{\partial E} \left(E^3 \vec{v} \cdot \vec{\nabla} f_{\mathrm{G}} \right) + \dot{f}_{\mathrm{source}} - \dot{f}_{\mathrm{esc}} \ , \tag{E.1}$$

where the specific flux $\vec{F}$ is defined as,

$$\vec{F} = -\kappa \vec{\nabla} f_{\mathrm{G}} - \frac{\vec{v} E}{3} \frac{\partial f_{\mathrm{G}}}{\partial E} \ , \tag{E.2}$$

with $\int_0^\infty 4\pi E^3 dE$, without the source or escape terms, that we get back the full Lagrangian of the relativistic particle energy density U_r,

$$\frac{DU_r}{Dt} = \frac{\gamma_r U_r}{\rho} \frac{D\rho}{Dt} - \vec{\nabla} \cdot \left(-\kappa \vec{\nabla} U_r \right) \ . \tag{E.3}$$

Start by integrating Equation (E.1) with with $\int_0^\infty 4\pi E^3 dE$, ignoring the source terms,

$$0 = -\int_0^\infty 4\pi \left(\vec{\nabla} \cdot \vec{F} \right) E^3 dE - \int_0^\infty 4\pi E^3 \frac{1}{3E^2} \frac{\partial}{\partial E} \left(E^3 \vec{v} \cdot \vec{\nabla} f_{\mathrm{G}} \right) dE \ . \tag{E.4}$$

Now branch out the vector components for the right-most term,

$$\begin{aligned} 0 = &-\int_0^\infty 4\pi \left(\vec{\nabla} \cdot \vec{F} \right) E^3 dE - \int_0^\infty 4\pi E^3 \left(\vec{v} \cdot \vec{\nabla} f_{\mathrm{G}} \right) dE \\ &+ \int_0^\infty 4\pi E^3 \frac{1}{3E^2} \left(E^3 \frac{\partial \vec{v}}{\partial E} \cdot \vec{\nabla} f_{\mathrm{G}} \right) dE + \int_0^\infty 4\pi E^3 \frac{1}{3E^2} \left(E^3 \vec{v} \cdot \frac{\partial \vec{\nabla} f_{\mathrm{G}}}{\partial E} \right) dE \ . \end{aligned} \tag{E.5}$$

Since $\vec{v}$ is not dependent on E,

$$0 = -\int_0^\infty 4\pi\left(\vec{\nabla}\cdot\vec{F}\right)E^3 dE - \int_0^\infty 4\pi E^3\left(\vec{v}\cdot\vec{\nabla}f_{\mathrm{G}}\right)dE \\ + \int_0^\infty 4\pi E^3 \frac{1}{3E^2}\left(E^3\vec{v}\cdot\frac{\partial\vec{\nabla}f_{\mathrm{G}}}{\partial E}\right)dE \; . \tag{E.6}$$

Next, substitute in Equation (E.2) in the left-most term,

$$-\int_0^\infty 4\pi\left(\vec{\nabla}\cdot\vec{F}\right)E^3 dE = -\int_0^\infty 4\pi\left(\vec{\nabla}\cdot\left[-\kappa\vec{\nabla}f_{\mathrm{G}} - \frac{\vec{v}E}{3}\frac{\partial f_{\mathrm{G}}}{\partial E}\right]\right)E^3 dE \; , \tag{E.7}$$

which after applying the distributive property becomes,

$$-\int_0^\infty 4\pi\left(\vec{\nabla}\cdot\vec{F}\right)E^3 dE = -\int_0^\infty 4\pi\left(\vec{\nabla}\cdot\left[-\kappa\vec{\nabla}f_{\mathrm{G}}\right] - \vec{\nabla}\cdot\left[\frac{\vec{v}E}{3}\frac{\partial f_{\mathrm{G}}}{\partial E}\right]\right)E^3 dE \; , \tag{E.8}$$

and finally,

$$-\int_0^\infty 4\pi\left(\vec{\nabla}\cdot\vec{F}\right)E^3 dE = -\int_0^\infty 4\pi\left(\vec{\nabla}\cdot\left[-\kappa\vec{\nabla}f_{\mathrm{G}}\right]\right)E^3 dE \\ + \int_0^\infty 4\pi\left(\vec{\nabla}\cdot\left[\frac{\vec{v}E}{3}\frac{\partial f_{\mathrm{G}}}{\partial E}\right]\right)E^3 dE \; . \tag{E.9}$$

Note that the first term of the right-hand-side of Equation (E.9) can be simplified down using $U_r \equiv \int_0^\infty 4\pi E^3 dE$,

$$\int_0^\infty 4\pi\left(\vec{\nabla}\cdot\left[-\kappa\vec{\nabla}f_{\mathrm{G}}\right]\right)E^3 dE = \vec{\nabla}\cdot\left[-\kappa\vec{\nabla}\int_0^\infty 4\pi E^3 f_{\mathrm{G}} dE\right] = \vec{\nabla}\cdot\left(-\kappa\vec{\nabla}U_r\right) \; . \tag{E.10}$$

Likewise, the second term of the right-hand-side of Equation (E.9) can be simplified down,

$$\int_0^\infty 4\pi \left(\vec{\nabla}\cdot\left[\frac{\vec{v}E}{3}\frac{\partial f_\mathrm{G}}{\partial E}\right]\right) E^3 dE = \vec{\nabla}\cdot\frac{\vec{v}}{3}\int_0^\infty 4\pi E^4 \frac{\partial f_\mathrm{G}}{\partial E} dE \ , \tag{E.11}$$

which after applying integration-by-parts,

$$\int_0^\infty 4\pi \left(\vec{\nabla}\cdot\left[\frac{\vec{v}E}{3}\frac{\partial f_\mathrm{G}}{\partial E}\right]\right) E^3 dE = \vec{\nabla}\cdot\frac{\vec{v}}{3}\left(4\pi E^4 \left. f_\mathrm{G}\right|_0^\infty - \int_0^\infty 16\pi E^3 f_\mathrm{G} dE\right) \ , \tag{E.12}$$

simplifies down to,

$$\begin{aligned}\int_0^\infty 4\pi \left(\vec{\nabla}\cdot\left[\frac{\vec{v}E}{3}\frac{\partial f_\mathrm{G}}{\partial E}\right]\right) E^3 dE &= -\vec{\nabla}\cdot\frac{\vec{v}}{3}\left(4\int_0^\infty 4\pi E^3 f_\mathrm{G} dE\right) \\ &= -\vec{\nabla}\cdot\frac{4\vec{v}}{3}U_r = -\frac{4}{3}\vec{\nabla}\cdot\left(\vec{v}U_r\right) \ .\end{aligned} \tag{E.13}$$

Note that the divergence term in Equation (E.13) can be expanded out as,

$$\vec{\nabla}\cdot\left(\vec{v}U_r\right) = U_r\left(\vec{\nabla}\cdot\vec{v}\right) + \vec{v}\cdot\vec{\nabla}U_r \ . \tag{E.14}$$

Also, the middle-term of Equation (E.6) can be simplified down,

$$\int_0^\infty 4\pi E^3 \left(\vec{v}\cdot\vec{\nabla}f_\mathrm{G}\right) dE = \vec{v}\cdot\vec{\nabla}\left(\int_0^\infty 4\pi E^3 f_\mathrm{G} dE\right) = \vec{v}\cdot\vec{\nabla}U_r \ . \tag{E.15}$$

Finally, we simplify down the last-term of Equation (E.6),

$$\int_0^\infty 4\pi E^3 \frac{1}{3E^2}\left(E^3\vec{v}\cdot\frac{\partial\vec{\nabla}f_\mathrm{G}}{\partial E}\right) dE = \frac{1}{3}\vec{v}\cdot\vec{\nabla}\left[\int_0^\infty 4\pi\left(E^4\frac{\partial f_\mathrm{G}}{\partial E}\right) dE\right] \ , \tag{E.16}$$

and after applying integration-by-parts, simplifies down to,

$$\begin{aligned}\int_0^\infty 4\pi E^3 \frac{1}{3E^2}\left(E^3\vec{v}\cdot\frac{\partial\vec{\nabla}f_{\mathrm{G}}}{\partial E}\right)dE &= \frac{1}{3}\vec{v}\cdot\vec{\nabla}\left(4\pi E^4\ f_{\mathrm{G}}\big|_0^\infty - \int_0^\infty 16\pi E^3 f_{\mathrm{G}}dE\right) \\ &= -\frac{1}{3}\vec{v}\cdot\vec{\nabla}\left(4\int_0^\infty 4\pi E^3 f_{\mathrm{G}}dE\right) = -\frac{4}{3}\vec{v}\cdot\vec{\nabla}U_r\ .\end{aligned} \tag{E.17}$$

Now we substitute in Equations (E.10), (E.13), (E.14), (E.15), (E.17) into Equation (E.6),

$$0 = -\vec{\nabla}\cdot\left(-\kappa\vec{\nabla}U_r\right) - \frac{4}{3}U_r\left(\vec{\nabla}\cdot\vec{v}\right) - \frac{4}{3}\vec{v}\cdot\vec{\nabla}U_r - \vec{v}\cdot\vec{\nabla}U_r + \frac{4}{3}\vec{v}\cdot\vec{\nabla}U_r\ , \tag{E.18}$$

which simplifies down to,

$$0 = -\vec{\nabla}\cdot\left(-\kappa\vec{\nabla}U_r\right) - \frac{4}{3}U_r\left(\vec{\nabla}\cdot\vec{v}\right) - \vec{v}\cdot\vec{\nabla}U_r\ , \tag{E.19}$$

and is rewritten as,

$$\vec{v}\cdot\vec{\nabla}U_r = -\vec{\nabla}\cdot\left(-\kappa\vec{\nabla}U_r\right) - \frac{4}{3}U_r\left(\vec{\nabla}\cdot\vec{v}\right)\ . \tag{E.20}$$

Applying the full Lagrangian (Equation 2.1) to the relativistic particle energy density U_r and focusing on the steady-state case,

$$\frac{DU_r}{Dt} = \frac{\partial U_r}{\partial t} + \vec{v}\cdot\vec{\nabla}U_r = \vec{v}\cdot\vec{\nabla}U_r\ , \tag{E.21}$$

and with the substitution of $\gamma_r = 4/3$, Equation (E.20) thus becomes,

$$\boxed{\frac{DU_r}{Dt} = -\vec{\nabla}\cdot\left(-\kappa\vec{\nabla}U_r\right) + \frac{\gamma_r U_r}{\rho}\frac{D\rho}{Dt}}\ . \tag{E.22}$$

Appendix F: Proof: Separation of Variables Function

Now in order to prove that the separation of variables function (Equation 3.63) works to verify Equation (3.65), let's start with a generic separation of variables function,

$$f_\lambda\left(E,r\right) = G\left(\lambda, E\right) Y\left(\lambda, r\right) \ . \tag{F.1}$$

Next we set the source term in Equation (3.61) to zero and make the equation homogeneous,

$$-Hv\frac{\partial f_{\mathrm{G}}}{\partial r} + \frac{1}{3r}\frac{\partial}{\partial r}\left(rHv\right)E\frac{\partial f_{\mathrm{G}}}{\partial E} - \frac{1}{r}\frac{\partial}{\partial r}\left(rH\kappa\frac{\partial f_{\mathrm{G}}}{\partial r}\right) + A_0 cH_*\delta\left(r-r_*\right)f_{\mathrm{G}} = 0 \ . \tag{F.2}$$

Now substitute in Equation (F.1),

$$-HvG\frac{\partial Y}{\partial r} + \frac{1}{3r}\frac{\partial}{\partial r}\left(rHv\right)EY\frac{\partial G}{\partial E} - \frac{1}{r}\frac{\partial}{\partial r}\left(rH\kappa G\frac{\partial Y}{\partial r}\right) + A_0 cH_*\delta\left(r-r_*\right)GY = 0 \ , \tag{F.3}$$

and then divide everything by GY,

$$-Hv\frac{1}{Y}\frac{\partial Y}{\partial r} + \frac{1}{3r}\frac{\partial}{\partial r}\left(rHv\right)E\frac{1}{G}\frac{\partial G}{\partial E} - \frac{1}{Y}\frac{1}{r}\frac{\partial}{\partial r}\left(rH\kappa\frac{\partial Y}{\partial r}\right) + A_0 cH_*\delta\left(r-r_*\right) = 0 \ . \tag{F.4}$$

Now we can separate out the radial spatial components to the LHS of Equation (F.4), as well as the energy components to the RHS,

$$3\left(\frac{d\ln\left(rHv\right)}{dr}\right)^{-1}\left[-\frac{1}{Y}\frac{dY}{dr} - \frac{1}{Y}\frac{1}{rHv}\frac{d}{dr}\left(rH\kappa\frac{dY}{dr}\right) + \frac{A_0 c}{v_*}\delta\left(r-r_*\right)\right] = -E\frac{1}{G}\frac{dG}{dE} \ , \tag{F.5}$$

which ensures that the LHS depends only on r and the RHS depends only on E. The only way for Equation (F.5) to hold is to have both the LHS and the RHS be equal to a common constant. This implies,

$$3\left(\frac{d\ln\left(rHv\right)}{dr}\right)^{-1}\left[-\frac{1}{Y}\frac{dY}{dr}-\frac{1}{Y}\frac{1}{rHv}\frac{d}{dr}\left(rH\kappa\frac{dY}{dr}\right)+\frac{A_0c}{v_*}\delta\left(r-r_*\right)\right]=-E\frac{1}{G}\frac{dG}{dE}=\lambda \tag{F.6}$$

where λ is a constant. The original PDE is now split into two ODEs, where we can focus on one,

$$-E\frac{1}{G}\frac{dG}{dE}=\lambda\ , \tag{F.7}$$

which becomes

$$\ln G=-\left(\ln E-\ln E_0\right)\lambda=-\ln\left(\frac{E}{E_0}\right)\lambda\ , \tag{F.8}$$

and thus a definitive function for $G(\lambda, E)$,

$$G(\lambda,E)=\left(\frac{E}{E_0}\right)^{-\lambda}\ , \tag{F.9}$$

in Equation (F.1),

$$f_\lambda\left(E,r\right)=\left(\frac{E}{E_0}\right)^{-\lambda}Y\left(\lambda,r\right)\ . \tag{F.10}$$

Now we plug in Equation (F.10) into Equation (F.2) and then separate out the variables, in which away from the shock ($r \neq r_*$), gets reduced to

$$\frac{d^2Y_n}{dr^2}+\left[\frac{v}{\kappa}+\frac{1}{r\kappa H}\frac{d}{dr}\left(rH\kappa\right)\right]\frac{dY_n}{dr}+\frac{\lambda_n}{3r\kappa H}\frac{d}{dr}\left(rHv\right)Y_n=0\ . \tag{F.11}$$

It should be noted that,

$$\frac{d}{dr}\left(rHv\right)=\left(rHv\right)\frac{d\ln\left(rHv\right)}{dr}\ . \tag{F.12}$$

Thus, plugging Equation (F.12) back into Equation (F.11) gets back Equation (29) from LB07,

$$\frac{d^2Y_n}{dr^2} + \left[\frac{v}{\kappa} + \frac{d\ln\left(rH\kappa\right)}{dr}\right]\frac{dY_n}{dr} + \frac{\lambda_n v Y_n}{3\kappa}\frac{d\ln\left(rHv\right)}{dr} = 0\ , \tag{F.13}$$

in which applying the diffusion coefficient function (Equation 2.48) brings it to,

$$\frac{d^2Y_n}{dr^2} + \left[\frac{r_{\mathrm{S}}}{\kappa_0\left(r - r_{\mathrm{S}}\right)^2} + \frac{d\ln\left(rHv\right)}{dr} + \frac{2}{\left(r - r_{\mathrm{S}}\right)}\right]\frac{dY_n}{dr} + \frac{\lambda_n r_{\mathrm{S}} Y_n}{3\kappa_0\left(r - r_{\mathrm{S}}\right)^2}\frac{d\ln\left(rHv\right)}{dr} = 0\ . \tag{F.14}$$

This is Equation (30) from LB07. Here, since I have the global solution for $v\left(r\right)$ and $H\left(r\right)$ for Model 3, I will be able to compute all of the coefficients in order to solve numerically for the spatial eigenfunction $Y_n\left(r\right)$.

Appendix G: Determining the Eigenfunction Jump Condition

The global solution for the eigenfunction $Y_n(r)$ must satisfy the continuity and derivative jump conditions associated with the presence of the shock/source at radius $r = r_*$. In order to do this we must integrate the vertically-integrated transport equation (Equation 3.65) with respect to the radius in the vicinity of the shock. From Equation (3.65),

$$-Hv\frac{dY_n}{dr} = \frac{\lambda_n}{3r}\frac{d}{dr}(rHv)\,Y_n + \frac{1}{r}\frac{d}{dr}\left(rH\kappa\frac{dY_n}{dr}\right) - A_0 cH_*\delta(r - r_*)\,Y_n\ , \tag{G.1}$$

let's multiply both sides by r first,

$$-Hvr\frac{dY_n}{dr} = \frac{\lambda_n}{3}\frac{d}{dr}(rHv)\,Y_n + \frac{d}{dr}\left(rH\kappa\frac{dY_n}{dr}\right) - A_0 cH_* r\delta(r - r_*)\,Y_n\ . \tag{G.2}$$

Now integrate Equation (G.2) with respect to the radius in the vicinity of the shock,

$$\begin{aligned} -\int Hvr\frac{dY_n}{dr}dr = \frac{\lambda_n}{3}\int \frac{d}{dr}(rHv)\,Y_n dr + \int \frac{d}{dr}\left(rH\kappa\frac{dY_n}{dr}\right)dr \\ -A_0 cH_*\int r\delta(r - r_*)\,Y_n dr\ , \end{aligned} \tag{G.3}$$

which expands out to,

$$\begin{aligned} -\int Hvr\frac{dY_n}{dr}dr = \frac{\lambda_n}{3}\left[-\Delta r_* HvY_n - \int rHv\frac{dY_n}{dr}dr\right] + \int d\left(rH\kappa\frac{dY_n}{dr}\right) \\ -A_0 cH_*\int r\delta(r - r_*)\,Y_n dr\ . \end{aligned} \tag{G.4}$$

Note, $\int Hvr\frac{dY_n}{dr}dr = 0$, thus Equation (G.4) reduces to,

$$0 = \frac{\lambda_n}{3}\left[-\Delta r_* H v Y_n\right] + \int d\left(rH\kappa\frac{dY_n}{dr}\right) - A_0 c H_* \int r\delta\left(r - r_*\right) Y_n dr \ , \tag{G.5}$$

which simplifies down to,

$$\boxed{\Delta\left(\frac{\lambda_n}{3}HvY_n + H\kappa\frac{dY_n}{dr}\right) = -A_0 c H_* Y_n\left(r_*\right)} \ , \tag{G.6}$$

where Δ denotes the difference between postshock and preshock quantities. It should be noted that Equation (G.6) is the generic jump derived and mainly applies to Model 3. For Model 1, where $H_+ = H_- = H_*$, this reduces down to

$$\boxed{\Delta\left(\frac{\lambda_n}{3}vY_n + \kappa\frac{dY_n}{dr}\right) = -A_0 c Y_n\left(r_*\right)} \ . \tag{G.7}$$

This establishes that $Y_n\left(r\right)$ must be continuous at the shock location, and its derivative must display a jump there.

Appendix H: Asymptotic Relations for the Eigenfunction

The purpose of this section is, to quote LB07, that "since the spatial eigenfunctions $Y_n(r)$ satisfy the second-order linear differential equation given in [Equation (3.65)], we must also impose two boundary conditions in order to determine the global solutions and the associated eigenvalues λ_n". Fortunately, it turns out that these required conditions can be based on the conditions set from the dynamical structure of the disk near the event horizon ($r \to r_{\rm S}$) and at large radii ($r \to \infty$, see Ch. 2 for details). As we move forward in this Appendix, we break down the eigenfunction boundary conditions for each of the Models.

H.1 Model 1

This, as well as the other Models, will rely on using Equation (3.65),

$$\frac{d^2 Y_n}{dr^2} + \left[\frac{r_{\rm S}}{\kappa_0 \left(r - r_{\rm S}\right)^2} + \frac{d \ln \left(r H v\right)}{dr} + \frac{2}{\left(r - r_{\rm S}\right)}\right] \frac{dY_n}{dr} + \frac{\lambda_n r_{\rm S}}{3\kappa_0 \left(r - r_{\rm S}\right)^2} \frac{d \ln \left(r H v\right)}{dr} Y_n = 0 \ , \tag{H.1}$$

to derive the various boundary conditions.

H.1.1 Near the Horizon ($r \to r_{\rm S}$)

In this region, LB07 noted that the Frobenius expansion method was useful in identifying the dominant terms in Equation (3.65). Let's first start with the disk half-thickness term for Model 1 (Equation 2.21) and combine it with Equations (1.14) and (2.65) to obtain

$$H = \frac{1}{\Omega_{\rm K}} \left[\frac{r^{3/2} \left(r - r_{\rm S}\right) v}{K_g}\right]^{(1-\gamma_g)/(\gamma_g+1)} = \frac{r^{1/2} \left(r - r_{\rm S}\right)}{GM} \left[\frac{r^{3/2} \left(r - r_{\rm S}\right) v}{K_g}\right]^{(1-\gamma_g)/(\gamma_g+1)} \ . \tag{H.2}$$

We know that as $r \to r_{\mathrm{S}}$, the bulk velocity v becomes (Equation 3.43)

$$v \propto (r - r_{\mathrm{S}})^{-1/2} \;, \qquad r \to r_{\mathrm{S}} \;. \tag{H.3}$$

Substituting this into Equation (H.2) yields,

$$H \propto (r - r_{\mathrm{S}})^{(\gamma_g+3)/2(\gamma_g+1)} \;, \qquad r \to r_{\mathrm{S}} \;. \tag{H.4}$$

Thus, we can apply Equation (H.3) and (H.4) to the logarithmic term in Equation (H.1) to show,

$$\frac{d \ln (rHv)}{dr} \approx \frac{1}{(\gamma_g + 1)} \frac{1}{(r - r_{\mathrm{S}})} \;, \qquad r \to r_{\mathrm{S}} \;, \tag{H.5}$$

which reduces Equation (H.1) to,

$$\frac{d^2 Y_n}{dr^2} + \left[\frac{r_{\mathrm{S}}}{\kappa_0 (r - r_{\mathrm{S}})^2} + \left\{ \frac{1}{(\gamma_g + 1)} + 2 \right\} \frac{1}{(r - r_{\mathrm{S}})} \right] \frac{dY_n}{dr} + \frac{\lambda_n r_{\mathrm{S}}}{3\kappa_0 (r - r_{\mathrm{S}})^3 (\gamma_g + 1)} Y_n = 0 \;. \tag{H.6}$$

Now we apply the Frobenius method for the zero-order term,

$$Y_n = (r - r_{\mathrm{S}})^{\alpha} \sum_{m=0}^{\infty} c_m (r - r_{\mathrm{S}})^m = \sum_{m=0}^{\infty} c_m (r - r_{\mathrm{S}})^{m+\alpha} \;, \tag{H.7}$$

and then the first-order term,

$$Y_n' = \sum_{m=0}^{\infty} (m + \alpha) \, c_m (r - r_{\mathrm{S}})^{m+\alpha-1} \;, \tag{H.8}$$

and finally the second-order term,

$$Y_n'' = \sum_{m=0}^{\infty} (m+\alpha)(m+\alpha-1)\, c_m \left(r - r_{\mathrm{S}}\right)^{m+\alpha-2} \ . \tag{H.9}$$

Now we combine Equations (H.6), (H.7), (H.8) and (H.9) to yield,

$$\begin{aligned} &\sum_{m=0}^{\infty} (m+\alpha)(m+\alpha-1)\, c_m \left(r - r_{\mathrm{S}}\right)^{m+\alpha-2} \\ &+ \left[\frac{r_{\mathrm{S}}}{\kappa_0 \left(r - r_{\mathrm{S}}\right)^2} + \left\{\frac{1}{(\gamma_g+1)} + 2\right\} \frac{1}{\left(r - r_{\mathrm{S}}\right)}\right] (m+\alpha)\, c_m \left(r - r_{\mathrm{S}}\right)^{m+\alpha-1} \\ &+ \frac{\lambda_n r_{\mathrm{S}}}{3\kappa_0 \left(r - r_{\mathrm{S}}\right)^3 (\gamma_g+1)} c_m \left(r - r_{\mathrm{S}}\right)^{m+\alpha} = 0 \ , \end{aligned} \tag{H.10}$$

which simplifies down to,

$$\begin{aligned} &\sum_{m=0}^{\infty} (m+\alpha)(m+\alpha-1)\, c_m \left(r - r_{\mathrm{S}}\right)^{m+\alpha-2} \\ &+ \left[\frac{r_{\mathrm{S}}}{\kappa_0 \left(r - r_{\mathrm{S}}\right)} + \left\{\frac{1}{(\gamma_g+1)} + 2\right\}\right] (m+\alpha)\, c_m \left(r - r_{\mathrm{S}}\right)^{m+\alpha-2} \\ &+ \frac{\lambda_n r_{\mathrm{S}}}{3\kappa_0 (\gamma_g+1)} c_m \left(r - r_{\mathrm{S}}\right)^{m+\alpha-3} = 0 \ . \end{aligned} \tag{H.11}$$

We can see that the $\alpha - 3$ terms are dominant, which we need to collect with $m = 0$,

$$\frac{r_{\mathrm{S}}}{\kappa_0} \alpha c_0 \left(r - r_{\mathrm{S}}\right)^{\alpha-3} + \frac{\lambda_n r_{\mathrm{S}}}{3\kappa_0 (\gamma_g+1)} c_0 \left(r - r_{\mathrm{S}}\right)^{\alpha-3} = 0 \ , \tag{H.12}$$

and solve for α,

$$\alpha = -\frac{\lambda_n}{3(\gamma_g+1)} \ . \tag{H.13}$$

Plugging this back into Equation (H.7) with $m = 0$ will yield the boundary condition near the horizon,

$$\boxed{Y_n \propto (r - r_{\rm S})^{-\lambda_n/3(\gamma_g+1)} \ , \qquad r \to r_{\rm S}} \ . \tag{H.14}$$

H.1.2 Towards Infinity ($r \to \infty$)

In Ch. 2 we learned that in this region, the bulk velocity v becomes (Equation 3.56),

$$v \propto r^{-5/2} \ , \qquad r \to \infty \ , \tag{H.15}$$

which can be plugged back into Equation (H.4) to show

$$H \propto r^{3/2} \ , \qquad r \to \infty \ , \tag{H.16}$$

which can then be applied to the logarithmic term in Equation (H.1) to obtain,

$$\frac{d \ln (rHv)}{dr} = 0 \ , \qquad r \to \infty \ . \tag{H.17}$$

The Frobenius Method

Now we will find the outer asymptotic by implementing the Frobenius method, just as it was done in the previous section. First we apply Equation (H.17) to Equation (H.1),

$$\frac{d^2 Y_n}{dr^2} + \left[\frac{r_{\rm S}}{\kappa_0 (r - r_{\rm S})^2} + \frac{2}{(r - r_{\rm S})} \right] \frac{dY_n}{dr} = 0 \ , \tag{H.18}$$

which in the limit $r \to \infty$ reduces to,

$$\frac{d^2 Y_n}{dr^2} + \left[\frac{r_{\rm S}}{\kappa_0 r^2} + \frac{2}{r} \right] \frac{dY_n}{dr} = 0 \ , \qquad r \to \infty \ . \tag{H.19}$$

Because this is a second-order differential equation, two linear independent solutions must be available in the asymptotic domain. One solution is simply

$$Y_n = C_0 \ , \tag{H.20}$$

where C_0 is a constant. To determine the second solution, we must employ the Frobenius method, in which the asymptotic solution is given by the power law expansion

$$Y_n = x^\beta \sum_{m=0}^{\infty} c_m x^m = \sum_{m=0}^{\infty} c_m x^{m+\beta} \ , \tag{H.21}$$

then the first-order term,

$$Y_n' = \sum_{m=0}^{\infty} (m+\beta)\, c_m x^{m+\beta-1} \ , \tag{H.22}$$

and finally the second-order term,

$$Y_n'' = \sum_{m=0}^{\infty} (m+\beta)\,(m+\beta-1)\, c_m x^{m+\beta-2} \ , \tag{H.23}$$

in which we've set $x = r/r_{\mathrm{S}}$. Combining Equations (H.21), (H.22) and (H.23) into Equation (H.19) will obtain

$$\sum_{m=0}^{\infty} (m+\beta)\,(m+\beta-1)\, c_m \left(\frac{r}{r_{\mathrm{S}}}\right)^{m+\beta-2} + \left[\frac{r_{\mathrm{S}}}{\kappa_0 r^2} + \frac{2}{r}\right] (m+\beta)\, c_m \left(\frac{r}{r_{\mathrm{S}}}\right)^{m+\beta-1} = 0 \ , \tag{H.24}$$

which when separated out becomes,

$$\sum_{m=0}^{\infty}(m+\beta)(m+\beta-1)\,c_m\left(\frac{r}{r_{\mathrm{S}}}\right)^{m+\beta-2}+2\,(m+\beta)\,c_m\left(\frac{1}{r_{\mathrm{S}}}\right)^{m+\beta-1}(r)^{m+\beta-2}$$
$$+\frac{1}{\kappa_0}(m+\beta)\,c_m\left(\frac{1}{r_{\mathrm{S}}}\right)^{m+\beta-2}(r)^{m+\beta-3}=0\ . \tag{H.25}$$

It can be shown that the most singular point occurs with the $\beta-2$ term, and at infinity the constant $1/r_{\mathrm{S}}$ is negated,

$$\sum_{m=0}^{\infty}(m+\beta)(m+\beta-1)\,c_m\,(r)^{m+\beta-2}+2\,(m+\beta)\,c_m\,(r)^{m+\beta-2}=0\ , \tag{H.26}$$

which shows that

$$\sum_{m=0}^{\infty}m+\beta=-2+1=-1\ . \tag{H.27}$$

Plugging this back into Equation (H.21), and combining it with Equation (H.20), reveals that the outer asymptotic form for the eigenfunction is given by

$$Y_n=\frac{C_1}{r}+C_0\ ,\qquad r\to\infty\ . \tag{H.28}$$

The Direct Method

Although, there is a more direct method for obtaining the same relationship in Equation (H.28). Continuing on with Equation (H.19),

$$\frac{d^2Y_n}{dr^2}+\left[\frac{r_{\mathrm{S}}}{\kappa_0 r^2}+\frac{2}{r}\right]\frac{dY_n}{dr}=0\ ,\qquad r\to\infty\ , \tag{H.29}$$

we can see that $1/r^2$ is the dominant term as $r \to \infty$, which simplifies down to,

$$\frac{d^2 Y_n}{dr^2} = -\frac{r_{\rm S}}{\kappa_0 r^2}\frac{dY_n}{dr} \ . \tag{H.30}$$

Thus, this results in the generic integrated form,

$$Y_n = \frac{C_1}{r} + C_0 \ , \qquad r \to \infty \ , \tag{H.31}$$

where C_0 and C_1 are constants of integration, in agreement with Equation (H.28). It should be noted that in Model 1, $C_0 = 0$ and $C_1 = 1$. Now we can move on determining the asymptotic forms for Models 2 and 3.

H.2 Models 2 and 3

In this region, just as we did in Model 1, we're going to first start with the disk half-thickness term for Models 2 and 3 (Equation 2.22) and combine it with Equation (1.14) to obtain

$$H = \frac{1}{\Omega_{\rm K}}\left[\frac{\gamma_g}{\gamma_r}a_r^2 + a_g^2\right]^{1/2} = \frac{r^{1/2}\left(r - r_{\rm S}\right)}{GM}\left[\frac{\gamma_g}{\gamma_r}a_r^2 + a_g^2\right]^{1/2} \ , \tag{H.32}$$

as well as use Equation (2.64) to show for the bulk velocity v,

$$v = \frac{K_g}{r^{3/2}\left(r - r_{\rm S}\right) a_g^{2/(\gamma_g - 1)}}\left[\frac{\gamma_g}{\gamma_r}a_r^2 + a_g^2\right]^{-1/2} \ . \tag{H.33}$$

Thus if we combine Equations (H.32) and (H.33) into the logarithmic term in Equation (H.1), we can show that

$$\frac{d\ln\left(rHv\right)}{dr} = \frac{d}{dr}\ln\left(\frac{K_g}{GM}a_g^{-2/(\gamma_g-1)}\right) \ , \tag{H.34}$$

meaning that the asymptotic terms either near the horizon or at large radii is dependent on those terms derived for the thermal sound speed a_g in those regions, which fortunately were done in Ch. 2 for Models 2 and 3.

H.2.1 Near the Horizon ($r \to r_\mathrm{S}$)

In the region close to the event horizon, we have worked out extensively in Ch. 2 that the asymptotic relation for the thermal sound speed a_g in Models 2 and 3 is given as (Equation 3.46),

$$a_g^2\left(r\right) \propto \left(r - r_\mathrm{S}\right)^{(1-\gamma_g)/(1+\gamma_g)} \quad , \qquad r \to r_\mathrm{S} \ , \tag{H.35}$$

which when plugged back into Equation (H.34) shows that

$$\frac{d\ln\left(rHv\right)}{dr} \approx -\frac{2}{\left(1+\gamma_g\right)}\frac{1}{\left(r - r_\mathrm{S}\right)} \ . \tag{H.36}$$

This is pretty much Equation (H.5) for Model 1, which means that if we applied Equation (H.36) back into Equation (H.1) for Models 2 and 3, we would likewise end up with the $\alpha - 3$ terms being dominant (with $m = 0$) via the Frobenius method, and thus we would derive the same asymptotic relation given by Equation (H.14).

H.2.2 Towards Infinity ($r \to \infty$)

In Ch. 2 we likewise learned that in this region, the thermal sound speed a_g becomes a constant, which means that Equation (H.34) becomes, essentially,

$$\frac{d\ln(rHv)}{dr} = 0 \ , \qquad r \to \infty \ . \tag{H.37}$$

This is exactly Equation (H.17) for Model 1, which means that if we applied either the Frobenius or direct method in this region, we would essentially achieve back the $1/r$ relation. However, for the purposes of this work as we will see in Ch. 4, we shall use Equation (H.31) to set the asymptotic boundary condition in this region for Models 2 and 3,

$$\boxed{Y_n = \frac{C_1}{r} + C_0 \ , \qquad r \to \infty} \ , \tag{H.38}$$

in which the constants of integration (C_0 and C_1) are yet to be assigned. Note that Equation (H.38) agrees with our earlier result given by Equation (H.31). Thus we can conclude that the asymptotic relationships are the same in all three Models.

Appendix I: Orthogonality of the Spatial Eigenfunctions

The following is the Appendix from Le & Becker (2007), with references made to my document. We can establish the orthogonality of the spatial eigenfunctions $Y_n(r)$ by starting with the Sturm-Liouville form (see Equation 3.73)

$$\frac{d}{dr}\left[S(r)\frac{dY_n}{dr}\right] + \lambda_n \omega(r) Y_n(r) = 0 \ , \tag{I.1}$$

where $\omega(r)$ and $S(r)$ are given by Equations (3.75) and (3.74), respectively. Let us suppose that λ_n and λ_m denote two distinct eigenvalues ($\lambda_n \neq \lambda_m$) with associated spatial eigenfunctions $Y_n(r)$ and $Y_m(r)$. Since Y_n and Y_m each satisfy Equation (I.1) for their respective values of λ, we can write

$$Y_n(r)\left\{\frac{d}{dr}\left[S(r)\frac{dY_m}{dr}\right] + \lambda_m \omega(r) Y_m(r)\right\} = 0 \ , \tag{I.2}$$

$$Y_m(r)\left\{\frac{d}{dr}\left[S(r)\frac{dY_n}{dr}\right] + \lambda_n \omega(r) Y_n(r)\right\} = 0 \ . \tag{I.3}$$

Subtracting Equation (I.3) from Equation (I.2) yields

$$Y_n(r)\frac{d}{dr}\left[S(r)\frac{dY_m}{dr}\right] - Y_m(r)\frac{d}{dr}\left[S(r)\frac{dY_n}{dr}\right] = (\lambda_n - \lambda_m)\,\omega(r)\,Y_n(r)\,Y_m(r) \ . \tag{I.4}$$

We can integrate Equation (I.4) by parts from $r = r_{\mathrm{S}}$ to $r = \infty$ to obtain

$$\begin{aligned} & Y_n(r)\, S(r)\, \frac{dY_m}{dr}\bigg|_{r_{\mathrm{S}}}^{\infty} - \int_{r_{\mathrm{S}}}^{\infty} S(r)\, \frac{dY_m}{dr}\frac{dY_n}{dr} dr \\ & - Y_m(r)\, S(r)\, \frac{dY_n}{dr}\bigg|_{r_{\mathrm{S}}}^{\infty} + \int_{r_{\mathrm{S}}}^{\infty} S(r)\, \frac{dY_n}{dr}\frac{dY_m}{dr} dr \\ & = (\lambda_n - \lambda_m) \int_{r_{\mathrm{S}}}^{\infty} \omega(r)\, Y_n(r)\, Y_m(r)\, dr\ . \end{aligned} \tag{I.5}$$

Upon cancellation of like terms, this expression reduces to

$$S(r)\left[Y_n(r)\, \frac{dY_m}{dr} - Y_m(r)\, \frac{dY_n}{dr}\right]_{r_{\mathrm{S}}}^{\infty} = (\lambda_n - \lambda_m) \int_{r_{\mathrm{S}}}^{\infty} \omega(r)\, Y_n(r)\, Y_m(r)\, dr\ . \tag{I.6}$$

On the basis of the asymptotic behaviors of $Y_n(r)$ as $r \to r_{\mathrm{S}}$ and $r \to \infty$ given by Equations (3.70) and (3.71), we conclude that the left-hand side of Equation (I.6) vanishes, leaving

$$\int_{r_{\mathrm{S}}}^{\infty} \omega(r)\, Y_n(r)\, Y_m(r)\, dr = 0, \quad m \neq n\ . \tag{I.7}$$

This result establishes that Y_m and Y_n are *orthogonal eigenfunctions* relative to the weight function $\omega(r)$ defined in Equation (3.75).

Bibliography

Bibliography

[1] A. A. Abdo, M. Ackermann, M. Ajello, W. B. Atwood, M. Axelsson, L. Baldini, J. Ballet, G. Barbiellini, D. Bastieri, K. Bechtol, R. Bellazzini, B. Berenji, R. D. Blandford, E. D. Bloom, E. Bonamente, A. W. Borgland, J. Bregeon, A. Brez, M. Brigida, P. Bruel, T. H. Burnett, G. A. Caliandro, R. A. Cameron, A. Cannon, P. A. Caraveo, J. M. Casandjian, E. Cavazzuti, C. Cecchi, . elik, E. Charles, C. C. Cheung, J. Chiang, S. Ciprini, R. Claus, J. Cohen-Tanugi, S. Colafrancesco, J. Conrad, L. Costamante, S. Cutini, D. S. Davis, C. D. Dermer, A. de Angelis, F. de Palma, S. W. Digel, D. Donato, E. d. C. e. Silva, P. S. Drell, R. Dubois, D. Dumora, Y. Edmonds, C. Farnier, C. Favuzzi, S. J. Fegan, J. Finke, W. B. Focke, P. Fortin, M. Frailis, Y. Fukazawa, S. Funk, P. Fusco, F. Gargano, D. Gasparrini, N. Gehrels, M. Georganopoulos, S. Germani, B. Giebels, N. Giglietto, P. Giommi, F. Giordano, M. Giroletti, T. Glanzman, G. Godfrey, I. A. Grenier, M.-H. Grondin, J. E. Grove, L. Guillemot, S. Guiriec, Y. Hanabata, A. K. Harding, M. Hayashida, E. Hays, D. Horan, G. Jhannesson, A. S. Johnson, R. P. Johnson, T. J. Johnson, W. N. Johnson, T. Kamae, H. Katagiri, J. Kataoka, N. Kawai, M. Kerr, J. Kndlseder, M. L. Kocian, M. Kuss, J. Lande, L. Latronico, M. Lemoine-Goumard, F. Longo, F. Loparco, B. Lott, M. N. Lovellette, P. Lubrano, G. M. Madejski, A. Makeev, M. N. Mazziotta, W. McConville, J. E. McEnery, C. Meurer, P. F. Michelson, W. Mitthumsiri, T. Mizuno, A. A. Moiseev, C. Monte, M. E. Monzani, A. Morselli, I. V. Moskalenko, S. Murgia, P. L. Nolan, J. P. Norris, E. Nuss, T. Ohsugi, N. Omodei, E. Orlando, J. F. Ormes, M. Ozaki, D. Paneque, J. H. Panetta, D. Parent, V. Pelassa, M. Pepe, M. Pesce-Rollins, F. Piron, T. A. Porter, S. Rain, R. Rando, M. Razzano, A. Reimer, O. Reimer, T. Reposeur, S. Ritz, L. S. Rochester, A. Y. Rodriguez, R. W. Romani, M. Roth, F. Ryde, H. F.-W. Sadrozinski, R. Sambruna, D. Sanchez, A. Sander, P. M. Saz Parkinson, J. D. Scargle, C. Sgr, M. S. Shaw, D. A. Smith, P. D. Smith, G. Spandre, P. Spinelli, M. S. Strickman, D. J. Suson, H. Tajima, H. Takahashi, T. Tanaka, G. B. Taylor, J. B. Thayer, D. J. Thompson, L. Tibaldo, D. F. Torres, G. Tosti, A. Tramacere, Y. Uchiyama, T. L. Usher, V. Vasileiou, N. Vilchez, A. P. Waite, P. Wang, B. L. Winer, K. S. Wood, T. Ylinen, M. Ziegler, D. E. Harris, F. Massaro, and . Stawarz, "Fermi Large Area Telescope Gamma-Ray Detection of the Radio Galaxy M87," *The Astrophysical Journal*, vol. 707, pp. 55–60, Dec. 2009.

[2] M. Abramowicz, M. Jaroszynski, and M. Sikora, "Relativistic, accreting disks," *Astronomy and Astrophysics*, vol. 63, pp. 221–224, Feb. 1978.

[3] M. A. Abramowicz, B. Czerny, J. P. Lasota, and E. Szuszkiewicz, "Slim accretion disks," *The Astrophysical Journal*, vol. 332, pp. 646–658, Sep. 1988.

[4] M. A. Abramowicz, M. Jaroszyski, S. Kato, J.-P. Lasota, A. Raska, and A. Sdowski, "Leaving the innermost stable circular orbit: the inner edge of a black-hole accretion disk at various luminosities," *Astronomy and Astrophysics*, vol. 521, p. A15, Oct. 2010.

[5] M. A. Abramowicz, "Innermost parts of accretion disks are thermally and secularly stable," *Nature*, vol. 294, p. 235, Nov. 1981.

[6] M. A. Abramowicz, G. Bjornsson, and J. E. Pringle, Eds., *Theory of Black Hole Accretion Discs*, 1st ed. Cambridge, UK ; New York: Cambridge University Press, Jan. 1999.

[7] M. A. Abramowicz and S. K. Chakrabarti, "Standing shocks in adiabatic black hole accretion of rotating matter," *The Astrophysical Journal*, vol. 350, pp. 281–287, Feb. 1990.

[8] M. A. Abramowicz, X. Chen, S. Kato, J.-P. Lasota, and O. Regev, "Thermal equilibria of accretion disks," *The Astrophysical Journal Letters*, vol. 438, pp. L37–L39, Jan. 1995.

[9] M. A. Abramowicz, "Physics of Black Hole Accretion," in *Theory of Black Hole Accretion Discs*, 1st ed., M. A. Abramowicz, G. Bjornsson, and J. E. Pringle, Eds. Cambridge, UK ; New York: Cambridge University Press, Jan. 1999, pp. 50–60.

[10] M. Abramowitz and I. A. Stegun, Eds., *Handbook of Mathematical Functions: with Formulas, Graphs, and Mathematical Tables*, 0009th ed. New York: Dover Publications, Jun. 1965.

[11] F. A. Aharonian, "Proton-synchrotron radiation of large-scale jets in active galactic nuclei," *Monthly Notices of the Royal Astronomical Society*, vol. 332, pp. 215–230, May 2002.

[12] E. Aliu, T. Arlen, T. Aune, M. Beilicke, W. Benbow, A. Bouvier, S. M. Bradbury, J. H. Buckley, V. Bugaev, K. Byrum, A. Cannon, A. Cesarini, L. Ciupik, E. Collins-Hughes, M. P. Connolly, W. Cui, R. Dickherber, C. Duke, M. Errando, A. Falcone, J. P. Finley, G. Finnegan, L. Fortson, A. Furniss, N. Galante, D. Gall, S. Godambe, S. Griffin, J. Grube, R. Guenette, G. Gyuk, D. Hanna, J. Holder, H. Huan, G. Hughes, C. M. Hui, T. B. Humensky, A. Imran, P. Kaaret, N. Karlsson, M. Kertzman, D. Kieda, H. Krawczynski, F. Krennrich, M. J. Lang, S. LeBohec, A. S. Madhavan, G. Maier, P. Majumdar, S. McArthur, A. McCann, P. Moriarty, R. Mukherjee, P. D. Nuez, R. A. Ong, M. Orr, A. N. Otte, N. Park, J. S. Perkins, A. Pichel, M. Pohl, H. Prokoph, J. Quinn, K. Ragan, L. C. Reyes, P. T. Reynolds, E. Roache, H. J. Rose, J. Ruppel, D. B. Saxon, M. Schroedter, G. H. Sembroski, G. D. entrk, C. Skole, D. Staszak, G. Tei, M. Theiling, S. Thibadeau, K. Tsurusaki, J. Tyler, A. Varlotta, V. V. Vassiliev, S. Vincent, M. Vivier, S. P. Wakely, J. E. Ward, T. C. Weekes, A. Weinstein, T. Weisgarber, D. A. Williams, and B. Zitzer, "VERITAS Observations of Day-scale Flaring of M 87 in 2010 April," *The Astrophysical Journal*, vol. 746, p. 141, Feb. 2012. [Online]. Available: http://adsabs.harvard.edu/abs/2012ApJ...746..141A

[13] S. W. Allen, T. Di Matteo, and A. C. Fabian, "Hard X-ray emission from elliptical galaxies," *Monthly Notices of the Royal Astronomical Society*, vol. 311, pp. 493–506, Jan. 2000.

[14] M. W. Anyakoha, P. N. Okeke, and S. E. Okoye, "Estimates of proton energies in extragalactic radio sources," *Astrophysics and Space Science*, vol. 132, pp. 65–72, Apr. 1987.

[15] A. Atoyan and C. D. Dermer, "Synchrotron versus Compton Interpretations for Extended X-Ray Jets," *The Astrophysical Journal*, vol. 613, pp. 151–158, Sep. 2004.

[16] ——, "TeV Emission from the Galactic Center Black Hole Plerion," *The Astrophysical Journal Letters*, vol. 617, pp. L123–L126, Dec. 2004.

[17] W. I. Axford, E. Leer, and G. Skadron, "The acceleration of cosmic rays by shock waves," *International Cosmic Ray Conference*, vol. 11, pp. 132–137, 1977.

[18] W. Baade and R. Minkowski, "On the Identification of Radio Sources." *The Astrophysical Journal*, vol. 119, p. 215, Jan. 1954.

[19] S. A. Balbus and J. F. Hawley, "A powerful local shear instability in weakly magnetized disks. I - Linear analysis. II - Nonlinear evolution," *The Astrophysical Journal*, vol. 376, pp. 214–233, Jul. 1991.

[20] ——, "A Powerful Local Shear Instability in Weakly Magnetized Disks. IV. Nonaxisymmetric Perturbations," *The Astrophysical Journal*, vol. 400, pp. 610–621, Dec. 1992.

[21] M. V. Barkov, V. Bosch-Ramon, and F. A. Aharonian, "Interpretation of the Flares of M87 at TeV Energies in the Cloud-Jet Interaction Scenario," *The Astrophysical Journal*, vol. 755, p. 170, Aug. 2012.

[22] P. A. Becker, S. Das, and T. Le, "Diffusive Particle Acceleration in Shocked, Viscous Accretion Disks: Green's Function Energy Distribution," *The Astrophysical Journal*, vol. 743, p. 47, Dec. 2011.

[23] P. A. Becker and D. Kazanas, "Exact Expressions for the Critical Mach Numbers in the Two-Fluid Model of Cosmic-Ray-modified Shocks," *The Astrophysical Journal*, vol. 546, pp. 429–446, Jan. 2001.

[24] P. A. Becker and T. Le, "Inner Boundary Conditions for Advection-dominated Accretion onto Black Holes," *The Astrophysical Journal*, vol. 588, pp. 408–424, May 2003.

[25] P. A. Becker, P. Subramanian, and D. Kazanas, "Relativistic Outflows from Advection-dominated Accretion Disks around Black Holes," *The Astrophysical Journal*, vol. 552, pp. 209–220, May 2001.

[26] P. A. Becker and P. Subramanian, "Restrictions on the Physical Prescription for the Viscosity in Advection-dominated Accretion Disks," *The Astrophysical Journal*, vol. 622, pp. 520–530, Mar. 2005.

[27] P. A. Becker, "First-order Fermi acceleration in spherically symmetric flows - Solutions including quadratic losses," *The Astrophysical Journal*, vol. 397, pp. 88–116, Sep. 1992.

[28] M. C. Begelman, "Black holes in radiation-dominated gas - an analogue of the Bondi accretion problem," *Monthly Notices of the Royal Astronomical Society*, vol. 184, pp. 53–67, Jul. 1978.

[29] ——, "Can a spherically accreting black hole radiate very near the Eddington limit," *Monthly Notices of the Royal Astronomical Society*, vol. 187, pp. 237–251, Apr. 1979.

[30] G. V. Bicknell and M. C. Begelman, "Understanding the Kiloparsec-Scale Structure of M87," *The Astrophysical Journal*, vol. 467, p. 597, Aug. 1996.

[31] J. A. Biretta, C. P. Stern, and D. E. Harris, "The radio to X-ray spectrum of the M87 jet and nucleus," *The Astronomical Journal*, vol. 101, pp. 1632–1646, May 1991.

[32] G. Bjornsson, "The Role of Electron-positron Pairs in Hot Accretion Flows," in *Theory of Black Hole Accretion Discs*, 1st ed., M. A. Abramowicz, G. Bjornsson, and J. E. Pringle, Eds. Cambridge, UK ; New York: Cambridge University Press, Jan. 1999, pp. 91–99.

[33] R. D. Blandford and J. P. Ostriker, "Particle acceleration by astrophysical shocks," *The Astrophysical Journal Letters*, vol. 221, pp. L29–L32, Apr. 1978.

[34] R. D. Blandford and D. G. Payne, "Hydromagnetic flows from accretion discs and the production of radio jets," *Monthly Notices of the Royal Astronomical Society*, vol. 199, pp. 883–903, Jun. 1982.

[35] R. D. Blandford and R. L. Znajek, "Electromagnetic extraction of energy from Kerr black holes," *Monthly Notices of the Royal Astronomical Society*, vol. 179, pp. 433–456, May 1977.

[36] R. D. Blandford and M. C. Begelman, "On the fate of gas accreting at a low rate on to a black hole," *Monthly Notices of the Royal Astronomical Society*, vol. 303, pp. L1–L5, Feb. 1999.

[37] H. Bondi and F. Hoyle, "On the mechanism of accretion by stars," *Monthly Notices of the Royal Astronomical Society*, vol. 104, p. 273, 1944.

[38] H. Bondi, "On spherically symmetrical accretion," *Monthly Notices of the Royal Astronomical Society*, vol. 112, p. 195, 1952.

[39] A. Brandenburg, "Disc Turbulence and Viscosity," in *Theory of Black Hole Accretion Discs*, 1st ed., M. A. Abramowicz, G. Bjornsson, and J. E. Pringle, Eds. Cambridge, UK ; New York: Cambridge University Press, Jan. 1999, pp. 61–90.

[40] A. E. Broderick, A. Loeb, and M. J. Reid, "Localizing Sagittarius A* and M87 on Microarcsecond Scales with Millimeter Very Long Baseline Interferometry," *The Astrophysical Journal*, vol. 735, p. 57, Jul. 2011.

[41] A. E. Broderick, R. Narayan, J. Kormendy, E. S. Perlman, M. J. Rieke, and S. S. Doeleman, "The Event Horizon of M87," *The Astrophysical Journal*, vol. 805, p. 179, Jun. 2015.

[42] B. W. Carroll and D. A. Ostlie, *An Introduction to Modern Astrophysics*, 1st ed. Reading, Mass: Benjamin Cummings, Dec. 1995.

[43] S. K. Chakrabarti and D. Molteni, "Smoothed Particle Hydrodynamics Confronts Theory: Formation of Standing Shocks in Accretion Disks and Winds around Black Holes," *The Astrophysical Journal*, vol. 417, p. 671, Nov. 1993.

[44] S. K. Chakrabarti, "A systematic study of the standing shocks in astrophysical flows near a compact object," *Publications of the Astronomical Society of Japan*, vol. 41, pp. 1145–1172, 1989.

[45] ——, *Theory of Transonic Astrophysical Flows.* Singapore ; Teaneck, N.J: World Scientific Pub Co Inc, Sep. 1990.

[46] S. Chandrasekhar, "The Stability of Non-Dissipative Couette Flow in Hydromagnetics," *Proceedings of the National Academy of Science*, vol. 46, pp. 253–257, Feb. 1960.

[47] ——, *Hydrodynamic and Hydromagnetic Stability*, dover edition ed. New York: Dover Publications, Feb. 1981.

[48] X. Chen, M. A. Abramowicz, J.-P. Lasota, R. Narayan, and I. Yi, "Unified description of accretion flows around black holes," *The Astrophysical Journal Letters*, vol. 443, pp. L61–L64, Apr. 1995.

[49] X. Chen, "Hot accretion discs with advection," *Monthly Notices of the Royal Astronomical Society*, vol. 275, pp. 641–648, Aug. 1995.

[50] H. D. Curtis, "Descriptions of 762 Nebulae and Clusters Photographed with the Crossley Reflector," *Publications of Lick Observatory*, vol. 13, pp. 9–42, 1918.

[51] S. Das, I. Chattopadhyay, A. Nandi, and S. K. Chakrabarti, "Computation of outflow rates from accretion disks around black holes," *Astronomy and Astrophysics*, vol. 379, pp. 683–689, Nov. 2001.

[52] S. Das, I. Chattopadhyay, and S. K. Chakrabarti, "Standing Shocks around Black Holes: An Analytical Study," *The Astrophysical Journal*, vol. 557, pp. 983–989, Aug. 2001.

[53] S. W. Davis, C. Done, and O. M. Blaes, "Testing Accretion Disk Theory in Black Hole X-Ray Binaries," *The Astrophysical Journal*, vol. 647, pp. 525–538, Aug. 2006.

[54] C. D. Dermer and G. Menon, *High Energy Radiation from Black Holes: Gamma Rays, Cosmic Rays, and Neutrinos.* Princeton University Press, Oct. 2009.

[55] V. Despringre, D. Fraix-Burnet, and E. Davoust, "First millimeter mapping of the jet and nucleus of M 87." *Astronomy and Astrophysics*, vol. 309, pp. 375–380, May 1996.

[56] T. Di Matteo, E. Quataert, S. W. Allen, R. Narayan, and A. C. Fabian, "Low-radiative-efficiency accretion in the nuclei of elliptical galaxies," *Monthly Notices of the Royal Astronomical Society*, vol. 311, pp. 507–521, Jan. 2000.

[57] L. O. Drury and J. H. Voelk, "Hydromagnetic shock structure in the presence of cosmic rays," *The Astrophysical Journal*, vol. 248, pp. 344–351, Aug. 1981.

[58] A. Eckart and R. Genzel, "Stellar proper motions in the central 0.1 PC of the Galaxy," *Monthly Notices of the Royal Astronomical Society*, vol. 284, pp. 576–598, Jan. 1997.

[59] J. A. Eilek and M. Kafatos, "The high-energy spectrum of hot accretion disks," *The Astrophysical Journal*, vol. 271, pp. 804–819, Aug. 1983.

[60] A. A. Esin, J. E. McClintock, J. J. Drake, M. R. Garcia, C. A. Haswell, R. I. Hynes, and M. P. Muno, "Modeling the Low-State Spectrum of the X-Ray Nova XTE J1118+480," *The Astrophysical Journal*, vol. 555, pp. 483–488, Jul. 2001.

[61] H. Falcke and P. L. Biermann, "The jet/disk symbiosis. III. What the radio cores in GRS 1915+105, NGC 4258, M 81 and SGR A* tell us about accreting black holes," *Astronomy and Astrophysics*, vol. 342, pp. 49–56, Feb. 1999.

[62] J. E. Felten, "The Radiation and Physical Properties of the M87 Jet," *The Astrophysical Journal*, vol. 151, p. 861, Mar. 1968.

[63] J. E. Felten, H. C. Arp, and C. R. Lynds, "The M87 Jet. II. Temperature, Ionization, and X-Radiation in a Secondary-Production Model," *The Astrophysical Journal*, vol. 159, p. 415, Feb. 1970.

[64] R. Feltman, "Stephen Hawking believes hes solved a huge mystery about black holes," *The Washington Post*, Aug. 2015. [Online]. Available: https://www.washingtonpost.com/news/speaking-of-science/wp/2015/08/25/stephen-hawking-believes-hes-solved-a-huge-mystery-about-black-holes/?postshare=8911440496769845

[65] L. G. Fishbone and V. Moncrief, "Relativistic fluid disks in orbit around Kerr black holes," *The Astrophysical Journal*, vol. 207, pp. 962–976, Aug. 1976.

[66] H. C. Ford, Z. I. Tsvetanov, L. Ferrarese, and W. Jaffe, "HST detections of massive black holes in the centers of galaxies (Review)," vol. 184, eprint: arXiv:astro-ph/9711299, 1998, p. 377.

[67] H. C. Ford, R. J. Harms, Z. I. Tsvetanov, G. F. Hartig, L. L. Dressel, G. A. Kriss, R. C. Bohlin, A. F. Davidsen, B. Margon, and A. K. Kochhar, "Narrowband HST images of M87: Evidence for a disk of ionized gas around a massive black hole," *The Astrophysical Journal Letters*, vol. 435, pp. L27–L30, Nov. 1994.

[68] J. Frank, A. King, and D. Raine, *Accretion Power in Astrophysics*, 3rd ed. Cambridge, UK ; New York: Cambridge University Press, Feb. 2002.

[69] R. J. Harms, H. C. Ford, Z. I. Tsvetanov, G. F. Hartig, L. L. Dressel, G. A. Kriss, R. Bohlin, A. F. Davidsen, B. Margon, and A. K. Kochhar, "HST FOS spectroscopy of M87: Evidence for a disk of ionized gas around a massive black hole," *The Astrophysical Journal Letters*, vol. 435, pp. L35–L38, Nov. 1994.

[70] J. F. Hawley, L. L. Smarr, and J. R. Wilson, "A numerical study of nonspherical black hole accretion. I Equations and test problems," *The Astrophysical Journal*, vol. 277, pp. 296–311, Feb. 1984.

[71] ——, "A numerical study of nonspherical black hole accretion. II - Finite differencing and code calibration," *The Astrophysical Journal Supplement Series*, vol. 55, pp. 211–246, Jun. 1984.

[72] L. C. Ho, A. V. Filippenko, and W. L. W. Sargent, "Demographics of nuclear activity in nearby galaxies," vol. 184, 1998, p. 463.

[73] F. Hoyle and R. A. Lyttleton, "The effect of interstellar matter on climatic variation," *Proceedings of the Cambridge Philosophical Society*, vol. 35, p. 405, 1939.

[74] ——, "On the accretion of interstellar matter by stars," *Proceedings of the Cambridge Philosophical Society*, vol. 36, p. 325, 1940.

[75] ——, "On the physical aspects of accretion by stars," *Proceedings of the Cambridge Philosophical Society*, vol. 36, p. 424, 1940.

[76] S. Ichimaru, "Bimodal behavior of accretion disks - Theory and application to Cygnus X-1 transitions," *The Astrophysical Journal*, vol. 214, pp. 840–855, Jun. 1977.

[77] M. Jaroszynski, M. A. Abramowicz, and B. Paczynski, "Supercritical accretion disks around black holes," *Acta Astronomica*, vol. 30, pp. 1–34, 1980.

[78] M. Kafatos and R. X. Yang, "Transonic Inviscid Disc Flows in the Schwarzschild Metric - Part One," *Monthly Notices of the Royal Astronomical Society*, vol. 268, p. 925, Jun. 1994.

[79] J. I. Katz, "X-rays from spherical accretion onto degenerate dwarfs," *The Astrophysical Journal*, vol. 215, pp. 265–275, Jul. 1977.

[80] D. Kazanas and D. C. Ellison, "The central engine of quasars and active galactic nuclei Hadronic interactions of shock-accelerated relativistic protons," *The Astrophysical Journal*, vol. 304, pp. 178–187, May 1986.

[81] K. I. Kellermann, R. Sramek, M. Schmidt, D. B. Shaffer, and R. Green, "VLA observations of objects in the Palomar Bright Quasar Survey," *The Astronomical Journal*, vol. 98, pp. 1195–1207, Oct. 1989.

[82] R. P. Kerr, "Gravitational Field of a Spinning Mass as an Example of Algebraically Special Metrics," *Physical Review Letters*, vol. 11, pp. 237–238, Sep. 1963.

[83] J. Kormendy and D. Richstone, "Inward Bound—The Search For Supermassive Black Holes In Galactic Nuclei," *Annual Review of Astronomy and Astrophysics*, vol. 33, p. 581, 1995.

[84] M. Kozlowski, M. Jaroszynski, and M. A. Abramowicz, "The analytic theory of fluid disks orbiting the Kerr black hole," *Astronomy and Astrophysics*, vol. 63, pp. 209–220, Feb. 1978.

[85] T. Le and P. A. Becker, "A Self-consistent Model for the Formation of Relativistic Outflows in Advection-dominated Accretion Disks with Shocks," *The Astrophysical Journal Letters*, vol. 617, pp. L25–L28, Dec. 2004.

[86] ——, "Particle Acceleration and the Production of Relativistic Outflows in Advection-dominated Accretion Disks with Shocks," *The Astrophysical Journal*, vol. 632, pp. 476–498, Oct. 2005.

[87] ——, "Particle Acceleration in Advection-dominated Accretion Disks with Shocks: Green's Function Energy Distribution," *The Astrophysical Journal*, vol. 661, pp. 416–429, May 2007.

[88] R. V. E. Lovelace, "Dynamo model of double radio sources," *Nature*, vol. 262, pp. 649–652, Aug. 1976.

[89] J.-F. Lu and F. Yuan, "Isothermal Shocks in Adiabatic Black-Hole Accretion Flows," *Publications of the Astronomical Society of Japan*, vol. 49, pp. 525–533, Oct. 1997.

[90] D. Lynden-Bell, "Galactic Nuclei as Collapsed Old Quasars," *Nature*, vol. 223, pp. 690–694, Aug. 1969.

[91] D. MacDonald and K. S. Thorne, "Black-hole electrodynamics - an absolute-space/universal-time formulation," *Monthly Notices of the Royal Astronomical Society*, vol. 198, pp. 345–382, Jan. 1982.

[92] G. M. Madejski, "Black Holes in Active Galactic Nuclei: Observations," in *Theory of Black Hole Accretion Discs*, 1st ed., M. A. Abramowicz, G. Bjornsson, and J. E. Pringle, Eds. Cambridge, UK ; New York: Cambridge University Press, Jan. 1999, pp. 21–40.

[93] H. L. Marshall, B. P. Miller, D. S. Davis, E. S. Perlman, M. Wise, C. R. Canizares, and D. E. Harris, "A High-Resolution X-Ray Image of the Jet in M87," *The Astrophysical Journal*, vol. 564, pp. 683–687, Jan. 2002.

[94] T. A. Matthews and A. R. Sandage, "Optical Identification of 3c 48, 3c 196, and 3c 286 with Stellar Objects." *The Astrophysical Journal*, vol. 138, p. 30, Jul. 1963.

[95] E. Meyer-Hofmeister, B. F. Liu, and F. Meyer, "The hard to soft spectral transition in LMXBs-affected by recondensation of gas into an inner disk," *Astronomy and Astrophysics*, vol. 508, pp. 329–337, Dec. 2009.

[96] R. Narayan, S. Kato, and F. Honma, "Global Structure and Dynamics of Advection-dominated Accretion Flows around Black Holes," *The Astrophysical Journal*, vol. 476, pp. 49–60, Feb. 1997.

[97] R. Narayan, R. Mahadevan, and E. Quataert, "Advection-Dominated Accretion around Black Holes," in *Theory of Black Hole Accretion Discs*, 1st ed., M. A. Abramowicz, G. Bjornsson, and J. E. Pringle, Eds. Cambridge, UK ; New York: Cambridge University Press, Jan. 1999, pp. 148–182.

[98] R. Narayan and I. Yi, "Advection-dominated accretion: A self-similar solution," *The Astrophysical Journal Letters*, vol. 428, pp. L13–L16, Jun. 1994.

[99] ——, "Advection-dominated accretion: Self-similarity and bipolar outflows," *The Astrophysical Journal*, vol. 444, pp. 231–243, May 1995.

[100] ——, "Advection-dominated Accretion: Underfed Black Holes and Neutron Stars," *The Astrophysical Journal*, vol. 452, p. 710, Oct. 1995.

[101] I. Novikov and K. Thorne, "Astrophysics of Black Holes," in *Black Holes*, C. DeWitt and B. DeWitt, Eds. Gordon and Breach, Paris, 1973, pp. 343–450.

[102] F. N. Owen, J. A. Eilek, and N. E. Kassim, "M87 at 90 Centimeters: A Different Picture," *The Astrophysical Journal*, vol. 543, pp. 611–619, Nov. 2000.

[103] B. Paczysky and P. J. Wiita, "Thick accretion disks and supercritical luminosities," *Astronomy and Astrophysics*, vol. 88, pp. 23–31, Aug. 1980.

[104] E. S. Perlman, W. B. Sparks, J. Radomski, C. Packham, R. S. Fisher, R. Pia, and J. A. Biretta, "Deep 10 Micron Imaging of M87," *The Astrophysical Journal Letters*, vol. 561, pp. L51–L54, Nov. 2001.

[105] B. M. Peterson, *An Introduction to Active Galactic Nuclei*, 1st ed. Cambridge; New York: Cambridge University Press, Feb. 1997.

[106] T. Piran, "The role of viscosity and cooling mechanisms in the stability of accretion disks," *The Astrophysical Journal*, vol. 221, pp. 652–660, Apr. 1978.

[107] J. E. Pringle, "Accretion discs in astrophysics," *Annual Review of Astronomy and Astrophysics*, vol. 19, pp. 137–162, 1981.

[108] R. J. Protheroe and D. Kazanas, "On the origin of relativistic particles and gamma-rays in quasars," *The Astrophysical Journal*, vol. 265, pp. 620–624, Feb. 1983.

[109] E. Quataert, "Radiatively Inefficient Accretion Flow Models of Sgr A*," *Astronomische Nachrichten Supplement*, vol. 324, pp. 435–443, Sep. 2003. [Online]. Available: http://adsabs.harvard.edu/abs/2003ANS...324..435Q

[110] R. Ramaty and R. E. Lingenfelter, "Galactic Cosmic-Ray Electrons," *Journal of Geophysical Research*, vol. 71, p. 3687, Aug. 1966.

[111] M. J. Rees, "Black Hole Models for Active Galactic Nuclei," *Annual Review of Astronomy and Astrophysics*, vol. 22, pp. 471–506, 1984.

[112] M. J. Rees, M. C. Begelman, R. D. Blandford, and E. S. Phinney, "Ion-supported tori and the origin of radio jets," *Nature*, vol. 295, pp. 17–21, Jan. 1982.

[113] M. J. Rees, "Accretion and the quasar phenomenon," *Physica Scripta*, vol. 17, pp. 193–200, Mar. 1978.

[114] M. Regis and P. Ullio, "Multiwavelength signals of dark matter annihilations at the Galactic center," *Physical Review D*, vol. 78, p. 043505, Aug. 2008.

[115] C. S. Reynolds, T. Di Matteo, A. C. Fabian, U. Hwang, and C. R. Canizares, "The 'quiescent' black hole in M87," *Monthly Notices of the Royal Astronomical Society*, vol. 283, pp. L111–L116, Dec. 1996.

[116] G. B. Rybicki and A. P. Lightman, *Radiative Processes in Astrophysics*, revised edition ed. New York: Wiley-VCH, Mar. 1985.

[117] E. E. Salpeter, "Accretion of Interstellar Matter by Massive Objects." *The Astrophysical Journal*, vol. 140, pp. 796–800, Aug. 1964.

[118] R. M. Sambruna, J. K. Gambill, L. Maraschi, F. Tavecchio, R. Cerutti, C. C. Cheung, C. M. Urry, and G. Chartas, "A Survey of Extended Radio Jets with Chandra and the Hubble Space Telescope," *The Astrophysical Journal*, vol. 608, pp. 698–720, Jun. 2004.

[119] W. L. W. Sargent, P. J. Young, C. R. Lynds, A. Boksenberg, K. Shortridge, and F. D. A. Hartwick, "Dynamical evidence for a central mass concentration in the galaxy M87," *The Astrophysical Journal*, vol. 221, pp. 731–744, May 1978.

[120] R. Schlickeiser, "Cosmic-ray transport and acceleration. I - Derivation of the kinetic equation and application to cosmic rays in static cold media. II - Cosmic rays in moving cold media with application to diffusive shock wave acceleration," *The Astrophysical Journal*, vol. 336, pp. 243–293, Jan. 1989.

[121] ——, "Cosmic-Ray Transport and Acceleration. II. Cosmic Rays in Moving Cold Media with Application to Diffusive Shock Wave Acceleration," *The Astrophysical Journal*, vol. 336, p. 264, Jan. 1989.

[122] M. Schmidt, "3c 273 : A Star-Like Object with Large Red-Shift," *Nature*, vol. 197, p. 1040, Mar. 1963.

[123] R. Schdel, T. Ott, R. Genzel, R. Hofmann, M. Lehnert, A. Eckart, N. Mouawad, T. Alexander, M. J. Reid, R. Lenzen, M. Hartung, F. Lacombe, D. Rouan, E. Gendron, G. Rousset, A.-M. Lagrange, W. Brandner, N. Ageorges, C. Lidman, A. F. M. Moorwood, J. Spyromilio, N. Hubin, and K. M. Menten, "A star in a 15.2-year orbit around the supermassive black hole at the centre of the Milky Way," *Nature*, vol. 419, pp. 694–696, Oct. 2002.

[124] N. I. Shakura and R. A. Sunyaev, "Black holes in binary systems. Observational appearance." *Astronomy and Astrophysics*, vol. 24, pp. 337–355, 1973.

[125] S. L. Shapiro, A. P. Lightman, and D. M. Eardley, "A two-temperature accretion disk model for Cygnus X-1 - Structure and spectrum," *The Astrophysical Journal*, vol. 204, pp. 187–199, Feb. 1976.

[126] Y. Shi, G. H. Rieke, D. C. Hines, K. D. Gordon, and E. Egami, "Thermal and Nonthermal Infrared Emission from M87," *The Astrophysical Journal*, vol. 655, pp. 781–789, Feb. 2007.

[127] W. B. Sparks, J. A. Biretta, and F. Macchetto, "The Jet of M87 at Tenth-Arcsecond Resolution: Optical, Ultraviolet, and Radio Observations," *The Astrophysical Journal*, vol. 473, p. 254, Dec. 1996.

[128] H. C. Spruit, "Stationary shocks in accretion disks," *Astronomy and Astrophysics*, vol. 184, pp. 173–184, Oct. 1987.

[129] P. Subramanian, P. A. Becker, and M. Kafatos, "Ion Viscosity Mediated by Tangled Magnetic Fields: an Application to Black Hole Accretion Disks," *The Astrophysical Journal*, vol. 469, p. 784, Oct. 1996.

[130] P. Subramanian, P. A. Becker, and D. Kazanas, "Formation of Relativistic Outflows in Shearing Black Hole Accretion Coronae," *The Astrophysical Journal*, vol. 523, pp. 203–222, Sep. 1999.

[131] J. C. Tan, H. Beuther, F. Walter, and E. G. Blackman, "A Search for Molecular Gas in the Nucleus of M87 and Implications for the Fueling of Supermassive Black Holes," *The Astrophysical Journal*, vol. 689, pp. 775–781, Dec. 2008.

[132] K. S. Thorne and R. H. Price, "Cygnus X-1 - an interpretation of the spectrum and its variability," *The Astrophysical Journal Letters*, vol. 195, pp. L101–L105, Feb. 1975.

[133] C. M. Urry and P. Padovani, "Unified Schemes for Radio-Loud Active Galactic Nuclei," *Publications of the Astronomical Society of the Pacific*, vol. 107, p. 803, Sep. 1995.

[134] E. P. Velikhov, "Stability of an ideally conducting liquid flowing between cylinders rotating in a magnetic field," *Soviet Physics JETP*, vol. Vol: 36 (Vol: 9 English), no. Number 5, pp. 1398–1404 (995–998 English), Nov. 1959.

[135] G. M. Webb and T. J. Bogdan, "Energetic particle acceleration in spherically symmetric accretion flows and shocks," *The Astrophysical Journal*, vol. 320, pp. 683–698, Sep. 1987.

[136] S. Weinberg, *Gravitation and Cosmology: Principles and Applications of the General Theory of Relativity*, 1st ed. New York: John Wiley & Sons, Inc., Jul. 1972.

[137] F. Yuan, S. Markoff, and H. Falcke, "A Jet-ADAF model for Sgr A*," *Astronomy and Astrophysics*, vol. 383, pp. 854–863, Mar. 2002.

[138] F. Yuan, "Possible evidence for the disc origin for the powering of jets in Sgr A* and nearby elliptical galaxies," *Monthly Notices of the Royal Astronomical Society*, vol. 319, pp. 1178–1184, Dec. 2000.

[139] F. Yusef-Zadeh, R. Arendt, H. Bushouse, W. Cotton, D. Haggard, M. W. Pound, D. A. Roberts, M. Royster, and M. Wardle, "A 3 pc Scale Jet-driven Outflow from Sgr A*," *The Astrophysical Journal Letters*, vol. 758, p. L11, Oct. 2012.

[140] A. Zee, *Einstein Gravity in a Nutshell.* Princeton: Princeton University Press, May 2013.

[141] Y. B. Zel'dovich and I. D. Novikov, "Mass of Quasi-Stellar Objects," *Soviet Physics Doklady*, vol. 9, p. 834, Apr. 1965.

Curriculum Vitae

My interest in physics began as a child when I was influenced by the *Back to the Future* series and *The Time Machine (1960 version)*. It was my introduction into the science-fiction culture and led to my curiosities of all things physics and technology related. While I'm naturally mechanically intuitive and could figure out how things worked (and fix accordingly), I was more interested in knowing why they worked. Though the subject of physics intimidated me in high school, I debated whether to pursue it as an undergrad at James Madison University. Torn between my interest in that as well as other fields, I settled on a Bachelor of Science in Integrated Science and Technology and graduated in Spring 2005. It was an interdisciplinary degree where my concentrations where in Energy and Biotechnology. However I was not completely satisfied with the level of physics I got there, and knowing that I would regret not achieving this childhood pursuit, I (on a whim) came to George Mason University during the Fall 2005 semester to see if I can apply for the Masters program in Applied and Engineering Physics. It was an attempt to see if I could learn this field for myself, and thanks to Maria taking a chance on me, I was accepted (on condition) for the Spring 2006 semester. It was indeed a struggle to work and play catchup at the same time (considering my background didn't include a traditional education in physics), but it nevertheless proved worth it when I achieved my Masters of Science in Spring 2008. During my time in the Masters program I dabbled at little in Quantum Information Science, in which the work I did I found out was considered more Doctorate level than Masters level. Encouraged to continue my studies further by many colleagues, I came back in the Spring of 2010, after taking a year and a half off to figure things out, to pursue a Doctorate degree in Physics, something I never thought I would ever do before. At the conclusion of this Dissertation, my academic background thus far would have been in Renewable Energy, Quantum Information Science, and Astrophysics.